

Studies of the emittance growth due to noise in the Crab Cavity RF systems



Thesis submitted in accordance with the requirements of the
University of Liverpool for the degree of Doctor in Philosophy

by

Natalia Triantafyllou

Day Month Year

Abstract

Acknowledgments

Contents

Abstract	iii
Acknowledgments	v
List of figures	xxv
List of tables	xxvii
List of symbols v2	xxxi
1 Introduction	1
1.1 The CERN accelerator complex	1
1.1.1 The CERN Super Proton Synchrotron	3
1.2 High-Luminosity LHC project and Crab Cavities	4
1.2.1 Crab cavities	5
1.3 Motivation, objectives and thesis outline	8
2 Basics of accelerator beam dynamics	12
2.1 Motion of charged particles in electromagnetic fields	13
2.2 Single-particle beam dynamics	16
2.2.1 Transverse motion	17
2.2.1.1 Linear dynamics	17
2.2.1.2 Non-linear dynamics	30
2.2.2 Longitudinal motion	31
2.3 Collective effects	34
2.3.1 Wakefields and impedance	35
2.4 Optics models for accelerators	40

2.5	Tracking simulation codes	41
2.5.1	PyHEADTAIL	41
2.5.2	Sixtracklib	44
3	Theory of Crab Cavity RF noise-induced emittance growth	46
3.1	Noise	46
3.2	Crab Cavity noise and emittance growth	49
3.2.1	Crab Cavity amplitude and phase noise	49
3.2.2	Emittance growth formulas	52
3.3	Studies in KEKB	54
4	Experimental studies 2018: emittance growth from Crab Cavity noise	55
4.1	Crab Cavities in the SPS	56
4.1.1	Considerations about the Crab Cavity operation	56
4.2	Experimental configuration and procedure	57
4.2.1	Preparatory experimental studies	58
4.2.2	Machine and beam configuration	58
4.2.3	Experimental procedure for emittance growth measurements .	59
4.3	Injected RF noise	60
4.3.1	Expected emittance growth from Mastoridis–Baudrenghien model	60
4.4	Measurement of Crab Cavity voltage	63
4.4.1	Crab Cavity phase offset	66
4.5	Emittance growth measurements	67
4.5.1	SPS Wire Scanners	67
4.5.2	Experimental results	70
4.6	Bunch length and intensity measurements	74
4.6.1	ABWLM and Wall Current Monitor	74
4.6.2	Bunch length measurements	75
4.6.3	Longitudinal profile measurements	75
4.6.4	Intensity measurements	77
4.7	Comparison of measured transverse emittance growth with the theoretical predictions	78

0. Contents

4.8 Conclusions and outlook	81
5 Investigation of the discrepancy between emittance growth theory and experimental data	82
5.1 Parametric studies based on the theoretical model	83
5.1.1 Sensitivity to bunch length	83
5.1.2 Sensitivity to CC voltage	84
5.2 Benchmarking theory against PyHEADTAIL	85
5.3 Benchmarking theory against Sixtracklib	90
5.3.1 Emittance growth simulations with CC noise modeled as transverse kicks on the angle co-ordinate.	91
5.3.2 Implementation of Crab Cavity in Sixtracklib	93
5.3.3 CC noise induced emittance growth in the presence of local CC scheme	97
5.3.4 CC noise induced emittance growth in the presence of global CC scheme	98
5.3.5 CC noise induced emittance growth with the measured noise spectrum	100
5.3.6 CC noise induced emittance growth with the non-linear SPS model	102
5.4 Conclusions and outlook	103
6 Simulation studies: Emittance growth suppression mechanism from the beam transverse impedance	106
6.1 SPS transverse impedance model	107
6.1.1 Testing the implementation in PyHEADTAIL	108
6.2 Emittance growth simulations setup	113
6.3 Suppression of noise induced emittance growth by the beam coupling impedance	115
6.4 Characterisation of the emittance growth suppression by the impedance	117
6.4.1 Sensitivity of CC RF phase noise induced emittance growth to amplitude-dependent tune shift	117
6.4.2 Amplitude noise	119

6.4.3	CC RF noise at 200 MHz	121
6.4.4	Pure dipolar noise	122
6.4.5	Sensitivity to linear chromaticity	124
6.4.6	Disentangling quadrupolar and dipolar impedance contributions	126
6.5	Suppression mechanism	128
6.5.1	Similar effects studied in the past and motivation	128
6.5.2	Intensity scans	129
6.5.3	Spectral analysis of the bunch centroid motion	131
6.5.4	Dependence on bunch length	134
6.6	Conclusions	137
7	Experimental studies 2022: investigation of the effect of impedance on emittance growth	138
7.1	Motivation	138
7.2	Experiment with CC as noise source	139
7.2.1	Machine and beam configuration	139
7.2.2	Experiment preparation and procedure	143
7.2.3	Calibration of CC phase offset and voltage measurement	146
7.2.4	Measurement of background growth rate in "coast" mode	148
7.2.5	Results of CC Experiment A: dependence of emittance growth rates on CC noise power	150
7.2.6	Results of CC Experiment B: sensitivity of emittance growth rates to amplitude-dependent tune shift	154
7.3	Experiment with dipole noise	160
7.4	Supplementary measurements with CC RF noise	163
7.4.1	Experimental setup	163
7.4.2	Calibration of CC phase offset and voltage measurements	164
7.4.3	Measurement of background growth rate in "coast" mode	165
7.4.4	Emittance growth measurements with strong octupoles	166
7.4.5	Comparison of measurements against PyHEADTAIL simulations with the SPS impedance model	168
7.4.6	Emittance growth measurements with dominant amplitude noise	169
7.5	Conclusions and outlook	170

0. Contents

8 Conclusions	172
8.1 Implications for HL-LHC	176
A Definitions and methods of statistical analysis	181
A.1 Basic terminology	181
A.1.1 Averages	181
A.1.2 Measuring the spread	182
A.1.3 Data sets with more than one variables - Covariance	183
A.2 Least squares fitting	184
A.3 Propagation of uncertainty	185
B Fundamentals of signal analysis and measurement	186
B.1 Continuous-time analysis	186
B.2 Discrete-time analysis	188
B.3 Measuring amplitude and phase noise	194
B.4 Applying a measured noise spectrum in numerical simulations	196
B.4.1 Crab cavity noise in numerical simulations	197
B.4.2 Measured noise spectrum	197
B.4.3 Generating time series	197
B.4.4 Validation of the time series reconstruction	199
C Appendix C	203
C.1 Solutions of betatron equations	203
C.2 Detuning with amplitude	204
C.2.1 Residual rms tune spread in the SPS	206
C.3 SPS octupoles calibration	207
C.4 Wire Scanner measurements in 2022	208
C.4.1 Example beam profiles	208
C.4.2 Example emittance growth measurements	209
C.5 Head-Tail monitor calibration for the 2022 analysis	210
C.6 Bunch length measurements in May 2022	210
C.6.1 Measurements during the experiment where the scan on the noise levels was performed	211

C.6.2 Measurements during the experiment where the scan on the octupole strength was performed	211
C.7 Transverse emittance growth measurements with dipole noise in 2022	213
C.8 Transverse emittance growth measurements with CC RF noise - September 12, 2022	215
C.9 Bunch length measurements in September 2022	215
D SPS Headt-Tail monitor as the main diagnostic for the Crab Cavity studies	218
D.1 General information	219
D.2 Post processing in the presence of Crab Cavities	220
D.2.1 Head-Tail monitor baseline correction	220
D.2.2 Crab Cavity voltage reconstruction	223
D.2.3 Demonstration of crabbing with proton beams	224
E Glossary and defintions	226
Bibliography	242

List of Figures

1.1	Schematic view of the CERN accelerator complex. The different colors correspond to the different machines. The year of commissioning and the type of particles used in each one of them are also indicated along with the circumference for the circular machines. The image is courtesy of CERN.	2
1.2	Visualisation of the CC kick (green line) on the bunch particles (blue dots). The bunch here appears much smaller than the CC wavelength which means that only the linear part of the kick affects the bunch. This will be the case for the HL-LHC scenario.	5
1.3	Layout of the LHC and the SPS. The CC location for the HL-LHC configuration is marked. Two CCs (one per ring) will be installed on each side of ATLAS (red) and CMS (orange). Two prototype CCs were also installed in the SPS (magenta) in 2018, to be tested before their installation in LHC. The layout can be found in Ref. [9] and was modified inspired by Ref. [10].	6
1.4	Collision with and without the use of CCs [11]. CCs restore the overlap between the bunches recovering the luminosity reduction caused by the crossing angle, θ_c . The blue and red colors indicate two bunches in the different rings.	6
2.1	Co-ordinate system used to describe particles motion in a synchrotron. This is a local co-ordinate system, with the origin following the reference trajectory around the accelerator. The unit vector \mathbf{e}_z is tangential to the reference trajectory at each point, \mathbf{e}_y is vertical, and \mathbf{e}_x is horizontal, and perpendicular to \mathbf{e}_z and \mathbf{e}_y	15

2.2 Phase space co-ordinates (u, u') turn by turn, for a particle moving along the ring but at a particular position s which is characterised by the following twiss parameters $[\alpha_u(s), \beta_u(s), \gamma_u(s)]$. In the labels shown on the diagram, the dependence on the s parameter has been omitted.	23
2.3 Normalised phase space: the trajectory shown represents the particle motion as the particle moves around the synchrotron. This is not the case in the regular (not normalised) phase space, since the shape of the phase space ellipse will change with position around the ring. The particle moves turn by turn in a circle of radius $\sqrt{2J_u}$	24
2.4 Transverse phase space of a Gaussian bunch. The figure is a courtesy of Tarsi Prebibaj [30].	26
2.5 The closed orbit and the betatron oscillations around it in the presence of dispersion [32]	28
2.6 Phase stability for particles in a circular accelerator which operates above transition.	34
2.7 Wakefield interaction, where the source particle (blue) affects the witness particle (yellow) travelling at a distance z behind it [42]. $(\Delta x_1, \Delta y_1)$ and $(\Delta x_2, \Delta y_2)$ are the transverse offsets of the source and witness particles respectively.	36
2.8 Longitudinal bunch slicing for the implementation of wakefield kicks in PyHEADTAIL. Without the slicing technique (left) the wake kicks on the red macroparticle are generated from all the green macroparticles resulting in computationally expensive simulations. Instead, when the bunch is sliced longitudinally (right) the wake kicks on the macroparticles in the red slice i are generated by the macroparticles in the green slices j , decreasing significantly the computation time. The figures are courtesy of M. Schenk [55]	43

0. List of Figures

2.9 Graphical representation of the accelerator model and tracking procedure in PyHEADTAIL (inspired by the graphs in Refs. [55, 57]). In this example the ring is split in four segments separated by the interaction points (IPs). Wakefield and multipole kicks are applied to the macroparticles in IP2 and IP4. The macroparticles are transported between the IPs by a linear transfer map (which can include detuning effects) in the transverse plane. The longitudinal coordinates are updated once per turn.	44
3.1 Modulation in amplitude or amplitude noise (left) and its impact on the particles within the bunch (right). The blue dots represent the individual particles while the red arrows indicate the direction of the noise kicks which act on them.	52
3.2 Modulation in phase or phase noise (left) and its impact on the particles within the bunch (right). The blue dots represent the individual particles while the red arrows indicate the direction of the noise kicks which act on them.	52
3.3 Correction term for amplitude (left) and phase noise (right) over a range of bunch length values.	54
4.1 Example amplitude (left) and phase (right) noise spectra measured with a spectrum analyzer E5052B [73] during the emittance growth studies with CCs in SPS. The noise extends up to 10 kHz (grey dashed line) overlapping the first betatron sideband at ~8 kHz (green dashed line). The spikes at high frequencies correspond to the harmonics of the revolution frequency and are a result of the beam induced signal from its passage through the CC.	61

4.2 Beam-based measurement of the CC voltage as reconstructed from the Head-Tail monitor before the emittance growth measurements in 2018 (red). The sinusoidal fit on the reconstructed voltage in order to obtain the CC voltage amplitude is also shown (blue solid line). The fit results, are given in the yellow box. The measured voltage amplitude, $V_{0,CC}$, was found to be 0.98 MV while its uncertainty, d , was measured at 0.04 MV. The measured voltage value agrees well with the requested value of 1 MV.	65
4.3 Sketch of the SPS rotational wire scanners [79]. The wire moves across the proton beam generating secondary particles which are then detecting by a scintillator and a photomultiplier. From the measured photomultiplier current the beam profile is reconstructed. . .	68
4.4 Vertical beam profile obtained from the BWS.41677.V instrument. The measured data points (light blue) are fitted with a four parameter gaussian (orange) to obtain the beam size. The calculated emittance and its uncertainty are also shown.	68
4.5 Bunch by bunch horizontal (top) and vertical (bottom) emittance evolution during the experiment on September, 15, 2018. The four different colors indicate the different bunches. The different applied noise levels are also shown while the moments when the noise level changed are indicated with the grey vertical dashed lines. The emittance growth rates along with their uncertainties for the seven different noise settings are displayed at the legend at the bottom of the plots.	72
4.6 Summary plot of the emittance growth study with CC noise in 2018. The transverse emittance growth rate, for the four bunches, is shown as a function of the different levels of applied noise.	73

0. List of Figures

4.7 Evolution of the beam in transverse and longitudinal planes during the CC noise induced emittance growth experiment. Top: Horizontal emittance growth measured with the SPS Wire Scanners. Middle: Vertical emittance growth measured with the SPS Wire Scanner. Bottom: Bunch length evolution measured with the ABWLM (small markers) and the Wall Current Monitor (bigger markers).	76
4.8 Longitudinal profiles (top) and relative bunch position with respect to the center of the RF bucket (bottom) acquired with the Wall Current Monitor. The acquisitions correspond to the times when the sudden jumps in the bunch length evolution are observed (see Fig. 4.7).	77
4.9 Intensity evolution as measured with ABLWM (smaller markers) and with the Wall Current Monitor (bigger markers) during the experiment with CC noise in 2018.	79
4.10 Summary plot of the emittance growth study with CC noise in 2018 focused on bunch 1 only. The measured emittance growth rate (blue) and the expected growths from the theoretical model (black) are shown as a function of the different levels of applied noise.	80
5.1 Vertical emittance growth for different bunch length values computed using the analytical formulas Eqs. (3.11) and (3.12) for the experimental configuration of 2018. The blue dot shows the average bunch length over all coasts in 2018. The blue box around it gives the upper and lower limits of its measurements.	84
5.2 Vertical emittance growth for different values of CC voltage computed using the analytical formulas Eq. (3.11) and (3.12) for the experimental configuration of 2018.	85
5.3 Power spectra of the CC amplitude (left) and phase (right) noise used in the PyHEADTAIL simulations.	87
5.4 Vertical emittance growth driven by CC RF amplitude noise (left) and phase noise (right) as simulated with PyHEADTAIL for a configuration close to the experimental conditions of the SPS CC tests in 2018.	90

<p>5.5 Vertical emittance growth driven by CC RF amplitude noise (left) and phase noise (right) as simulated with Sixtracklib simulation tool for a configuration close to the experimental conditions of the SPS CC tests in 2018. The CC noise is modeled as uncorrelated kicks on the angle variables of the particle every turn following Eqs. (3.8) and. (3.7) for phase and amplitude noise respectively.</p> <p>5.6 Vertical orbit shift at the location of the horizontal Wire Scanner (SPS.BWS.51995.H.) induced by the CC element as computed analytically (blue) and from tracking simulations with Sixtracklib (orange).</p> <p>5.7 Vertical orbit shift at the location of the horizontal Wire Scanner (SPS.BWS.51995.H.) as obtained with Sixtracklib tracking through the nominal SPS lattice. <i>Green</i>: Only CC1 operates at 1 MV and $\phi_{RF-Mult,1}=90$ deg. <i>Red</i>: Only CC2 operates at 1 MV and $\phi_{CC2}=270$ deg. <i>Orange</i>: The two CCs operate at the same voltage but in opposite phase: $\phi_{RF-Mult,1}=90$ deg and $\phi_{RF-Mult,2}=270$ deg. <i>Blue</i>: Orbit shift calculated analytically using Eq. (5.4).</p> <p>5.8 Vertical emittance growth driven by CC RF amplitude noise (left) and phase noise (right) as simulated with Sixtracklib simulation tool for a configuration close to the experimental conditions of the SPS CC tests in 2018 but for a local CC scheme. The CC noise is applied on CC1, following Eq. (5.5).</p> <p>5.9 Vertical emittance growth driven by CC RF amplitude noise (left) and phase noise (right) as simulated with Sixtracklib simulation tool for a configuration close to the experimental conditions of the SPS CC tests in 2018 but for a global CC scheme. The CC noise is applied on CC1 which operates at 1 MV, following Eq. (5.5), while CC2 is switched OFF.</p>	<p>92</p> <p>95</p> <p>98</p> <p>99</p> <p>99</p>
---	---

0. List of Figures

5.10 Example amplitude (left) and phase (right) noise spectra measured with a spectrum analyzer E5052B [73] during the emittance growth studies with CCs in SPS. The noise extends up to about 10 kHz (grey dashed line) overlapping the first betatron sideband at \sim 8 kHz (green dashed line). The spikes at high frequencies correspond to the harmonics of the revolution frequency and are a result of the bunch crossing.	100
5.11 Vertical emittance growth driven by CC RF amplitude noise (left) and phase noise (right) as simulated with the Sixtracklib simulation tool for a configuration close to the experimental conditions of the SPS CC tests 2018. The measured phase and amplitude noise spectra from Coast3-Setting3 are used for the simulations. The CC noise is applied on CC2 which operates at 1 MV, following Eq. (5.5), while CC1 is switched off.	101
5.12 Vertical emittance growth driven by CC RF amplitude and phase noise as simulated with the Sixtracklib simulation tool for a configuration close to the experimental conditions of the SPS CC tests 2018. The measured phase and amplitude noise spectra from Coast3-Setting3 are used for the simulations. Both types of noise are applied on CC2 which operates at 1 MV, following Eq. (5.5), while CC1 is switched off.	102
5.13 Vertical emittance growth driven by CC RF phase noise as simulated with Sixtracklib simulation tool for a configuration close to the experimental conditions of the SPS CC tests 2018. The measured phase and amplitude noise spectra from Coast3-Setting3 are used for the simulations. The non-linear model (including multipole components of the main dipole magnets) of the SPS machine was used for the tracking. Both types of noise are applied on CC2 which operates at 1 MV, following Eq. (5.5), while CC1 is switched OFF	104

6.1 Horizontal (left) and vertical (right) impedance model of the SPS. The contributions from the wall, the kickers and the step transitions are visible at the low frequencies (up to ~ 0.4 GHz). The impedance of the RF cavities and the beam position monitors (BPMs) correspond to the peaks observed between $\sim 0.4\text{-}1$ GHz.	108
6.2 Horizontal (left) and vertical (right) wakefunctions of the SPS. The wake functions are available in the public GitLab repository of [90]. For comparison the bunch length in the SPS CC experiments is ~ 1.85 ns ($4\sigma_t$).	108
6.3 Horizontal (left) and vertical (right) coherent tunes as a function of intensity in the presence of the beam coupling SPS impedance obtained using analytical formula (blue dashed line) and PyHEADTAIL tracking simulations (orange line). The impedance model and the wake functions used are available in [90].	111
6.4 Horizontal (left) and vertical (right) coherent tunes as a function of intensity in the presence of the beam coupling SPS impedance obtained using analytical formula (blue dashed line) and PyHEADTAIL tracking simulations (orange line). The impedance model is available in [90]. The PyHEADTAIL simulations use the "updated wakefields model" (in contrast with the results of Fig. 6.3) which can be found in [100].	112
6.5 Transverse emittance growth driven by CC RF phase noise without (blue) and with (orange) the impedance effects for the beam and machine conditions of the CC tests in SPS during 2018.	116
6.6 Transverse emittance growth driven by CC RF phase noise (as a function of detuning coefficient), without (blue) and with (orange) impedance effects.	119
6.7 Transverse emittance growth driven by CC RF amplitude noise (as a function of detuning coefficient), without (blue) and with (orange) impedance effects.	120

0. List of Figures

6.8 Transverse emittance growth driven by CC RF noise, assuming a CC frequency of 200 MHz, without (blue) and with (orange) the impedance effects as a function of tune spread.	121
6.9 Transverse emittance growth driven by a pure dipolar noise kick without (blue) and with (orange) the impedance effects as a function of tune spread.	123
6.10 Transverse emittance growth driven by CC RF phase noise, assuming a CC frequency of 400 MHz, without (blue) and with (orange) the impedance effects as a function of tune spread is shown for five different values of linear chromaticity increasing from top left to bottom right.	125
6.11 Transverse emittance growth driven by CC RF phase noise, for a CC frequency of 400 MHz, without (blue) and with (orange) the impedance effects as a function of tune spread. <i>Top:</i> Simulation results with only the dipolar (left) and quadrupolar (right) impedance contribution. <i>Bottom:</i> Simulation results with the dipolar and quadrupolar impedance contributions combined.	127
6.12 PyHEADTAIL simulations illustrating the effect of the beam intensity on the transverse emittance growth driven by CC RF phase noise in the presence of impedance effects. The blue vertical line shows the intensity value during the SPS CC tests in 2018.	130
6.13 Power spectral density of the vertical bunch centroid motion on a logarithmic scale in the presence of the SPS transverse impedance model, calculated over 10^6 turns with 5×10^4 macroparticles for different values of intensity increasing from top left to bottom right. . . .	133
6.14 PyHEADTAIL simulations illustrating the impact of the bunch length on the transverse emittance growth driven by CC RF phase noise in the absence (blue) and in the presence (orange) of impedance effects. The analytically predicted emittance growth rates (not including impedance effects) are also shown (black). The regime of the realistic bunch length values during the SPS CC tests of 2018 is depicted with the grey stripe.	135

7.1 Transverse emittance growth driven by CC RF phase noise without (blue) and with (orange) the impedance effects. The green and yellow areas indicate regimes where the octupoles require less than 200 A and 400 A respectively for their operation.	145
7.2 Calibration plot for the CC1 as obtained during the experiment on 16 May 2022, displaying the CC voltage at the center of the bunch $t = 0$ for different values of the inspector phase.	148
7.3 Horizontal (blue) and vertical (red) background emittance growth measured during the experiment with CC1 on May 16, 2022, with no artificial noise injected in the CC RF system and with the Landau octupoles switched off.	149
7.4 Horizontal (blue) and vertical (red) emittance evolution of a single bunch during the CC experiment on 16 May, 2022. The different phase noise levels injected in the RF system of CC1, are shown in the caption for each plot.	151
7.5 Overview plot of the emittance growth study with noise injected in the CC1 in 2022. The measured horizontal (blue) and vertical (red) emittance growth rates are shown as a function of the different power levels of applied phase noise. The error bars indicate the error of the linear fit to the emittance values (see Section 4.5).	152
7.6 Summary plot of the emittance growth study with different noise levels injected in the RF system of CC1 in 2022. The vertical measured growth rate (red) and the expected growths from the Mastoridis–Baudrenghien model (black) are shown as a function of the different levels of applied phase noise. The error bars indicate the error of the linear fit on the emittance values (see Section 4.5)	153
7.7 Horizontal (blue) and vertical (red) emittance evolution of a single bunch during the CC experiment on 16 May, 2022 driven by phase noise of -104.7 dBc/Hz. The different octupole settings are displayed in the captions of each plot.	155

0. List of Figures

7.8 Example of the evolution of the horizontal oscillation of the bunch centroid during the CC measurements for $k_{\text{LOD}} = -10 \text{ /m}^4$. This measurement is acquired with the BBQ instrument [113].	156
7.9 Measured horizontal (blue) and vertical (red) emittance growth driven by phase noise of -104.7 dBc/Hz injected in the RF system of CC1 for different octupole settings. The growth predicted from the analytical model without taking into account the impedance induced emittance growth suppression is $\sim 19 \mu\text{m/h}$	158
7.10 Measured (magenta) and simulated (orange) vertical emittance growth driven by phase noise injected in the RF system of CC1 for different octupole settings. Both measured and simulated rates are normalised with the corresponding prediction from the Mastoridis–Baudrenghien model.	159
7.11 Measured horizontal (blue) and vertical (red) emittance growth driven by dipole noise introduced with the SPS beam kicker in the vertical plane for different octupole settings.	162
7.12 Calibration plot for the CC1 as obtained during the experiment on September 12, 2022, displaying the CC voltage at the center of the bunch $t = 0$ for different values of the inspector phase.	164
7.13 Horizontal (blue) and vertical (red) background emittance growth measured during the experiment with CC1 on September 12, 2022, with no artificial noise injected in the CC RF system and with $k_{\text{LOD}} = +30 \text{ /m}^4$	165
7.14 Measured horizontal (blue) and vertical (red) emittance growth driven by phase noise of -103.3 dBc/Hz injected in the RF system of CC1 for different octupole settings. The growth predicted from the analytical model without taking into account the impedance induced emittance growth suppression is $\sim 28 \mu\text{m/h}$	167

7.15 Measured (magenta-May 2022, green-September 2022) and simulated (orange) vertical emittance growth driven by phase noise injected in the RF system of CC1 for different octupole settings. Both measured and simulated rates are normalised with the corresponding prediction from the Mastoridis–Baudrenghien model.	168
7.16 Horizontal (blue) and vertical (red) emittance growth measured during the experiment with CC1 on September 12, 2022	170
B.1 Sampling of the continuous signal $y(t)$ at a finite number of points N . The sampled signal is the discrete-time signal $y(n\Delta t)$ with Δt the sampling interval and n an integer such that $n \in [0, N - 1]$	188
B.2 Example of a signal sampled at discrete time intervals, and the corresponding discrete Fourier transform.	189
B.3 Power spectrum of $y = \sin(2\pi f t)$, $f = 50$ Hz.	191
B.4 Single-sided power spectrum of the signal shown in Fig. B.2(a).	192
B.5 Instantaneous voltage of an oscillator in the presence of (a) amplitude noise, (b) phase noise, and (c) both amplitude and phase noise.	196
B.6 Steps required to generate the sequence of noise kicks to be applied in the simulations from the measured noise spectrum.	200
B.7 Power spectral density computed from the time series ϕ_n produced from a measured power spectrum (black), compared with the original measured power spectrum (green).	201
B.8 Comparison between emittance growth found from simulations in PyHEADTAIL and emittance growth expected from an analytical model [63]. The emittance growth is driven by amplitude and phase noise, with kicks in the simulations generated from a measured power spectrum.	202
C.1 Calibration curve for the LOF SPS family as obtained from LSA. b_3 is defined in Eq. (2.4).	207
C.2 Calibration curve for the LOD SPS family as obtained from LSA. b_3 is defined in Eq. (2.4).	208

0. List of Figures

C.3 Transverse beam profiles as obtained from SPS.BWS.51637.H during the CC experiment in the SPS in 2022. The data points from the IN (OUT) scan are shown with blue (orange) color.	209
C.4 Transverse beam profiles as obtained from SPS.BWS.51637.H during the CC experiment in the SPS in 2022. The data points from the IN (OUT) scan are shown with blue (orange) color.	210
C.5 The calibration was performed by T. Levens by performing orbit bumps (around the reference orbit) and measuring the normalised position of the bunch in the vertical plane (plane of interest). The normalised position is obtained as the difference of the signal divided by the sum. More details on the calibration procedure are given in [132]. This plot is courtesy of T. Levens	211
C.6 Evolution of the bunch length during the CC experiment on May 16, 2022. The different phase noise levels injected in the RF system of CC1, are displayed at the captions of each plot.	212
C.7 Evolution of the bunch length during the CC experiment on May 16, 2022. The different octupole settings are displayed at the captions of each plot.	213
C.8 Horizontal (blue) and vertical (red) emittance evolution of a single bunch during the experiment with dipole noise on May 16-17, 2022. The different octupole settings are displayed at the captions of each plot.	214
C.9 Horizontal (blue) and vertical (red) emittance evolution of a single bunch during the experiment with dipole noise on September 12, 2022. The different octupole settings are displayed at the captions of each plot.	216
C.10 Evolution of the bunch length during the CC experiment on September 12, 2022. The different octupole settings are displayed at the captions of each plot.	217

D.1 Diagram of the SPS Head-Tail monitor [135]. The beam is passing through a straight stripline coupler which is followed by a 180° hybrid. This configuration provides the sum (Σ) and the difference (Δ) signal of the two electrodes.	219
D.2 Example difference and sum signals (top and bottom plots, respectively) from the Head-Tail monitor, in time scale, with respect to the longitudinal position within the bunch over several SPS revolutions, after the basic post processing [135] but before the baseline correction. The different colors indicate the signals from different turns (every 100 turns).	220
D.3 2D representation of example difference and sum signals with respect to the longitudinal position within the bunch obtained from the Head-Tail monitor over several SPS revolutions.	221
D.4 Head-Tail monitor baseline correction for the SPS CC tests. The baseline signal (blue dashed line) refers to the mean of the difference signals acquired before the CC - main RF synchronisation. The measured signal (blue solid line) corresponds to the mean of the difference signal acquired after the synchronisation. Last, the corrected signal (orange solid line) is obtained after subtracting the baseline from the measured signal.	222
D.5 Head-Tail acquisitions before and after the synchronisation of the SPS main RF with the CC.	222
D.6 Intra-bunch offset from the CC kick expressed in millimeters after the removal of the baseline.	223
D.7 CC voltage reconstruction from the HT monitor.	224
D.8 Demonstration of the crabbing from the Head-Tail monitor signal. CC voltage and sum signal (longitudinal line density) measured from the Head-Tail monitor (top) together with the density plot (bottom) which visualises the effect of the CC kick on the beam.	225

List of Tables

4.1	Crab Cavities design parameters for the SPS tests.	56
4.2	Main machine and beam parameters for the emittance growth studies with CCs in SPS in 2018.	59
4.3	Phase and amplitude noise levels injected in the CC RF system for the emittance growth studies of 2018. The listed values correspond to the average power spectral density values over a frequency range of \pm 500 Hz around the first betatron sideband, f_b . The calculated effective phase noise for the parameters of the first bunch are also listed.	64
4.4	Comparison between the measured and the calculated transverse emittance growth rates for bunch 1 for the different noise levels, and average bunch length for each case.	81
5.1	Simulation parameters used to benchmark the theoretically predicted emittane growth in Chapter 5.	89
5.2	Parameters for computing the vertical orbit shift induced by the CC element (at the location s_0) at the location of the horizontal Wire Scanner (SPS.BWS.51995.H.), s_1	96
5.3	Multipole errors from SPS non-linear model, at 270 GeV [72].	103
6.1	PyHEADTAIL simulation parameters used to study impedance induced effects for the SPS.	110
6.2	PyHEADTAIL simulation parameters used for the implementation of the CC RF noise kicks for the emittance growth studies. This table is complementary of Table 6.1.	114

7.1	Main machine and beam parameters for the emittance growth studies with CCs in SPS in 2022.	140
7.2	Phase and amplitude noise levels injected in the CC RF system for the emittance growth studies of 2022 along with the analytically expected growths. The listed noise values correspond to the power spectral density values at the first vertical betatron sideband, f_b , at ~ 8 kHz. The analytical emittance growth rates were computed using Eq. (3.11) and (3.12) for bunch length of $4\sigma_t=1.83$ ns and the measured amplitude of CC voltage, $V_{CC,0}=1.1$ MV.	141
7.3	Comparison between the measured and the calculated transverse emittance growth rates for the different phase noise levels during the CC experiment of 2022. The analytical emittance growth rates were computed using Eq. (3.12) for bunch length of $4\sigma_t=1.83$ ns and CC voltage, $V_{CC,0} = 1.1$ MV. The background growth rate measured in the vertical plane of $0.84 \mu\text{m}/\text{h}$ is subtracted from the measured values. . .	153
8.1	Overview of the design parameters for the SPS and HL-LHC [4]. The listed values for the SPS correspond to its operation as a storage ring for studying the long-term emittance evolution. The listed values for HL-LHC case are for beams at collision energy.	177
D.1	Parameters for computing the CC voltage from the example Head-Tail monitor measurements discussed in this chapter.	224

List of Symbols

\mathcal{L}	Instantaneous luminosity of a collider.
$f_{\text{rev}}, \omega_{\text{rev}}$	Revolution frequency of the machine in [Hz] and in [rad/s] respectively.
σ_x, σ_y	Horizontal and vertical rms beam size in [m].
$\sigma_z, \sigma_t, \sigma_\phi$	rms bunch length in units of [m], [s] and [rad] respectively.
C_0	Circumference of the accelerator.
\mathbf{F}_L	Lorentz force vector.
\mathbf{E}	Electric field vector.
\mathbf{B}	Magnetic field vector.
\mathbf{v}	Velocity vector.
C	Circumference of an accelerator ring.
R	Radius of an accelerator ring.
E_0, p_0, v_0	Reference energy, momentum and velocity.
β_0, γ_0	Relativistic beta and gamma (Lorentz factor).
e, m_p	The proton charge and rest mass respectively.
ρ	Bending radius.
c	Speed of light in vaccum.

s	Location along the ring.
(x, x')	Horizontal co-ordinates: position and normalised momentum to the momentum of the reference particle in units of [m] and [rad] respectively.
(y, y')	Vertical co-ordinates: position and normalised momentum to the momentum of the reference particle in units of [m] and [rad] respectively.
(z, δ)	Longitudinal co-ordinates: position in units of [m] and momentum offset (no units).
(p_x, p_y, p_z)	Particle's momentum in the horizontal, vertical and longitudinal plane respectively.
t	Time in [s].
b_n, a_n	Normal and skew multipole coefficients.
k_n	Normalised normal multipole coefficient.
$\psi_u(s)$	Phase advance from the start of the ring, s_0 , where $u = (x, y)$.
$\Delta\psi_u$	Phase advance between two locations along the ring, with $u = (x, y)$.
$\alpha_u(s), \beta_u(s), \gamma_u(s)$	Alpha, beta and gamma functions respectively or Twiss or Courant-Snyder parameters, with $u = (x, y, z)$.
Q_x, Q_y	Horizontal and vertical betatron tunes.
Q_{x0}, Q_{y0}	Horizontal and vertical working points of an accelerator.
J_x, J_y	Horizontal and vertical action.
u_N, u'_N	Normalised transverse co-ordinates, with $u = (x, y)$.
$\epsilon_x^{\text{geom}}, \epsilon_y^{\text{geom}}$	Horizontal and vertical geometric emittance of the beam.

0. List of Symbols

ϵ_x, ϵ_y	Horizontal and vertical normalised emittance of the beam.
D_x, D_y	Horizontal and vertical dispersion functions.
$Q_x^{(n)}, Q_y^{(n)}$	Horizontal and vertical chromaticity of nth order.
Q'_x, Q''_x	Horizontal chromaticity first and second order respectively.
Q'_y, Q''_y	Vertical chromaticity first and second order respectively.
$\alpha_{xx}, \alpha_{yy}, \alpha_{xy}$	Horizontal, vertical and cross-term detuning coefficients respectively in units of [1/m].
T_{rev}	Revolution period of an accelerator.
ϕ_{RF}	The phase of the main RF system of an accelerator.
ω_{RF}	The angular frequency of the main RF system of an accelerator.
h	Harmonic number.
ϕ_s	The phase of the synchronous particle.
$V_{\text{RF}}, f_{\text{RF}}$	Voltage and frequency of the main RF system of an accelerator.
α_p	Momentum compaction factor.
η_p	Phase slip factor.
γ_{tr}	Transition energy.
Q_s, ω_s	Synchrotron tune and angular synchrotron frequency respectively.
$W_x^{\text{const}}(z), W_y^{\text{const}}(z)$	Horizontal and vertical constant wake functions.
$W_x^{\text{dip}}(z), W_y^{\text{dip}}(z)$	Horizontal and vertical dipolar wake functions.
$W_x^{\text{quad}}(z), W_y^{\text{quad}}(z)$	Horizontal and vertical quadrupolar wake functions.
$Z_x(\omega), Z_y(\omega)$	Horizontal and vertical impedance.

$\Delta\Omega_u^{(l)}$	Horizontal and vertical complex coherent frequency shift of headtail mode l , with $u = (x, y)$.
i	Imaginary unit.
$V_{0,\text{CC}}$	Peak amplitude of the Crab Cavity voltage.
f_{CC}	Frequency of the Crab Cavity.
ϕ_{CC}	Phase of the Crab Cavity.
$\beta_{u,\text{CC}}, \alpha_{u,\text{CC}}, D_{u,\text{CC}}$	Transverse beta and alpha and dispersion functions at the location of Crab Cavity, with $u = (x, y)$.
ΔA	Relative deviation from the nominal amplitude of the signal or amplitude noise (no units).
$\Delta\phi$	Deviation from the nominal phase of the signal or phase noise in units of [rad ²].
S_θ	Power spectral density of dipole noise in units of [rad ² /Hz].
$S_{\Delta A}, S_{\Delta\phi}$	Power spectral density of amplitude and phase noise signal in units of [1/Hz] and [rad ² /Hz], respectively.
$I_n(x)$	Modified Bessel function of the first kind.
Γ	Gamma function.
N_{mp}	Number of macroparticles used in PyHEADTAIL or Sixtracklib simulations.
N_{turns}	Number of turns used in PyHEADTAIL or Sixtracklib simulations.
q_x, q_y, q_s	Decimal part of the horizontal betatron tune, vertical betatron tune and synchrotron tune respectively.

1 | Introduction

Particle accelerators were first developed in the early 20th century as a tool for high-energy physics research. By increasing particles' energy they allow us to investigate the subatomic structure of the world and to study the properties of the elementary particles and the fundamental forces. On a basic level, accelerators increase the energy of charged particles using electric fields. Through the years significant technological progress has been achieved resulting in higher energies and greatly enhanced performance of the machines. Additionally, various types of accelerators have been developed (cyclotrons, linacs, synchrotrons etc) using different types of particles (hadrons or leptons) and their use was also expanded in other fields such as medicine and industrial research.

1.1 The CERN accelerator complex

CERN (European Organisation of Nuclear Research), located on the Franco-Swiss border near Geneva, is at the forefront of the accelerator physics research as it operates an extensive network of accelerators, illustrated in Fig. 1.1, including the well-known Large Hadron Collider (LHC) [1].

LHC is a circular machine, 27 km long, built about 100 m underground and is currently the largest and most powerful accelerator. It accelerates and collides two counter-rotating beams of protons or ions (circulating in two different rings) at the four main experiments which are located around the LHC ring, namely ATLAS, CMS, ALICE and LHCb. The highlight of CERN and of the LHC operation up to now was the discovery of the Higgs boson in 2012 from ATLAS [2] and CMS [3], from proton collisions at 3.5 TeV (center-of-mass energy of 7 TeV), which was a milestone for the standard model.

1. Introduction

The beams used by the LHC are produced and gradually accelerated by the injector chain which is a sequence of smaller machines boosting the energy of the beam. In particular, Linac4 (which replaced Linac2 in 2020) accelerates the protons up to 160 MeV, the Proton Synchrotron Booster (PSB) up to 2 GeV, the Proton Synchrotron (PS) up to 26 GeV and the the Super Proton Synchrotron (SPS) up to 450 GeV. Finally, the protons are injected in the LHC where they are accelerated up to the collision energy of 6.5 TeV (center-of-mass energy of 13 TeV). It should be noted, that LHC delivered collisions with center-of-mass energy of 7 TeV during Run 1 (2010-2013) which was increased to 13 TeV for the Run 2 (2015-2018) and for Run 3 (2020-present).



Figure 1.1: Schematic view of the CERN accelerator complex. The different colors correspond to the different machines. The year of commissioning and the type of particles used in each one of them are also indicated along with the circumference for the circular machines. The image is courtesy of CERN.

It is worth mentioning that not only protons but also lead ions are accelerated in the LHC, starting their journey from Linac3 and LEIR and then following the same route as proton beams.

Finally, the accelerators in the injector chain not only prepare the beam for the LHC but also provide beams to various other facilities and experiments at lower energies. Examples are the Anti-proton Decelerator (AD) which studies antimatter, the Online Isotope Mass Separator (ISOLDE) which studies the properties of the atomic nuclei using radioactive beams, and the Advanced Proton Driven Plasma Wakefield Acceleration Experiment (AWAKE) which investigates particle acceleration by proton-driven plasma wakefields.

1.1.1 The CERN Super Proton Synchrotron

The research described in this thesis was conducted using the Super Proton Synchrotron (SPS). Thus, some additional information about this machine is provided here. The SPS (shown with light blue color in Fig. 1.1) was first commissioned in 1967 and has a circumference of 6.9 km. It used to operate as a proton-antiproton collider ($Spp\bar{S}$) and later on as an injector for the Large Electron Positron collider (LEP) while it also provided beams for fixed-target experiments (e.g. in the North Area). Even though the SPS can accelerate various particle types (protons, antiprotons, electrons, and heavy ions) the following information will concern its operation with proton beams which is the topic of the research presented in this thesis.

Currently, the SPS is the second biggest accelerator at CERN and it can accelerate protons from 26 GeV up to 450 GeV. Due to its past use as a collider, it can also operate as a storage ring. This operational mode is called "coast" and was used for the majority of the experimental studies presented in this thesis. During coast, the bunches circulate in the machine for long periods at constant energy. The highest energy at which SPS can operate in coast is 270 GeV due to limited cooling of the magnets to transfer away the heating when operating at high energy and consequently at large currents for long periods.

1.2 High-Luminosity LHC project and Crab Cavities

High-Luminosity LHC (HL-LHC) [4, 5] is the upgrade of the LHC machine which will extend its potential for discoveries. In particular, it aims to increase the instantaneous luminosity by a factor of 5 beyond the current operational values and the integrated luminosity by a factor of 10.

The luminosity, along with the energy, is a key parameter defining the performance of a collider as is a measure of the collision rate. The instantaneous luminosity is expressed as [6]:

$$\mathcal{L} = \frac{n_b f_{\text{rev}} N_1 N_2}{4\pi \sigma_x \sigma_y} \frac{1}{\sqrt{1 + (\frac{\sigma_z}{\sigma_{\text{xing}}} \frac{\theta_c}{2})^2}}, \quad (1.1)$$

where f_{rev} is the revolution frequency of the machine (the number of times per second a particle performs a turn in the accelerator, definition; in Chapter 2), n_b is the number of colliding bunch pairs, $N_{1,2}$ is the number of particles per bunch, $\sigma_{x,y}$ is the transverse beam size at the interaction point, σ_z the rms bunch length, σ_{xing} the transverse beam size in the crossing plane and θ_c is the full crossing angle between the colliding beams. The crossing angle, is often introduced between the bunches in a collider to reduce parasitic collisions and get rid of the remnants after the collision. For reference, in the LHC, the crossing angle has order of magnitude 10^{-4} radians.

The integrated luminosity is the one that ultimately defines the performance of the machine as it provides the total number of recorded events. It depends both on the instantaneous luminosity and on the machine availability. The integrated luminosity, is expressed as [4]:

$$\mathcal{L}_I \equiv \int_{\Delta t} \mathcal{L} dt, \quad (1.2)$$

where \mathcal{L} is the instantaneous luminosity as defined in Eq. (1.1).

HL-LHC aims to achieve instantaneous luminosity of $\mathcal{L} \sim 5 \cdot 10^{34} \text{ cm}^{-2}\text{s}^{-1}$ and an increase on the integrated luminosity from 300 fb^{-1} to 3000 fb^{-1} over its lifetime of 10-12 years and considering 160 days of operation per year [7].

1.2.1 Crab cavities

To achieve its luminosity goals, HL-LHC will employ numerous innovative technologies. Crab cavity technology (will be denoted as CC in this thesis) [8] is one of the key components of the project as it will be employed to restore the luminosity reduction caused by the crossing angle, θ_c (see Eq. (1.1)).

A crab cavity is an RF cavity which provides a transverse, sinusoidal like, kick to the particles depending on their longitudinal position within the bunch. A graphical visualisation of the kick is shown in Fig. 1.2. It can be seen that the head (leading part) and the tail (trailing part) of the bunch receive opposite deflection while the particles at the center remain unaffected.

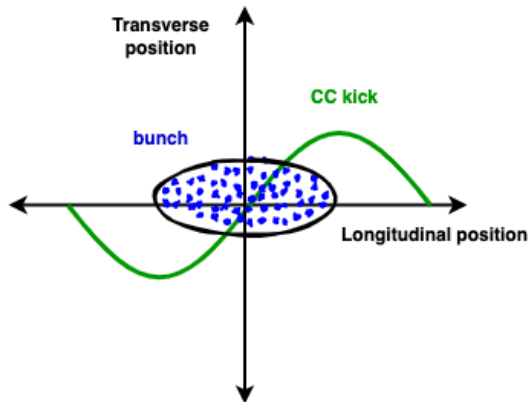


Figure 1.2: Visualisation of the CC kick (green line) on the bunch particles (blue dots). The bunch here appears much smaller than the CC wavelength which means that only the linear part of the kick affects the bunch. This will be the case for the HL-LHC scenario.

The CCs will be installed in the two main interaction points of LHC, ATLAS and CMS. According to the plan, two CCs will be installed on each ring and on each side of the interaction points (eight in total). This is displayed in Fig. 1.3 with the red (ATLAS) and orange (CMS) markers. The reason why two CCs are needed in each ring on each side of the IP is discussed in the following paragraphs (local vs global scheme).

1. Introduction



Figure 1.3: Layout of the LHC and the SPS. The CC location for the HL-LHC configuration is marked. Two CCs (one per ring) will be installed on each side of ATLAS (red) and CMS (orange). Two prototype CCs were also installed in the SPS (magenta) in 2018, to be tested before their installation in LHC. The layout can be found in Ref. [9] and was modified inspired by Ref. [10].

In this configuration, the bunches receive the transverse deflection from the first pair of CCs just before reaching the interaction point. This results in a rotation of the bunch, which mitigates the crossing angle and restores the head-on collisions. The deflection is cancelled once the bunches reach the second pair of CCs which are symmetrically placed at the opposite side of the interaction point. The collision of the bunches in the presence of the CCs is illustrated in Fig. 1.4 [11].

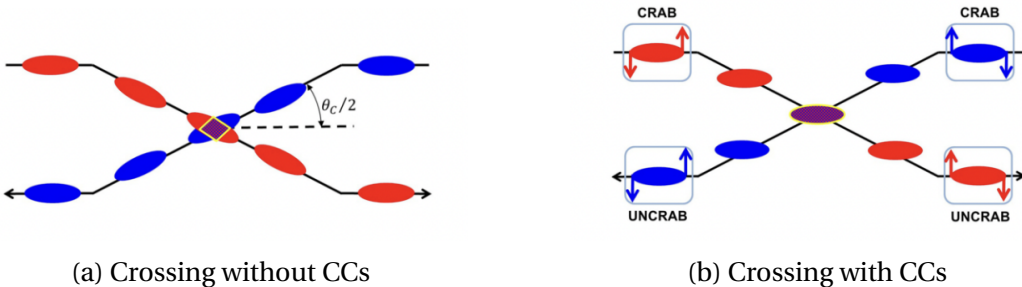


Figure 1.4: Collision with and without the use of CCs [11]. CCs restore the overlap between the bunches recovering the luminosity reduction caused by the crossing angle, θ_c . The blue and red colors indicate two bunches in the different rings.

The above scheme, with CCs before and after the interaction point, is called the local crabbing scheme. An alternative scheme, named the global crabbing scheme, was also under discussion in the first stages of the project. In such a scheme, the closed orbit distortion that is caused by the fact that the head and the tail of the bunch are kicked in opposite directions propagates in the ring, resulting in transverse bunch oscillations [5]. This scheme is cost-efficient compared to the local scheme as it only requires two CCs. However, it introduces significant constraints on the betatron phase advance between the interaction points and the CCs. The constraints are enhanced by the fact that the bunch crossing in ATLAS takes place in the vertical plane while in CMS in the horizontal. To this end, the local CC scheme was chosen for the HL-LHC configuration.

In order to accommodate the crossing in both transverse planes two CC designs have been developed: the Double-Quarter Wave (DQW) and the RF dipole (RFD), which provide vertical and horizontal deflection respectively. Information on their design can be found in Refs. [12, 13, 14, 15]

The CCs have already been successfully used in the KEKB collider [16] in Japan, during 2007-2010, with lepton beams ($e^+ - e^-$) [17, 18, 19]. However, there are significant differences in the beam dynamics in the presence of CCs in leptons and hadrons (HL-LHC case). One of the most crucial points is the impact of errors (e.g. RF noise) which leads to beam degradation [20, 21]. This is not an issue of concern for lepton beams as they nevertheless experience emittance damping due to synchrotron radiation. For proton beams, the synchrotron radiation damping is much weaker meaning that the beam degradation can lead to emittance growth which eventually can result in loss of luminosity.

As the CCs have never been used with protons before, two prototype superconducting CCs were installed in the SPS (Fig. 1.3, magenta markers) to test the technical systems, to validate their operation with proton beams and to identify and address potential issues before their installation in LHC. The SPS provides an ideal test bed for these studies as it allows testing under conditions that are closer to those in HL-LHC than any other machine. In particular, the SPS operates with proton beams, can run in storage-ring mode, and in terms of the

1. Introduction

energy reach is second only to LHC. The two CCs that were installed in SPS [22] were identical, fabricated at CERN and of the DQW type (like the ones that will be used in ATLAS interaction point in HL-LHC).

1.3 Motivation, objectives and thesis outline

As mentioned above, one of the main concerns regarding the CC operation with protons is the emittance growth due to noise in their RF system as it leads to luminosity loss. For the HL-LHC, the target values regarding the luminosity loss and emittance growth are very tight. In particular the maximum allowed luminosity loss due to CC RF noise induced emittance growth is targeted at just 1%, during a physics fill, which corresponds to an CC RF noise induced emittance growth of 2 %/h [23, 24, 25]. To this end, a good understanding and characterization of the emittance growth mechanism is crucial for the HL-LHC project.

For reference, a physics fill is the time period during which the beams are successfully injected in the LHC at the desired conditions, they are accelerated at the desired energy and they are kept in the machine for consecutive collisions. After some hours, due to beam degradation the beams are dumped and a new fill is prepared. A fill in the HL-LHC will last a couple of hours.

This thesis focuses on understanding, characterising and evaluating the mechanism of CC RF noise-induced emittance growth including numerical and experimental studies. The studies presented in this thesis were conducted for the SPS machine since it has proton crabbing operational experience and allows direct comparison of predictions from models and experimental data. It should be emphasised that the CC tests in SPS constitute the first experimental beam dynamics studies with CCs and proton beams. The results and the understanding obtained from this research are essential for the HL-LHC, in order to predict the long-term emittance and to define limits on the acceptable noise levels for the CCs.

This thesis reports research that was carried out between 2018 and 2022, based at CERN and it structured as follows:

Chapter 2 presents the basics of accelerator beam dynamics focusing on the concepts that are relevant for understanding the studies presented in this thesis. In particular, definitions are given for single-particle beam dynamics, addressing both transverse and longitudinal motion. Furthermore, the collective effects are introduced focusing on the effect of wakefields. A brief discussion on optics models for accelerators is also provided. Finally, the two simulation codes used in this thesis for macroparticle tracking, PYHEADTAIL and Sixtracklib, are described.

The available theoretical model for predicting the emittance growth driven by Crab Cavity RF noise is described in Chapter 3. The modelling of the noise effects in the simulations is also discussed. Last, a short reference to the CC experiment at KEKB in Japan is also made.

Chapter 4 is devoted to the methodology used for the calibration of the CCs. The first sections provide some general details on the CC installation and operation in the SPS. The instrument that is used as the main diagnostic is described. Finally, the post-processing of the measurements to characterise the CC voltage and phase is explained.

The results from the first experimental studies of the emittance growth from CC RF noise in the SPS are presented in Chapter 5. First, the experimental configuration and procedure is reported. Second the artificial noise injected in the CC RF system for the measurements is discussed in detail. Subsequently, the emittance growth measurements are presented along with the measured bunch length and intensity evolution for completeness. Last the measured emittance growth rates are compared with the predictions from the theoretical model (described in Chapter 3). It was found the the measured growth rates were systematically a factor of 4 on average lower than the predictions.

Various possible factors were investigated as a possible explanation for this discrepancy. These extensive studies, which took place over two years are described in Chapter 6. Initially, the theory was benchmarked with different simulation software: PyHEADTAIL and Sixtracklib. The sensitivity of the emittance evolution on the non-linearities of the SPS machine (which was not included in the

1. Introduction

theory of Chapter 3) was also tested. Last, thorough studies were performed to exclude the possibility that the discrepancy is not a result of possible errors in the analysis of the experimental data or the actual noise levels applied on the CCs. However, none of these factors could explain the discrepancy.

Finally, simulations including the SPS transverse impedance model (not included in the theory (of Chapter 3) showed a significant impact on the emittance growth. Chapter 7 discusses the investigation and characterisation the phenomenon of the emittance growth suppression from the beam coupling impedance as observed in simulations with PyHEADTAIL. It was shown that the suppression is related to the dipole motion which is excited by the CC RF phase noise.

Chapter 8, presents the results from the second round of emittance growth measurements with CCs in SPS that took place in 2022. The objective of these experimental studies was to validate the mechanism of the suppression of the CC RF noise-induced emittance growth from the beam coupling impedance as observed in simulations (described in Chapter 7). This would also confirm that this impedance-induced effect is the reason for the discrepancy observed in the 2018 experiment between the measurements and the theoretical predictions. The experiments of 2022 successfully confirmed the suppression mechanism, despite the very challenging conditions of the studies.

In Chapter 9, further experimental results with the use of the SPS transverse damper as a source of noise are shown. The measurements took place in 2022, after the CC experiment for the same machine and beam conditions. The objective was to obtain further measurements which would validate the mechanism of the suppression of the noise-induced emittance growth by the impedance. The use of the damper is an appropriate configuration as it provides dipolar noise kicks in the beam and as shown in Chapter 7 the suppression mechanism is related to the dipole motion. The experimental results from use of the damper are also compared with the predictions from a recently developed theoretical model from X. Buffat which describes the emittance growth suppression from a collective force.

Last, Chapter 10 summarizes the conclusions of the thesis. The project is viewed from a broad perspective highlighting its importance. Potential follow up studies

1.3. Motivation, objectives and thesis outline

are proposed. **Comment on Appendix?**

2 | Basics of accelerator beam dynamics

In this chapter, the basic concepts of accelerator beam physics that are essential for understanding the studies presented here are introduced. A more complete description can be found in the books of the following references: [26, 27, 28]. The focus is put on the concepts for synchrotrons with proton beams. Additionally, in the last section, the tracking simulation codes used in this work are described.

Synchrotrons are circular accelerators where the particles follow a fixed closed-loop path. In a synchrotron, electric fields accelerate the particles while magnetic fields steer and focus them. The magnetic fields are not constant but they vary according to the particles' energy, allowing acceleration and operation at very high (relativistic) energies. The LHC and SPS machines at CERN are synchrotrons like many of the machines used for High Energy Physics experiments. Usually, in synchrotrons, the beams consist of multiple bunches, longitudinally spaced around the machine. Although the bunches interact with each other, these interactions are not relevant to the studies presented later in this thesis, and will not be considered further

Finally, at this point, it is appropriate to introduce the terms incoherent and coherent effects. Incoherent effects (microscopic approach) affect the individual particles affect individual particles. Any theory or model of incoherent effects has to treat the beam as a collection of a large number of individual particles, each with its own behaviour. In contrast, coherent effects can be understood in terms of their impact on the beam as a whole, and can be modelled by representing each bunch, for example, as a single 'macroparticle', with mass and charge corresponding to the total number of particles it contains.

2.1 Motion of charged particles in electromagnetic fields

The motion of a particle with charge q and velocity $\mathbf{v} = (v_x, v_y, v_z)$ moving in an electric field \mathbf{E} and a magnetic field \mathbf{B} is defined by the influence of the Lorentz force:

$$\mathbf{F}_L = q(\mathbf{E} + \mathbf{v} \times \mathbf{B}). \quad (2.1)$$

At this point, it is appropriate to mention that in this thesis the vectors are denoted in bold font (e.g. \mathbf{E}).

In synchrotrons, the electric fields, which are generated by radiofrequency (RF) cavities, are used for accelerating the beams. The magnetic fields, are used to steer (dipoles) and focus (quadrupoles) and apply corrections (sextupoles, octupoles and higher order multipoles) to the motion of the beam. The sequence of the various electromagnetic elements around the accelerator ring is called the machine lattice.

Reference trajectory and reference momentum

Here the concepts of reference momentum and reference trajectory are introduced. They both can be chosen arbitrary and are used as a reference for describing the particles motion in the magnetic fields of an accelerator. It might be the case that no particle follows the reference trajectory and has the reference momentum.

The reference trajectory is a chosen curved path in space which acts as a reference for the alignment of the accelerator components. It is defined by the dipoles and is typically chosen such as it passes from the center of all the magnets. The total length of the reference trajectory in a circular accelerator is called the circumference, C_0 .

The particle that follows this trajectory is called the reference particle and has a momentum p_0 , an energy E_0 , and a velocity v_0 . This particle is often called the synchronous particle as it crosses an RF cavity always at the same phase (assuming constant speed and no losses). For a proton, the reference momentum is given by:

2. Basics of accelerator beam dynamics

$p_0 = \gamma_0 m_p v_0$, where m_p is the proton rest mass, and $\gamma_0 = \frac{1}{\sqrt{1-\beta_0^2}}$ is the relativistic gamma or Lorentz factor, where $\beta_0 = v_0/c$ is the relativistic β with c being the speed of light.

Mangetic rigidity

At this point, it is appropriate to introduce the concept of magnetic rigidity, $B_0\rho$, which is often used in accelerators as a normalisation factor and is a measure of how the charged particles resist bending by a dipolar magnetic field. Assuming that a proton moves only under the influence of a uniform vertical dipole field $\mathbf{B}_0 = (0, B_0, 0)$, it would follow a circular path of radius ρ (it will be often referred to as bending radius) which is defined by the Lorentz force (Eq. (2.1)) being equal to the centripetal force, as follows:

$$ev_0 B_0 = \frac{\gamma_0 m_p v_0^2}{\rho} \Rightarrow B_0 \rho = \frac{\gamma_0 m_p v_0}{e} \Rightarrow B_0 \rho = \frac{p_0}{e}, \quad (2.2)$$

where e and m_p are the charge and rest mass of a proton respectively, p_0 is the reference momentum, and γ_0, β_0 the relativistic gamma and beta. In the ultra-relativistic regime which is the case in the studies presented in this thesis, the approximation $\beta_0 = 1$ is often used. From Eq. (2.2) it becomes clear that the magnetic rigidity is another way of stating the reference momentum, p_0 .

If the particle momentum is given in GeV/c (which are the usual units in high energy accelerators) then the unit of magnetic rigidity is T · m.

Co-ordinate system

However, the individual particles do not follow the reference trajectory due to small deviations in their initial conditions: an example trajectory is shown in Fig. 2.1 with the blue line. The co-ordinate system used to describe the individual trajectories of the beam particles around the accelerator is illustrated in Fig. 2.1 and it is known as Frenet-Serret system. It consists of the orthogonal co-ordinate system $\Sigma(s) = (\mathbf{e}_x, \mathbf{e}_y, \mathbf{e}_z)$ whose origin moves along the reference trajectory (red line) together with the beam.

The variable s denotes the distance along the reference trajectory. In accelerator physics, s is usually chosen as the independent variable instead of time, t .

Therefore, at any given location s around the ring, the coordinates $(x(s), y(s), z(s))$ give the horizontal, vertical, and longitudinal position of the particle with respect to the origin of the orthogonal moving system Σ . In the following paragraphs, the dependence of the co-ordinates on the position s along the ring is omitted when possible to facilitate the notation (e.g. $x(s)$ will be denoted as x).



Figure 2.1: Co-ordinate system used to describe particles motion in a synchrotron. This is a local co-ordinate system, with the origin following the reference trajectory around the accelerator. The unit vector \mathbf{e}_z is tangential to the reference trajectory at each point, \mathbf{e}_y is vertical, and \mathbf{e}_x is horizontal, and perpendicular to \mathbf{e}_z and \mathbf{e}_y .

At any point s along the reference trajectory each particle is represented by the six-dimensional "phase space" vector $(x, x', y, y', z, \delta)$ where:

$$x' = \frac{dx}{ds} = \frac{dx}{dt} \frac{dt}{ds} = \frac{v_x}{v_z} = \frac{p_x}{p_z} \approx \frac{p_x}{p_0}, \quad (2.3a)$$

$$y' = \frac{dy}{ds} = \frac{dy}{dt} \frac{dt}{ds} = \frac{v_y}{v_z} = \frac{p_y}{p_z} \approx \frac{p_y}{p_0}, \quad (2.3b)$$

$$\delta = \frac{\Delta p}{p_0} = \frac{p - p_0}{p_0}, \quad (2.3c)$$

$$z = \beta_0 c(t_0 - t), \quad (2.3d)$$

where p_0 and β_0 are the momentum and relativistic (scaled) velocity, respectively, of the reference particle, t_0 is the time which the reference particle arrives at the location s and t is the time at which the individual particle arrives at the same location. It can be seen that δ is the relative momentum offset from the reference particle. In order to avoid a possible misconception it seems appropriate to clarify here, that the longitudinal parameter z indicates the longitudinal offset from the

2. Basics of accelerator beam dynamics

reference particle at the center of the bunch. If $z > 0$ ($z < 0$) the corresponding particle arrives earlier (later) than the center of the bunch at an arbitrary reference point. Last, in the ultra-relativistic regime the momentum of the particles in the \mathbf{e}_z direction is much larger than the transverse ones and almost equals the reference momentum: $p_x, p_y \ll p_z \approx p_0$. This is why the values of x' and y' are close to p_x/p_0 and p_y/p_0 , respectively.

To summarize, the motion of the particles is treated separately in the transverse and longitudinal planes where it is described with the (x, x', y, y') and (z, δ) co-ordinates respectively. As an example the co-ordinates of the reference particle are $(x = 0, x' = 0, y = 0, y' = 0, z = 0, \delta = 0 (p_z = p_0))$.

Last, (x, y, z) are expressed in meters, (x', y') in radians while δ is dimensionless.

2.2 Single-particle beam dynamics

In this section, the interactions between the particles within a bunch are neglected, hence the term single-particle beam dynamics.

Two-dimensional complex fields

As already discussed, the motion of the charged particles inside a circular accelerator is controlled by magnetic fields. In this thesis, the magnets are considered purely transverse elements. Their effect is therefore described with two-dimensional multipole fields, acting in the horizontal and vertical planes¹.

The description of two-dimensional magnetic fields in accelerator physics is discussed using the concept of multipole expansion and is expressed as a complex quantity. The complex quantity allows to describe a two-dimensional field in (x, y) space (to be compatible with the co-ordinates used for describing the particle's trajectory as discussed in the previous section). Therefore, the magnetic field

¹Examples of three-dimensional treatment can be found in [26, 29]. However, the two-dimensional treatment is most often used in accelerator physics as it provides a good description for the majority of the magnetic elements.

around the beam is expressed as follows [26]:

$$B_y(x, y) + iB_x(x, y) = \sum_{n=1}^{\infty} C_n (x + iy)^{n-1}, \quad (2.4)$$

where n indicates the order of the field component: $n=1$ for a dipole (steering), $n=2$ for quadrupole (focusing), $n=3$ for sextupoles (chromaticity correction), $n=4$ for octupole (error or field correction) etc. $C_n = (b_n + ia_n)$ is a complex constant which denotes the strength and orientation of the multipole field. The coefficients $b_n = \frac{1}{(n-1)!} \frac{\partial^{n-1} B_y}{\partial x^{n-1}}$ and $a_n = \frac{1}{(n-1)!} \frac{\partial^{n-1} B_x}{\partial x^{n-1}}$ denote the strength of a normal and skew (normal multipole rotated by $\pi/2(n)$) multipole respectively in units of T/m^{n-1} .

Usually, in accelerator physics the values of the multipole strengths are quoted normalised to the magnetic rigidity as defined in Eq. (2.2) and are denoted by:

$$k_n = \frac{b_n}{B_0 \rho}, \quad (2.5)$$

where k_n is expressed in units of m^{-n} . This is the convention that will be used in this thesis.

It should be clarified here, that the notations of B_0 and b_1 are equivalent. However, in accelerator physics the magnetic rigidity is denoted as $B_0 \rho$ as a convention due to its derivation at the early stages of the analysis (see Eq.(2.2)). This notation will be used throughout this thesis.

2.2.1 Transverse motion

In the transverse plane the motion is orthogonal to the reference trajectory (see Fig. 2.1) and its co-ordinates are (x, x', y, y') . For the discussion on the transverse beam dynamics, the (x, x') and (y, y') co-ordinates will be both described by (u, u') when possible to facilitate the notation.

2.2.1.1 Linear dynamics

Here the transverse motion of a particle moving through the two-dimensional fields described in Eq. (2.4) is discussed. For now, the discussion is limited only to

2. Basics of accelerator beam dynamics

dipolar and quadrupolar components ($n = 1$ and $n = 2$) which are considered the basic magnetic elements, as in the absence of magnetic errors or momentum deviations between the particles they are sufficient to create a synchrotron.

As mentioned above, the particles transversely oscillate around the reference trajectory (except for a nominal reference particle which follows it). This motion, through an arbitrary periodic sequence of dipoles and quadrupoles, is called betatron motion and can be described by the following equations of motion [28]:

$$x'' - \frac{\rho + x}{\rho^2} = -\frac{B_y}{B_0\rho} \frac{p_0}{p} \left(1 + \frac{x}{\rho}\right)^2, \quad (2.6)$$

$$y'' = \frac{B_x}{B_0\rho} \frac{p_0}{p} \left(1 + \frac{x}{\rho}\right)^2, \quad (2.7)$$

where $B_0\rho$ and ρ the magnetic rigidity and radius as defined in Eq. (2.2), B_y, B_x the transverse magnetic fields of Eq. (2.4), and p_0 the reference momentum.

In the case of dipole and quadrupole fields, linear approximations to the equations of motion (equations describing the particle motion through the fields) provide good representations of the dynamics, at least in the case of the transverse motion. Hence the name linear dynamics. For the linear approximation the following assumptions are made: the transverse offset and angle of motion of the rest of the particles (x, x', y, y') are very small and close to the reference trajectory and only the linear terms in x and y of the magnetic field (described in Eq. (2.4)) are taken into account, such as [28]:

$$B_y = B_0 + \frac{\partial B_y}{\partial x} x = B_0 + b_2 x, \quad B_x = \frac{\partial B_x}{\partial x} y = b_2 y. \quad (2.8)$$

Note that the term B_0 doesn't appear in the horizontal magnetic field due to the fact that, as mentioned earlier, only vertical dipole fields are considered.

Expanding Eqs. (2.6) and (2.7) to the first order of x and y respectively, setting $\delta = (p - p_0)/p_0$, and $k_2 = b_2/(B_0\rho)$ the linear equations of motion are

obtained [28]:

$$x'' + \left(\frac{1-\delta}{\rho^2(1+\delta)} + \frac{k_2(s)}{1+\delta} \right) x = \frac{\delta}{\rho(1+\delta)}, \quad (2.9)$$

$$y'' - \left(\frac{k_2(s)}{1+\delta} \right) y = 0, \quad (2.10)$$

where the sign-convention is $k_2 > 0$ ($k_2 < 0$) for focusing in the horizontal (vertical) plane. It is worth commenting that $1/\rho = B_0/(B_0\rho) = b_1/(B_0\rho) = k_1$ the normalised dipole strength.

For on-momentum particles (with $\delta = 0$) ² the linear equations of motion are simplified even more to the equation for a harmonic oscillator (but with an s dependent strength $K_u(s)$), named Hill's equation [28]:

$$u''(s) + K_u(s) u(s) = 0, \quad (2.11)$$

where $u = (x, y)$ and:

$$K_u(s) = \begin{cases} \frac{1}{\rho^2(s)} + k_2(s), & u = x \\ -k_2(s), & u = y \end{cases} \quad (2.12)$$

with $k_2(s)$ being the normalised quadrupole strength. It should be noted that for Eq. (2.11) it is assumed the motion in the horizontal plane is independent of the motion in the vertical plane, and vice-versa, i.e. the motion is uncoupled.

As already mentioned, Eq. (2.11) resembles the equation of motion for a harmonic oscillator, but with an oscillation frequency that varies with position along the beamline (i.e. varies with s). For a circular accelerator K_u is periodic: $K_u(s + C_0) = K_u(s)$, where C_0 is the periodicity of the accelerator and real-valued. The general solution of Hill's equations in this case is (using the Floquet transformation) [28]:

$$u(s) = Aw(s) \cos(\psi_u(s) + \psi_{u,0}), \quad (2.13)$$

where A and $\psi_{u,0}$ the integration constants and $w(s)$ and $\psi_u(s)$ are the amplitude and betatron phase functions, which are periodic functions with the same periodicity as K_u .

²The solution of the equation of motion for off-momentum particles is discussed in the paragraph "Off-momentum effects: dispersion" later in this section.

2. Basics of accelerator beam dynamics

After substituting for $u(s)$ from Eq. (2.13) in Eq. (2.11), we find after some calculation (see Appendix C.1) that the amplitude and phase functions fulfill the following equations:

$$w_u'' + K_u(s) w_u(s) - \frac{1}{w_u(s)^3} = 0, \quad (2.14)$$

where:

$$\psi'_u(s) = \frac{1}{w_u(s)^2} \Rightarrow \psi_u(s) = \int_{s_0}^s \frac{ds}{w_u(s)^2} \quad (2.15)$$

The above equations are called the betatron envelope and phase equations.

Courant-Snyder parameters

At this point it is appropriate to introduce the betatron or Twiss or Courant-Snyder:

$$\beta_u(s) = w_u(s)^2, \quad (2.16a)$$

$$\alpha_u(s) = -\frac{1}{2} \beta'_u(s), \quad (2.16b)$$

$$\gamma_u(s) = \frac{1 + \alpha_u(s)^2}{\beta_u(s)}, \quad (2.16c)$$

with $\beta'_u(s) = d\beta_u(s)/ds$.

The betatron phase advance from Eq. (2.15) can be re-written using the beta twiss function as:

$$\psi_u(s) = \int_{s_0}^s \frac{ds}{\beta_u(s)}. \quad (2.17)$$

The advantage of the Twiss parameters over using $w_u(s)$ and $\psi_u(s)$ is that they can be also used to describe the properties of a bunch of particles while the latter describe the motion of each particle individually. This is discussed in further details in the following paragraph "Transverse emittance".

Betatron tune

Another important quantity in accelerator physics is the betatron tune of the machine, Q_u , which is the phase advance for one complete revolution around the machine divided by 2π :

$$Q_u = \frac{\psi_u(s+C) - \psi_u(s)}{2\pi} = \frac{1}{2\pi} \oint_C \frac{ds}{\beta_u(s)}, \quad (2.18)$$

where C is the circumference of the machine. As it can be seen, the tune also represents the number of betatron oscillations that a particle undergoes during one full revolution around the machine.

The tune of the individual particles may vary due to effects such as the chromaticity, the detuning with their transverse amplitude, and collective forces (e.g. impedance) that will be discussed in the following paragraphs. The horizontal and vertical tune of the reference particle will be referred to as the bare tunes and define what is called the working point of the machine, (Q_{x0}, Q_{y0}) .

Matrix formalism

Knowing the lattice (element per element structure of the accelerator) the solutions $w_u(s)$ and $\psi_u(s)$ of the Hill's equation can also be described using a matrix formalism as follows:

$$\begin{pmatrix} u \\ u' \end{pmatrix}_{s_1} = M_u(s_1|s_0) \begin{pmatrix} u \\ u' \end{pmatrix}_{s_0}, \quad (2.19)$$

where $u = (x, y)$. The transfer matrix from the position s_0 to the s_1 , $M_u(s_1|s_0)$, can be expressed in terms of the Courant-Snyder parameters as [28]:

$$M_u(s_1|s_0) = \begin{pmatrix} \sqrt{\frac{\beta_u(s_1)}{\beta_u(s_0)}}(\cos \Delta\psi_u + \alpha_u(s_0) \sin \Delta\psi_u) & \sqrt{\beta_u(s_0)\beta_u(s_1)} \sin \Delta\psi_u \\ -\frac{1+\alpha_u(s_0)\alpha_u(s_1)}{\sqrt{\beta_u(s_0)\beta_u(s_1)}} \sin \Delta\psi_u + \frac{\alpha_u(s_0)-\alpha_u(s_1)}{\sqrt{\beta_u(s_0)\beta_u(s_1)}} \cos \Delta\psi_u & \sqrt{\frac{\beta_u(s_0)}{\beta_u(s_1)}}(\cos \Delta\psi_u + \alpha_u(s_1) \sin \Delta\psi_u) \end{pmatrix} \\ = \begin{pmatrix} \sqrt{\beta_u(s_1)} & 0 \\ -\frac{\alpha_u(s_1)}{\sqrt{\beta_u(s_1)}} & \frac{1}{\beta_u(s_1)} \end{pmatrix} \begin{pmatrix} \cos \Delta\psi_u & \sin \Delta\psi_u \\ -\sin \Delta\psi_u & \cos \Delta\psi_u \end{pmatrix} \begin{pmatrix} \frac{1}{\sqrt{\beta_u(s_0)}} & 0 \\ \frac{\alpha_u(s_0)}{\sqrt{\beta_u(s_0)}} & \sqrt{\beta_u(s_0)} \end{pmatrix}, \quad (2.20)$$

where $\Delta\psi_u = \psi_u(s_1) - \psi_u(s_0)$ is the betatron phase advance between the two locations while $\alpha_u(s_i)$ and $\beta_u(s_i)$ are the Courant-Snyder parameters at the location s_i , where $i = (0, 1)$. Transfer matrices provide a very convenient approach to accelerator beam dynamics, and will be used extensively throughout this thesis to study the motion of the particles in the accelerator lattice.

2. Basics of accelerator beam dynamics

Action-angle variables and phase space ellipse

The action variable is introduced here as it is used in the definition of emittance which is one of the parameters of primary interest for this thesis. Additionally, the octupole magnets that will be used in the CC studies introduce betatron detuning which is linearly expressed in terms of action (see Eqs. (2.43) and (2.44)).

The solution of equation of motion (Eq. (2.11)) can alternatively be expressed in action-angle co-ordinates (J_u, ψ_u) as follows:

$$u(s) = \sqrt{2\beta_u(s)J_u} \cos(\psi_u(s)). \quad (2.21)$$

By differentiation the divergence u' is written as:

$$u'(s) = -\sqrt{\frac{2J_u}{\beta_u(s)}} (\sin(\psi_u(s)) + \alpha_u(s) \cos(\psi_u(s))), \quad (2.22)$$

where $\beta_u(s), \alpha_u(s)$ are the Twiss parameters as defined in Eq. (2.16), $\psi_u(s)$ the betatron phase as defined in Eq. (2.15) and J_u is an integration constant which is defined by the initial conditions.

The action, J_u is an invariant of the motion and can be written in terms of the Twiss parameters as:

$$J_u = \frac{1}{2}(\gamma_u(s)u^2(s) + 2\alpha_u(s)u(s)u'(s) + \beta_u(s)u'^2(s)) = \text{constant}. \quad (2.23)$$

The trajectory of each individual particle can be plotted in phase space (u, u') at a given position s in the ring turn after turn. In phase space, the particle's path is an ellipse whose shape and orientation are determined by the Twiss parameters at the position s . This ellipse, named phase space or Courant-Snyder ellipse, is illustrated in Fig. 2.2 and it has an area of $2\pi J_u$. It is worth mentioning, that the ellipse's size is different for each particle as it depends on their individual actions, J_u i.e. their individual initial conditions. The center of the ellipse is the closed orbit which, in the absence of steering errors in a synchrotron, can be identified with the reference trajectory and is also shown in the plot.

Normalised phase space



Figure 2.2: Phase space co-ordinates (u, u') turn by turn, for a particle moving along the ring but at a particular position s which is characterised by the following twiss parameters $[\alpha_u(s), \beta_u(s), \gamma_u(s)]$. In the labels shown on the diagram, the dependence on the s parameter has been omitted.

Often in accelerator physics, it is useful to transform the transverse phase space ellipse into a normalised phase space circle. In the normalised phase space the co-ordinates (u, u') are normalised with the twiss parameters (α_u, β_u) for the particular location s around the ring, as follows [27]:

$$u_N(\phi) = \frac{u(s)}{\sqrt{\beta_u(s)}}, \quad (2.24)$$

$$u'_N(\phi) = \frac{du_N}{d\phi} = \sqrt{\beta_u(s)} u'(s) + \frac{\alpha_u(s)}{\beta_u(s)} u(s), \quad (2.25)$$

where $\phi = \frac{\psi_u}{Q_u}$. It can be seen that the independent variable in the normalised co-ordinates is the phase advance (normalised with the betatron tune), ϕ , instead of the location s along the ring. Both of the normalised co-ordinates, (u_N, u'_N) are expressed in units of $m^{1/2}$.

Combining Eq. (2.23), Eq. (2.16), Eq. (2.24) and Eq. (2.25) the action variable can also be written as:

$$J_u = \frac{1}{2}(u_N^2 + u'^2_N). \quad (2.26)$$

The phase space in normalised co-ordinates is shown in Fig. 2.3.

Transverse emittance



Figure 2.3: Normalised phase space: the trajectory shown represents the particle motion as the particle moves around the synchrotron. This is not the case in the regular (not normalised) phase space, since the shape of the phase space ellipse will change with position around the ring. The particle moves turn by turn in a circle of radius $\sqrt{2J_u}$.

Up to now, the Twiss parameters were used to describe the dynamics of single particles. However, they also describe the distribution of the particles within a bunch. The statistical average of u^2 over all particles at a given point s along the reference trajectory, from Eq. (2.21) equals to [26]:

$$\langle u^2(s) \rangle = 2\beta_u(s) \langle J_u \cos^2 \psi_u(s) \rangle. \quad (2.27)$$

Assuming that the angle and action variables are uncorrelated Eq. (2.27) becomes:

$$\langle u^2(s) \rangle = 2\beta_u(s) \langle J_u \rangle \langle \cos^2 \psi_u(s) \rangle. \quad (2.28)$$

Considering that the angle variables are uniformly distributed from 0 to 2π , it is written:

$$\langle \cos^2 \psi_u(s) \rangle = \int_{s_0}^{s_0+C} \cos^2 \psi_u(s) ds = \int_0^{2\pi} \cos^2 \psi_u(\phi) d\phi = \frac{\pi}{2\pi} = \frac{1}{2}. \quad (2.29)$$

where for the integration the phase advance ϕ is used instead of the location s along the ring for convenience.

Inserting Eq. (2.29) in Eq. (2.27) gives:

$$\langle u^2(s) \rangle = \beta_u(s) \epsilon_u, \quad (2.30)$$

where

$$\epsilon_u^{\text{geom}} = \langle J_u \rangle \quad (2.31)$$

is the geometric emittance of the bunch. Considering the same assumption Eq. (2.21) and Eq. (2.22) results to:

$$\langle u(s) u'(s) \rangle = -\alpha_u(s) \epsilon_u^{\text{geom}}, \quad (2.32)$$

$$\langle u'^2(s) \rangle = \gamma_u(s) \epsilon_u^{\text{geom}}. \quad (2.33)$$

Combining the above equations, the geometric emittance is expressed in terms of the particles' distribution as:

$$\epsilon_u^{\text{geom}} = \sqrt{\langle u^2(s) \rangle \langle u'^2(s) \rangle - \langle u(s) u'(s) \rangle^2} \quad (2.34)$$

which, also equals the square root of the determinant of the covariance or Sigma matrix of the particles' distribution:

$$\Sigma = \begin{pmatrix} \langle u^2(s) \rangle & \langle u(s) u'(s) \rangle \\ \langle u(s) u'(s) \rangle & \langle u'^2(s) \rangle \end{pmatrix} = \begin{pmatrix} \sigma_u^2(s) & \langle u(s) u'(s) \rangle \\ \langle u(s) u'(s) \rangle & \sigma_{u'^2(s)} \end{pmatrix} \quad (2.35)$$

The square root of the top-left element of the covariance matrix, σ_u , is defined as the rms beam size and is also a variable that is used extensively in accelerator physics. The definition of rms and of others of the statistical analysis can be found in Appendix A.

Figure 2.4 illustrates the concepts of emittance and rms beam size. It shows the phase space of a transverse Gaussian bunch along with the histograms of the u (top) and u' (right) variables at a particular point s along the ring. Each particle follows its individual ellipse (of different sizes but with the same orientation) depending on its initial conditions. The rms beam size, σ_u , and the rms

2. Basics of accelerator beam dynamics

normalised momentum spread, $\sigma_{u'}$, are shown in the top and right histograms of Fig.2.4 with the blue vertical lines. This corresponds to the area of the ellipse enclosed in the blue line in the phase space plot and equals the rms or geometric emittance, ϵ_u^{geom} , as defined in Eq. (2.34).



Figure 2.4: Transverse phase space of a Gaussian bunch. The figure is a courtesy of Tarsi Prebibaj [30].

It should be noted, that there are also other conventions to define the emittance such as the 90% emittance (green lines in Fig. 2.4) or the 3-sigma emittance (yellow lines in Fig. 2.4). However, here the term geometric emittance will refer to the rms geometric emittance.

According to Liouville's theorem [26], assuming that there are no interactions between the particles and that the energy of the beam is not changing, the geometric emittance remains constant and therefore is an invariant of bunch motion (similarly to the action J_u for the single-particle motion). The geometric emittance does not remain constant during acceleration, instead, the normalised emittance is defined as:

$$\epsilon_u = \beta_0 \gamma_0 \epsilon_u^{\text{geom}} \quad (2.36)$$

The normalised emittance is conserved during acceleration and is often used as an alternative to the geometric emittance, especially in situations where the beam undergoes acceleration or deceleration. It is highlighted here, that throughout this thesis the term "emittance" will refer to the rms normalised emittance.

It is worth noting that for the simulation studies presented in this thesis, the emittance is computed using the statistical definition introduced in Eq. (2.34). In the experimental studies, the emittance is obtained from the rms beam size at a point in the beamline where the beta function is known. The procedure is explained in more detail in Chapter 4, but here we simply note that from Eqs. (2.30), (A.11) and (2.36), we can express the emittance as:

$$\epsilon_u = \frac{\sigma_u(s)^2}{\beta_u(s)} \beta_0 \gamma_0, \quad (2.37)$$

where $\sigma_u(s)$ is the rms beam size, $\beta_u(s)$ is the beta function, at specific location s along the accelerator and β_0, γ_0 are the relativistic parameters.

It should be highlighted that the emittance definitions of Eq. (2.34) (after normalisation with the relativistic parameters) and of Eq. (2.37) are equivalent.

Finally, despite Liouville's theorem, in a real accelerator there are various phenomena that change the emittance such as [31]: scattering by residual gas, intra-beam scattering, beam-beam scattering, stochastic or electron cooling, synchrotron radiation emission, filamentation due to non-linearities of the machine, space charge and noise effects. The studies in this thesis focus on the emittance growth due to noise effects (discussed in more detail in Chapter 3).

Off-momentum effects: dispersion

Up to now, the discussion was limited to on-momentum particles $\delta = 0$: their momentum equals the reference momentum, p_0 . In a more realistic beam, however, the momenta of the individual particles are spread around the reference momentum, p_0 . The "spread" of momenta (or simply "momentum spread") is described by the rms momentum deviation $\sigma_\delta = \sqrt{\langle \delta^2 \rangle}$. As an example, in the SPS machine, which is of interest for this thesis, σ_δ is in the order of magnitude of 10^{-4}

2. Basics of accelerator beam dynamics

to 10^{-3} .

The response of the off-momentum particles to a given force, during their passage from the different magnets in an accelerator, varies with their momentum. Here their motion through the dipole magnets which leads to dispersion effects is discussed.

Particles with $\delta < 0$ ($\delta > 0$) undergo larger (smaller) deflections from the dipole magnets than the reference particle due to lower (higher) magnetic rigidity. Therefore, they travel along the accelerator performing betatron oscillations not around the reference trajectory but around a different closed orbit as illustrated in Fig. 2.5 which depends on their momentum deviation, δ . The change in the closed orbit with respect to the momentum deviation is called dispersion. It is evident that the dispersion introduces a coupling between the longitudinal and transverse planes.



Figure 2.5: The closed orbit and the betatron oscillations around it in the presence of dispersion [32]

The following discussion is focused on the horizontal plane due to the fact that (as stated already) only vertical dipolar fields are considered.³ The equation of motion for the off-momentum particles has already been discussed in Eq. (2.9). Its solution is [28]:

$$x(s) = x_H(s) + D_x(s)\delta, \quad (2.38)$$

where $x_H(s)$ is the homogeneous solution shown in Eq. (2.21) (and corresponding here to betatron oscillations around the off-momentum closed orbit) and $D_x(s)$ is

³A corresponding discussion can be done for the vertical plane to obtain the vertical dispersion but it is out of the scope of this thesis.

the dispersion function which can be expressed as:

$$D_x''(s) + K_x(s)D_x(s) = \frac{1}{\rho(s)}, \quad (2.39)$$

where $K_x(s) = \frac{1}{\rho^2(s)} + k_2(s)$ like in Eq. (2.12). As an example, the rms horizontal dispersion of the SPS machine is about 1.8 m (model value).

The dispersion function can be represented using the matrix formalism which therefore allows the addition of the dispersive contribution in the transfer matrix introduced in Eq. (2.19). This aspect is not discussed here, as it is not relevant for the studies in this thesis (the simulation studies consider zero dispersion function in both transverse planes). However, a detailed discussion can be found in Chapter 2 of Ref. [28].

The dispersion was introduced above as it affects the definition of the normalised beam emittance, which is used to compute the emittance values from experimental measurements (see Chapter 4). In particular, in the presence of dispersion the normalised beam emittance (Eq. (2.37)) becomes:

$$\epsilon_u = \frac{\sigma_u(s)^2 - \sigma_\delta^2 D_u^2(s)}{\beta_u(s)} \beta_0 \gamma_0, \quad (2.40)$$

where $\sigma_u(s)$ is the rms beam size, $\beta_u(s)$ is the beta function, $D_u(s)$ is the dispersion at a specific location s along the accelerator, σ_δ is the momentum spread and β_0, γ_0 the relativistic parameters. The subscript $u = (x, y)$ denotes the horizontal and vertical plane. The impact of the vertical dispersion is included here, as only the model vertical dispersion equals zero. In a real machine, vertical dispersion can be introduced by sources such as steering errors of the dipole or quadrupole magnets [33]. For reference, the rms vertical dispersion in the SPS machine is measured to be about 10 cm.

Additionally, the off-momentum particles receive different focusing due to gradient errors in the quadrupoles. This effect is known as chromaticity and is discussed in detail in the next Section 2.2.1.2 which focuses on non-linear beam dynamics.

2.2.1.2 Non-linear dynamics

Up to now, only linear elements (dipoles and quadrupoles) were considered as in theory they are sufficient to create a synchrotron. However, in a real machine non-linearities are also present due to factors such as imperfections in the magnets field and alignment, particles' momentum spread, and higher order magnets (sextupoles, octupoles, etc). Here, the preceding discussion is expanded to include the non-linear beam dynamics. The discussion is limited to the two effects that are important for the work presented in this thesis: the chromaticity and the detuning with transverse amplitude.

Chromaticity

We define the chromaticity as the variation of the betatron tune Q_u with the relative momentum deviation delta. This is a result of the fact that particles with $\delta < 0$ ($\delta > 0$) are focused more (less) strongly from the quadrupoles due to their smaller (larger) magnetic rigidity. The tune shift introduced by the chromaticity for each particle, $\Delta Q_u(\delta) = Q_u - Q_{u0}$, is:

$$\Delta Q_u(\delta) = \sum_{n=1}^m \frac{1}{n!} Q_u^{(n)} \delta^n, \quad (2.41)$$

where:

$$Q_u^{(n)} = \left. \frac{\partial^n Q_u}{\partial \delta^n} \right|_{\delta=0}, n \in \mathbb{N}, \quad (2.42)$$

denotes the chromaticity of order n . The studies in this thesis, are limited to the chromaticity at the first order in δ ($n = 1$) which is often called linear chromaticity. Note that the betatron tune shift of Eq. (2.41) is referred to as an "incoherent" tune shift, since each particle is affected differently, depending on its individual momentum deviation.

Large values of chromaticity can lead to instabilities and therefore to beam loss [28]. Sextupole magnets are typically used to control the natural chromaticity of a machine and achieve the desired values for its operation.

Similarly to the tune, the chromaticity is a property of the machine lattice.

Octupoles and detuning with amplitude

Octupole magnets are most often used to increase the transverse tune spread of the beam particles to avoid resonances⁴ and instability effects⁵. This property, of providing incoherent betatron tune spread in a controlled way is used extensively in this thesis and therefore some further details are discussed in the following.

The betatron tune spread or linear detuning that is introduced by the octupoles is action-dependent in both transverse planes. In terms of the action variable it is written as follows:

$$\Delta Q_x(J_x, J_y) = 2(\alpha_{xx}J_x + \alpha_{xy}J_y), \quad (2.43)$$

$$\Delta Q_y(J_x, J_y) = 2(\alpha_{yy}J_y + \alpha_{yx}J_x), \quad (2.44)$$

where J_x, J_y the transverse action as introduced in Eq. (2.26), α_{xx}, α_{yy} and $\alpha_{xy} = \alpha_{yx}$ are the detuning coefficients with units 1/m. The detuning coefficients depend on the octupoles strength, the beta functions at their location and the magnetic rigidity [35]. This detuning with the transverse action (or amplitude) is an incoherent effect as it depends on the individual action of each particle.

In the SPS and LHC rings, the octupoles are installed in families (focusing and defocusing) in order to avoid the excitation of resonances. They are usually referred to as "Landau octupoles" since they are used to create a betatron tune spread that provides the mechanism of Landau damping [36] (to stabilise the beam).

2.2.2 Longitudinal motion

In the longitudinal plane, the motion is parallel to the reference trajectory and is described by the co-ordinates (z, δ) . In the next paragraphs, only the basic concepts that are required for the explanation of the equations of motion are discussed, as the studies in this thesis mostly concern transverse beam dynamics. However, a complete discussion can be found in Chapter 9 of Ref. [27].

⁴Resonances in circular accelerators are a result of perturbation terms in the equation of motion once the perturbation frequency matches the frequency of the particles' oscillatory motion. The topic of resonances is out of the scope of this thesis, however, more details can be found in Chapter 16 of Ref. [27]

⁵Beam instabilities in an accelerator are a result of the interplay of the wakefields (which will be discussed in Section 2.3.1) and a perturbation (e.g. noise) on equations of motion of the beam particles. Similar to the resonances their detailed study is out of the scope of this thesis, however, more details can be found in Ref. [34].

2. Basics of accelerator beam dynamics

Synchronous phase

The time that the reference particle needs to complete one complete revolution around the machine is called the revolution period, T_{rev} . Its angular revolution frequency is $\omega_{\text{rev}} = 2\pi/T_{\text{rev}}$ in rad/s or $f_{\text{rev}} = 1/T_{\text{rev}} = v_0/C = \beta_0 c/C$ in Hz, where v_0 the speed of the reference particle, β_0 the relativistic beta, c the speed of light and C the circumference of the accelerator.

In the longitudinal plane the acceleration and the focusing (in phase) of particles are achieved by the longitudinal time-dependent electric field of the main RF cavities:

$$E_{\text{RF}}(t) = E_A \sin(\phi_{\text{RF}} + \phi_s), \quad (2.45)$$

where E_A it the amplitude of the electric field, $\phi_{\text{RF}}(t) = \omega_{\text{RF}} t$ the phase of the RF system, ω_{RF} the angular frequency of the RF system and ϕ_s is the phase of the synchronous or reference particle. The angular frequency needs to be an integer multiple of the revolution frequency: $\omega_{\text{RF}} = h\omega_{\text{rev}}$, where h is called the harmonic number. The harmonic number (number of RF cycles per revolution) defines the maximum number of bunches that can be accelerated (or stored) in the ring. In a synchrotron during the energy ramp the angular frequency increases in order to follow the increasing revolution frequency.

Assuming that the synchronous or reference particle arrives at the RF cavity at phase ϕ_s every turn, the energy gain equals:

$$\Delta E_0 = eV_{\text{RF}} \sin(\phi_s), \quad (2.46)$$

where V_{RF} the amplitude of the RF cavity voltage. The rest of the particles will arrive at the RF cavity at phases $\phi = \phi_s \pm \delta\phi$ and they will gain or lose a different amount of energy per turns which equals: $\Delta E_p = eV_{\text{RF}} \sin(\phi)$.

Dispersion effects

As discussed in the previous chapter, in the presence of dispersion a particle with a momentum offset, δ , from the reference particle will have a different closed orbit of different length (see Fig. 2.5). This change of the orbit length with respect to the momentum offset of each particle is described with the momentum compaction

factor [37]:

$$\alpha_p = \frac{\Delta C/C}{\delta} = \frac{1}{C} \oint_C \frac{D_x(s)}{\rho(s)} ds, \quad (2.47)$$

where C is the circumference of the accelerator and $D_x(s)$ and $\rho(s)$ are the horizontal dispersion and bending radius respectively at a given point s .

With the change of the closed orbit length due to the momentum offset the revolution frequency of the particles also changes. The change of the angular frequency depending on the momentum offset is described with the phase slip factor:

$$\eta_p = -\frac{\Delta\omega/\omega_0}{\delta} = \alpha_p - \frac{1}{\gamma_0^2} = \frac{1}{\gamma_{\text{tr}}^2} - \frac{1}{\gamma_0^2}, \quad (2.48)$$

where ω_0 is the angular frequency of the reference particle, γ_0 is the Lorentz factor and $\gamma_{\text{tr}} = 1/\sqrt{\alpha_p}$ is called the transition energy. When $\gamma_0 < \gamma_{\text{tr}} \Rightarrow \eta_p < 0$ ($\gamma_0 > \gamma_{\text{tr}} \Rightarrow \eta_p > 0$) and the machine operates below (above) transition. For the nominal optics configuration, the SPS machine always operates above transition as $\gamma_{\text{tr}} = 22.8$ which is smaller than the relativistic gamma even for the injection energy ($\gamma_0 = 27.7$ at 26 GeV).

Phase stability and synchrotron oscillations

Even though the particles arrive at different times in the RF cavity, they stay in the vicinity of the reference particle thanks to the effect of longitudinal or phase focusing, which is explained by the concept of phase stability [38, 39, 40]. Its principle is illustrated in Fig. 2.6 for a machine operating above transition. Above transition a particle with $\delta < 0$ will follow a shorter closed orbit (than the reference trajectory) and therefore it will arrive at the RF cavity slightly earlier, than the reference particle and hence it will see a larger voltage. Therefore, it will be accelerated more than the reference particle and subsequently it will need less time to complete the next revolution and, over a number of revolutions, will fall back longitudinally towards the reference particle. The situation is the opposite for a particle with $\delta > 0$.

In particular, the non-synchronous particles oscillate around the phase of the synchronous particle performing synchrotron oscillations (similarly to the betatron oscillations in the transverse plane). It is worth mentioning, that a

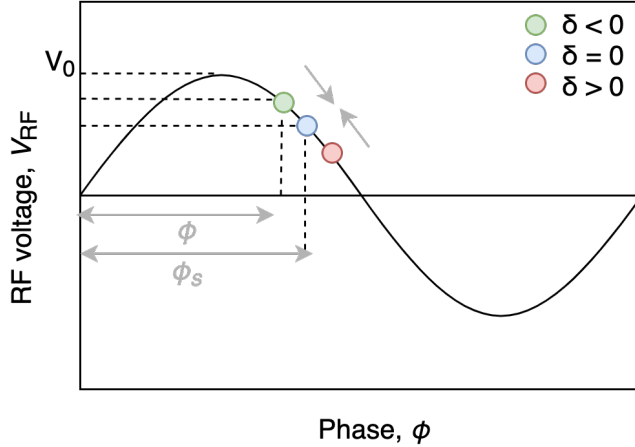


Figure 2.6: Phase stability for particles in a circular accelerator which operates above transition.

complete synchrotron oscillation can take many (~ 100) turns, in contrast to the betatron oscillations (of which there are usually many complete oscillations per turn). The equations of motion for a particle passing through a system of synchronised RF cavities located around the accelerator are [26]:

$$z' = -\eta_p \delta, \quad (2.49)$$

$$\delta' = -\frac{qV_{\text{RF}}}{cp_0 C} \left(\sin \phi_s - \sin \left(\phi_s - \frac{\omega_{\text{RF}} z}{c} \right) \right), \quad (2.50)$$

where $z' = dz/ds$, $\delta' = d\delta/ds$, e is the charge of a proton, c is the speed of light, p_0 is the reference momentum, C is the circumference of the machine, ω_{RF} is the angular frequency of the RF system, ϕ_s is the phase of the synchronous particle and η_p is the phase slip factor.

The synchrotron tune, Q_s , is the number of synchrotron oscillations performed during one complete revolution around the machine and is computed as follows [26]:

$$Q_s = \frac{1}{2\pi} \sqrt{-\frac{eV_{\text{RF}}}{cp_0} \frac{\omega_{\text{RF}} C}{c} \eta_p \cos \phi_s}. \quad (2.51)$$

2.3 Collective effects

Up to now, the motion of the particles was studied neglecting the interaction between them within the bunch. Collective effects in an accelerator describe the

phenomena in which the motion of the particles depends on their interaction with each other or with electromagnetic fields. Examples are beam-beam interactions, space charge effects, wakefields and intra-beam scattering [41]. The collective effects usually become crucial for high-intensity beams as they can lead to instabilities⁶ which then may degrade beam quality, or lead to beam losses. In either case, the performance of the accelerator can be adversely affected. The discussion here is limited in the description of the wakefields and the impedance they are relevant for the studies presented in this thesis. A complete overview of the collective effects can be found in [26, 41].

2.3.1 Wakefields and impedance

The discussion in this section is based in the discussion in Refs. [26, 34, 42, 43, 44].

Wakefields

The charged particles within a beam interact electromagnetically with their surroundings in the beam pipe such as the resistive vacuum pipe walls, the RF cavities, etc. If these structures are not smooth (presence of discontinuities) or not perfectly conducting the interaction with the charged particles will result in electromagnetic perturbations called wakefields. Studying the effects of the wakefields is crucial as they act back on the beam affecting the beam dynamics.

For the study of the wakefields, it is considered that each particle acts as a source of wakefields for the rest of the particles⁷ which are called witnesses. In the ultrarelativistic regime (which is also the regime of these studies) the wakefields from a source particle act only on the particles behind it, hence the term "wake". Wakefields can also act back on the charge generating them when that charge returns to a given location in a storage ring over successive turns. This is the multi-turn effect of the wakefields. In this thesis, only the multi-turn effect from

⁶A beam is called unstable when one of its co-ordinates $(x, x', y, y', z, \delta)$ undergoes exponential growth. Further details on the beam instabilities can be found in Ref. [34]

⁷In studying collective effects, the terms "source particle" and "witness particle" are sometimes used for particles generating wakefields and particles affected by the wakefields, though in reality all charges act as sources of wakefields, and are affected by them

2. Basics of accelerator beam dynamics

the resistive wall will be considered as it is the only one that has a significant impact on the dynamics.

The longitudinal and transverse wakefields can often be treated separately. In the following only the transverse components will be discussed as the focus of the thesis is on the transverse beam dynamics.

Wake functions

Consider two particles of charge q_1 and q_2 moving with ultrarelativistic speed through a structure of length L as shown in Fig. 2.7 [42]. The particle of charge q_1 is the source particle while the witness particle of charge q_2 travels behind it at a constant distance z . $(\Delta x_1, \Delta y_1)$ are the transverse offsets of charge q_1 , and $(\Delta x_2, \Delta y_2)$ are the transverse offsets of charge q_2 from the symmetric axis of the beam pipe. From the interaction of the source particle with the structure of length L a wakefield is generated.



Figure 2.7: Wakefield interaction, where the source particle (blue) affects the witness particle (yellow) travelling at a distance z behind it [42]. $(\Delta x_1, \Delta y_1)$ and $(\Delta x_2, \Delta y_2)$ are the transverse offsets of the source and witness particles respectively.

The wakefields in time domain are described with the concept of wake functions, $W_u(z)$, where $u = (x, y)$ denotes the horizontal and vertical wakefunction. The wakefunction can be expressed as a series of its multipole components as follows:

$$W_u(\Delta u_1, \Delta u_2, z) = W_u^{\text{const}}(z) + W_u^{\text{dip}}(z)\Delta u_1 + W_u^{\text{quad}}(z)\Delta u_2 + o(\Delta u_1, \Delta u_2), \quad (2.52)$$

where $u = (x, y)$ and $W_u^{\text{const}}(z)$, $W_u^{\text{dip}}(z)$, $W_u^{\text{quad}}(z)$ are the transverse constant, dipolar, and quadrupolar wakefunctions respectively. Last, $o(\Delta u_1, \Delta u_2)$ is the higher order term however only the first-order terms will be considered for the rest of the analysis.

The dipolar and quadrupolar wakefunctions were named after the way they act on the witness particle. The dipolar wakefunction acts like a dipole magnet: its impact is the same regardless of the transverse position of the witness particle; it depends only on the position of the source particle. The quadrupolar wakefunction acts like a quadrupole magnet: its impact increases linearly with the transverse position of the witness particle (independent of the position of the source particle).

The constant term can change the closed orbit while the dipolar and quadrupolar terms can modify the tunes [43]. The dipolar term is often referred to as a driving term for coherent instabilities. The quadrupolar term is often referred to as the detuning term as it modifies the betatron frequencies of individual particles.

The effect of the wakefields on the witness particles can be modeled as the following kicks on the transverse normalised momentum [45]:

$$\Delta u'_2 = \int_0^L F_u(s, z, \Delta u_1, \Delta u_2) ds = -q_1 q_2 [W_u^{\text{const}}(z) + W_u^{\text{dip}}(z)\Delta u_1 + W_u^{\text{quad}}(z)\Delta u_2], \quad (2.53)$$

where F_u is the transverse force of the wakefield over the length L . If the structure leading to the wakefield is axially symmetric, then the constant term of the wakefunction is zero.

Beam coupling impedance

The beam coupling impedance is the frequency spectrum of the wakefields in a given component or section of the accelerator. The impedance can be obtained from the wakefunction through a Fourier transform and vice versa as shown below [44]:

$$W_u(z) = -\frac{i}{2\pi} \int_{-\infty}^{+\infty} Z_u(\omega) e^{i\omega z/c} d\omega, \quad (2.54)$$

$$Z_u(\omega) = \frac{i}{c} \int_{-\infty}^{+\infty} W_u(z) e^{-i\omega z/c} dz, \quad (2.55)$$

where $u = (x, y)$, i is the imaginary unit and c is the speed of light.

In order to study the beam dynamics effects due to wakefields, impedance models of the particle accelerators have been developed. Details on how an impedance model is built can be found in Ref. [43]. The impedance model for the SPS is discussed in Chapter 6 while its implementation in the simulations is discussed in

2. Basics of accelerator beam dynamics

Section 2.5.1.

Head-tail modes

The Vlasov equation [46] is often used to describe the beam motion in the presence of wakefields as it allows its mode representation (in frequency domain): the beam motion is described by a superposition of modes. Solving the Vlasov equations for the coupled system between the particle motion (synchrotron and betatron) and wakefield kicks the eigenmodes and eigenfrequencies are obtained. These modes are often referred to as headtail modes as they are related to the betatron phase shift between the head and tail of the bunch in a synchrotron. The headtail modes can either be stable, damped, or excited; in the latter case, they evolve into instabilities. For the beam to become unstable the wakefield kicks (source of energy) need to be synchronized with the bunch motion (e.g. with chromaticity) [42].

Sacherer formulae and complex coherent frequency shift

One of the impedance induced effects, that is relevant for the studies of the thesis, is the complex tune shift. The complex tune shift can be computed analytically based on the Vlasov formalism [46] through the use of perturbation theory. Formulae expressing the results were derived by Sacherer [47, 48].

The headtail modes introduce an exponential dependence on the amplitude of the bunch centroid as follows [45]:

$$u(t) \propto e^{i(\Omega_{u0}^{(l)} + \Delta\Omega_u^{(l)})t} = e^{i(\Omega_{u,0}^{(l)} + \Delta\Omega_{u,re}^{(l)})t} e^{-\Delta\Omega_{u,im}^{(l)}t}, \quad (2.56)$$

where $\Omega_{u0}^{(l)}$ is the real-valued, unperturbed frequency of mode l , and $\Delta\Omega_u^{(l)} = \Delta\Omega_{u,re}^{(l)} + i\Delta\Omega_{u,im}^{(l)}$ is the complex coherent frequency shift introduced by the beam impedance. From Eq. (2.56) it can be seen that the the real part $\Delta\Omega_{u,re}^{(l)}$ modifies the oscillation frequency. The second term $e^{-\Delta\Omega_{u,im}^{(l)}t}$ illustrates that the amplitude of the motion grows for $\Delta\Omega_{u,im}^{(l)} < 0$ (unstable bunch) and is damped for $\Delta\Omega_{u,im}^{(l)} > 0$ (stable bunch).

The complex coherent frequency shift for the mode l for a bunched beam is

(Chapter 6 in Ref. [44]):

$$\Delta\Omega_u^{(l)} = \Omega_{u0}^{(l)} - \omega_{u0} - l\omega_s = -\frac{1}{4\pi} \frac{\Gamma(l+1/2)}{2^l l!} \frac{N_b r_0 c^2}{\gamma_0 T_{\text{rev}} \omega_{u0} \sigma_z} i Z_{\text{eff}}, \quad (2.57)$$

where ω_{u0} and ω_s are the unperturbed betatron and synchrotron frequencies, $\Gamma(x)$ is the gamma function, N_b is the number of particles in the bunch, $r_0 = 1.535 \cdot 10^{-16}$ is the classical radius of the proton, c is the speed of light, γ_0 is the relativistic gamma, T_{rev} is the revolution period, σ_z is the rms bunch length, i is the imaginary unit and Z_{eff} is the effective impedance.

The effective impedance Z_{eff} is computed as follows:

$$Z_{\perp\text{eff}}^{(l)} = \frac{\sum_{p=-\infty}^{+\infty} Z_{\perp}^{(l)}(\omega_p) h_l(\omega_p - \omega_\xi)}{\sum_{p=-\infty}^{+\infty} h_l(\omega_p - \omega_\xi)}, \quad (2.58)$$

where $\omega_p = (p + Q_u)\omega_0$ is the discrete spectrum of the transverse bunch oscillations with $-\infty < p < +\infty$ for a single bunch (which is the case in the following studies) or several bunches oscillating independently and $\omega_\xi = (\xi\omega_u)/\eta_p = Q'\omega_0/\eta_p$ is the chromatic angular frequency with η_p being the phase slip factor.

Last, h_l , is the power spectral density (definition in Appendix B) of a Gaussian bunch of l azimuthal mode. h_l is described by:

$$h_l(\omega) = (\omega\sigma_z/c)^{2l} e^{-(\omega\sigma_z/c)^2}, \quad (2.59)$$

where σ_z is the rms bunch length and c the speed of light.

It should be highlighted that all the parameters inserted in Eq. (2.57), Eq. (2.58) and Eq. (2.59) should be converted in CGS (centimetre–gram–second) units. For the conversion from SI to CGS system the following relations are useful:

$$1[\Omega] = \frac{1}{9} \cdot 10^{-11} [\text{s}/\text{cm}], \quad (2.60)$$

where Ω (Ohm) is the SI unit of resistance.

Finally, the imaginary part of the impedance, leads to a real coherent frequency shift

2. Basics of accelerator beam dynamics

which can be expressed in tune units as follows [49]:

$$\Delta Q_u^{(l)} = \frac{\Delta\Omega_{u,\text{re}}^{(l)}}{\omega_{\text{rev}}}, \quad (2.61)$$

where $\Delta\Omega_{u,\text{re}}^{(l)}$ the real part of the complex tune shift as defined in Eq. (2.57). The real part of the impedance, leads to an imaginary coherent frequency shift which is also known as the growth (+ sign) or damping (- sign) rate of the mode l and is given by [49]:

$$1/\tau_u^{(l)} = -\frac{\Delta\Omega_{u,\text{im}}^{(l)}}{T_{\text{rev}}}, \quad (2.62)$$

where $\Delta\Omega_{u,\text{im}}^{(l)}$ the imaginary part of the complex tune shift as defined in Eq. (2.57). The $1/\tau_u^{(l)}$ is expressed in units of 1/turns.

The real coherent tune shift appears proportional to the beam intensity. This dependence plays a crucial role in the CC studies discussed in the following.

2.4 Optics models for accelerators

For the study of beam dynamics, it is essential to know the detailed arrangement of the magnets (position and strength) in the lattice, which will be referred to as optics. The optics also provide information on the Twiss parameters and phase advances along the ring.

MAD-X [50] is a code which is used extensively for the design and simulation of the accelerators at CERN. The official optics repositories of the CERN machines can be found in Ref. [51].

SPS optics

The studies presented in this thesis are performed for the nominal SPS optics for the LHC filling which are called Q26 optics as the integer part of the tune in both planes is 26. The model for the Q26 optics can be found in the official CERN repository [52] and will be referred to as the nominal SPS model in this thesis. The values of the optics parameters in what follows correspond to the model values unless stated otherwise.

2.5 Tracking simulation codes

In this section the two tracking simulation codes used in this thesis to study the noise-induced emittance growth are presented. Both codes are macroparticle tracking libraries that simulate the particle motion in the six-dimensional (6D) phase space $(x, x', y, y', z, \delta)$. The first code (PyHEADTAIL) performs tracking between interaction points around a circular accelerator at which the particles receive kicks from magnetic elements or from collective effects. The second code (Sixtracklib), uses the detailed optics model of the machine for the tracking. In both cases, the tracking is performed with the use of transfer matrices.

2.5.1 PyHEADTAIL

PyHEADTAIL [53] is an open-source 6D macroparticle tracking code, developed at CERN, which was originally designed to study collective effects in circular machines and to be easily extensible with custom elements. Details on its implementation and its features can be found in Refs. [54, 55]. Below the main steps of a simulation are listed:

1. **Machine initialisation:** The accelerator ring is split into a number of segments of equal length, after each of which there is an interaction point⁸ (IP). At the interaction points the macroparticles experience kicks from various accelerator components (feedback system, multipoles etc) or from collective effects such as the wakefields. The machine parameters, such as the circumference, the betatron and synchrotron tunes and the optics at the interaction points are defined. It should be noted that PyHEADTAIL uses smooth approximation which means that only a few segments are defined per turn.
2. **Bunch initialisation:** A particle bunch is represented by a collection of macroparticles, each of which represents a clustered collection of physical particles. Each macroparticle is described by four transverse (x, x', y, y') and two longitudinal coordinates (z, δ) , a mass and an electric charge. For the

⁸It should be clarified that this is not an "interaction point" in the sense of collision between counter-circulating beams.

2. Basics of accelerator beam dynamics

studies presented in this thesis 10^5 macroparticles are sufficient for an accurate representation of the bunch, unless it is stated otherwise. There are various distributions available. In this thesis the simulations are performed using a Gaussian distribution in transverse and longitudinal planes.

3. **Transverse tracking:** In the transverse plane, the macroparticles are transported from one interaction point to another (e.g. from IP0 to IP1) following the matrix formalism of Eq. (2.19). The linear transfer matrices, M , introduced in Eq. (2.20) take into account the optics parameters at the beginning and the end of the corresponding segment. The phase advance, for each segment equals:

$$\Delta\psi_{u,\text{IP0}\rightarrow\text{IP1}} = Q_u \frac{L}{C}, \quad (2.63)$$

where Q_u is the transverse betatron tune, C the machine circumference and L the length of the corresponding segment. It should be noted that if no detuning source is added (see next step) the matrix M is the same for all particles.

4. **Chromaticity and detuning with transverse amplitude:** The chromaticity (up to higher orders) and amplitude detuning are implemented as a change of the phase advance of each individual particle as follows (example for the horizontal plane):

$$\Delta\psi_{x,i\text{IP0}\rightarrow\text{IP1}} = \Delta\psi_{x,\text{IP0}\rightarrow\text{IP1}} + (\xi_x^1 \delta_i + \alpha_{xx} J_{x,i} + \alpha_{xy} J_{y,i}) \frac{\Delta\psi_{x,\text{IP0}\rightarrow\text{IP1}}}{2\pi Q_x}, \quad (2.64)$$

where $i = 1, \dots, N$ with N being the number of macroparticles, $\Delta\psi_{x,\text{IP0}\rightarrow\text{IP1}}$ is the phase advance for all macroparticles defined in the previous step, ξ_x^1 the horizontal chromaticity of first order (see Eq. (2.42) for $n = 1$) normalised to the betatron tune, α_{xx} and α_{xy} are the detuning coefficients, while J_x and J_y are the horizontal and vertical actions of the macroparticle. Therefore, in the presence of detuning the elements of the M matrix (introduced in Eq. (2.20)) are different for every particle.

5. **Longitudinal tracking:** The longitudinal coordinates are advanced once per

turn after solving numerically the equations of motion introduced in Eq. (2.49) and Eq. (2.50). The motion can be linear or not (non-linear RF system). The studies presented in this thesis use the linear longitudinal tracking.

6. **Transverse impedance effects:** In PyHEADTAIL, wakefield kicks are used to implement the effect of the transverse impedance in the time domain. To improve the computational efficiency, the total impedance of the full machine is lumped at one of the interaction points along the ring and the kicks are applied to the macroparticles once per turn. Additionally, instead of computing the wakefield kicks from each particle to the rest individually, the bunch is divided into a number of slices longitudinally and the macroparticles in each slice receive a wakefield kick generated by the preceding slices⁹ [56]. This is illustrated schematically in Fig. 2.8. A large number of slices is required such as the wakes can be assumed constant within the slice. A high number of macroparticles is also needed in order to avoid statistical noise effects caused by undersampling [54]. For the studies presented, 500 slices are used over a range of three rms bunch lengths in both directions from the bunch center with the bunch being represented by 10^6 macroparticles (instead of 10^5 required for simulations without impedance effects).



Figure 2.8: Longitudinal bunch slicing for the implementation of wakefield kicks in PyHEADTAIL. Without the slicing technique (left) the wake kicks on the red macroparticle are generated from all the green macroparticles resulting in computationally expensive simulations. Instead, when the bunch is sliced longitudinally (right) the wake kicks on the macroparticles in the red slice i are generated by the macroparticles in the green slices j , decreasing significantly the computation time. The figures are courtesy of M. Schenk [55]

The wakefield kicks are computed using a convolution of the wake function with the moments of each particle. The wake functions are available from

⁹This is valid in the ultrarelativistic scenario when no wakefield is generated in front of the bunch. The condition applies for the SPS experiments described in this thesis, performed at 270 GeV.

2. Basics of accelerator beam dynamics

detailed impedance model of the machine which are obtained from a combination of theoretical computations and electromagnetic simulations and can be imported in PyHEADTAIL in form of tables. Typically, the impedance model of an accelerator is provided normalised with the average value of the horizontal and vertical beta functions over the machine at the respective plane. Therefore the transverse beta functions at the location where the wakefield kicks are applied on the beam must equal these average values. More details on the SPS impedance model are provided in Section 6.1.

7. **Data acquisition:** The updated macroparticle coordinates after each turn are available at IP0 for post-processing. Typically, 10^5 turns are required for the noise-induced emittance growth simulations presented in this thesis.

Figure 2.9 shows a graphic representation of the accelerator model and the tracking procedure supporting the steps described above.



Figure 2.9: Graphical representation of the accelerator model and tracking procedure in PyHEADTAIL (inspired by the graphs in Refs. [55, 57]). In this example the ring is split in four segments separated by the interaction points (IPs). Wakefield and multipole kicks are applied to the macroparticles in IP2 and IP4. The macroparticles are transported between the IPs by a linear transfer map (which can include detuning effects) in the transverse plane. The longitudinal coordinates are updated once per turn.

2.5.2 Sixtracklib

Sixtracklib [58] is a library for performing single charged particle simulations developed at CERN. It simulates the motion of the particles in the six-dimensional (6D) phase space. The individual trajectories are computed taking into account the interactions with all the magnetic elements in the machine using the detailed design optics model described in Section 2.4. The particles advance from one

element to the other with transfer maps. Simulations with Sixtracklib are time efficient as the library can run on Graphical Processing Units (GPUs). Further details on Sixtracklib implementation and usage can be found in Ref. [59] and Ref. [60].

Since Sixtracklib code was not used as extensively as PyHEADTAIL for the studies presented here, and was not modified or extended in any way where it was used, we do not give further description here, but refer the reader to the references mentioned above.

3 | Theory of Crab Cavity RF noise-induced emittance growth

This section describes the theoretical formalism which predicts the transverse emittance growth in the presence of CC RF noise. First, it introduces the concept of noise in accelerator physics. The second section focuses on the CC amplitude and phase noise and it provides the equations to predict the noise-induced emittance growth. The last section comments briefly on the experiments that were carried out in KEKB: the work at KEKB constitutes the only experimental study of the effect of crab cavity RF noise prior to the work performed in the SPS

3.1 Noise

In particle accelerators, the presence of noise in components controlling the beam or observing the beam behaviour is a concern. Random fluctuations in the electric and magnetic fields seen by the beam can lead to emittance growth, orbit instability, and in extreme cases, particle loss. Examples of noise sources are ripples in the power converters which lead to fluctuations of the magnetic fields, ground motion, and various elements in the accelerator structure such as the transverse damper and the Crab Cavities.

Emittance growth

The thesis focuses on the problem of noise-induced emittance growth, which has been studied extensively in the past [61, 62, 63]. In principle, if the spectrum of the noise, overlaps with the sidebands of the betatron frequencies, $(k \pm q_u)f_{\text{rev}}$ (where k is an integer, q_u is the fractional part of the transverse betatron tune with $u = (x, y)$ denoting the horizontal and vertical planes respectively, and f_{rev} is the

revolution frequency), it drives coherent betatron oscillations. For these betatron oscillations to result in emittance growth requires the presence of a tune spread. The mechanism behind the emittance growth is that the tune spread leads to a phase mixing of the particles within the bunch causing decoherence of the betatron oscillations, which then results in emittance growth [61]. It should be highlighted, that for all the studies presented in this thesis, the decoherence rate is fast comparing to the growth of betatron oscillations and thus the emittance growth rate is independent of the exact value of betatron tune spread [61]. For machines with working points far from non-linear (high-order) betatron resonances the emittance growth is linear with time and proportional to the power spectral density of the noise spectra at the betatron frequencies, $(k \pm q_u)f_{\text{rev}}$, mentioned above [61]. This scenario holds for the work of this thesis. The definition of the power spectral density can be found in Appendix B.

White noise

In the studies presented in this thesis (simulations, theoretical and experimental studies), it is considered that the beam is subject to white noise. In signal analysis, white noise is a random signal with the same amplitude (intensity) at all frequencies, which results in a uniform power spectral density. For the computational analysis (i.e. simulation studies), it is considered that the particle motion is influenced by the noise once per turn [61, 62, 63]. To this end, the white noise signal is sampled at a finite number of points (equal the number of turns considered for the computational study) which are called discrete time steps. In this case, the white noise can be considered as a sequence of uncorrelated random values taken from a Gaussian distribution with zero mean and given standard deviation. For reference, the power spectral density of such a white noise signal that was used for the simulations that will be presented in this thesis can be found in Fig. 5.3. More details on the continuous and discrete time analysis can be found in Appendix B.

Dipole noise

From the various noise sources that are present in an accelerator, this thesis focuses on the dipolar noise and on the CC noise. Dipolar noise affects all particles in the same, i.e. the noise kick is constant along the bunch. On the other hand, the way

3. Theory of Crab Cavity RF noise-induced emittance growth

the CC noise affects the particles depends on their longitudinal position within the bunch.

In this paragraph, the modeling of dipole noise is introduced as it constitutes the basics for understanding the more complex effects of CC noise. The details on the CC noise (which is the main focus of the work presented here) are discussed further in a dedicated section (see Section 3.2).

Past studies [61, 62] have shown that the dipole white noise can be modeled as a sequence of random kicks (stochastic process) that affect the particles within a bunch by changing their transverse angle each turn as follows:

$$\Delta u'_j = \theta_j, \quad (3.1)$$

where $j = \{0, \dots, N_{\text{turns}}\}$ denotes the turn number with N_{turns} being the total number of turns that the beam experiences the noise and $u = (x, y)$ denoting horizontal or vertical position co-ordinate. The parameter θ_j corresponds to the noise kick and is the j^{th} element of a set of N_{turns} samples, drawn from a Gaussian distribution (with size N_{turns}) with zero mean and standard deviation σ_θ . This way it is ensured that the noise kicks are uncorrelated.

The standard deviation σ_θ characterises the strength of the noise. As discussed in Appendix B (see Eq. (B.24)) for a white noise spectrum, it is related to its power spectral density, S_θ , as follows:

$$S_\theta = \frac{\sigma_\theta^2}{f_{\text{rev}}}, \quad (3.2)$$

where f_{rev} is the revolution frequency of the machine.

The power spectral density, S_θ , is expressed in terms of the square of the amplitude of the signal per unit frequency. The noise is applied in the angle co-ordinates, hence the units of the power spectral density are rad^2/Hz . In Eq. (3.2) the noise appears independent of the frequency since for the white noise spectrum the power spectral density is the same for all frequencies.

In this thesis, the term "noise" will refer to white noise, which can be modeled with the above-mentioned stochastic process.

3.2 Crab Cavity noise and emittance growth

The presence of noise in the CC low-level RF system is an issue of major concern for the HL-LHC project as it results in transverse emittance growth and subsequently in loss of luminosity. To this end, in 2015, P. Baudrenghien and T. Mastoridis developed a theoretical model [63] which predicts this transverse emittance growth induced by CC noise focusing in the HL-LHC scenario. In particular, the model assumes a hadron machine, zero synchrotron radiation damping, long bunches (in the order of cm), and white RF noise (discrete spectral lines are excluded). Additionally, it is assumed that the phase of the CC is set such that the zero-crossing of the voltage coincides with the longitudinal centre of the bunch.

Since we will refer to theoretical model of P. Baudrenghien and T. Mastoridis [63] frequently through the thesis we will often use the term "Mastoridis–Baudrenghien model" for simplicity.

The Mastoridis–Baudrenghien model is also applicable to the SPS (where the same conditions apply), where the CCs will be tested before their installation in the HL-LHC (Section 1.3). The equations and formulas from this model that are essential for the understanding of the studies are discussed below.

3.2.1 Crab Cavity amplitude and phase noise

The unperturbed instantaneous CC voltage can be written as:

$$V_{\text{CC}}(t) = V_{0,\text{CC}} \sin(2\pi f_{\text{CC}} t + \phi_{\text{CC}}), \quad (3.3)$$

where $V_{0,\text{CC}}$ is the peak amplitude of the CC voltage, f_{CC} the CC frequency, and ϕ_{CC} the CC phase. The following analysis, will consider $\phi_{\text{CC}} = 0$ as this is the case for the most of the studies presented in this thesis unless it is stated otherwise. To this end the above equation becomes:

$$V_{\text{CC}}(t) = V_{0,\text{CC}} \sin(2\pi f_{\text{CC}} t), \quad (3.4)$$

3. Theory of Crab Cavity RF noise-induced emittance growth

Equation (3.4) can be re-written as a function of the longitudinal position within the bunch z instead of time t as follows:

$$V_{\text{CC}}(z) = V_{0,\text{CC}} \sin\left(\frac{2\pi f_{\text{CC}}}{\beta_0 c} z\right), \quad (3.5)$$

where β_0 is the relativistic parameter and c is the speed of light. In the presence of modulations in amplitude and phase Eq. (3.6) becomes (details in Appendix B.3):

$$V_{\text{CC}}(z) = V_{0,\text{CC}}(1 + \Delta A) \sin\left(\frac{2\pi f_{\text{CC}}}{\beta_0 c} z + \Delta\phi\right), \quad (3.6)$$

where $\Delta\phi$ is the deviation from the nominal phase, $2\pi f_{\text{CC}}z/(\beta_0 c)$, and will be referred to as phase noise in the following. $\Delta A = \Delta V_{0,\text{CC}}/V_{0,\text{CC}}$ is the relative deviation from the nominal amplitude $V_{0,\text{CC}}$ and will be referred to as amplitude noise. The units of $\Delta\phi$ is radians while ΔA has no units as it defines a scaling factor applied to the amplitude, rather than stating directly the change in the amplitude.

In the calculation of the RF noise effects it is assumed that RF phase and amplitude noises are uncorrelated. The validity of this hypothesis depends on the actual architecture of the low-level RF responsible for the regulation of the cavity field. The low-level RF system for the HL-LHC CCs is presently being designed at CERN. Further details can be found in Ref. [15] of the above-mentioned publication of P. Baudrenghien and T. Mastoridis [63], but discussing them in more detail is out of the scope of this thesis.

To this end, and following the analysis in [63] and in accordance with Eq. (3.1) the change of the trajectory of each particle within a bunch as a result of the phase and amplitude CC RF noise can be modeled as follows:

$$\textbf{Amplitude noise: } \Delta u'_j = \frac{eV_{0,\text{CC}}}{E_b} \Delta A_j \sin\left(\frac{2\pi f_{\text{CC}}}{c\beta_0} z_j\right), \quad (3.7)$$

$$\textbf{Phase noise: } \Delta u'_j = +\frac{eV_{0,\text{CC}}}{E_b} \Delta\phi_j \cos\left(\frac{2\pi f_{\text{CC}}}{c\beta_0} z_j\right), \quad (3.8)$$

where $j = \{0, \dots, N_{\text{turns}}\}$ denotes the turn number with N_{turns} being the total number of turns that the bunch experiences the noise and e is the elementary charge.

Furthermore, u' , with $u = (x, y)$, is the angle co-ordinate and z the longitudinal co-ordinate of each particle as defined in Eq. (2.3). The parameters ΔA_j and $\Delta \phi_j$, are the j^{th} elements of a set of N_{turns} samples, drawn from Gaussian distributions of size N_{turns} , with zero mean and standard deviation of $\sigma_{\Delta A}$ and $\sigma_{\Delta \phi}$, respectively. A typical value of σ_A and σ_ϕ that will be used in the simulations later is 2.7×10^{-3} . It is reminded that σ_ϕ is expressed in radians, while σ_A has no units.

The power spectral density of these noise kicks for a white noise spectrum can be computed as follows (see discussion in Appendix B and Eq. (B.24)):

$$S_{\Delta A} = \frac{\sigma_{\Delta A}^2}{f_{\text{rev}}}, \quad (3.9)$$

and

$$S_{\Delta \phi} = \frac{\sigma_{\Delta \phi}^2}{f_{\text{rev}}}, \quad (3.10)$$

where f_{rev} is the revolution frequency of the machine. $S_{\Delta A}$ is the power spectral density of the amplitude noise and is expressed in Hz^{-1} , while $S_{\Delta \phi}$ is the power spectral density of the phase noise and is expressed in $\text{rad}^2 \text{Hz}^{-1}$.

Figures 3.1 and 3.2 show schematically the effects of the amplitude and phase noise (respectively) on the crab cavity voltage, and on the particles within a single bunch. It can be seen that in the presence of amplitude noise the head and the tail of the bunch are kicked in opposite directions which results in intra-bunch oscillations. On the other hand, in the presence of phase noise, the particles in the bunch receive kicks that are in phase. This results in a shift of the bunch centroid which is dipole (or mode 0) motion.

For the LHC, HL-LHC and SPS CCs the amplitude and phase RF noise are represented by white noise spectra. In that case, they can be considered as a sequence of uncorrelated random variables taken from a Gaussian distribution with zero mean and standard deviation $\sigma_{\Delta A}$ and $\sigma_{\Delta \phi}$, respectively. The variances, $\sigma_{\Delta A}^2$ and $\sigma_{\Delta \phi}^2$ equal the total noise power (see Appendix B.2 for definitions).

3. Theory of Crab Cavity RF noise-induced emittance growth



Figure 3.1: Modulation in amplitude or amplitude noise (left) and its impact on the particles within the bunch (right). The blue dots represent the individual particles while the red arrows indicate the direction of the noise kicks which act on them.

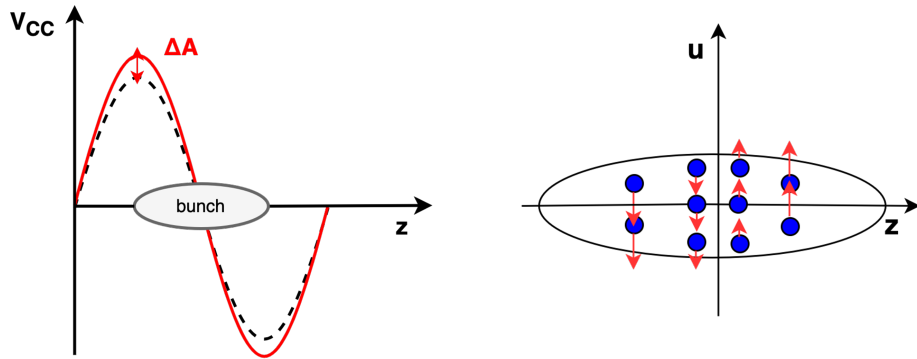


Figure 3.2: Modulation in phase or phase noise (left) and its impact on the particles within the bunch (right). The blue dots represent the individual particles while the red arrows indicate the direction of the noise kicks which act on them.

3.2.2 Emittance growth formulas

The theoretical formalism for predicting the transverse emittance growth in the presence of CC RF amplitude and phase noise was derived in [63]. The derivation assumes a single bunch is crossing the crab cavity and the phase of the CC is set such that the zero-crossing of the voltage coincides with the longitudinal centre of the bunch, as well as no coupling between the transverse planes and constant energy (no acceleration).

The noise kicks are represented as a stochastic process with uniform spectrum across the betatron tune distribution.

Taking these conditions into account, the emittance growth resulting from

amplitude noise is derived as [63]:

$$\frac{d\epsilon_u^{\text{geom}}}{dt} = \beta_{u,\text{CC}} \left(\frac{eV_{0,\text{CC}} f_{\text{rev}}}{2E_b} \right)^2 C_{\Delta A}(\sigma_\phi) \sum_{k=-\infty}^{+\infty} S_{\Delta A}[(k \pm \bar{q}_u \pm \bar{q}_s) f_{\text{rev}}]. \quad (3.11)$$

For phase noise, the emittance growth is derived as [63]:

$$\frac{de_u^{\text{geom}}}{dt} = \beta_{u,\text{CC}} \left(\frac{eV_{0,\text{CC}} f_{\text{rev}}}{2E_b} \right)^2 C_{\Delta\phi}(\sigma_\phi) \sum_{k=-\infty}^{+\infty} S_{\Delta\phi}[(k \pm \bar{q}_u) f_{\text{rev}}]. \quad (3.12)$$

In these formulas, which are valid for both transverse planes as $u = (x, y)$, $\beta_{u,\text{CC}}$ is the transverse beta function at the location of the CC, $V_{0,\text{CC}}$ the CC voltage, f_{rev} the revolution frequency of the beam, E_b the beam energy, and \bar{q}_u and \bar{q}_s the mean of the betatron and synchrotron tune distribution¹ where q_u, q_s (with lower case) denote the fractional part of the betatron and synchrotron tunes, respectively. $S_{\Delta A}$ and $S_{\Delta\phi}$ are the power spectral densities (PSD) of the noise at all the betatron and synchrobetatron (for the amplitude noise case) sidebands and they are expressed in units of Hz^{-1} and $\text{rad}^2\text{Hz}^{-1}$, respectively. In particular, $k \in \mathbb{Z}$ is the harmonic number of the revolution frequency and the \pm signs refer to the upper (+) and lower (-) sidebands at each multiple of the revolution frequency, $k f_{\text{rev}}$.

The definition of the power spectral density along with the fundamental terminology for the signal-processing can be found in Appendix B. As all the studies presented in this thesis are done with white noise, the power spectral densities can be computed using Eqs. (3.9) and (3.10).

The terms $C_{\Delta A}$ and $C_{\Delta\phi}$ are correction terms to account for the bunch length:

$$C_{\Delta A}(\sigma_\phi) = e^{-\sigma_\phi^2} \sum_{l=0}^{+\infty} I_{2l+1}(\sigma_\phi^2), \quad (3.13)$$

$$C_{\Delta\phi}(\sigma_\phi) = e^{-\sigma_\phi^2} \left[I_0(\sigma_\phi^2) + 2 \sum_{l=1}^{+\infty} I_{2l}(\sigma_\phi^2) \right], \quad (3.14)$$

with σ_ϕ the rms bunch length, in radians, with respect to the CC frequency f_{CC} , and $I_n(x)$ the modified Bessel function of the first kind.

Figure 3.3 illustrates the correction term for different values of bunch length for

¹For white noise spectra the effect of noise is independent of the actual tune distribution, hence the use of the mean quantities. The generic formulas can be found in [63].

3. Theory of Crab Cavity RF noise-induced emittance growth

amplitude (left) and phase noise (right). The SPS nominal bunch length used in the CC tests is indicated by an orange dot for reference.

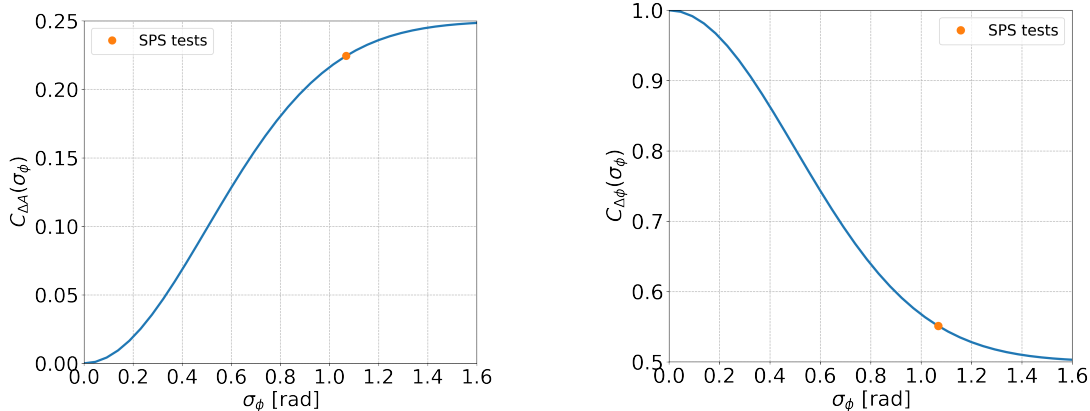


Figure 3.3: Correction term for amplitude (left) and phase noise (right) over a range of bunch length values.

3.3 Studies in KEKB

CCs have been tested in the past with lepton beams at KEKB in Japan [17, 18, 19]. The tests included studies of the effects of RF noise in the CC on the beam. However, there were significant differences in KEKB, compared to SPS, LHC and HL-LHC. In particular, the studies in KEKB were conducted for lepton bunches, rather than hadron bunches. The bunch length in KEKB was smaller by an order of magnitude than in SPS or HL-LHC: this means that the effects of amplitude noise would be negligible in KEKB. Furthermore, synchrotron radiation in lepton storage rings provides significant damping. Finally, the RF noise in KEKB was characterised by a single spectral line, rather than white noise. Due to these differences, the studies performed at KEKB [64] are not applicable to the studies presented in this thesis and will thus not be discussed in more detail.

Now that the theoretical formulas for the CC RF noise-induced emittance growth have been introduced, they will be used through the following chapters for comparison against numerical simulations and experimental measurements (in the SPS) for developing confidence in the theoretical model and its predictions for the HL-LHC.

4 | Experimental studies 2018: emittance growth from Crab Cavity noise

In Chapter 3 the theoretical model (Mastoridis–Baudrenghien model) for the transverse emittance growth caused by amplitude and phase noise in a CC was discussed. On September 5, 2018, a dedicated experiment was conducted in the SPS to benchmark this model against experimental data and confirm the analytical predictions. In particular, the aim was to inject artificial noise into the CC RF system and compare the measured emittance growth rates with the theoretically computed ones. In this chapter, the measurement results from the SPS are presented and discussed. However, since a similar experiment has not been performed before, this chapter does not present only the emittance growth measurements. It also discusses in detail the experimental conditions and the available measurements of other parameters of interest such as the CC voltage, the RF noise spectra, the bunch length, and the bunch intensity, aiming to provide a full understanding.

Section 4.1 provides some information on the installation of the CCs in the SPS that are essential for the studies in this thesis and elaborates on some considerations regarding their operation in the SPS. Afterward, Section 4.2 describes the machine setup and the beam configuration for the emittance growth measurements. This includes a summary of the preparatory studies conducted in the previous years. In Section 4.3 information on the noise injected in the CC RF system is provided while in Section 4.4 the beam-based measurement of the CC voltage is presented. The measurements of transverse emittance growth are presented in Section 4.5 while the complementary measurements of bunch length and intensity in Section 4.6. Section 4.7 compares the measured transverse emittance growth against the

predictions of Mastoridis–Baudrenghien model. The conclusions of the first experimental campaign with CC noise in SPS are drawn in Section 4.8.

4.1 Crab Cavities in the SPS

For the SPS tests of 2018 two prototype CCs of the Double Quarter Wave (DQW) type¹, which will be referred to as CC1 and CC2 through this thesis, were fabricated by CERN and were assembled in the same cryomodule. For its installation an available space was found at the SPS Long Straight Section 6 (SPS-LSS6) zone. As this section is also used for the extraction of the beam to the LHC, the cryomodule was placed on a mobile transfer table [65] which moved the cryomodule in the beamline for the CC tests and out of it for the usual SPS operation without breaking the vacuum.

The main CCs' parameters are listed in Table 4.1. Their location along the SPS ring is also indicated, in case someone would like to repeat the analysis described in this thesis.

Table 4.1: Crab Cavities design parameters for the SPS tests.

Parameter	Value	
	CC1	CC2
crabbing plane	vertical	vertical
s-location*	6312.72 m	6313.32 m
CC voltage, $V_{0,CC}$	≤ 3.4 MV	≤ 3.4 MV
CC frequency, $V_{0,CC}$	400.78 MHz	400.78 MHz
Horizontal / Vertical beta function, $\beta_{x,CC} / \beta_{y,CC}$	29.24 m / 76.07 m	30.31 m / 73.82 m
Horizontal / Vertical alpha function, $\alpha_{x,CC} / \alpha_{y,CC}$	-0.88 m / 1.9 m	-0.91 m / 1.86 m
Horizontal / Vertical dispersion, $D_{x,CC} / D_{y,CC}$	-0.48 m / 0 m	-0.5 m / 0 m

* The s-location is referred to the location of the elements along the SPS ring with respect to the start of the lattice i.e. element QF10010 which is a focusing quadrupole. The s-location is given to allow the studies to be reproduced.

4.1.1 Considerations about the Crab Cavity operation

The experimental studies presented in this thesis, were performed with the CCs operating at a fixed frequency of 400.78 MHz (unless it is stated otherwise) and at a target peak voltage of about 1 MV. Even though the CC modules installed in the SPS

¹The RFD type CCs are expected to be ready by the end of 2022 - beginning of 2023.

can operate at a maximum voltage of 3.4 MV (see Table 4.1), the experiments were performed with peak voltage of 1 MV since for that value the stable CC operation for long periods was ensured. Further details on the hardware aspects of the CC operation in the SPS are not discussed here as they are out of the scope of this thesis.

Energy ramp

SPS receives the proton beam at 26 GeV from the PS. It was found that the ramp to higher energies could not be performed with the CC switched on, since during the acceleration one of the vertical betatron sidebands was crossing the CC frequency resulting to resonance excitation and beam loss [66, 67]. Changing the CC frequency during the ramp so that it stays synchronous with the beam was not an option due to hardware limitations [67]. Therefore, it was established that the acceleration has to be performed with the CC switched off and its voltage must be set up only after the energy of interest has been achieved. It is worth noting that this approach will also be used in the HL-LHC.

Crab Cavity - main SPS RF synchronisation

In order to ensure that the beam will experience the same kick from the CC each turn the SPS main RF system operating at \sim 200 MHz needed to be synchronous with the CC operating at 400.78 MHz. Due to the larger bandwidth of the SPS main RF system the CC was used as a master. Therefore the CC was operating at a fixed frequency, while the main accelerating cavities were adjusted to the exact half of the CC frequency so that they become synchronous with the crabbing signal. For studies at higher energies the synchronisation took place at the end of the energy ramp shortly a few seconds after the CC was switched on [66].

4.2 Experimental configuration and procedure

This section gives an overview of the experimental setup and the procedure that was followed. First, it briefly discusses the preparatory studies that were performed during 2012-2017 [68, 69, 70], explaining the choice of the intensity and energy values for which the emittance growth measurements were conducted. Furthermore, it presents in detail the rest of the beam and machine conditions

4. Experimental studies 2018: emittance growth from Crab Cavity noise

during the experiment. Last, the experimental procedure is explained.

4.2.1 Preparatory experimental studies

For studying the long-term emittance evolution a special mode of operation was set up in the SPS which is called "coast" (in other machines, it is referred to as storage ring mode) with bunched beams. In this mode, the bunches circulate in the machine at constant energy for long periods, from a few minutes up to several hours, similar to the HL-LHC case.

To make sure that the SPS can be used as a testbed for the emittance growth studies with CCs an extensive preparatory campaign was carried out through 2012-2017 [68, 69, 70]. The primary concern was the emittance growth that was observed in the machine from other sources than injected noise and will be referred to as the natural emittance growth in this thesis. The natural emittance growth needs to be well characterised and be kept sufficiently small in order to distinguish and understand the contribution from the CC noise.

From these studies, it was concluded that the optimal coast setup is at high energies, with low chromaticity and bunches of low intensity as it minimises the natural emittance growth [70]. The highest energy for which the SPS could operate in coast was 270 GeV and thus the experiments were performed at this energy. That limitation was introduced due to limited cooling of the magnets to transfer away the heating when operating at high energy and thus at large currents for long periods. Moreover, as the natural emittance growth was found to be a single bunch effect four bunches were used. That choice was made to reduce the statistical uncertainty of the measurements but not to increase the beam intensity.

4.2.2 Machine and beam configuration

During the experiment the Landau octupoles were switched off. Nevertheless, a residual non-linearity was present in the machine mainly due to multipole components in the dipole magnets [71, 72]. The transverse feedback system was also switched off. Unfortunately, no measurements of chromaticity are available from the day of the experiment. However it was ensured that the chromaticity was

corrected to small positive values. Last, only one CC, CC2, was used for simplicity and it operated at 1 MV.

The main machine and beam parameters used for the emittance growth measurements in 2018 are listed in Table 4.2.

Table 4.2: Main machine and beam parameters for the emittance growth studies with CCs in SPS in 2018.

Parameter	Value
Beam energy, E_b	270 GeV
Revolution frequency, f_{rev}	43.375 kHz
Main RF voltage / frequency, $V_{\text{RF}} / f_{\text{RF}}$	3.8 MV / 200.39 MHz
Horizontal / Vertical betatron tune, Q_{x0} / Q_{y0}	26.13 / 26.18
Horizontal / Vertical first order chromaticity, Q'_x / Q'_y	~ 1.0 / ~ 1.0
Synchrotron tune, Q_s	0.0051
CC2 voltage / frequency, $V_{0,\text{CC}} / f_{\text{CC}}$	1 MV / 400.78 MHz
Number of protons per bunch, N_b	3×10^{10} p/b*
Number of bunches	4
Bunch spacing	524 ns
Rms bunch length, $4\sigma_t$	1.8 ns*
Horizontal / Vertical normalised emittance, $\epsilon_x^n / \epsilon_y^n$	2 μm / 2 μm *
Horizontal / Vertical rms tune spread, $\Delta Q_x^{rms} / \Delta Q_y^{rms}$	1.9×10^{-5} / 2.1×10^{-5} †

* The value corresponds to the requested initial value at the start of each coast. The measured evolution of the parameter through the experiment is presented in the Sections 4.5 and 4.6.

† Here the rms betatron tune spread includes only the contribution from the detuning with amplitude present in the SPS machine. The calculations for the listed values can be found in Appendix C.2.

4.2.3 Experimental procedure for emittance growth measurements

The emittance growth experiment took place on September 5, 2018, and was given a total time window of about 6 hours (start:~10:30, end:~17:00). In order to characterize the CC noise induced emittance growth, different levels of controlled noise were injected into the low-level RF system and the bunch evolution was recorded for about 20-40 minutes (for each noise setting). The experiment was conducted over three coasts, since a new beam was injected every time the quality of the beam was seen to be degraded e.g. very large beam size. In the following, the different noise settings will be denoted as "CoastN-SettingM", where N stands for the coast number and M for the different noise levels applied in each coast in

chronological order. After the experiment, the measured growth rates would be compared with the theoretically expected values from the model described in Chapter 3.

4.3 Injected RF noise

The noise injected in the CC RF system was a mixture of amplitude and phase noise up to 10 kHz. The phase noise was always dominant. The noise levels were measured with a spectrum analyzer E5052B [73] and are expressed as $10\log_{10}\mathcal{L}(f)$ [dBc/Hz]. $\mathcal{L}(f)$ follows the IEEE definitions in [74] is the standard measure for characterising instabilities in the frequency domain. It should be emphasised that $\mathcal{L}(f)$ as defined in [74] is two-sided, which means that it has both positive and negative frequencies and as a real signal is symmetric around the DC component, $f = 0$ Hz. However, since the spectrum analyser E5052B displays the logarithmic quantity $10\log_{10}\mathcal{L}(f)$ only the positive frequencies are displayed.

The relation between the measured noise levels and the power spectral densities in Eq. (3.11) and Eq. (3.12) following the IEEE conventions [74] is given by $S_{\Delta A, \Delta \phi}(f) = \mathcal{L}(f)$ (see Table A.1 in [74]), with $S_{\Delta A}$ in Hz^{-1} and $S_{\Delta \phi}$ in $\text{rad}^2\text{Hz}^{-1}$.

Figure 4.1 displays an example measurement of amplitude (left) and phase (right) noise acquired during the experiment. The spectrum analyzer E5052B [73], was directly attached to the RF antenna inside the CC which monitors the amplitude and the phase of its field. To this end, the voltage induced by the passage of the bunch through the CC was visible in the measured spectra: spikes at high frequencies and in particular at harmonics of the revolution frequency.

4.3.1 Expected emittance growth from Mastoridis–Baudrenghien model

Here, some comments on the use of the Eq. (3.11) and Eq. (3.12) for predicting the emittance growth rate from the above described noise spectra injected in the CC RF system are made.

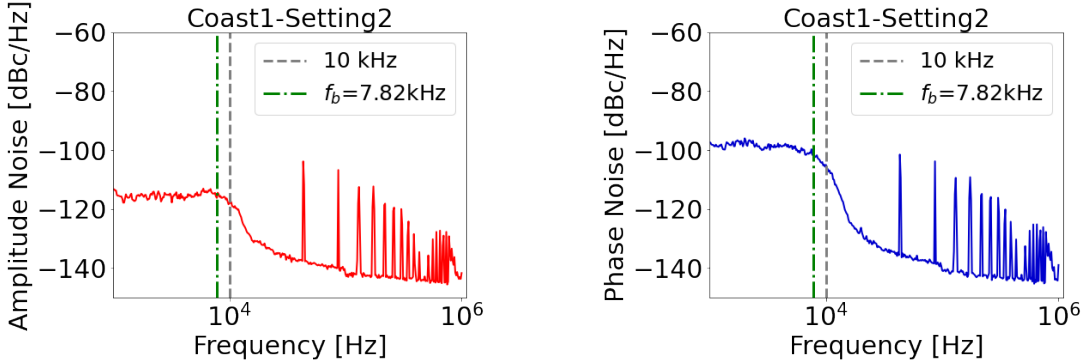


Figure 4.1: Example amplitude (left) and phase (right) noise spectra measured with a spectrum analyzer E5052B [73] during the emittance growth studies with CCs in SPS. The noise extends up to 10 kHz (grey dashed line) overlapping the first betatron sideband at ~ 8 kHz (green dashed line). The spikes at high frequencies correspond to the harmonics of the revolution frequency and are a result of the beam induced signal from its passage through the CC.

First, the emittance growth in the vertical plane is considered since the CC module (DQW) installed in the SPS provides a vertical deflection on the beam. As already discussed in Chapter 3 the noise induced emittance growth in the vertical plane depends on the noise power at the vertical betatron and synchrobetatron sidebands for the phase and amplitude noise respectively (see Eq. (3.12) and Eq. (3.11)). During the experiment (see parameters listed in Table 4.2): $q_y = 0.18$, $f_{\text{rev}} = 43.38$ kHz, and $q_s = 0.0051$.

The upper and lower sidebands of the first and second vertical betatron sidebands are observed in the following frequencies:

$$k = 0 : (0 \pm q_y) f_{\text{rev}} = \pm 0.18 \times 43.38 \text{ kHz} \approx \pm 7.8 \text{ kHz}, \quad (4.1)$$

$$k = \pm 1 : (\pm 1 \pm q_y) f_{\text{rev}} = (\pm 1 \pm 0.18) \times 43.38 \text{ kHz} \approx \begin{cases} -51.2 \text{ kHz and } -35.6 \text{ kHz,} & \text{for } k = -1 \\ 51.2 \text{ kHz and } 35.6 \text{ kHz,} & \text{for } k = 1 \end{cases} \quad (4.2)$$

The upper and lower sidebands of the first and second vertical synchrobetatron

4. Experimental studies 2018: emittance growth from Crab Cavity noise

sidebands are observed in the following frequencies:

$$k = 0 : (0 \pm q_y \pm q_s) f_{\text{rev}} = (\pm 0.18 \pm 0.0051) \times 43.38 \text{ kHz} \approx \pm 8.02 \text{ kHz and } \pm 7.6 \text{ kHz.} \quad (4.3)$$

$$k = \pm 1 : (\pm 1 \pm q_y \pm q_s) f_{\text{rev}} = (\pm 1 \pm 0.18 \pm 0.0051) \times 43.38 \text{ kHz} \approx \\ \approx \begin{cases} -35.35, -35.79, -50.96, -51.40 \text{ kHz,} & \text{for } k = -1 \\ 35.35, 35.79, 50.96, 51.40 \text{ kHz,} & \text{for } k = 1 \end{cases}. \quad (4.4)$$

It is evident, that the noise spectra injected in the CC RF, which extends with approximately constant power spectral density up to 10 kHz, overlaps and primarily excites only the the first betatron and synchrobetatron sidebands, for $k = 0$ (upper and lower).

To this end, for the experimental conditions of 2018 Eq. (3.11) and Eq. (3.12) can be re-written as follows:

$$\frac{d\epsilon_u^{\text{geom}}}{dt} = 4 \times \beta_{u,\text{CC}} \left(\frac{eV_{0,\text{CC}} f_{\text{rev}}}{2E_b} \right)^2 C_{\Delta A}(\sigma_\phi) S_{\Delta A}, \quad (4.5)$$

and

$$\frac{d\epsilon_u^{\text{geom}}}{dt} = 2 \times \beta_{u,\text{CC}} \left(\frac{eV_{0,\text{CC}} f_{\text{rev}}}{2E_b} \right)^2 C_{\Delta\phi}(\sigma_\phi) S_{\Delta\phi}. \quad (4.6)$$

for amplitude and phase noise, respectively. The multiplication factors 4 and 2, show the contribution from to the first synchrobetatron and betatron sidebands at the frequencies computed in Eqs. (4.3) and (4.1), respectively.

It is reminded, that the power spectral densities $S_{\Delta A}$ and $S_{\Delta\phi}$ appear independent of the frequency since the noise spectra are considered constant up to ± 10 kHz. They can be computed from the measured spectra expressed in $10 \log_{10} \mathcal{L}$ [dBc/Hz] through the relation $S_{\Delta A, \Delta\phi} = \mathcal{L}$ introduced earlier in this section.

Power spectral density values of interest

It can be clearly seen from Fig. 4.1 that the measured noise spectra are noisy²: random changes in amplitude are observed from point to point within the signal.

²This is not surprising since it is in the nature of the noise.

To get a more precise value of the power spectral density value at the first betatron sideband, f_b , the average of the power spectral density values over a frequency range of ± 500 Hz around it is considered while its uncertainty equals the standard deviation over that range. In the following, it is also assumed for simplicity that the noise power between the synchrobetatron sidebands and the first betatron sideband is smooth as they lie very close to each other.

The emittance growth measurements were performed with seven different noise levels. The values of the phase and amplitude noise for each setting are listed in Table 4.3.

Effective phase noise

In order to make a meaningful comparison between the different levels of noise, the concept of effective phase noise is introduced: this is the phase noise level that would lead to the same emittance growth as that from both phase and amplitude noise according to Mastoridis–Baudrenghien model.

For the calculation of the effective phase noise the averaged bunch length for each case is used (bunch length measurements at Section 4.6). The uncertainty on the effective phase noise is computed following the standard procedure of the propagation of the uncertainty (Appendix A.3). **Do I need to show all the calculations?** The calculated effective phase noise values for the experimental conditions are also listed in Table 4.3. The values shown correspond to the results using the parameters of the first bunch. However, the difference between the values for the other bunches is very small and is also within the displayed uncertainties. The noise levels mentioned in the following analysis of the experimental data correspond to the calculated effective phase noise.

4.4 Measurement of Crab Cavity voltage

As mentioned above, CC2 operated at 1 MV. Before the start of the emittance growth measurements, this value was validated with beam-based measurements from the Head-Tail monitor [75]. The Head-Tail monitor measures the transverse

4. Experimental studies 2018: emittance growth from Crab Cavity noise

Table 4.3: Phase and amplitude noise levels injected in the CC RF system for the emittance growth studies of 2018. The listed values correspond to the average power spectral density values over a frequency range of ± 500 Hz around the first betatron sideband, f_b . The calculated effective phase noise for the parameters of the first bunch are also listed.

	$10 \log_{10} \mathcal{L}(f)$ [dBc/Hz]		
	Phase noise	Amplitude noise	Effective phase noise
Coast1-Setting1	-122.6 ± 0.6	-128.1 ± 0.6	-121.8 ± 0.5
Coast1-Setting2	-101.4 ± 0.8	-115.2 ± 0.6	-101.3 ± 0.8
Coast2-Setting1	-115.0 ± 0.8	-124.1 ± 0.5	-114.6 ± 0.7
Coast2-Setting2	-111.4 ± 0.6	-115.7 ± 0.4	-110.2 ± 0.5
Coast3-Setting1	-110.9 ± 0.9	-116.9 ± 0.4	-110.1 ± 0.8
Coast3-Setting2	-106.4 ± 0.3	-112.9 ± 0.6	-105.8 ± 0.3
Coast3-Setting3	-101.4 ± 0.7	-106.9 ± 0.5	-100.6 ± 0.6

displacement within the bunch which can be used to reconstruct the CC voltage experienced by the beam. A detailed description of the post-processing procedure is provided in Appendix D.

The beam-based measurement of the CC voltage can only be performed right after the acceleration ramp at 270 GeV and not during the coast mode for reasons that are explained in Appendix D. Therefore, the CC voltage was measured at the beginning of the emittance growth experiment. The CC settings remained unchanged for the rest of the experimental procedure.

The beam-based measurement of the CC voltage (reconstructed from the Head-Tail monitor) is displayed in Fig. 4.2 with red color. The horizontal axis shows the longitudinal position in nanoseconds with respect the center of the bunch as it passes through the Head-Tail monitor. The voltage amplitude, $V_{0,CC}$, is obtained from a sinusoidal fit (blue solid line in Fig. 4.2) on the reconstructed voltage, $V_{CC}(t)$, from the Head-Tail monitor reading. The standard procedure of least squares fitting (see Appendix section A.2) is followed. In particular, $V_{CC}(t)$ is fitted with the following three-parameter (A , θ , d) model function which also provides the CC phase and voltage offset:

$$f(x) = A \sin(2\pi f_{CC}x + \theta) + d, \quad (4.7)$$

where A is the amplitude, θ is the phase and d is the vertical offset of the measured

CC voltage. In Eq. (4.7) the CC frequency, $f_{CC}=400.78$ MHz, and is not a parameter of the fit since its operational value is fixed and well known.

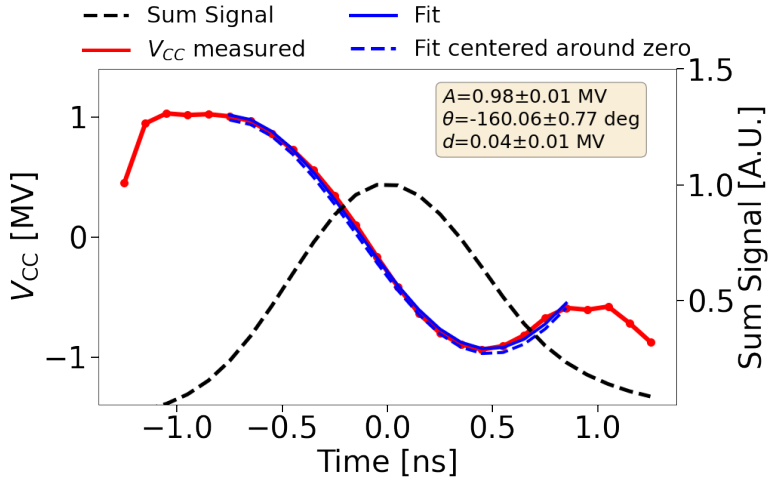


Figure 4.2: Beam-based measurement of the CC voltage as reconstructed from the Head-Tail monitor before the emittance growth measurements in 2018 (red). The sinusoidal fit on the reconstructed voltage in order to obtain the CC voltage amplitude is also shown (blue solid line). The fit results, are given in the yellow box. The measured voltage amplitude, $V_{0,CC}$, was found to be 0.98 MV while its uncertainty, d , was measured at 0.04 MV. The measured voltage value agrees well with the requested value of 1 MV.

The offset parameter, d , is added to the model function as measurements from other dedicated studies³ that took place during this first experimental campaign with CCs in the SPS have shown that the reconstructed CC voltage, $V_{CC}(t)$, is not centered around zero in the vertical axis (see Appendix Figs. D.7 and D.8). A possible explanation for the asymmetry is that it is a result of the cable response of the Head-Tail monitor pick up [76]. However, its origin is not yet fully understood and will have to be addressed in the future. Furthermore, it was found that the vertical offset varied between the different dedicated studies and it outweighs the error on the voltage amplitude obtained by the sinusoidal fit. To this end, in this thesis, this vertical offset d , will be defined as the uncertainty of the measured voltage amplitude.

In order to obtain results that correspond to the experimental conditions the following constraints are imposed to the fit. First the voltage amplitude, A , is

³A total of seven different dedicated experiments with CCs took place in SPS in 2018 in order to address various questions on the operation of the CC with proton beams [66]. The emittance growth experiment was the fifth in chronological order.

4. Experimental studies 2018: emittance growth from Crab Cavity noise

requested to always be positive and higher than 0.7 MV. Furthermore, the part of the signal that corresponds to the tails of the bunch is excluded from the fit in order not to degrade its quality. Consequently, only the part of the signal for which the corresponding normalised sum signal of the Head-Tail monitor⁴ (black dashed line) is above 0.4 is used for the fit.

The results of the sinusoidal fit are illustrated in the yellow box in Fig. 4.2. The measured CC voltage is defined to be: $V_{0,CC} = A \pm d = 0.98 \pm 0.04$ MV. The measured value is very close to the targetd value of 1 MV.

4.4.1 Crab Cavity phase offset

This paragraph might need to be refined. It is worth commenting that, the CC phase was found to be about -160° from the sinusoidal fit. This means, that the CC was operating at opposite polarity than the nominal (see Eq. (3.4)). This means, that the CC was operating at opposite polarity than the nominal (see Eq. (3.4)) which is also visible from the reconstructed $V_{CC}(t)$ in Fig. 4.2. The opposite polarity does not affect the emittance growth measurements. Overlooking the opposite polarity, the phase obtained from the fit becomes: $\sim 180^\circ - 160^\circ = 20^\circ$.

However, the CC phase that was set by the CC operators during the experiment, which will be referred to "inspector phase" throught this thesis, was set to 0° . It is evident that there is a phase offset of about 20° between the inspector phase and the phase experienced by the beam.

This was not known during the measurement as the above mentioned analysis was performed at a later time and hence the phase offset could not be corrected. Nevertheless, simulation studies performed with Sixtracklib have shown that for the long bunches ($\sigma_z \sim 14$ cm) that were used in the for the tests in 2018, the phase offset of the CC has no significant impact on the phase noise⁵ induced emittance growth [77].

The procedure of measuring the voltage amplitude from the Headt-Tail monitor

⁴The sum signal is the longitudinal line density. Further details are provided in Appendix D

⁵It is reminded here that for the emittance growth experiments the CC RF phase noise was always dominant.

reading and calibrating the phase offset was optimised and automated, so that it can be perfomed during the experiment, for the campaigns that took place in 2022 (see Chapter 7.2.3).

4.5 Emittance growth measurments

This section presents the transverse emittance growth measurements with CC RF noise. It discusses first the measurement of the beam emittance with the SPS Wire Scanners (WS) and then it provides an overview of the emittance growth measurements for the four bunches over all the different noise settings.

4.5.1 SPS Wire Scanners

The SPS is equipped with wire scanners (WS) to measure the transverse beam emittance. The SPS Wire Scanner system is described in detail in Ref. [78, 79]. For the SPS tests in 2018, the emittance was measured with Wire Scanners both for the horizontal and vertical plane (BWS.51995.H and BWS.41677.V respectively).

The working principle is shown in Fig. 4.3. A thin wire rapidly moves across the proton beam and a shower of secondary particles is generated. The signal from the secondary particles is then detected by a system of scintillator and photomultiplier (PM) detectors outside of the beam pipe. By measuring the photomultiplier current as a function of wire position over multiple turns the transverse beam profile is reconstructed. An example of a vertical profile is shown in Fig. 4.4.

Fitting of transverse profiles

Assuming gaussian beams and for $u = (x, y)$ being the index that respectively corresponds to the horizontal and vertical plane, the rms beam size, σ_u , is obtained following the standard procedure of least squares fitting (see Appendix A.2). In particular, the measured beam profiles from each scan are fitted with the following four-parameter (A, k, μ, σ_u) gaussian function:

$$f(x) = k + Ae^{-\frac{(x-\mu)^2}{2\sigma_u^2}}, \quad (4.8)$$

4. Experimental studies 2018: emittance growth from Crab Cavity noise

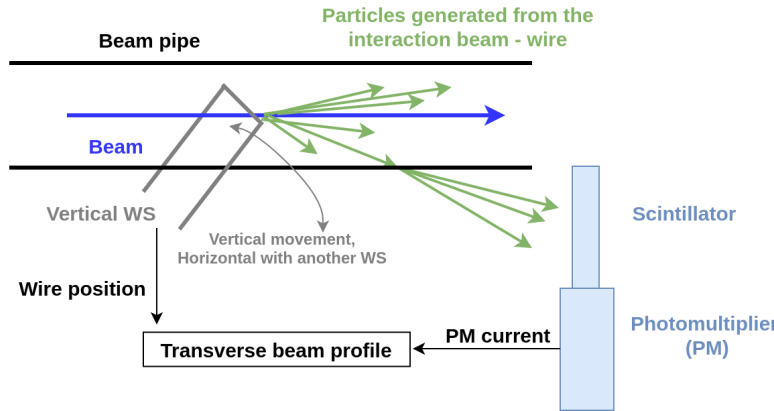


Figure 4.3: Sketch of the SPS rotational wire scanners [79]. The wire moves across the proton beam generating secondary particles which are then detected by a scintillator and a photomultiplier. From the measured photomultiplier current the beam profile is reconstructed.

where k is the signal offset of the PM, A is the signal amplitude, μ is the mean of the gaussian distribution and σ_u its standard deviation. The uncertainty of the measured rms beam size, $\Delta\sigma_u$, is defined as the error of the fit of the σ_u parameter (see Appendix A.2).

An example of the beam profile measured from the SPS Wire Scanner at a specific time is shown in Fig. 4.4 (light blue dots) along with the gaussian fit (orange line).

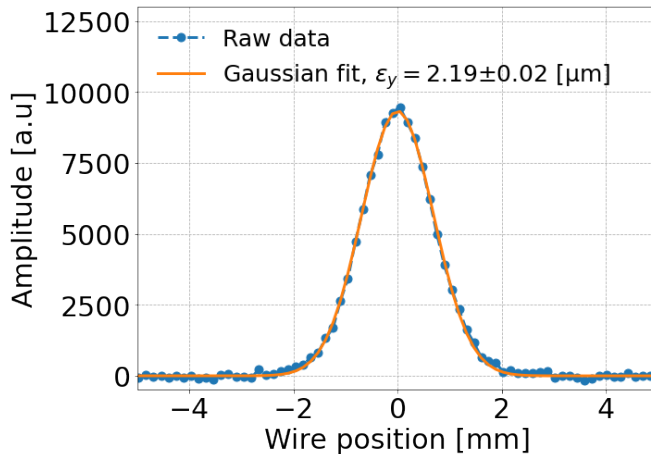


Figure 4.4: Vertical beam profile obtained from the BWS.41677.V instrument. The measured data points (light blue) are fitted with a four parameter gaussian (orange) to obtain the beam size. The calculated emittance and its uncertainty are also shown.

Computing the normalised beam emittance

The formula for computing the normalised beam emittance from the beam size, σ_u is given by:

$$\epsilon_u = \frac{\sigma_u^2}{\beta_{u,WS}} \beta_0 \gamma_0, \quad (4.9)$$

where σ_u is the rms beam size, $\beta_{u,WS}$ the beta function at the Wire Scanner location and β_0, γ_0 the relativistic parameters. Note that $u = x, y$ is the index that respectively corresponds to the horizontal and vertical plane.

Assuming that the relativistic parameters are free of error, the uncertainty of the computed emittance, $\Delta\epsilon_u$, depends on the uncertainty of the measured beam size, $\Delta\sigma_u$ and of the beta function at the location of the Wire Scanner, $\Delta\beta_{u,WS}$, as follows:

$$\Delta\epsilon_u = \sqrt{\left(\frac{\partial\epsilon_u}{\partial\sigma_u}\right)^2 \Delta\sigma_u^2 + \left(\frac{\partial\epsilon_u}{\partial\beta_{u,WS}}\right)^2 \Delta\beta_{u,WS}^2} = \epsilon_u \sqrt{\left(\frac{2\Delta\sigma_u}{\sigma_u}\right)^2 + \left(\frac{\Delta\beta_{u,WS}}{\beta_{u,WS}}\right)^2}. \quad (4.10)$$

For the computation of the emittance values from the CC experiment of 2018, the following points were considered. First, in the 2018 SPS operational configuration, the dispersion was small at the Wire Scanner location and thus its contribution to the beam size was considered to be negligible⁶. Moreover, for the studies at 270 GeV beam energy, $\beta_0 \gamma_0$ equals 287.8 and the beta functions were 81.5 m and 62.96 m at the locations of the horizontal and vertical Wire Scanner respectively. Last, the uncertainty on the beta functions at the location of the Wire Scanner, $\Delta\beta_{u,WS}$, is 5% in both planes, which represents the rms beta-beating in the SPS [82].

Further considerations

It is worth noting here that during each measurement with the Wire Scanner the beam profile is actually acquired twice as the wire crosses the beam in the forward direction (IN scan) and then in the reverse direction (OUT scan). For the 2018

⁶BWS.51995.H location in 2018 was located at a low-dispersion region $D_x < 0.5$ m [80]. At 270 GeV, the energy spread, δ , is of the order of 10^{-4} . Thus, from Eq. (2.37) the horizontal normalised emittance from the dispersion is expected at the order of $9 \times 10^{-3} \mu\text{m}$. Comparing to the observed beam size during the CC tests of a few microns the dispersion is negligible and hence it will not be considered in the following. This is also confirmed by past studies [80]. The measured vertical dispersion has similar value with the horizontal [81] hence its contribution in the measured vertical emittance will also not be considered in the following

4. Experimental studies 2018: emittance growth from Crab Cavity noise

measurements the emittance values obtained from IN and OUT scans, $\epsilon_{\text{IN}} \pm \Delta\epsilon_{\text{IN}}$ and $\epsilon_{\text{OUT}} \pm \Delta\epsilon_{\text{OUT}}$, were found to be very similar. In the analysis of the 2018 measurements, the average emittance from the two scans, $\epsilon_{\text{avg}} = \langle \epsilon_{\text{IN}}, \epsilon_{\text{OUT}} \rangle$, is used. The uncertainty in the average, $\Delta\epsilon_{\text{avg},1}$, is given by [83]:

$$\Delta\epsilon_{\text{avg},1} = \frac{|\epsilon_{\text{IN}} - \epsilon_{\text{OUT}}|}{2\sqrt{2}}. \quad (4.11)$$

The propagated uncertainty from the measurement errors, $\Delta\epsilon_{\text{IN}}$ and $\Delta\epsilon_{\text{OUT}}$, is given by:

$$\Delta\epsilon_{\text{avg},2} = \frac{1}{2} \sqrt{\Delta\epsilon_{\text{IN}}^2 + \Delta\epsilon_{\text{OUT}}^2}. \quad (4.12)$$

Assuming that $\Delta\epsilon_{\text{avg},1}$ and $\Delta\epsilon_{\text{avg},2}$ are independent, the combined uncertainty in the average, $\Delta\epsilon_{\text{avg}}$, is given by:

$$\Delta\epsilon_{\text{avg}} = \sqrt{\Delta\epsilon_{\text{avg},1}^2 + \Delta\epsilon_{\text{avg},2}^2}. \quad (4.13)$$

Finally, some emittance increase is expected during each wire scan, due to multiple Coulomb scattering. This effect has been extensively studied in [80]. For the rotational SPS Wire Scanners and the energy of 270 GeV, at which the CC experiments were performed the expected emittance growth from the Wire Scanner is expected to be a few nanometeres per scan in both transverse planes [80] which is very small with respect to the emittance values of a few micrometers. Nevertheless, a conservative number of scans were carried out, ~ 20 scans per bunch and per plane during ~ 1 hour, in order to minimise the contribution from this effect.

4.5.2 Experimental results

In this section, an overview of the emittance growth measurements is presented. Figure 4.5 displays the bunch by bunch transverse emittance evolution through the total duration of the experiment. The three different coasts are distinguished in this plot with the blue dashed vertical lines. The values of the effective phase noise are also displayed (see Table 4.3), while the moments when the noise level changed are

shown with the grey vertical lines. The four different colors (blue, orange, red, green) correspond to the four different bunches. For the bunches the notation "bunch N " will be used, where $N = \{1, 2, 3, 4\}$ according to their position in the bunch train. The errorbars of the emittance values correspond to the uncertainty computed using Eq. 4.13. However, as they are very small compared to the scale of the plots they are barely visible. Last, the emittance growth rates, $d\epsilon_u/dt$, for each setting and for each bunch are displayed at the bottom of each plot along with their uncertainties. The growth rates are obtained following the standard procedure of weighted least squares fitting (see Appendix A.2). In particular, the measured beam profiles from each scan are fitted with the following polynomial:

$$p(x) = c_0 + c_1 \times t \quad (4.14)$$

where t is the time in seconds, c_0 is called the intercept and shows where the line estimated from the fit crosses the y-axis, and c_1 determines the slope of the line estimated from the fit. In the case of the emittance growth measurements, c_0 corresponds to the initial value of the emittance in meters, while c_1 is the growth rate, $d\epsilon_u/dt$, in meters per second. The uncertainties of the growth rates correspond to the error of the fit (see Appendix A.2).

First observations and comments

Figure 4.5 demonstrates a clear emittance growth in the vertical plane which is expected due to the vertical CC. However, the CC noise is observed to induce growth also in the horizontal emittance as a result of residual coupling in the machine. Thus, the total emittance growth given by $d\epsilon_x/dt + d\epsilon_y/dt$ will be considered in the following. That was confirmed by PyHEADTAIL simulations [84] in the presence of CC RF noise and transverse coupling.

Furthermore, both the phase and amplitude noise levels for Coast1-Setting1 were found to be below the noise floor of the CC. Therefore, the transverse emittance growth observed during that case is a result of other sources (natural emittance growth, see Section 4.2.1) and will be considered as the background growth rate in the analysis below.

4. Experimental studies 2018: emittance growth from Crab Cavity noise

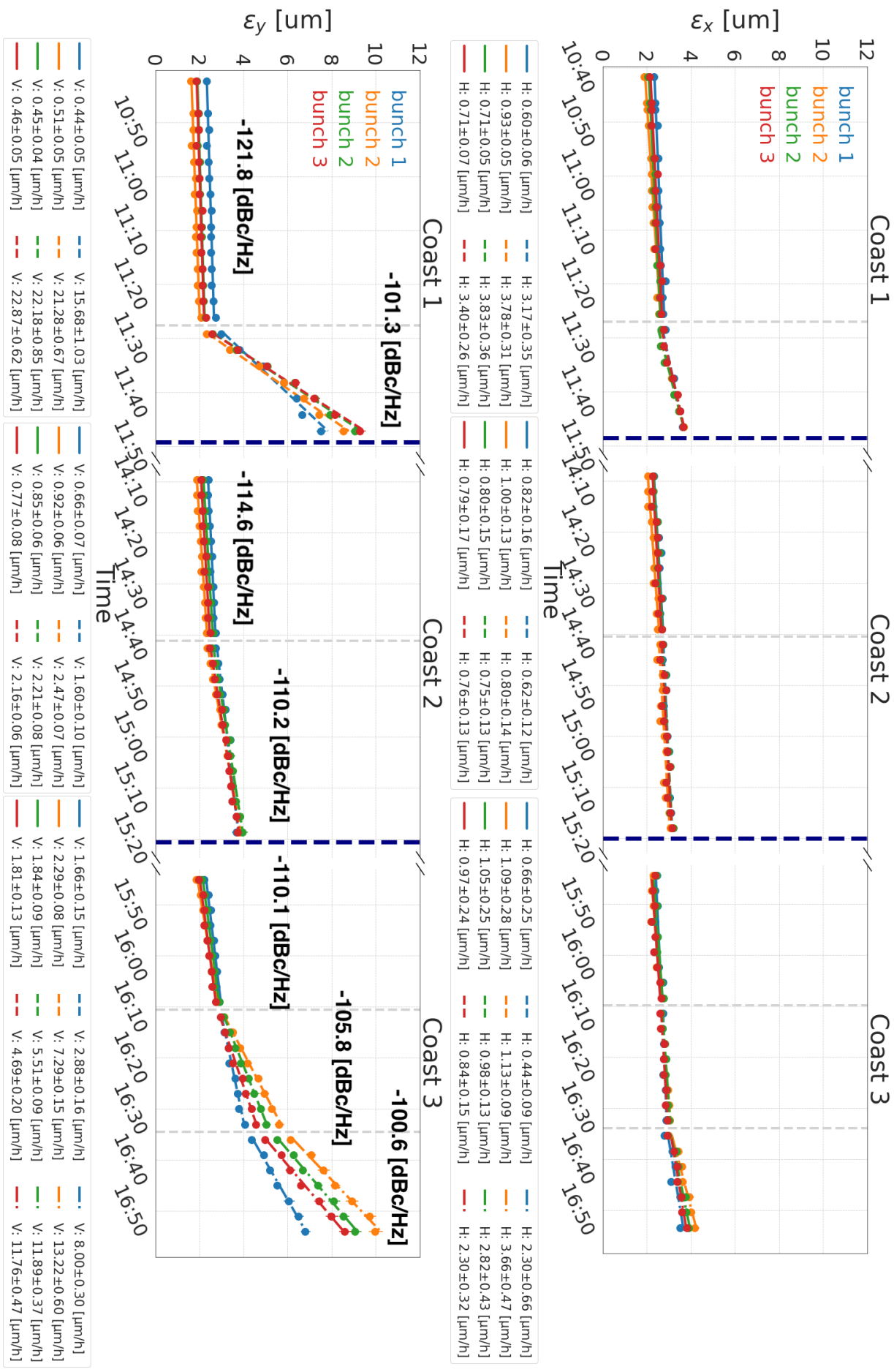


Figure 4.5: Bunch by bunch horizontal (top) and vertical (bottom) emittance evolution during the experiment on September, 15, 2018. The four different colors indicate the different bunches. The different applied noise levels are also shown while the moments when the noise level changed are indicated with the grey vertical dashed lines. The emittance growth rates along with their uncertainties for the seven different noise settings are displayed at the legend at the bottom of the plots.

Summary plot

Figure 4.6 provides a clearer view of the measurements presented in Fig. 4.5. It displays the measured emittance growth rates for each one of the four bunches for the different levels of injected noise. The horizontal error bars correspond to the uncertainty of the effective phase noise (see Section 4.3) while the vertical error bars correspond to the uncertainty of the total transverse emittance growth calculated from the uncertainties of the horizontal and vertical growth rates following the standard procedure of the propagation of the uncertainty (see Appendix A.3).

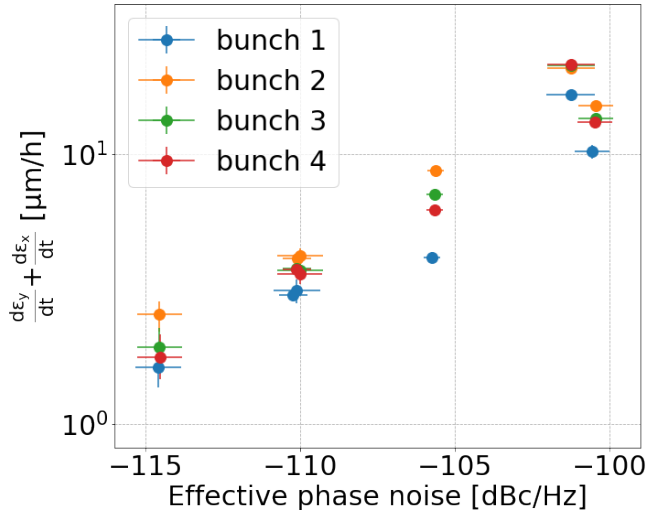


Figure 4.6: Summary plot of the emittance growth study with CC noise in 2018. The transverse emittance growth rate, for the four bunches, is shown as a function of the different levels of applied noise.

From the plot it becomes clear that the measured emittance growth was different for the four different bunches. Furthermore, the first bunch (blue) had systematically the smallest growth rate.

An attempt to understand these observations will be presented in the following section, based on a possible correlation between the transverse emittance growth and the beam evolution in the longitudinal plane.

4.6 Bunch length and intensity measurements

The measurements of the bunch length and intensity that took place in parallel with the emittance growth measurements are presented in this section. The goal is to get a more complete insight of the experimental conditions and possibly explain the different emittance growth rates observed for the four bunches which was discussed in the previous section. Initially, a short introduction on the instruments used for the measurements is provided. After that, the evolution of the longitudinal plane and of the intensity is analysed and discussed.

4.6.1 ABWLM and Wall Current Monitor

The bunch length was measured with two different instruments the ABWLM⁷ [85] and the Wall Current Monitor [86]. Both ABWLM and Wall Current Monitor acquire the longitudinal bunch profiles, while ABWLM is much faster than the Wall Current Monitor. In the ABWLM case the bunch length is obtained by performing a gaussian fit on the acquired profiles. Only the calculated bunch length values are available but not the profiles themselves. For the case of the Wall Current Monitor the bunch length is estimated by computing the full width half maximum of the profiles and then using it to estimate the standard deviation of a gaussian distribution. The longitudinal profiles and the calculated bunch lengths are available for each acquisition. Furthermore, the Wall Current Monitor provides additional information on the relative bunch position with respect to the center of the RF bucket, which will also be used in the following analysis. No further details on the operation of these instruments are discussed here as the offline analysis was not performed by the author.

The intensity values obtained from the ABWLM and the Wall Current Monitor are obtained by integration of the longitudinal bunch profiles. Since there is no available calibration for this procedure the measured intensity cannot be expressed in protons per bunch. To this end, the intensity evolution is presented normalised with the initial intensity value (see Fig. 4.9).

⁷(A for RF, B for Beam, W for Wideband, L for Longitudinal, M for Measurement)

4.6.2 Bunch length measurements

The bunch length measurements that took place during the CC noise induced emittance growth studies are shown in the bottom plot in Fig. 4.7. The small markers correspond to the data acquired with the ABWLM while the bigger markers correspond to the data acquired with the Wall Current Monitor. The two upper plots contain the transverse emittance growth as discussed in Section 4.5.2. This is for easier comparison of the beam evolution in the transverse and in the longitudinal plane. The color code corresponds to the four different bunches.

Four main observations can be made. First, the plot demonstrates a very good agreement between the ABLWM and the Wall Current monitor. Second, an approximately bunch length increase of $\sim 9\%/\text{h}$ is observed for bunch 1 (blue) in all the three coasts. This rate, which is computed from the ABWLM data, is similar to the blow-up observed in the SPS for similar machine conditions [69]. Third, the bunch length increase for the last three bunches (2, 3, and 4) is larger than the increase for bunch 1. However, bunches 2, 3, and 4 seem to be longitudinally unstable as sudden jumps appear in their bunch length evolution and this could explain the faster bunch length increase. Last, no correlation is observed between the bunch length evolution and the change of noise level. In order to validate that bunches 2, 3, and 4 are unstable, the longitudinal profiles acquired with the Wall Current Monitor are studied in the next paragraph.

4.6.3 Longitudinal profile measurements

Two example longitudinal profile acquisitions from the Wall Current Monitor are discussed here as they can provide further insight on the sudden jumps observed in the bunch length values for bunches 2, 3, and 4. The selected acquisitions correspond to the moments where the sudden jumps are performed in the second and third coast and are shown in Fig 4.8. The relative bunch position with respect to the center of the RF bucket of each bunch for an acquisition period of 7 ms is also illustrated in the bottom plots of Fig. 4.8 for completeness.

4. Experimental studies 2018: emittance growth from Crab Cavity noise

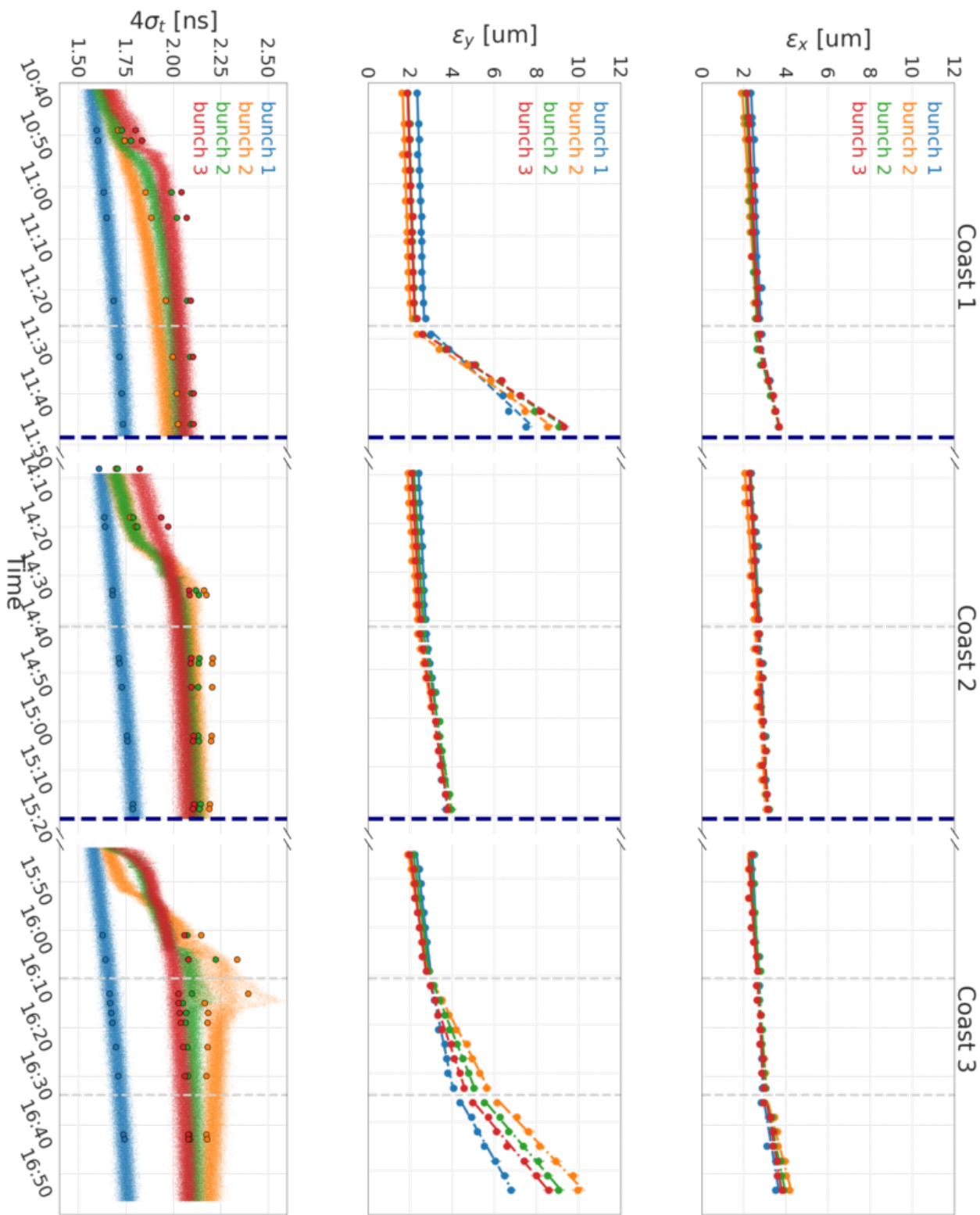


Figure 4.7: Evolution of the beam in transverse and longitudinal planes during the CC noise induced emittance growth experiment. Top: Horizontal emittance growth measured with the SPS Wire Scanners. Middle: Vertical emittance growth measured with the SPS Wire Scanner. Bottom: Bunch length evolution measured with the ABWLM (small markers) and the Wall Current Monitor (bigger markers).

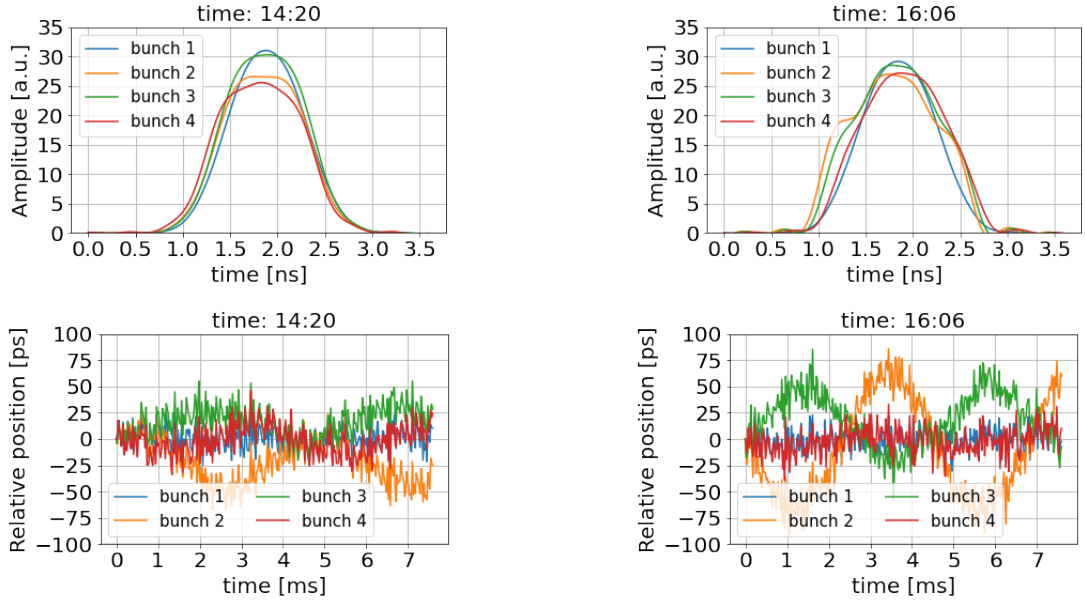


Figure 4.8: Longitudinal profiles (top) and relative bunch position with respect to the center of the RF bucket (bottom) acquired with the Wall Current Monitor. The acquisitions correspond to the times when the sudden jumps in the bunch length evolution are observed (see Fig. 4.7).

The oscillations of the relative bunch position (bottom) of the bunches 2,3 and 4 (orange, green, and red) indicate that the bunches are longitudinally unstable. This is also reflected in the longitudinal profiles (top) which appear distorted. The reason behind the longitudinally unstable bunches is believed the fact that that the phase loop was sampling only the first bunch because of the large bunch spacing of 525 ns [87]. For this reason, the following analysis is focused only on bunch 1, which was not affected by the instability. However, in the next paragraph the intensity measurements for all the four bunches are exceptionally illustrated.

4.6.4 Intensity measurements

The bunch by bunch intensity measurements that were performed along the experiment with artificial CC noise are displayed in Fig. 4.9. In particular the intensity values normalised with the intial value are shown for each bunch. The four different bunches are indicated with the four different colors. The acquisitions from both the ABWLM and the Wall Current Monitor are illustrated with the small and bigger markers respectively.

The following observations can be made. First, there is very good agreement

4. Experimental studies 2018: emittance growth from Crab Cavity noise

between the measurements from the ABLWM and the Wall Current Monitor. Second, losses of $\sim 2\text{-}4\%/\text{h}$, computed from the ABLWM acquisitions, are observed for bunch 1 (blue) in all the three coasts. This rate is even smaller than observed in the SPS in coast studies without external noise ($\sim 10\%/\text{h}$) [69]. Last, more significant losses are observed for the longitudinally unstable bunches (bunch 2,3, and 4). However, this is not of concern as the last three bunches will not be included in the following analysis as discussed in the previous paragraph.

4.7 Comparison of measured transverse emittance growth with the theoretical predictions

This section focuses on the main objective of the experiment which was the comparison of the measured transverse emittance growth with the expected values as computed from the Mastoridis–Baudrenghien model introduced in Chapter 3. As already discussed (Section 4.6.3), the comparison considers only bunch 1 as the other three bunches were found to be longitudinally unstable.

Figure 4.10 compares the measured (blue) and the theoretically calculated (black) emittance growth rates of bunch 1 for the different noise levels. For the comparison, the background growth rate from other sources (measured during Coast1-Setting1, as discussed in Section 4.5) is subtracted from the measured values. In particular the background growth was measured $0.6\,\mu\text{m}/\text{h}$ and $0.44\,\mu\text{m}/\text{h}$ for the horizontal and vertical plane respectively. One should keep in mind that background subtraction has practically no impact for high noise levels. Instead, it is significant for small noise levels.

The expected emittance growth due to CC noise was estimated for all noise settings using Eq. (3.12). The growth was computed for the beam energy of 270 GeV, considering the vertical beta function at the location of the CC2 of 73.82 m and the revolution frequency of SPS which is 43.37 kHz. For each setting, the measured noise power spectral densities (i.e. effective phase noise) and the average bunch length over each observation window were used in the calculation. These values are listed in the first two columns of Table 4.4.

4.7. Comparison of measured transverse emittance growth with the theoretical predictions



Figure 4.9: Intensity evolution as measured with ABLWM (smaller markers) and with the Wall Current Monitor (bigger markers) during the experiment with CC noise in 2018.

4. Experimental studies 2018: emittance growth from Crab Cavity noise

The horizontal error bars, for both measured and calculated growths, correspond to the uncertainty of the effective phase noise values (see Table 4.3). The vertical error bars for the measured growth are defined as the error of the linear fit on the emittance values (see Section 4.5). The vertical error bars on the theoretically calculated rates are computed following the standard procedure of propagation of the uncertainty. It should be mentioned here that only the uncertainties on the effective phase noise ($\sim 13\%$ on average for bunch 1) are included in the error propagation. The beam energy and the revolution frequency are assumed to be free of error, while the uncertainties of the rest of the parameters: bunch length, CC voltage and beta function ($\sim 2\%$, 0.01% , and 5% respectively) are not included as they are much smaller than those of the noise.

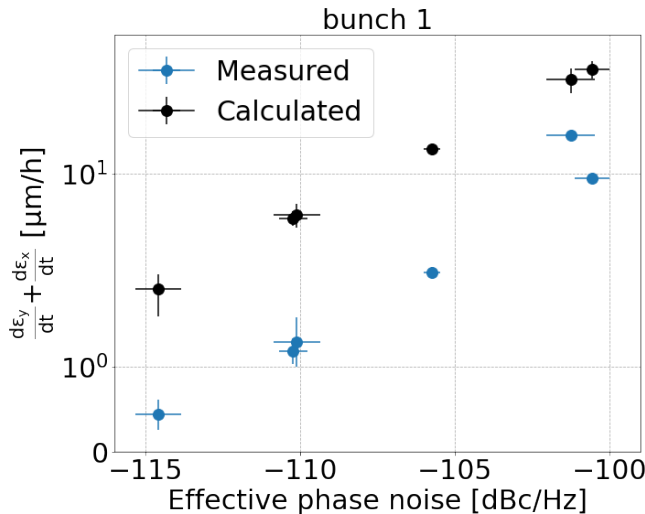


Figure 4.10: Summary plot of the emittance growth study with CC noise in 2018 focused on bunch 1 only. The measured emittance growth rate (blue) and the expected growths from the theoretical model (black) are shown as a function of the different levels of applied noise.

From Fig. 4.10 it becomes evident that the theory systematically overestimates the measured growth rates. The averaged discrepancy over all noise levels is a factor of 4: numerical values are given in Table 4.4. The measurements seem to go in the good direction but actually they show that there is a significant uncertainty on the predictions of the theoretical model. The accuracy of the model is essential for defining the specifications for the design of the HL-LHC CC LLRF. Therefore, understanding the reason behind the observed discrepancy with the measurements which would also allow to decide if the reduction of the factor 4 can

be propagated for the HL-LHC predictions is fundamental. The studies performed to explain the discrepancy will be described in the following chapters.

Table 4.4: Comparison between the measured and the calculated transverse emittance growth rates for bunch 1 for the different noise levels, and average bunch length for each case.

$10 \log_{10} \mathcal{L}(f)$ [dBc/Hz]	$\langle \sigma_\phi \rangle$ [rad]	Growth rate [$\mu\text{m/h}$]	
		Measured	Calculated
-114.6	1.05	0.44	1.9
-110.2	1.10	1.18	5.10
-110.1	1.03	1.28	5.38
-105.8	1.06	2.28	14.50
-101.3	1.08	17.81	40.55
-100.6	1.09	47.42	9.26

4.8 Conclusions and outlook

The objective of the first experimental campaign with CC noise in the SPS was to benchmark the available theoretical model of Mastoridis–Baudrenghien which predicts the noise induced transverse emittance growth against measurements. For this reason, a dedicated experiment took place in the SPS in September of 2018, with different levels of artificial noise injected in the CC RF system. Four bunches circulated in the machine for long periods of time and their emittance evolution was recorded to be compared with the theoretical predictions.

The experiment demonstrated that the transverse emittance of all the four bunches increased for stronger noise. However, during the analysis it was found that only the first bunch of the train was stable in the longitudinal plane. For this reason, only the data from the first bunch were used for the comparison with the theoretically calculated emittance growth rates from Mastoridis–Baudrenghien model. The comparison showed that the theory overestimates the measurements by a significant factor of 4. The reason behind this discrepancy needs to be understood as the predictions of the theoretical model will be used to define limits and acceptable noise levels for the HL-LHC CCs. Therefore, the next chapters focus on explaining the observed discrepancy.

5 | Investigation of the discrepancy between emittance growth theory and experimental data

In Chapter 4 the analysis of the experiment data from the CC experiments in 2018 was presented. It was found that the Mastoridis–Baudrenghien model [63] which predicts the emittance growth in the presence of noise in the CC RF system overestimates the corresponding measurements by a factor of 4 on average. The reason behind this discrepancy needs to be understood in order to gain confidence in the predictions of the Mastoridis–Baudrenghien model in order to correctly define the acceptable noise levels for the low-level RF system of the HL-LHC project. Therefore, this observation triggered a series of studies which are presented in this chapter.

This chapter is structured as follows: First, in Section 5.1 parametric studies based on the theoretical model are presented, exploring the sensitivity of the emittance growth rates to the CC voltage and rms bunch length. In the following two sections, the theory is benchmarked against two different simulation tools: PyHEADTAIL (in Section 5.2) and Sixtracklib (in Section 5.3). Finally, the main observations and conclusions are discussed in Section 5.4.

The PyHEADTAIL and Sixtracklib simulation results that are presented in this chapter were performed at an early stage of this PhD project. In particular they were performed before the thorough analysis of the experimental data described in Chapter 4. To this end, the simulations were performed for beam and machine conditions similar to the ones of the SPS during the tests with CCs in 2018, but with

some small deviations in the bunch length and the beta function at the location of the CC, the value of linear chromaticity and the synchrotron tune. However, it should be highlighted, that since the objective of these studies was to benchmark the Mastoridis–Baudrenghien model against different simulation codes these small differences in the parameters do not affect the validity of the study. This statement is validated by the simulation studies that will be presented in Chapter 7 which were undertaken with more accurate parameters for the 2018 experiment.

5.1 Parametric studies based on the theoretical model

The basics of the existing theoretical model which describes the emittance growth in the presence of amplitude and phase noise in CCs in a storage ring have been introduced in Chapter 3. In this section, this theory is used to study the sensitivity of the noise-induced emittance growth on the CC voltage and rms bunch length. The objective of the study is to investigate if the uncertainty in the measurements of these two variables could explain the observed discrepancy of a factor ~ 4 between measured emittance growth and the analytically predicted values (see Section 4.7).

The parametric studies in this section were performed for parameters similar to the experimental configuration of 2018: beam energy of 270 GeV, vertical beta function of 73 m (at the location of CC2), and phase and amplitude noise of -111.4 and -115.7 dBc/Hz respectively (Coast2-Setting2). The phase and amplitude noise are considered here independently, instead of the effective phase noise, due to the different dependence of the correction term (see Fig. 3.3).

5.1.1 Sensitivity to bunch length

Using Eqs. (3.11) and (3.12) with the above mentioned parameters and CC voltage, CC = 1 MV the normalised vertical emittance growth is computed as a function of different values of bunch length over a range from 0.001 ns to 2.5 ns (expressed in $4\sigma_t$). The results are illustrated in Fig. 5.1.

5. Investigation of the discrepancy between emittance growth theory and experimental data

A clear dependence of the vertical emittance growth on the bunch length is observed. However, there is only a strong dependence for bunch lengths within a certain range. In the regime of the measured bunch length during the CC experiment for bunch 1 (~ 1.6 ns- 2.0 ns) the sensitivity to the bunch length is very small and cannot explain the factor of about 4 that was observed between measurements and theoretical predictions in SPS CC tests in 2018.



Figure 5.1: Vertical emittance growth for different bunch length values computed using the analytical formulas Eqs. (3.11) and (3.12) for the experimental configuration of 2018. The blue dot shows the average bunch length over all coast in 2018. The blue box around it gives the upper and lower limits of its measurements.

5.1.2 Sensitivity to CC voltage

Here, the sensitivity of the vertical emittance growth is studied for the parameters mentioned above and bunch length of $4\sigma_t = 1.7$ ns. The vertical emittance growth is computed again analytically using Eqs. (3.11) and (3.12) over a range of CC voltage values equally spaced from 0.6 to 1.3 MV.

Figure 5.2 illustrates the computed vertical emittance as a function of the CC voltage. From the analysis in 2018, the calibration of the CC voltage (which showed 1 MV) was not straightforward. However, from the plot it is evident that

even if the actual voltage was 30% lower due to measurement errors this would lead to just a factor of 2 lower vertical emittance growth. An error of this scale is not realistic. To this end, it is concluded that uncertainties on the beam based measurements of the CC voltage cannot explain the experimental observations of 2018, where there was a factor 4 between measured and predicted emittance growth.



Figure 5.2: Vertical emittance growth for different values of CC voltage computed using the analytical formulas Eq. (3.11) and (3.12) for the experimental configuration of 2018.

5.2 Benchmarking theory against PyHEADTAIL

As mentioned in Chapter 3 the Mastoridis–Baudrenghien model which predicts the emittance growth driven by CC RF phase and amplitude noise was benchmarked against simulation results with the HEADTAIL [63] simulation tool. In this section, the predictions of the model are benchmarked against the PyHEADTAIL simulation tool. PyHEADTAIL is the implementation of the HEADTAIL (which was written in C/C++ language) in Python, so that it can be more easily maintained and extended [55]. Further details on the PyHEADTAIL are provided in the introductory Subsection 2.5.1.

5. Investigation of the discrepancy between emittance growth theory and experimental data

The parameters used for setting up the linear transfer map, the longitudinal tracking, and the initialisation of the beam distribution are shown in Table 5.1: they are similar to the parameters in the SPS CC experiments of 2018. The accelerator ring consists of one segment, with one interaction point, where the beam receives the noise kicks from the CC every turn. In particular, at that location, the angle variable, y' , of each particle within the bunch is updated every turn following the description of Eqs. (3.7) and (3.8) for modeling the phase and amplitude noise respectively. The vertical angle co-ordinate is updated to study the vertical emittance growth following the experiments of 2018 where the CC module that was used provided a vertical deflection to the bunches. Nevertheless, the beam dynamics are the same in the horizontal plane.

The simulations were performed for both phase and amplitude CC RF noise. The noise level was chosen to be much stronger than the levels used in the experiment of 2018 in order to observe a reasonable emittance growth in the 10^5 turns simulated. For reference, this corresponds to about 2.5 s in the SPS machine.

In particular, the simulations were performed using a sequence of noise kicks with length $N_{\text{turns}} = 10^5$, mean 0 and standard deviation of $\sigma_{\Delta\phi} = 2.7 \times 10^{-3}$ rad for phase noise and $\sigma_{\Delta A} = 2.7 \times 10^{-3}$ for amplitude noise. This corresponds to a total noise power of $\sigma_{\Delta\phi}^2 = 7.3 \times 10^{-6}$ rad 2 and $\sigma_{\Delta A}^2 = 7.3 \times 10^{-6}$ or to a power spectral density of 1.68×10^{-10} rad 2 /Hz or 1/Hz (for phase and amplitude noise respectively).

In the simulations, the beam particles encounter the phase or amplitude noise kicks once per turn. This means that the sampling frequency of the noise spectrum in the frequency domain equals, $f_s = f_{\text{rev}} = 43.37$ kHz. Thus, the frequency spectrum of the noise applied in the simulations extends from $-f_s/2 \approx -22$ kHz to $+f_s/2 \approx 22$ kHz. This is visible in the power spectra of the sequence of amplitude and phase noise kicks (discrete-time signal) which are plotted in Fig. 5.3. The power spectral densities are computed using Eq. (B.11).

Following the discussion in Section 4.3.1 it is evident that the noise applied in the simulations also overlaps and excites the first betatron and synchrobetatron sidebands. Therefore, to predict the vertical emittance growth from CC RF and

amplitude and phase noise according to Mastoridis–Baudrenghien model, one can use the simplified Eqs. (4.5) and (4.6), respectively.



Figure 5.3: Power spectra of the CC amplitude (left) and phase (right) noise used in the PyHEADTAIL simulations.

The simulations were performed for a single bunch. The initial bunch was generated with Gaussian distributions in transverse and longitudinal planes¹. The bunch intensity of 3×10^{10} protons was represented by 10^5 macroparticles.

The beta function at the location of the interaction point was chosen to be the value at the location of CC1 for both horizontal and vertical planes (values are listed in Table 5.1). At the same location, the Twiss parameter alpha and the dispersion were chosen to be zero. This is a valid assumption for the studies since these parameters have no direct impact on the noise-induced emittance growth [63]. This is also confirmed, with simulations with the Sixtracklib code which are presented in the following section. The Sixtracklib simulations use the detailed optics of the machine for the tracking. It will be shown that the emittance growth rates from the two simulation tools are in good agreement.

The mechanism responsible for the emittance growth in the presence of noise is the spread of the betatron tunes [61]. As explained earlier (in Section 3.1) the tune spread leads to a phase mixing of the particles within the bunch causing a decoherence of the betatron oscillations which then results in emittance growth [61]. The time scale of the decoherence equals the inverse of the betatron

¹The longitudinal distribution in reality is not a Gaussian but it was found that the shape of the longitudinal profile has no significant impact on the predicted emittance growth rates. These studies were performed by T. Mastoridis and P. Baudrenghien [88]. The simulation studies presented in this thesis used a Gaussian longitudinal distribution following the studies presented in Ref. [63].

5. Investigation of the discrepancy between emittance growth theory and experimental data

frequencies [61]:

$$\tau_{\text{decoh}} = \frac{1}{2\pi f_{\text{rev}} \text{rms}(\Delta Q_u)}, \quad (5.1)$$

where $u = (x, y)$ indicates the horizontal or vertical plane, f_{rev} the revolution frequency, and $\text{rms}(\Delta Q_u)$ the rms betatron tune spread. The latter can be computed by Eqs. (C.12) and (C.13) for the vertical and horizontal planes respectively.

Therefore, it becomes clear that in order to observe some emittance growth a source of tune spread must be included in the simulations. For the simulations presented here detuning with transverse amplitude is introduced as described in Section 2.5.1, by applying a change of the phase advance of each individual particle depending on its action variable and the detuning coefficients. Detuning in both transverse planes is thus introduced for horizontal detuning coefficient $\alpha_{xx} = 179.35/\text{m}$, vertical detuning coefficient $\alpha_{yy} = -30.78/\text{m}$ and for cross-term coefficient $\alpha_{yx} = -441.34/\text{m}$. These coefficients were computed using MAD-X [50] for the nominal SPS lattice (introduced in Section 2.4) and for $Q'_{x,y} = 0.5$. It should be noted that the detuning in the vertical plane is the value of interest since the emittance evolution will be investigated in the vertical plane. Using Eq. (C.12) for the above mentioned coefficients and the initial transverse actions of the bunch yields $\text{rms}(\Delta Q_y) \approx 7 \times 10^{-6}$.

For the emittance growth studies to be valid the simulation time should be much longer than the decoherence time defined in Eq. (5.1). For the above value of rms vertical tune spread, the decoherence time is computed to be $\tau_{\text{decoh}} \approx 0.5 \text{ s}$. Therefore, the simulation time of about 2.5 s is reasonable for these studies.

The tracking was performed for 10^5 turns and the geometric emittance was computed every 100 turns (for computational efficiency) using the statistical definition introduced in Eq. (2.34). The normalised emittances were obtained using Eq. (2.36). To reduce the statistical uncertainty of the results, due to the way the noise kicks are applied, the simulation was performed for 30 different runs. The initial bunch distribution and the sequence of the uncorrelated noise kicks were randomly regenerated every run (a different seed was used in the random

Table 5.1: Simulation parameters used to benchmark the theoretically predicted emittance growth in Chapter 5.

Parameter	Value
Beam energy, E_b	270 GeV
Machine circumference, C_0	6911.56 m
Horizontal / vertical betatron tune, Q_{x0} / Q_{y0}	26.13 / 26.18
Synchrotron tune, Q_s	0.0035
Momentum compaction factor, α_p	1.9×10^{-3}
Number of bunches	1
Rms bunch length, σ_z	15.5 cm
Horizontal / vertical normalised emittance, ϵ_x / ϵ_y	2 μm / 2 μm
Horizontal / vertical beta function, $\beta_{x,CC1}/\beta_{y,CC1}$	29.24 m / 76.07 m [†]
Number of macroparticles, N_{mp}	10^5
Number of turns, N_{turns}	10^5

[†] Model values for the Q26 optics.

generator).

The PyHEADTAIL simulation results are summarised in Fig. 5.4. The simulated vertical emittance evolution in the presence of amplitude noise (left) and phase noise (right) is plotted as a function of time. For both noise types, the theoretically predicted emittance growth (computed using Eqs. (4.5) and (4.6) for the above mentioned parameters) is shown with the red line. The dark orange and dark blue lines show the evolution of the averaged emittance values over the different runs. The shaded areas, (light orange and light blue color), depict the standard deviation of the different emittance values over the 30 runs. The emittance growth rate is obtained with a linear fit to the averaged normalised emittance values over the simulation time. The slope that corresponds to the emittance growth rate obtained by this fit is also drawn in the plot in black color. The uncertainty on the slope of the fit is displayed in the legend.

It is worth commenting, that the emittance growth rates here are expressed in nm/s instead of $\mu\text{m}/\text{h}$ that was used for the experimental results. This is due to the time scale of the simulations.

It can be seen, that for the amplitude noise case there is excellent agreement between the theoretical prediction, from Mastoridis–Baudrenghien model, and the simulated emittance growth rate. For the phase noise case, the agreement between

5. Investigation of the discrepancy between emittance growth theory and experimental data



Figure 5.4: Vertical emittance growth driven by CC RF amplitude noise (left) and phase noise (right) as simulated with PyHEADTAIL for a configuration close to the experimental conditions of the SPS CC tests in 2018.

expected and simulated emittance growth is very good. The simulated growth appears slightly lower than the theoretical predictions. However, this difference is insignificant comparing to the factor of about 4 observed between the theory and the measurements of 2018. A possible reason for the small discrepancy between simulation and theory is the very small tune spread. Later simulations with larger vertical tune spread (closer to the realistic tune spread in the SPS during the 2018 experiments (see Section 6.3)) show excellent agreement between the PyHEADTAIL results and the theoretically computed values. Nevertheless, this small difference does not affect the conclusions drawn from the results, as will be shown in the following chapters.

In general, it can be concluded that the transverse emittance growth driven by CC RF noise obtained by PyHEADTAIL simulations is in good agreement with the theoretically expected values from the Mastoridis–Baudrenghien model. In the following section the theory is benchmarked against a more complete simulation tool, Sixtracklib.

5.3 Benchmarking theory against Sixtracklib

This section summarises the results of validating the Mastoridis–Baudrenghien theoretical model against numerical simulations with Sixtracklib [58]. The additional comparison between theory and simulation is motivated by the fact that

PyHEADTAIL and theory may miss some beam dynamics effects that could explain the discrepancy between their results and the experimental observations of 2018. Sixtracklib is a more complete simulation tool than PyHEADTAIL as the tracking simulations use the detailed optics of the machine and therefore is considered appropriate for this study. Calculations can be performed on GPU decreasing the required computational time. For the simulations presented in this section the nominal SPS model for Q26 optics will be used [51] as introduced in Section 2.4 except if it is stated otherwise.

5.3.1 Emittance growth simulations with CC noise modeled as transverse kicks on the angle co-ordinate.

The emittance growth simulations presented in the previous section, were repeated with Sixtracklib instead of PyHEADTAIL. This basically means, that the detailed optics of the SPS machine elements including non-linear elements are used for the tracking instead of modelling the ring as simple transfer map with one interaction point where the CC kick is applied. The nominal SPS lattice of MAD-X is used: dipoles, quadrupoles, and chromatic sextupoles as discussed in Section 2.4. It can be found in the GitLab repository of [51]. The linear chromaticity was adjusted to be in the range $1 < Q'_{x,y} < 2$. The relevant machine and beam parameters are listed in Table 5.1.

The rms betatron tune spread here is slightly higher than 7×10^{-6} that was computed in the previous section, due to the larger values of linear chromaticity. To this end, tracking for 10^5 turns is reasonable also for these studies. The initial distribution of 10^5 particles follows a gaussian both in transverse and longitudinal planes.

The emittance growth was simulated in Sixtracklib in the presence of both amplitude and phase noise. The noise kicks were implemented as kicks on the vertical angle co-ordinate of each particle following the previous PyHEADTAIL simulations. The noise kicks were applied on the beam at the location of CC1. The power spectral density of the noise at the betatron frequency was $1.68 \times 10^{-10}/\text{Hz}$ and rad^2/Hz for amplitude and phase noise respectively. This corresponds to a total noise power of $\sigma_{\Delta A}^2 = 7.3 \times 10^{-6}$ and $\sigma_{\Delta \phi}^2 = 7.3 \times 10^{-6} \text{ rad}^2$ respectively.

5. Investigation of the discrepancy between emittance growth theory and experimental data

The emittance and emittance growth values were computed with the same procedure followed for the previous PyHEADTAIL simulations (see Section 5.2). Figure 5.5 summarizes the simulated emittance growth driven by amplitude (left) and phase noise (right). For both types of noise, the theoretical prediction of the emittance growth is shown by the red line. The dark blue and dark orange lines show the evolution of the averaged emittance values over 30 different runs. The shaded areas, shown with light blue and light orange colors, depict the standard deviation of the emittance values over the 30 different runs. The emittance growth rate is obtained with a linear fit to the averaged normalised emittance values over the simulation time. The resulting fits are shown in the plots as black lines. The uncertainty on the slope of the fit is displayed in the legend.

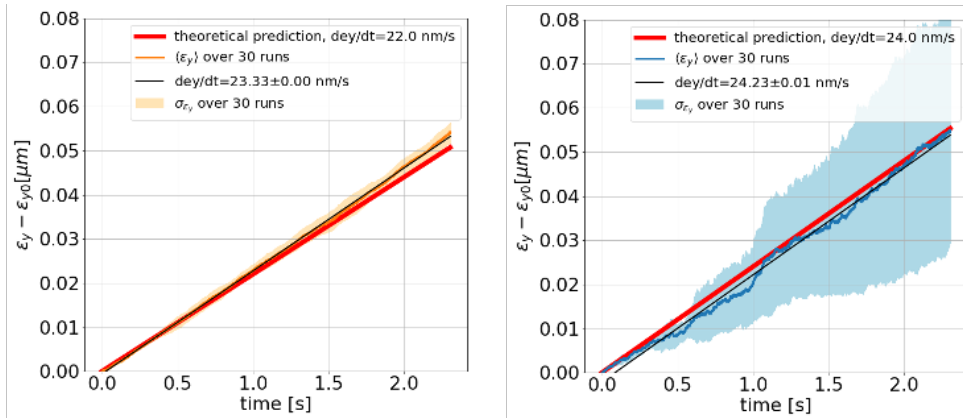


Figure 5.5: Vertical emittance growth driven by CC RF amplitude noise (left) and phase noise (right) as simulated with Sixtracklib simulation tool for a configuration close to the experimental conditions of the SPS CC tests in 2018. The CC noise is modeled as uncorrelated kicks on the angle variables of the particle every turn following Eqs. (3.8) and. (3.7) for phase and amplitude noise respectively.

From these plots, it becomes evident that there is an excellent agreement between the theoretical predicted vertical emittance growth and the simulation results with Sixtracklib. The emittance growth rates from Sixtracklib simulations are also in agreement with the results from PyHEADTAIL. To this end, it is concluded that taking into account the detailed optics including machine non-linearities of the SPS cannot explain the discrepancy between expected and measured emittance growth that was observed in the SPS CC tests in 2018.

Finally, the spread between the emittance values obtained from the different runs in Sixtracklib and PyHEADTAIL simulations is commented here. By comparing

Figs. 5.4 and 5.5 it is evident that in the presence of phase noise (right) the spread of the emittance growth between the different simulation runs is similar. However, in the presence of amplitude noise (left) the spread of the emittance growth between different runs is significantly smaller in Sixtracklib results compared to the PyHEADTAIL results. It should be noted, however, that the simulated emittance growth is quite small and even small differences in the two codes could lead to different behavior and might explain the different results. For example, in Sixtracklib simulations non-linear elements are included. On the contrary in PyHEADTAIL non-linear elements are not included and the amplitude detuning is introduced as a change of the phase advance of each individual particle. Nevertheless, the codes agree on the average emittance growth rate and this issue does not affect the conclusions drawn from the results presented in this thesis.

5.3.2 Implementation of Crab Cavity in Sixtracklib

Sixtracklib provides the possibility to perform tracking simulations in the presence of an actual CC element on which noise can be added, instead of modeling only the transverse momentum kicks due to phase and amplitude noise in the RF system of the cavity (as was done in PyHEADTAIL). This provides the opportunity to study the CC RF noise-induced emittance growth in a more realistic scenario and therefore it will be used for the rest of the simulations presented in this chapter.

In Sixtracklib the CC is represented by the "RF-Multipole" element [58] that has the properties of a multipole magnet oscillating at a specified frequency. To simulate the vertical CC, the multipole field component corresponds to a skew RF dipole.

When a particle passes through this element, the change in the vertical angle of each particle is the following:

$$\Delta\gamma'_j = \frac{eV_{0,CC}}{p_0 c} \cos\left(\phi_{RF-Mult} - \frac{2\pi f_{CC}}{c} \frac{z\beta_0}{\beta^2}\right), \quad (5.2)$$

where $j = 0, \dots, N_{\text{turns}}$ denotes the turn number with N_{turns} being the total number

5. Investigation of the discrepancy between emittance growth theory and experimental data

of turns that the beam passes through the element. In Eq. (5.2), y' is the vertical angle co-ordinate and z is the longitudinal co-ordinate of each particle, $\phi_{\text{RF-Mult}}$ is the phase of the RF-Multipole, f_{CC} is the CC frequency, c is the speed of light, e the elementary charge, β_0 is the relativistic beta, $V_{0,\text{CC}}$ is the amplitude of the CC voltage and p_0 the reference momentum.

Before using this element for the emittance growth simulations its implementation in Sixtracklib was tested. The CC element installed at a location s_0 , acts like a single dipole field error with strength depending on the longitudinal position z of the particle. To this end, the induced orbit shift from the CC (represented by the RF-Multipole element) as detected at another location s_1 is benchmarked against the theoretically expected orbit shift.

The theoretically expected orbit shift can be computed with Eq. (5.3). Equation (5.3), which is obtained from Eq. (1) from chapter 4.7.1 in [89], gives the vertical orbit shift (in meters) from the CC kick (at the location s_0), at the location s_1 as follows:

$$\Delta y_{s_1} = \frac{\sqrt{\beta_{y,s_1}}}{2 \sin(\pi Q_{y0})} \Delta y' \sqrt{\beta_{y,s_0}} \cos(\pi Q_{y0} - |\psi_{y,s_1} - \psi_{y,s_0}|), \quad (5.3)$$

which after inserting, $\Delta y'$ from Eq. (5.2) for any turn becomes:

$$\Delta y_{s_1} = \frac{\sqrt{\beta_{y,s_1} \beta_{y,s_0}}}{2 \sin(\pi Q_{y0})} \left(\frac{e V_{0,\text{CC}}}{p_0 c} \cos\left(\phi_{\text{RF-Mult}} - \frac{2\pi f_{\text{CC}}}{c} \frac{z \beta_0}{\beta^2}\right) \right) \cos(\pi Q_{y0} - |\psi_{y,s_1} - \psi_{y,s_0}|), \quad (5.4)$$

where Q_{y0} is the vertical tune, β_{y,s_0} and β_{y,s_1} are the vertical beta function at the locations s_0 and s_1 respectively and $|\psi_{y,s_1} - \psi_{y,s_0}|$ is the vertical phase advance in radians between the locations s_0 and s_1 .

Figure 5.6 plots the vertical co-ordinate at the location s_1 (orange) after tracking 1000 particles for 500 turns with Sixtracklib in the presence in the presence of the above-mentioned CC element (which is installed at the location of CC1, location s_0). The locations s_1 is the start of the lattice, which for this study it was considered

to be the horizontal rotational Wire Scanner, BWS.51995.H. The simulations took place using an initial Gaussian bunch distribution in the six-dimensional phase space. The initial normalised emittances were $\epsilon_x = 2.5 \mu\text{m}$ and $\epsilon_y = 2.5 \times 10^{-6} \mu\text{m}$ for the horizontal and vertical plane respectively. The distribution was chosen to be so small in the vertical plane so there is practically no initial offset which facilitates the observation of the orbit shift. The most relevant parameters are listed in Table 5.2.

The orbit shift computed analytically using Eq. (5.4) is also plotted in Fig. 5.6 (blue) for same parameters used in the simulation. The orbit shift was computed over a range of equally spaced z co-ordinates from -0.6 to 0.6 m ($\sim 3\sigma_z$ of the initial distribution used in the simulations).

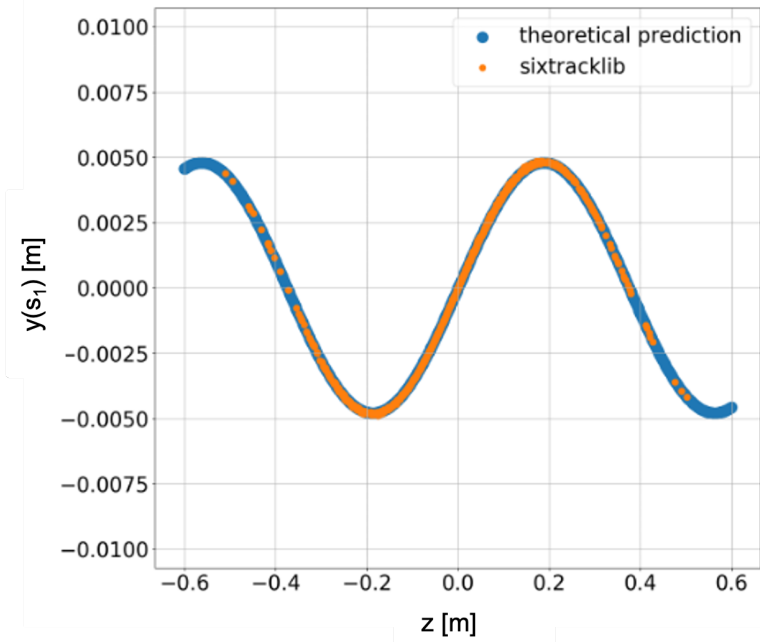


Figure 5.6: Vertical orbit shift at the location of the horizontal Wire Scanner (SPS.BWS.51995.H.) induced by the CC element as computed analytically (blue) and from tracking simulations with Sixtracklib (orange).

By looking at Fig. 5.6 it is concluded, that using Sixtracklib the result of CC element on the orbit is as expected from the analytical calculations.

The amplitude and phase noise in the CC element are modeled as the following change of the vertical angle of each particle (modifying Eq. (5.2)):

5. Investigation of the discrepancy between emittance growth theory and experimental data

Table 5.2: Parameters for computing the vertical orbit shift induced by the CC element (at the location s_0) at the location of the horizontal Wire Scanner (SPS.BWS.51995.H.), s_1 .

Parameter	Value
Beta function at the Wire Scanner, β_{y,s_1}	27.47 m
Phase advance to the Wire Scanner*, $\psi_{y,HT}$	0
Beta function at the CC1, $\beta_{y,CC1}$	76.07 m
Phase advance to the CC1*, $\psi_{y,CC1}$	$4.05 \times 2\pi$
Vertical betatron tune, Q_{y0}	26.18
Beam energy, E_b	26 GeV
rms bunch length, σ_z	0.22 m
rms momentum spread, σ_δ	1e-4
CC voltage, $V_{0,CC}$	3 MV
CC frequency, f_{CC}	400 MHz
RF-Multipole phase, $\phi_{RF-Mult}$	90 deg [†]

* The phase advances are measured from the start of the lattice which is considered the element SPS.BWS.51995.H that is the horizontal rotational Wire Scanner.

[†] It was found that in the definition of the RF-Multipole the phase of the cavity is shifted by 90 degrees compared to the standard (theoretical) crab cavity kick.

$$\Delta y'_j = \frac{e(V_{0,CC} + \Delta V_{0,CC,j})}{p_0 c} \cos \left((\phi_{RF-Mult} + \Delta\phi_j) - \frac{2\pi f_{CC}}{c} \frac{z\beta_0}{\beta^2} \right), \quad (5.5)$$

where $j = 0, \dots, N_{\text{turns}}$ denotes the turn number with N_{turns} being the total number of turns that the beam passes through the element. Furthermore, $\Delta\phi_j$ is the deviation from the nominal phase (phase noise level), and $\Delta V_{0,CC,j}$ is the deviation from the nominal amplitude $V_{0,CC}$ (amplitude noise level) at the j^{th} turn.

In the following simulations (unless it is stated otherwise) the parameters $\Delta\phi_j$ and $\Delta V_{0,CC,j}$ are the j^{th} elements of a set of N_{turns} samples, drawn from Gaussian distributions of size N_{turns} , with mean zero and standard deviation of $\sigma_{\Delta\phi}$ and $\sigma_{\Delta V_{0,CC}}$ respectively. The typical values that will be used in the following simulations for phase and amplitude noise respectively are: $\sigma_{\Delta\phi} = 2.7 \times 10^{-3}$ rad and $\sigma_{\Delta V_{0,CC}} = 0.0027$ MV.

The parameter $\Delta V_{0,CC,j}$ is related to the relative deviation from the nominal amplitude ΔA_j of Eq. (3.7) as follows: $\Delta A_j = (\Delta V_{0,CC,j} / V_{0,CC})c$. Consequently, one can write: $\sigma_{\Delta A} = (\sigma_{V_{0,CC}} / V_{0,CC}) = 2.7 \times 10^{-3}$. These values result in power spectral densities at the betatron frequency of: $S_{\Delta A}(f_b) = 1.68 \times 10^{-10} / \text{Hz}$ for amplitude

noise and $S_{\Delta\phi}(f_b) = 1.68 \times 10^{-10}$ rad²/Hz for phase noise (same as in the simulations presented already in this chapter).

5.3.3 CC noise induced emittance growth in the presence of local CC scheme

In this section, the emittance growth driven by CC RF noise is simulated with Sixtracklib in the presence of a local CC scheme. As previously mentioned, in the local CC scheme (Fig. 1.4) two CCs are used with opposite phase, to cancel out the orbit distortion.

The benchmark with the local scheme is performed as it is closer to the case that was studied previously: where the CC RF noise is modeled as noise kicks in the transverse angle co-ordinate of the individual particles. Both configurations avoid introducing any orbit distortion from the crab cavities.

The simulation studies presented in Section 5.3.1 were repeated here but this time the CCs (represented by the RF-Multipole) were implemented and switched on. Both CC1 and CC2 operated at 1 MV, for $\phi_{RF-Mult,1}=90$ deg and $\phi_{RF-Mult,2}=270$ deg. Figure 5.7 shows that the orbit shifts from two CCs operating in opposite phase cancel out as expected. The results shown are obtained from Sixtracklib simulations that were conducted following the same procedure as the equivalent study presented in Section 5.3.2 (see Fig. 5.6.)

For the emittance growth simulations, the noise was applied only in CC1. The amplitude and phase noise were treated separately and for the simulation parameters a growth of 22 nm/s and 24 nm/s is expected respectively. The simulation results are illustrated in Fig. 5.8.

The simulations show an excellent agreement between the theoretically computed and simulated growth rates for both noise types. They also demonstrate that the modeling of the noise as kicks on the angle co-ordinate provides equivalent results to "real" noise which is applied through the CC (represented by the RF-Multipole) of Sixtracklib.

5. Investigation of the discrepancy between emittance growth theory and experimental data



Figure 5.7: Vertical orbit shift at the location of the horizontal Wire Scanner (SPS.BWS.51995.H.) as obtained with Sixtracklib tracking through the nominal SPS lattice. *Green*: Only CC1 operates at 1 MV and $\phi_{RF-Mult,1}=90$ deg. *Red*: Only CC2 operates at 1 MV and $\phi_{CC2}=270$ deg. *Orange*: The two CCs operate at the same voltage but in opposite phase: $\phi_{RF-Mult,1}=90$ deg and $\phi_{RF-Mult,2}=270$ deg. *Blue*: Orbit shift calculated analytically using Eq. (5.4).

5.3.4 CC noise induced emittance growth in the presence of global CC scheme

Here, the simulations presented above were repeated but for a global CC scheme. As already mentioned, in the global CC scheme only one CC (represented by the RF-Multipole element) is in operation and the closed orbit shift is present during the circulation of the bunch around the machine. This scheme is the realistic case for the experiments of 2018, where for the emittance growth measurements only one CC was used.

For the simulations presented here, CC2 was switched off. CC1 operated at 1 MV, for $\phi_{RF-Mult,1}=90$ deg. The noise was applied as described in Eq. (5.5) for the same noise levels as before. For this study, where only one CC is switched on, its voltage is slowly increased to the chosen value of 1 MV, so that the new closed orbit includes the full CC kick. Without this dynamic ramping, emittance blow-up is observed during the first turns in the simulation. Previous studies have shown that using a ramp of 200

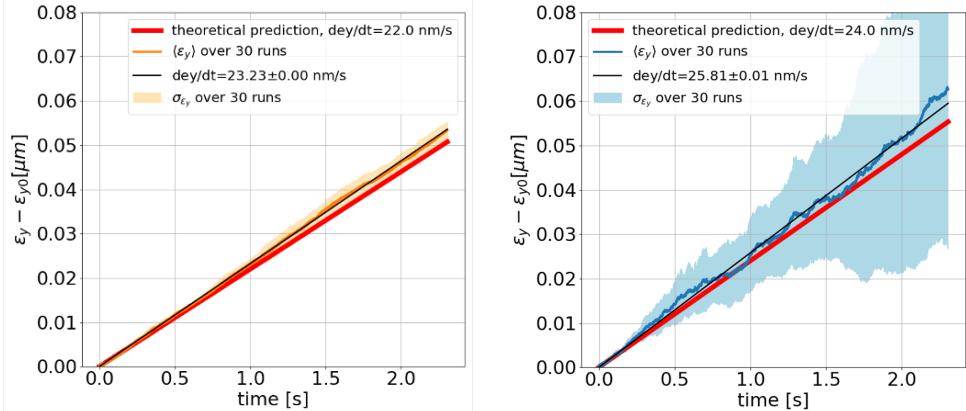


Figure 5.8: Vertical emittance growth driven by CC RF amplitude noise (left) and phase noise (right) as simulated with Sixtracklib simulation tool for a configuration close to the experimental conditions of the SPS CC tests in 2018 but for a local CC scheme. The CC noise is applied on CC1, following Eq. (5.5).

turns is sufficient to avoid emittance blow-up. The first 200 turns, are excluded from the linear fit used to obtain the emittance growth rates.

Figure 5.9 illustrates the simulated emittance growth driven by amplitude (left) and phase (right) noise in the presence of a global CC scheme. Once again, an excellent agreement is observed with the theoretically expected growth and also with the simulated growth rates for the different configurations discussed previously in this chapter.

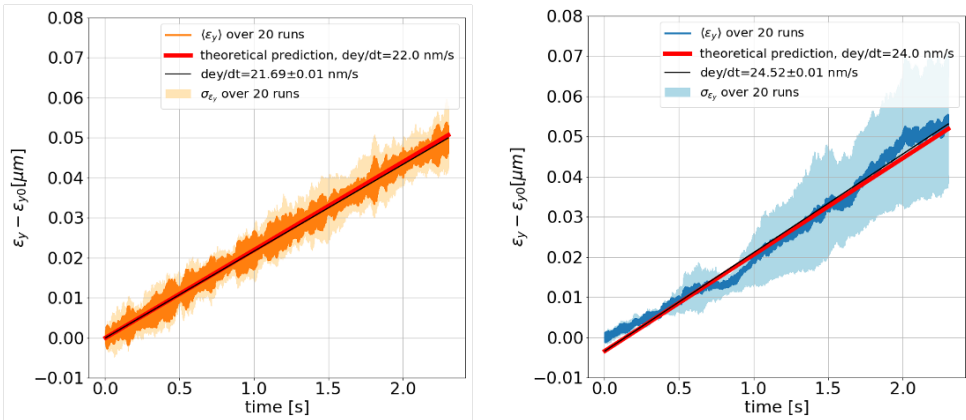


Figure 5.9: Vertical emittance growth driven by CC RF amplitude noise (left) and phase noise (right) as simulated with Sixtracklib simulation tool for a configuration close to the experimental conditions of the SPS CC tests in 2018 but for a global CC scheme. The CC noise is applied on CC1 which operates at 1 MV, following Eq. (5.5), while CC2 is switched OFF.

5. Investigation of the discrepancy between emittance growth theory and experimental data

5.3.5 CC noise induced emittance growth with the measured noise spectrum

All the simulations discussed up to now were performed considering a white noise spectrum where the sequence of the uncorrelated random noise kicks were taken from a Gaussian distribution. However, as discussed in Section 4.3, measurements are available of the phase and amplitude noise that were injected in the CC RF system for the emittance growth studies in the SPS in 2018.

Here, the simulation studies presented in the previous Subsection 5.3.4 (with global CC scheme) were repeated but this time the emittance growth is simulated using the measured noise spectrum.

The phase and amplitude noise spectra from Coast3-Setting3 (see Fig. 5.10) were used since they were the strongest noise levels from all the coasts. To this end, one can ensure the observation of reasonable emittance growth in our simulation time, which for this particular set of simulations was increased to ~ 10 s (5×10^5 turns).

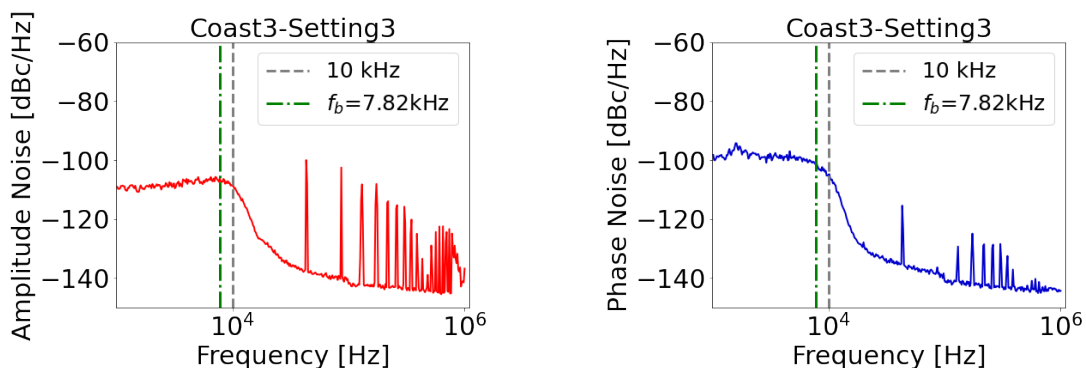


Figure 5.10: Example amplitude (left) and phase (right) noise spectra measured with a spectrum analyzer E5052B [73] during the emittance growth studies with CCs in SPS. The noise extends up to about 10 kHz (grey dashed line) overlapping the first betatron sideband at ~ 8 kHz (green dashed line). The spikes at high frequencies correspond to the harmonics of the revolution frequency and are a result of the bunch crossing.

Additionally, some of the simulation parameters were refined to be closer to the experimental conditions of 2018. In particular, the synchrotron tune and bunch length were set to $Q_s = 0.0051$ and $\sigma_z = 0.138$ m. Following the experimental configuration of 2018, CC1 was switched off, while CC2 operated at 1 MV (with the

voltage being slowly ramped up during the first 200 turns). For reference, the vertical beta function at the location of CC2 is 73.8 m.

The measured spectra of Fig. 5.10 were converted to a discrete time series that can be used in the numerical simulations as described in Appendix B.4.

In Figure 5.11 the simulation results where the phase and amplitude noise from Coast3-Setting3 are applied separately on CC2 are summarised. Once again, the agreement between the theory and the simulations is excellent for both cases.

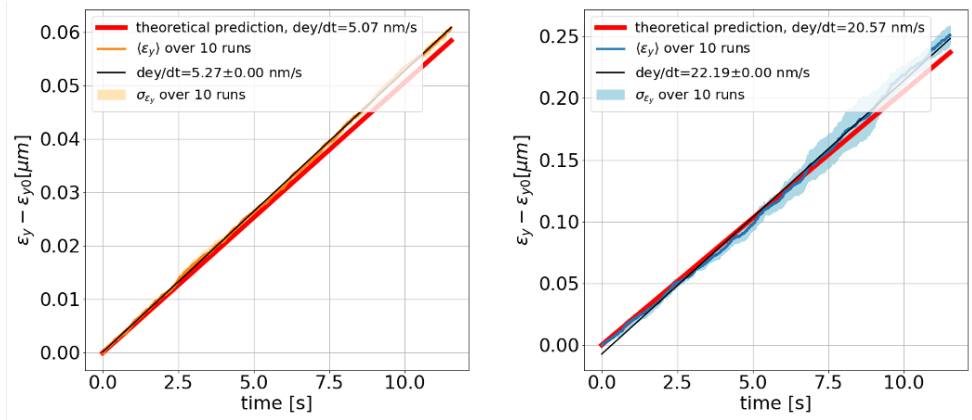


Figure 5.11: Vertical emittance growth driven by CC RF amplitude noise (left) and phase noise (right) as simulated with the Sixtracklib simulation tool for a configuration close to the experimental conditions of the SPS CC tests 2018. The measured phase and amplitude noise spectra from Coast3-Setting3 are used for the simulations. The CC noise is applied on CC2 which operates at 1 MV, following Eq. (5.5), while CC1 is switched off.

By looking at the plots, it is evident that there is significantly less variation in the emittance growth rates over the different runs. This is due to the fact that as discussed in Appendix B.4, in the time series generated by the measured spectra the random factor is included in the set of random phases which leads to much less deviation in the values than the sequence of white noise kicks where the random factor is in their amplitude. To this end, the simulation here is repeated for just 10 different runs to reduce the uncertainty.

Finally, the same simulation is repeated in the presence of both amplitude and phase noise together. The results are shown in Fig. 5.12 where it is clear that the agreement with the analytically predicted rates is very good.

5. Investigation of the discrepancy between emittance growth theory and experimental data

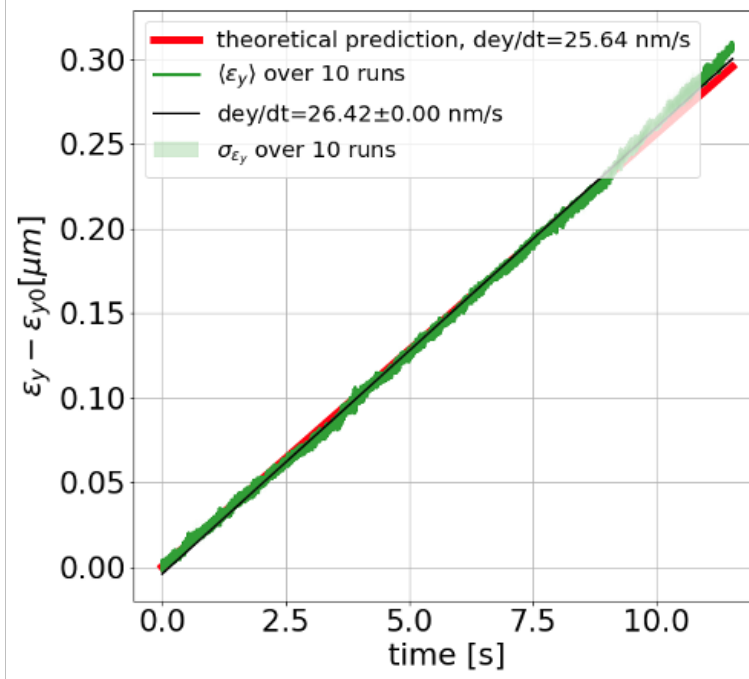


Figure 5.12: Vertical emittance growth driven by CC RF amplitude and phase noise as simulated with the Sixtracklib simulation tool for a configuration close to the experimental conditions of the SPS CC tests 2018. The measured phase and amplitude noise spectra from Coast3-Setting3 are used for the simulations. Both types of noise are applied on CC2 which operates at 1 MV, following Eq. (5.5), while CC1 is switched off.

5.3.6 CC noise induced emittance growth with the non-linear SPS model

The nominal SPS model includes only the non-linear fields produced by the chromatic sextupoles. However, one of the most important sources of non-linearities in SPS are the higher-order multipole components of its main dipole magnets. In this subsection, their impact on the beam dynamics studies is considered, as a possible contribution to the observed discrepancy between predicted and measured emittance growth rates in the present of CC RF noise. To this end the multipole components of the SPS main dipoles should be included in the nominal SPS model that was used up to now.

Magnetic measurements of the precise multipole errors of the SPS main dipoles are not available. On this ground a non-linear optics model of the SPS has been established with beam-based measurements of the chromatic detuning over a range of momentum deviation [71, 72]. The optics model was obtained by

assigning systematic multipole components to the main lattice magnets, in the nominal model of SPS, in order to reproduce the tune variation with momentum deviation as it was measured in the real machine. The calculations were performed with MAD-X.

The values of the multipole components up to seventh order obtained from this method are given in Table 5.3 where, (b_3^A, b_3^B) , (b_5^A, b_5^B) and (b_7^A, b_7^B) stand for the sextupolar, decapolar and decatetrapolar mutipoles respectively. Note that different values have been obtained for each of the two different kinds of SPS main dipoles (MBA and MBB) which are marked with the indices A and B respectively.

Table 5.3: Multipole errors from SPS non-linear model, at 270 GeV [72].

Multipole	Value
b_3^A, b_3^B	$8.1 \times 10^{-4} \text{ m}^{-2}, 1.1 \times 10^{-3} \text{ m}^{-2}$
b_5^A, b_5^B	$9.2 \text{ m}^{-4}, -10 \text{ m}^{-4}$
b_7^A, b_7^B	$1.3 \times 10^5 \text{ m}^{-6}, 1.4 \times 10^5 \text{ m}^{-6}$

These values were assigned to the main dipoles of the SPS and the simulations presented in Section 5.3.5 were repeated. The simulations were performed in the presence of the measured phase noise spectrum only which was dominant during the SPS experiments in 2018. The results are displayed in Fig. 5.13. It is clear that there is a very good agreement between the theory and the simulations when the non-linear model of SPS is used. Hence, it is concluded that since the theoretical estimate does not take into account the multipole errors, the inclusion of these errors has no significant impact on the emittance growth rates

5.4 Conclusions and outlook

The work presented in this chapter focused on investigating possible explanations for the discrepancy of a factor of about 4 observed between the theoretically predicted and measured emittance growth driven by CC RF noise during the experiments of 2018 in the SPS. The following points were checked:

- Sensitivity to possible uncertainties in the measured parameters and in

5. Investigation of the discrepancy between emittance growth theory and experimental data



Figure 5.13: Vertical emittance growth driven by CC RF phase noise as simulated with Sixtracklib simulation tool for a configuration close to the experimental conditions of the SPS CC tests 2018. The measured phase and amplitude noise spectra from Coast3-Setting3 are used for the simulations. The non-linear model (including multipole components of the main dipole magnets) of the SPS machine was used for the tracking. Both types of noise are applied on CC2 which operates at 1 MV, following Eq. (5.5), while CC1 is switched OFF.

particular in the CC voltage and bunch length.

- Benchmarking of the theory with two different simulation codes: PyHEADTAIL and Sixtracklib.
- Sensitivity of the simulated emittance growth to the detailed optics and the presence of a real CC element.
- Sensitivity to the measured noise spectrum.
- Sensitivity to the non-linearities of the SPS lattice.

All these factors were excluded as possible sources of the discrepancy since for all of these study cases the simulated emittance growth demonstrated an excellent agreement with the theoretically predicted values using the Mastoridis–Baudrenghien model. It was also confirmed that the detailed optics of the SPS, its non-linearities and the orbit shift induced by the CC (represented by

the RF-Multipole element in Sixtracklib) have no impact on the CC RF noise-induced emittance growth. To this end, in the next chapters, the simulations will be performed with the PyHEADTAIL simulation tool which also provides the possibility of including collective effects (such as the impedance), which were not addressed so far in the context of these studies.

6 | Simulation studies: Emittance growth suppression mechanism from the beam transverse impedance

During the dedicated experiment that took place in the SPS in 2018 with the CCs, the measured emittance growth due to CC RF noise was found to be a factor of four (on average) lower than expected from the theory (see Section 4.7). The reason for this discrepancy remained unresolved for some time, as detailed follow-up studies (see Chapter 5) investigated and excluded a number of possible explanations for the discrepancy. It was recently found, that the beam transverse impedance, which is not included in the theory [63] used for the comparison with the measurements may impact the noise-induced emittance growth and explain the experimental observations. Here, the damping mechanism from the beam transverse impedance is investigated in PyHEADTAIL simulations.

The structure of this chapter is as follows: Section 6.1 provides information on the impedance model of the SPS machine and benchmarks its implementation in PyHEADTAIL against theoretical calculations. In Section 6.2 the simulation setup for the emittance growth studies is discussed and the beam and machine parameters (following the 2018 CC experiment) are listed. Section 6.3 presents simulation results which showed for the first time that the transverse beam impedance (which was not included in the theory [63] and the simulations up to now) significantly suppresses the noise-driven emittance growth. Furthermore, PyHEADTAIL simulations were carried out aiming to characterise the effect of the emittance growth suppression in order to understand the mechanism behind it.

These studies are presented in Section 6.4. The suppression mechanism is investigated through parametric studies and with studies in the frequency domain in Section 6.5. Finally, the main results are summarised in Section 6.6

6.1 SPS transverse impedance model

The PyHEADTAIL studies presented in this chapter are performed including the detailed transverse impedance model of the SPS machine [90]. This model has been developed through a combination of theoretical computations and electromagnetic simulations and was benchmarked with beam-based measurements [56, 91, 92, 93]. It includes the contributions from all the individual elements in the SPS lattice, i.e. the resistive wall, the indirect space charge, the kickers, the RF cavities (200 MHz and 800 MHz), the step transitions, and the horizontal and vertical beam position monitors [93]. As discussed in Section 2.5.1, the model needs to represent the global impedance of the full machine. Thus, the total impedance is obtained by summing up the impedance of each element weighted with the beta function at its location and dividing the sum by the value of the beta function at which the wakefield kick is applied in the simulations, which is chosen to be the average beta function around the machine. For the Q26 optics, the average horizontal and vertical beta functions are 42.09 m, and 42.01 m, respectively. Figure 6.1 shows the complete transverse impedance model of the SPS machine with the dipolar (blue) and quadrupolar (orange) terms plotted separately.

Wake functions

As already discussed in Section 2.5.1, in order to include the impedance effects in PyHEADTAIL simulations the real-value wakefields in the time domain are used in order to update the angle co-ordinate of the particles according to Eq.... ([update once you add the equation in chapter 2](#)). The total transverse dipolar (blue) and quadrupolar (orange) wake functions for both planes of the SPS can be found in the GitLab repository of [90] and they are plotted in Fig 6.2.

For reference, the impedance model is used as an input in the Sacherer formula

6. Simulation studies: Emittance growth suppression mechanism from the beam transverse impedance

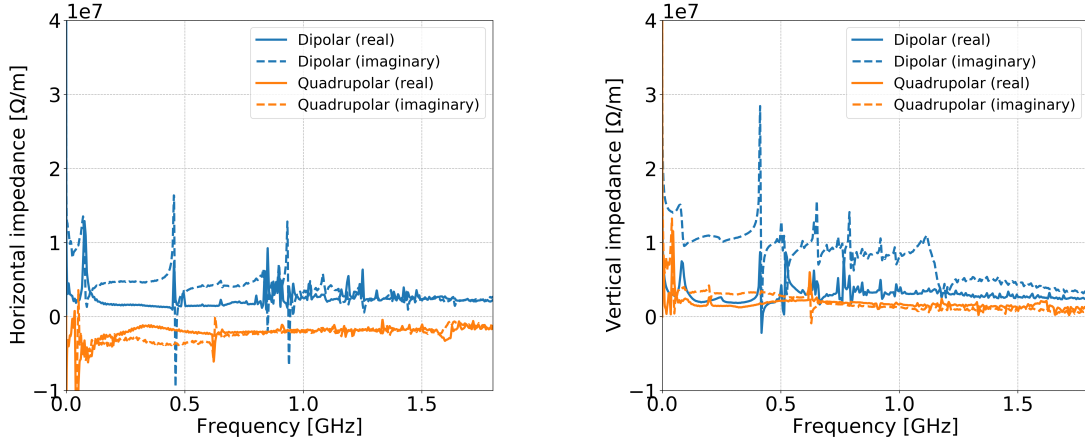


Figure 6.1: Horizontal (left) and vertical (right) impedance model of the SPS. The contributions from the wall, the kickers and the step transitions are visible at the low frequencies (up to ~ 0.4 GHz). The impedance of the RF cavities and the beam position monitors (BPMs) correspond to the peaks observed between ~ 0.4 -1 GHz.

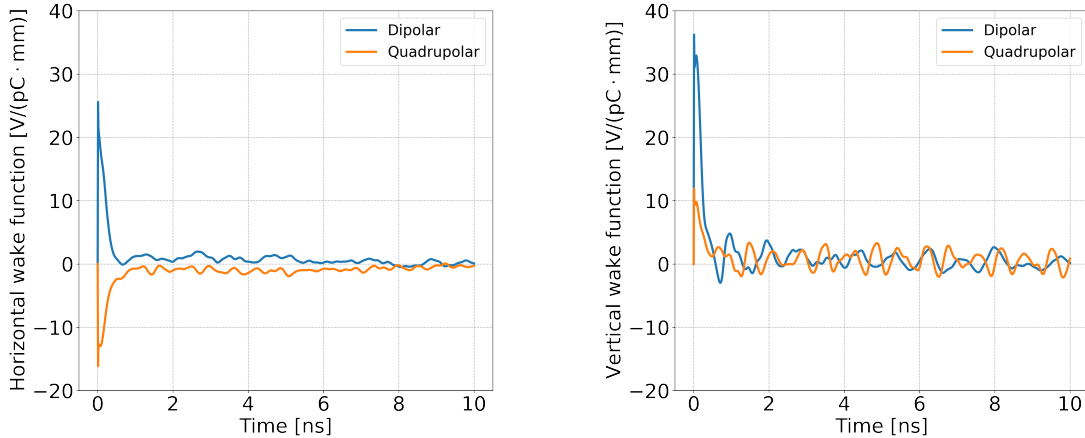


Figure 6.2: Horizontal (left) and vertical (right) wakefunctions of the SPS. The wake functions are available in the public GitLab repository of [90]. For comparison the bunch length in the SPS CC experiments is ~ 1.85 ns ($4\sigma_t$).

(Eq. (2.57)) for analytical estimations while the wake functions are used as an input in simulation codes such as PyHEADTAIL.

Last, these wake functions are obtained with an inverse Fast Fourier Transform algorithm (iFFT) on the impedance model as described in the references provided above.

6.1.1 Testing the implementation in PyHEADTAIL

As discussed in Section 2.3.1 the imaginary part of the impedance leads to a coherent tune shift which depends on the bunch intensity. One of the most

common ways to test the correct implementation of the impedance model in a tracking simulation code is to benchmark the simulated intensity-dependent coherent tune shift with the theoretically predicted behavior (using Eqs. (2.57) and (2.61)).

Typically, in tracking simulations, the coherent tune is obtained by applying a frequency analysis technique to the oscillations of the centroid of the particle distribution (the center of mass of the bunch). Here, the analysis is limited to the coherent mode $l = 0$, as the study of mode $l = 0$ is sufficient for the purpose of the studies presented here. For simplicity in the following the term "coherent tune" will refer to the coherent tune of mode $l = 0$.

Simulations setup

The parameters used for setting up the linear transfer map, the longitudinal tracking and the beam initialisation are shown in Table 6.1 and are the ones used in the SPS CC experiment of 2018. The ring is modelled by a linear transport map, with one interaction point at which the beam interacts with the wakefields. At that location, the horizontal and vertical beta functions equal the corresponding average beta functions over the SPS machine (see Section 2.5.1). The latest transverse wakefield model (as of February 2019 in Ref. [90]) of the SPS was used.

The initial bunch was generated with Gaussian distributions in transverse and longitudinal planes. The bunch population of the different intensity values was represented by 5×10^5 macroparticles and the number of slices of the longitudinal distribution was 500.

For all the PyHEADTAIL simulation studies presented in this thesis, the Twiss parameter $\alpha_u(s)$ and the dispersion function $D_u(s)$ equal zero. This is a valid assumption for the studies as these parameters have no direct impact on the effects under investigation.

To facilitate the observation of the coherent tune, the bunch was initialised with a static offset of $0.15\sigma_{x,y}$ in both transverse planes, so that it performs dipole oscillations around the machine. The parameter $\sigma_{x,y}$ is the rms transverse beam

6. Simulation studies: Emittance growth suppression mechanism from the beam transverse impedance

Table 6.1: PyHEADTAIL simulation parameters used to study impedance induced effects for the SPS.

Parameter	Value
Beam energy, E_b	270 GeV
Machine circumference, C_0	6911.5623 m
Horizontal / Vertical betatron tune, Q_{x0} / Q_{y0}	26.13 / 26.18
Synchrotron tune, Q_s	0.0051
Momentum compaction factor, α_p	1.9×10^{-3}
Number of bunches	1
Rms bunch length, $4\sigma_t$	1.7 ns *
Horizontal / vertical normalised emittance, ϵ_x / ϵ_y	2 μm / 2 μm
Average horizontal / vertical beta function, $\langle\beta_x\rangle/\langle\beta_y\rangle$	42.0941 m / 42.0137 m †
Number of macroparticles, N_{mp}	5×10^5
Number of longitudinal slices, N_{slices}	500

* This value corresponds to the average measured bunch length of bunch 1 over all the coasts of 2018. The value for bunch 1 is used here since it was the only stable bunch in the SPS CC tests of 2018.

† Model values for the Q26 optics.

size (see Eq. (2.35)) at the only interaction point along the ring i.e. at the location where the beam interacts with the wakefields. It was tracked for 600 turns and the coherent tune was computed using a NAFF algorithm [94, 95], which provides a refined FFT analysis on the turn-by-turn centroid motion. The Python implementation, NAFFlib, can be found in [96]. The coherent tune shift was computed by subtracting the obtained tune value from the unperturbed coherent tune (in the absence of impedance) which equals the Q_{u0} value.

Last, the dependence of the coherent tune on the bunch intensity value was studied in the absence of other detuning effects (such as chromaticity or detuning with transverse amplitude).

The simulation was repeated for a range of bunch intensities, N_b , equally-spaced from 0 to 5×10^{10} protons per bunch. This range was chosen to be in the vicinity of the bunch intensity of the CC experiments of 2018, where N_b was 3×10^{10} protons per bunch. $N_b = 0$ is not a realistic value. However, it is used here as the reference point for which the coherent betatron tune shift equals zero. The simulation results are compared with the theoretically expected tune shifts in Fig. 6.3.

The theoretically expected values are computed from Eqs. (2.57) and (2.61) for $l = 0$

and using only the imaginary part of the impepdance. Given that $\Gamma(1/2) = \sqrt{\pi}$ and $Q_u = \omega_{u0}/\omega_{\text{rev}}$ equation Eq. (2.57) becomes:

$$\Delta\Omega_u^{(0)} = \Omega_{u0}^{(0)} - \omega_{u0} = \frac{\sqrt{\pi}}{4\pi} \frac{N_b r_0 c^2}{\gamma_0 \frac{2\pi}{\omega_{\text{rev}}} \omega_u \sigma_z} Z_{\text{eff,im}} = \frac{N_b r_0 c^2}{8\pi^{3/2} \gamma_0 Q_u \sigma_z} Z_{\text{eff,im}} \quad (6.1)$$

All the parameters inserted in Eq. (6.1) need to be converted into cgs (centimetre–gram–second) units. The coherent betatron tune shift is computed by inserting the result of Eq. (6.1) in Eq. (2.61) such that:

$$\Delta Q_u = \frac{\Delta\Omega_u^{(0)}}{\omega_{\text{rev}}} \quad (6.2)$$

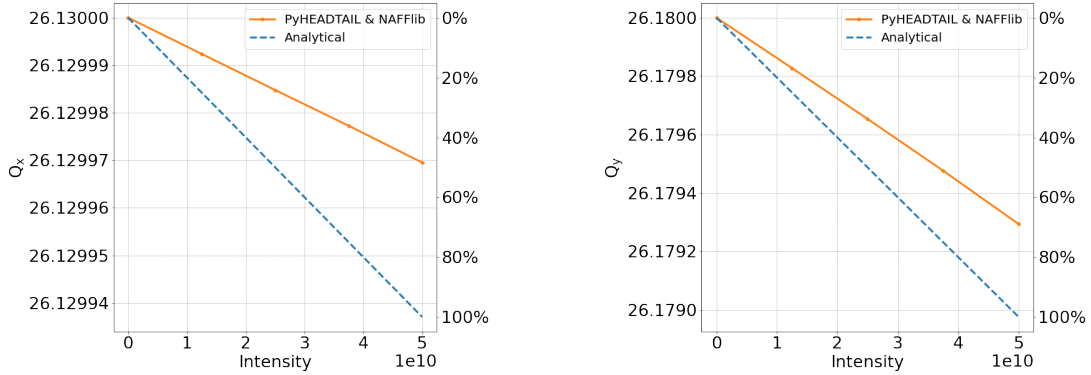


Figure 6.3: Horizontal (left) and vertical (right) coherent tunes as a function of intensity in the presence of the beam coupling SPS impepdance obtained using analytical formula (blue dashed line) and PyHEADTAIL tracking simulations (orange line). The impedance model and the wake functions used are available in [90].

Figure 6.3 shows that the coherent tune shift from the analytical model does not agree with simulation results. In particular, the wakefields used in the PyHEADTAIL simulations result in between roughly 50% and 70% of the coherent tune shift computed analytically using the corresponding impedance. This discrepancy has not been observed previously, such a comparison has not been conducted for such low intensities (the usual intensity range for this type of study is in the order of 10^{11} protons per bunch [97]) and short bunches. The analytical predictions from Sacherer formula have been successfully benchmarked against beam measurements [98, 99] which indicates that there is an issue with the model of the wakes or with their implementation in the simulation. Given the fact that the

6. Simulation studies: Emittance growth suppression mechanism from the beam transverse impedance

studies with CCs are sensitive to the coherent tune shift¹ (and its dependence on the beam intensity), it is important to identify the cause of the discrepancy between the simulation and analytical results, and to resolve it.

After several studies and discussions with the experts on the topic² it was identified that higher accuracy is needed at the lower frequencies. Thus, the components of the resistive wall and the step transitions were refined by being computed analytically directly in time domain so no FFT is involved. The details of this work are not discussed here as they are out of the scope of this thesis and they were not performed by the author. The re-computed wake functions (of the resistive wall and the step transitions) along with the rest of the components of the original model can be found in [100] and it will be referred to as the "updated wakefields" model.

The coherent betatron tune as a function of intensity obtained using PyHEADTAIL and the updated wakefields model is plotted in Fig. 6.4 in comparison with the analytical predictions from Sacherer formula. In both transverse planes, the results from the simulations and the theory are in very good agreement ($\leq 5\%$) which is within the uncertainty that one can expect from the model implementation.

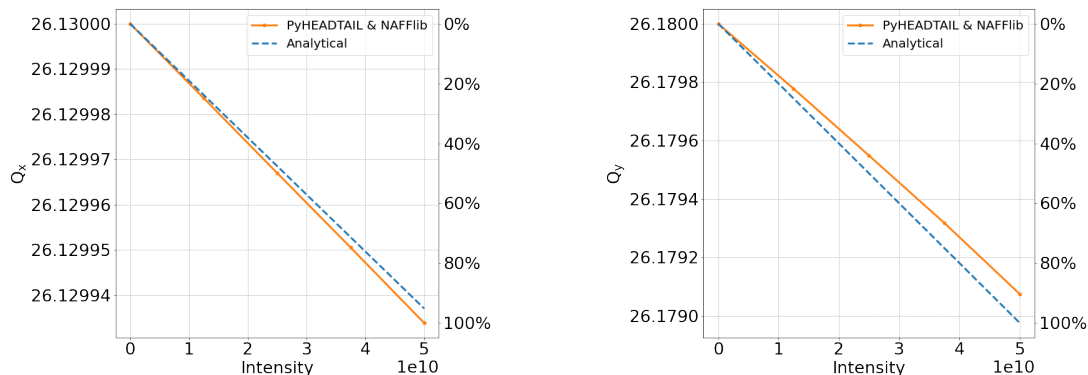


Figure 6.4: Horizontal (left) and vertical (right) coherent tunes as a function of intensity in the presence of the beam coupling SPS impedance obtained using analytical formula (blue dashed line) and PyHEADTAIL tracking simulations (orange line). The impedance model is available in. [90]. The PyHEADTAIL simulations use the "updated wakefields model" (in contrast with the results of Fig. 6.3) which can be found in [100].

¹The sensitivity of the dynamics with crab cavities to the coherent tune shifts will be discussed later in this chapter.

²In particular with Carlo Zannini, carlo.zannini@cern.ch.

The above figure demonstrates that the updated wakefields model is reliable and validates the implementation in PyHEADTAIL. Therefore it will be used to study the interplay of the CC noise induced emittance growth with impedance induced effects. These studies are presented in the following chapter.

6.2 Emittance growth simulations setup

The simulations that were performed to investigate the impact of the beam coupling impedance on the CC RF noise-induced emittance growth were performed following the procedure and using the parameters that are described below. Any change in the choice of parameters, e.g. for some of the parametric studies, will be mentioned at the appropriate point.

The parameters used for setting up the linear transfer map, the longitudinal tracking and the beam initialisation are shown in Table 6.1 and are the ones used in the SPS CC experiment of 2018. The ring is modelled by two linear transfer maps and two interaction points. Kicks representing noise from the crab cavities are applied at the first interaction point, and wakefield kicks are applied at the second. The updated wakefields model [100] of the SPS was used.

At the location of the CC RF noise kick the horizontal and vertical beta functions equal the values at the location of the CC2 which was used in the experiments of 2018. At the location where the wakefield kicks are applied the transverse beta functions equal the corresponding average beta functions over the SPS machine (see Section 2.5.1). The simulations are performed for the Twiss parameter $\alpha_u(s)$ and the dispersion function $D_u(s)$ equal zero. This is a valid assumption for the studies as these parameters have no direct impact on the effects under investigation.

The emittance growth studies were performed for the intensity of 3×10^{10} protons per bunch in accordance with the 2018 experiments. The bunch population was represented by 5×10^5 macroparticles and the number of longitudinal slices was 500. The emittance growth was also simulated without including the wakefields. For the latter case, the bunch population was represented by 10^5 particles. The studies

6. Simulation studies: Emittance growth suppression mechanism from the beam transverse impedance

were performed using an initial Gaussian bunch distribution in the six-dimensional phase space. This is a good approximation for the bunches used in the experimental studies of 2018.

At the location of the CC, the change of the angle, y' , of each particle within the bunch as a result of phase and amplitude CC RF noise is modeled according to Eqs. (3.7) and (3.8) for amplitude and phase noise respectively. The simulations performed for a total noise power of $\sigma_{\Delta A}^2 = 7.3 \times 10^{-6}$ and $\sigma_{\Delta\phi}^2 = 7.3 \times 10^{-6} \text{ rad}^2$ except if it is stated otherwise. This noise level, which corresponds to power spectral density at the betatron frequency of $1.68 \cdot 10^{-10} \text{ rad}^2/\text{Hz}$ or $1/\text{Hz}$ for phase and amplitude noise respectively is much stronger than the ones of the actual CC RF system and was chosen such as it results in a reasonable growth in the simulation time of 10^5 turns (it corresponds to ~ 2.5 seconds in the SPS). The higher noise level in the simulation means that the emittance growth over 10^5 turns is comparable to the emittance growth observed over the full measurement time in the SPS experiments. This approach is valid due to the linear growth of emittance with time and the linear scaling with the noise level [63]. The parameters used for the implementation of the CC RF noise kick in the simulations are shown in Table 6.2.

Table 6.2: PyHEADTAIL simulation parameters used for the implementation of the CC RF noise kicks for the emittance growth studies. This table is complementary of Table 6.1.

Parameter	Value
Horizontal / vertical beta function, $\beta_{x,\text{CC}}/\beta_{y,\text{CC}}$	30.31 m / 73.82 m
CC frequency, f_{CC}	400.78 MHz
Total amplitude and phase noise power, $\sigma_{\Delta A}^2 / \sigma_{\Delta\phi}^2$	$7.3 \times 10^{-6} / 7.3 \times 10^{-6} \text{ rad}^2$

Last, the emittance growth simulation studies were performed for non-zero linear chromaticity and non-zero detuning with the transverse amplitude. Both effects were introduced as changes in the phase advance of the individual particles according to Eq. (2.64). The value of the linear chromaticity, $Q'_{x,y} = 0.5$ was used for most of the studies according to the experimental conditions of 2018. Higher-order chromaticities are negligible. The values of the detuning coefficients will be given in the following sections.

6.3. Suppression of noise induced emittance growth by the beam coupling impedance

In the following sections, the emittance growth rates will be expressed in nm/s due to the simulation time scale and will be referred to as the growth of the normalised emittance values to be in agreement with the analysis of the measured data in Chapter 4.

6.3 Suppression of noise induced emittance growth by the beam coupling impedance

A first set of emittance growth simulations were performed for the beam and machine conditions of the 2018 experiments. The parameters are listed in Tables 6.1 and 6.2 and the detailed procedure is described in Section 6.2.

As mentioned in Chapter 4 the Landau octupoles were switched off during the 2018 CC experiment. Nevertheless, multipole components in the dipole magnets of the SPS, as well as the chromatic sextupoles create some non-linearities [71, 72]. The rms tune spread in the vertical plane from these non-linearities is computed at $\sim 2\text{-}3 \times 10^{-5}$. In order to reproduce this tune spread value in the simulations, the vertical amplitude detuning coefficient was set at $\alpha_{yy} = 2000/\text{m}$. For simplicity, the horizontal and cross-term coefficient were both set zero, $\alpha_{xx} = \alpha_{yx} = 0$.

The simulations were performed with CC phase noise as it was the dominant type of noise in the 2018 experiment, with a power spectral density of $1.68 \times 10^{-10} \text{ rad}^2/\text{Hz}$ which corresponds to a total noise power of $\sigma_{\Delta\phi} = 7.3 \times 10^{-6} \text{ rad}^2$. For this noise power a growth rate of about 25 nm/s is expected (exciting the first betatron sidebands at $\pm 7.8 \text{ kHz}$, see further discussion in Section 3.2.2).

The geometric emittance value was computed every 100 turns (for computational efficiency) using the statistical definition which can be found in Eq. (2.34). The emittance growth rate was computed by performing a linear fit to the normalised emittance values over the simulation turns ($N_{\text{turns}} = 10^5$). Twenty simulation runs were conducted, to reduce the uncertainty of the results. The initial bunch distribution and the sequence of the uncorrelated noise kicks were regenerated

6. Simulation studies: Emittance growth suppression mechanism from the beam transverse impedance

randomly for every run. The mean and the standard deviation (including the uncertainty on the slope of the fit) were computed over all the simulation runs.

The simulations were performed with and without wakefield kicks, to study the impact of machine impedance on the emittance growth induced by CC RF phase noise. The results are illustrated in Fig. 6.5. The average emittance evolution (over the 20 different runs) in the absence of impedance effects is shown with dark blue color while in the presence of impedance effects with the dark orange color. The shaded areas with light blue and light orange colors show the standard deviation over the 20 runs. The simulated emittance growth without the wakefields is in very good agreement with the theoretically expected value of ~ 25 nm/s (black dashed line). However, once the impedance model is included the phase noise-induced emittance growth is strongly suppressed.

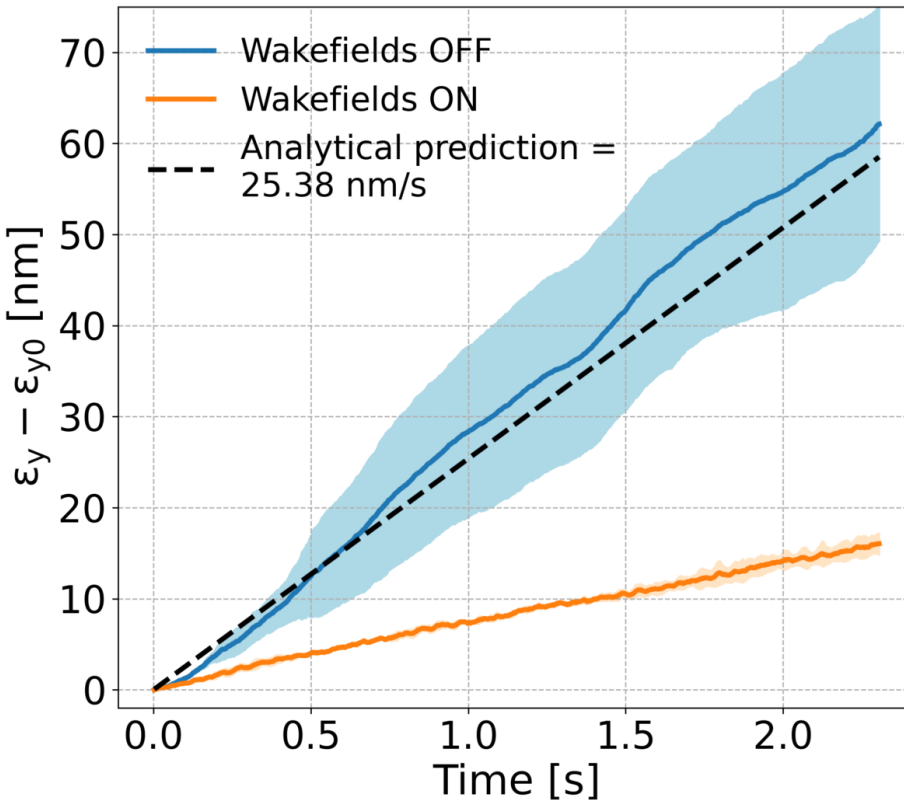


Figure 6.5: Transverse emittance growth driven by CC RF phase noise without (blue) and with (orange) the impedance effects for the beam and machine conditions of the CC tests in SPS during 2018.

It is worth noting that the large spread in the emittance growth rates over the

6.4. Characterisation of the emittance growth suppression by the impedance

different simulation runs in the absence of wakefields is a result of the very small tune spread. The wakefields introduce some additional tune spread, on top of the one from the vertical tune shift with amplitude, which reduces the uncertainty of the simulated growth rates.

To conclude, PyHEADTAIL simulations showed for the first time that the transverse beam impedance (which is not included in the theory [63]) has a significant impact on the emittance growth driven by CC RF noise. The effect of the suppression of noise-induced emittance growth from the impedance has not been observed before. To characterise this effect and to be able to understand the mechanism behind it, a series of exploratory studies were conducted and are discussed in the following section.

6.4 Characterisation of the emittance growth suppression by the impedance

In this section, we discuss the results of the exploratory simulation studies which investigate the suppression of the CC RF noise-induced emittance growth by the transverse beam coupling impedance. The goal is to characterise the effect and understand the mechanism behind it.

The simulations were conducted following the same pattern as the case discussed in the previous section. Nevertheless, the main relevant parameters for each case will also be listed in the corresponding section.

6.4.1 Sensitivity of CC RF phase noise induced emittance growth to amplitude-dependent tune shift

As the machine non-linearities were not explicitly characterised during the experiment, the dependence on the octupole-like amplitude dependent tune spread was studied. Instead of using an actual octupolar (non-linear) element which would cause excitation of a resonance³, the amplitude dependent tune shift

³In the real SPS machine the Landau octupoles are installed in families of focusing and defocusing in order to avoid the excitation of resonances.

6. Simulation studies: Emittance growth suppression mechanism from the beam transverse impedance

was modelled as a change to the phase advance of the particles depending on their individual betatron action as discussed in Eq. (2.64). More specifically, the dependence on the detuning coefficient in the vertical plane, α_{yy} , was studied. For the studies presented here and in the following sections of this chapter, the horizontal detuning coefficient and the cross-term were left at zero for simplicity, i.e. $\alpha_{xx} = \alpha_{xy} = 0$. The sensitivity on the cross-term is discussed in the Chapter 7.

The simulations were performed with and without the SPS impedance model to study its impact on the emittance growth induced by CC noise. Figure 6.5 shows the dependence of the average growth rates (over the 20 different runs) on the amplitude detuning coefficient, α_{yy} . The error bars indicate the standard deviation over the 20 runs. The secondary horizontal axis shows the resulting rms tune spread computed using Eq. (C.12). Incoherent tune shift from sources other than the detuning with transverse amplitude are not included. In particular PyHEADTAIL simulations (see Fig. 6.10) for a range of linear chromaticity values show that there is no big impact on the overall behavior even in the presence of impedance effects and of the head-tail mode 0. The incoherent tune shift from the impedance is considered negligible.

It can be seen that when the wakefield kicks are not applied to the beam the emittance growth rate agrees very well with the value predicted by Eq. (4.6) and (within the reproducibility of the simulation) is independent of the detuning coefficient value. Furthermore, even for $\alpha_{yy} = 0$ some emittance growth is observed. The origin for this growth is not well understood yet since in the absence of tune spread no emittance growth is expected (see Section 3.1). A possible explanation for this could be that the orbit shift from the CC noise kick over the bunch length is not linear which might result to some phase mixing of the particles within the bunch causing decoherence of the betatron oscillations and hence emittance growth. Regarding, the fact that the observed emittance growth appears slower than expected from the Mastoridis–Baudrenghien model, a possible explanation could be that the tune spread (introduced by the non-linearities of the CC kicks) is very small and results in a slow decoherence (see Eq. (5.1)) meaning

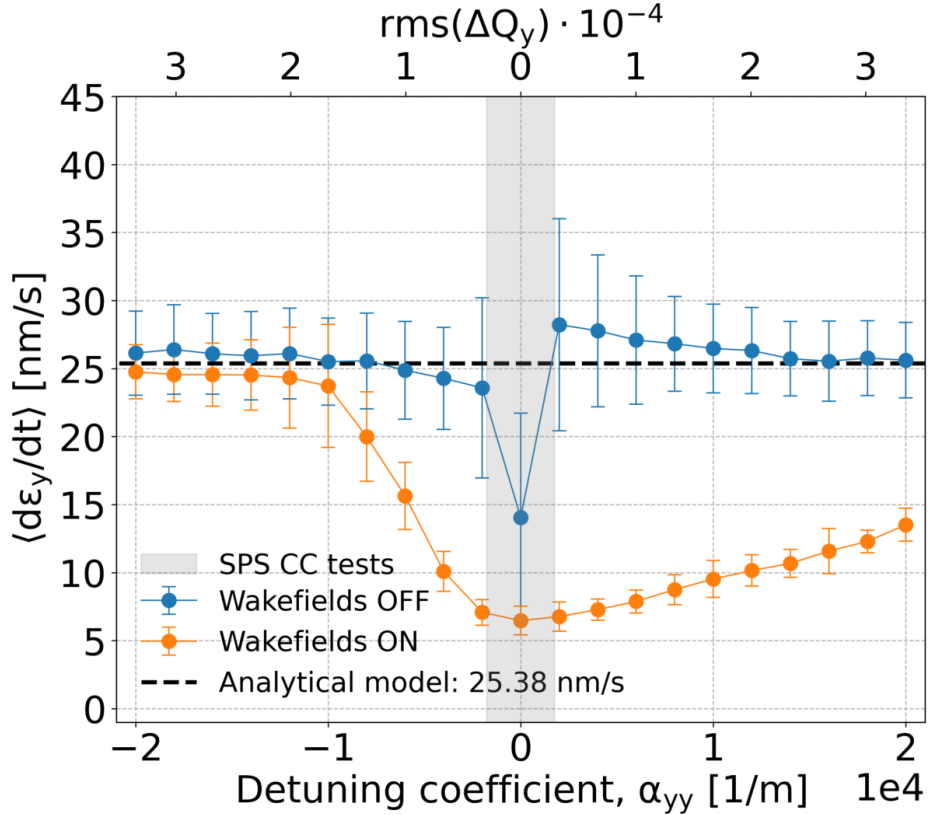


Figure 6.6: Transverse emittance growth driven by CC RF phase noise (as a function of detuning coefficient), without (blue) and with (orange) impedance effects.

that the 2.5 s of simulation time are not sufficient to obtain valid results.

Figure 6.5 shows a clear suppression of the transverse emittance growth when the wakefield kicks are included, depending on the tune spread and is asymmetric between positive and negative detuning coefficients. Over a realistic range of tune spread values (estimated with MAD-X [50] including the non-linearities of SPS [71, 72] and $Q'_{x,y} = 0.5$, and shown by the grey shaded area in Fig. 6.5) the suppression reaches up to a factor 4-5. This suppression is very close to that observed in the experiments and suggests that the impedance effects might explain the discrepancy between the measured and theoretically estimated emittance growth rates.

6.4.2 Amplitude noise

The simulations discussed here were performed with and without the SPS impedance model in the presence of CC RF amplitude noise, with total power of

6. Simulation studies: Emittance growth suppression mechanism from the beam transverse impedance

$\sigma_{\Delta A}^2 = 7.3 \times 10^{-6}$ which corresponds to a power spectral density of $1.68 \times 10^{-10} \text{ /Hz}$. The total power of the amplitude noise equals the one of the phase noise used in the previous section. The results are shown in Fig. 6.7.

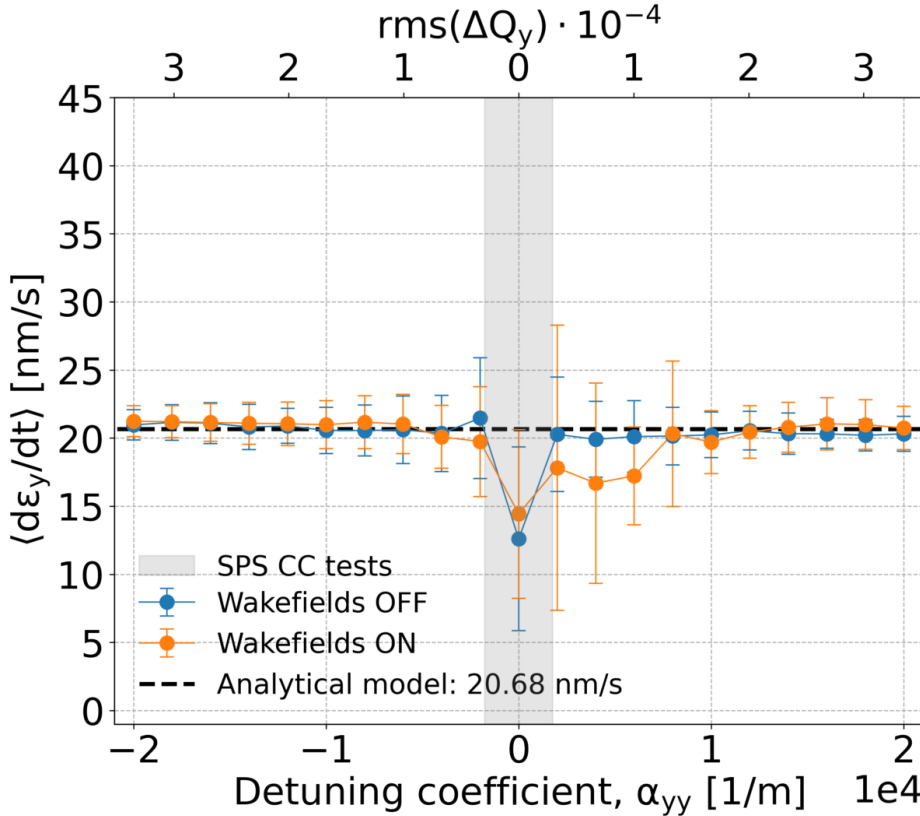


Figure 6.7: Transverse emittance growth driven by CC RF amplitude noise (as a function of detuning coefficient), without (blue) and with (orange) impedance effects.

It can be seen that the emittance growth rate agrees very well with the value predicted by Eq. (4.5) and (within the reproducibility of the simulation) is independent of the tune spread value both when the wakefields are included and when they are not. In other words, the simulations demonstrate that the emittance growth driven by CC RF amplitude noise is not suppressed by impedance induced effects.

The difference in the PyHEADTAIL simulations including the SPS impedance model between the CC RF phase and amplitude noise could be explained by the fact that the phase noise (which is similar to a dipolar noise kick but with a high order distortion) is associated with the head-tail mode 0, while the amplitude noise is associated with the head-tail mode 1. The hypothesis, that the emittance growth suppression from

6.4. Characterisation of the emittance growth suppression by the impedance

impedance induced effects is related to head-tail mode 0 will be studied in details in the following sections and will also be tested experimentally in 2022.

6.4.3 CC RF noise at 200 MHz

In the HL-LHC the main RF system and the CCs will operate at the same frequency ($f_{CC} = f_{RF-LHC} = 400$ MHz). To replicate this scenario in the SPS, the sensitivity on the amplitude-dependent tune spread was simulated assuming a CC frequency of 200 MHz, i.e. $f_{CC} = 200$ MHz, which equals the frequency of the main accelerating RF system of the SPS (see Table 4.2).

The simulations were performed with and without wakefield kicks, in the presence of both amplitude and phase noise with power spectral density of 1.21×10^{-10} rad²/Hz ($\sigma_{\Delta A}^2 = 7.3 \times 10^{-6} \times 0.72$) and 3.06×10^{-10} /Hz ($\sigma_{\Delta \phi}^2 = 7.3 \times 10^{-6} \times 1.82$) respectively. The noise strength was scaled so that it results in ~ 25 nm/s to be comparable with the initial studies presented in Section 6.3.

The PyHEADTAIL simulation results are summarised in Fig. 6.8. The first plot (left) displays the amplitude detuning dependent emittance growth in the presence of amplitude noise while the second plot (right) shows the emittance growth in the presence of phase noise.

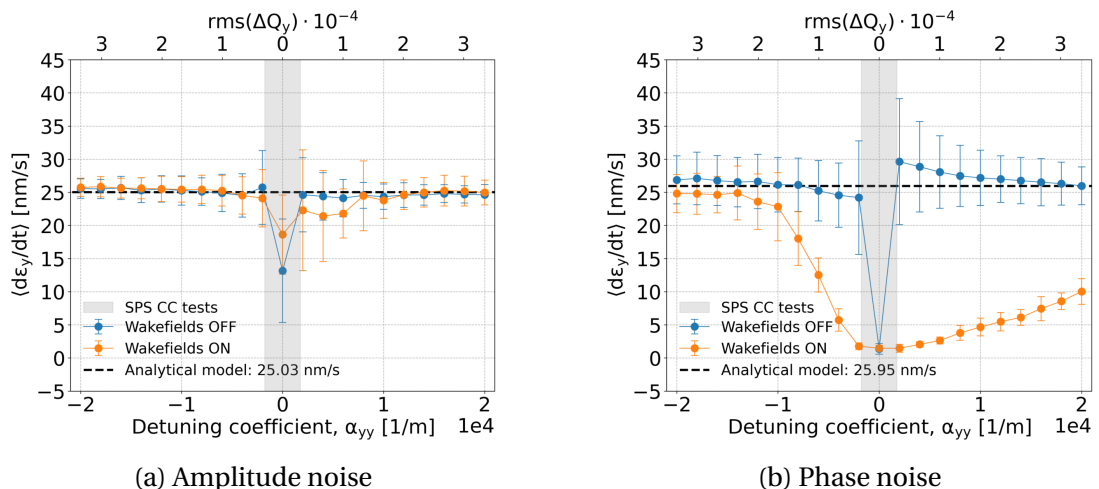


Figure 6.8: Transverse emittance growth driven by CC RF noise, assuming a CC frequency of 200 MHz, without (blue) and with (orange) the impedance effects as a function of tune spread.

6. Simulation studies: Emittance growth suppression mechanism from the beam transverse impedance

Comparing Fig. 6.8 (left) and Fig. 6.7 it becomes evident that the behavior of the amplitude noise induced emittance growth is consistent for noise at 200 and 400 MHz (both with and without wakefields). In neither case is there any significant suppression of the emittance growth from amplitude detuning while the obtained growth rates agree very well with the theoretical predictions from Eq. (3.11).

Comparing Fig. 6.8 (right) and Fig. 6.5 it can be seen that emittance growth driven by CC phase noise in the absence of wakefield kicks (blue) is in excellent agreement for noise at 200 and 400 MHz except for the case with zero amplitude detuning, $\alpha_{yy} = 0$. It is already discussed, that for $f_{CC}=400$ MHz the observed emittance growth of ~ 15 nm/s is a result of the geometric distortion of the beam caused by the CC kick. This geometric distortion is reduced for the lower CC frequency resulting in almost zero emittance growth.

Repeating the last comparison but in the presence of wakefield kicks (orange) it can be seen that emittance growth driven by CC phase noise is in good agreement with the results for noise at 200 and 400 MHz. Suppression of the emittance growth, which depends on the amplitude detuning, is observed in both cases. However, in the case of phase noise at 200 MHz the suppression factor reaches up to a factor of 10 instead of just 4-5 in the case of noise at 400 MHz. This observation agrees with the hypothesis that the emittance growth suppression by impedance induced effects is related to head-tail mode 0. In particular, in the case where the CC has the same frequency as the main RF system the CC kick is closer to a pure dipole excitation hence the enhanced effect of emittance growth suppression.

6.4.4 Pure dipolar noise

To validate that the effect of the suppression of the noise-driven emittance growth from the beam coupling impedance is associated with the dipolar motion (head-tail mode 0), the same simulations as in the previous section were conducted but instead of the longitudinally dependent noise kicks a pure dipolar noise kick was applied on the beam. The dipolar noise kick was modeled by the transformation of Eq. (3.1) for $\sigma_\theta^2 = 7.3 \times 10^{-6} \times 2$ which corresponds to a power

6.4. Characterisation of the emittance growth suppression by the impedance

spectral density of $3.36 \text{ rad}^2/\text{Hz}$. The noise strength was scaled so that it results in $\sim 25 \text{ nm/s}$ to be comparable with the initial studies presented in Section 6.3.

Figure 6.9 shows the noise-induced vertical emittance growth as a function of amplitude-dependent tune spread with and without the presence of wakefield kicks. One can see that in the absence of wakefields (blue) the behavior of the dependence of the growth rates on the amplitude detuning matches the one obtained from CC RF phase noise kicks (see Figs. 6.7 and 6.8 (right)). The models that predict the emittance growth are not valid for zero tune spread. The PyHEADTAIL simulations for $\alpha_{yy} = 0$ showed zero emittance growth which is explained by the fact that in the absence of tune spread there is no decoherence of the betatron oscillations and hence no emittance growth.

In the presence of wakefield kicks (orange) strong suppression of emittance growth is observed. The suppression reaches up to a factor of 10 for the small values of amplitude detuning (within the gray area which indicates the tune spread present in the SPS during the 2018 CC experiments). The fact that the suppression of the emittance growth intensifies in the presence of dipolar noise, is a way to associate the phenomenon with the head-tail mode 0.

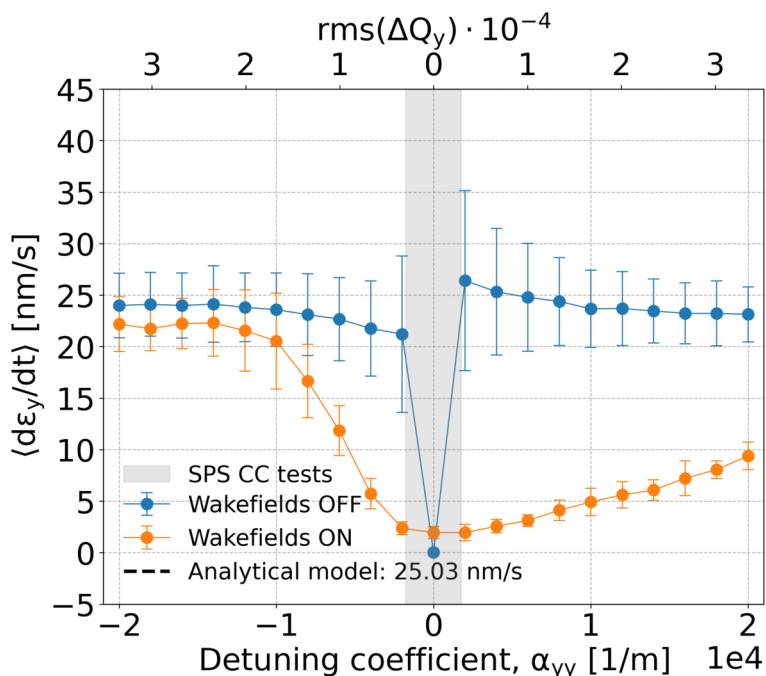


Figure 6.9: Transverse emittance growth driven by a pure dipolar noise kick without (blue) and with (orange) the impedance effects as a function of tune spread.

6.4.5 Sensitivity to linear chromaticity

The PyHEADTAIL simulations discussed up to now cover the case for linear chromaticity $Q'_{x,y} = 0.5$, which is believed to be the case for the emittance growth measurements in SPS in 2018. To understand the effect of the linear chromaticity on the suppression of the noise-induced emittance growth from the SPS impedance the same simulations as in Section 6.3 were repeated for a range of different chromaticities. In particular, five different values were studied: $Q'_{x,y} = 0.0, 0.5, 1.0, 2.5, 5.0$. The study is limited to small positive chromaticity values following past experimental chromaticity scans for emittance growth studies, $Q'_{x,y} < 10.0$ [70, 68]. An additional reason for not extending the study to the negative chromaticity values is that they would lead to head-tail mode 0 instability induced by the impedance, since the SPS experiments were performed above transition [44].

The simulations for this subsection were performed using the setup and the parameters of Section 6.3 (i.e. for a crab cavity frequency of 400 MHz with phase noise). The results of the scan in $Q'_{x,y}$ are displayed in Fig. 6.10, where each subfigure shows the results for one chromaticity value, increasing in value from top left to bottom right.

In the absence of impedance effects (blue), the CC RF noise-induced emittance growth rates appear independent of both the amplitude detuning coefficient and the value of linear chromaticity. This is in agreement with the predictions of the Mastoridis–Baudrenghien model for the white noise spectrum.

In the presence of impedance effects (orange), suppression of the emittance growth is observed for all the studied values of linear chromaticity. An examination of the results shows that the impact of the linear chromaticity on the maximum suppression, which is observed for $\alpha_{yy} = 0$, is negligible. Yet, the simulated emittance growth rates exhibit a slightly different dependence on the vertical detuning coefficient, α_{yy} , for each of the five chromaticity values. This difference appears mainly for the negative values of α_{yy} . In particular, it appears that for increasing linear chromaticity, the provided tune spread from amplitude detuning

6.4. Characterisation of the emittance growth suppression by the impedance



Figure 6.10: Transverse emittance growth driven by CC RF phase noise, assuming a CC frequency of 400 MHz, without (blue) and with (orange) the impedance effects as a function of tune spread is shown for five different values of linear chromaticity increasing from top left to bottom right.

6. Simulation studies: Emittance growth suppression mechanism from the beam transverse impedance

is becoming less sufficient for recovering the emittance growth rates expected from the Mastoridis–Baudrenghien model. Nevertheless, for the regime of the realistic SPS tune spread (grey stripe) the dependence of the suppression factor on the chromaticity appears negligible. The fact that there are no exact chromaticity measurements available from the SPS CC tests of 2018 is thus not an issue.

The weak dependence of the emittance growth rates (for different values of the detuning coefficient) on the chromaticity is not surprising as the damping or growth time of head-tail mode 0, is chromaticity-dependent. Nevertheless, overall, it can be concluded that there is no strong sensitivity of the suppression induced by the beam coupling impedance to the linear chromaticity.

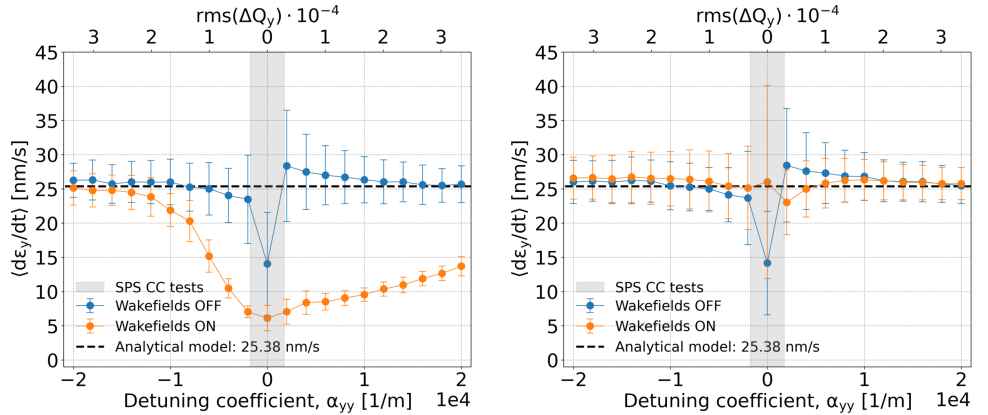
6.4.6 Disentangling quadrupolar and dipolar impedance contributions

The simulation described in Section 6.3 is repeated taking into account the quadrupolar (detuning) and dipolar (driving) terms of the wakefields separately, in order to investigate their individual contribution to the phenomenon of emittance growth suppression. This is easily achievable since in the SPS impedance model the quadrupolar and dipolar terms are provided separately (see Section 6.1). The linear chromaticity for this study was set to $Q'_{x,y}=0.5$ units.

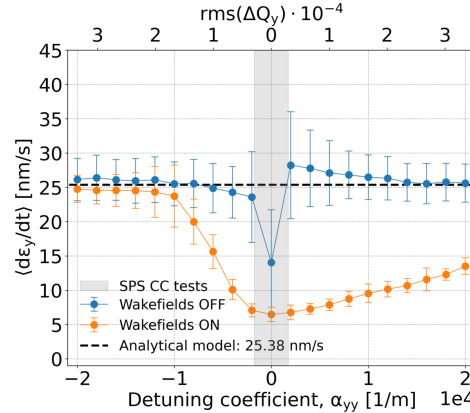
The results are summarised in Fig. 6.11. The upper plots illustrate the individual effect of the dipolar (left) and quadrupolar (right) terms of the SPS wakefields on the noise-induced emittance growth while the bottom plot shows the combined effect of the two terms. For each study case, the simulation results without including the impedance effects are also shown (blue) for reference. As usual, without including the impedance, the simulated growth rates appear independent of the vertical detuning coefficient and are in very good agreement (within the errorbars) with the theoretical predictions of the Mastoridis–Baudrenghien model which does not take into account impedance effects.

Looking at the emittance growth rates obtained in the presence of wakefield kicks (orange), it becomes evident that the dipolar contribution (Fig. 6.11a) results in a

6.4. Characterisation of the emittance growth suppression by the impedance



(a) Only dipolar (driving) impedance contribution. (b) Only quadrupolar (detuning) impedance contribution.



(c) Dipolar (driving) and quadrupolar (detuning) impedance contribution.

Figure 6.11: Transverse emittance growth driven by CC RF phase noise, for a CC frequency of 400 MHz, without (blue) and with (orange) the impedance effects as a function of tune spread. *Top:* Simulation results with only the dipolar (left) and quadrupolar (right) impedance contribution. *Bottom:* Simulation results with the dipolar and quadrupolar impedance contributions combined.

6. Simulation studies: Emittance growth suppression mechanism from the beam transverse impedance

strong suppression of the emittance growth which has the same dependence on the tune spread with the simulations that include both the dipolar and quadrupolar terms. In contrast, the emittance growth remains unaffected when only the quadrupolar contribution is taken into account (Fig. 6.11b). Thus, it is evident, that the effect of the suppression is a result of the dipolar term of the impedance.

The significance of the dipolar term is that it leads to coherent tune shift (see Section 2.3.1). Therefore, these simulation results show that the observed suppression of the noise-induced emittance growth is associated with the coherent tune shift from the dipolar impedance contribution. This suggestion and consequently the mechanism behind the observed suppression will be further explored in the next section.

6.5 Suppression mechanism

6.5.1 Similar effects studied in the past and motivation

As concluded in Section 6.4, the effect of the emittance growth suppression from the beam coupling impedance is associated with the coherent tune shift, caused by the dipolar impedance term. This triggered the idea, that overlap between the coherent tune and the incoherent betatron tune spectrum could explain the observed effect of the suppression.

The motivation for this idea came from past theoretical studies [101, 102], which showed that in hadron colliders the efficiency of the feedback system at suppressing the emittance growth depends on the overlap between the frequency of the coherent mode and the incoherent tune spectrum. In particular, it was observed that the decoherence of dipole oscillations is drastically suppressed if the coherent tune of the beam is outside of the incoherent tune spectrum. This theory has been verified by numerical simulations and experimental studies for LHC [103, 104, 105]. For reference, additional simulation studies for the LHC case which deal with the above-mentioned phenomenon of decoherence suppression can be found in [106, 107].

Move here the part of chapter 7.

However, in the previous studies, the frequency of the coherent modes was shifted by the beam-beam effect⁴ and not by the beam coupling impedance. Adjusting the theoretical approach of [101] for the impedance-induced tune shift is not straightforward ([Do i need to comment further on it?](#)). To this end, the strategy that was followed to further explore the mechanism of the emittance growth suppression by the transverse impedance was tracking simulations with PyHEADTAIL. These simulation studies will be presented and discussed in the following subsections.

6.5.2 Intensity scans

To test the hypothesis that the observed suppression of the emittance growth is a result of the separation of the coherent mode from the incoherent spectrum the emittance growth in the presence of CC RF phase noise and impedance is studied as a function of the bunch intensity. As discussed in the Introduction (Section 2.3.1) and illustrated in Section 6.1.1 the shift of the coherent tune increases (in absolute value) linearly for increasing intensity. Therefore, when simulating the emittance growth in the presence of wakefields over a range of different intensities a cut-off effect should be expected at the point where the frequency of the coherent mode is shifted outside of the incoherent spectrum.

The simulation was performed for the beam and machine conditions of the 2018 CC experiments in the SPS as described in Section 6.3. The CC RF phase noise kick that was acting on the beam had a power spectral density of $1.68 \text{ rad}^2/\text{Hz}$, which results in an emittance growth of about 25 nm/s .

In Section 6.3, it was shown that in order to reproduce the realistic rms tune spread ($\sim 2 - 3 \times 10^{-4}$) that was present in SPS during the 2018 experiments (from intrinsic non-linearities), the vertical amplitude detuning coefficient should be $|\alpha_{yy}|=2000/\text{m}$, which results however in a comparably small tune spread and thus results in a strong suppression of the emittance growth. Therefore, the intensity

⁴Beam-beam effects, are the ones induced by the perturbation of the two beams in a collider as they cross each other. Further details on these effects and the beam-beam interaction can be found in [108] but their analysis is out of the scope of this thesis.

6. Simulation studies: Emittance growth suppression mechanism from the beam transverse impedance

scan was performed for $\alpha_{yy}=6000/\text{m}$ which reduces the emittance growth suppression, while remaining close to the realistic machine conditions of 2018.



Figure 6.12: PyHEADTAIL simulations illustrating the effect of the beam intensity on the transverse emittance growth driven by CC RF phase noise in the presence of impedance effects. The blue vertical line shows the intensity value during the SPS CC experiments in 2018.

The study was conducted over a range of bunch intensities from 0 to 5×10^{10} protons per bunch. This range was chosen to be in the vicinity of the CC experiments in SPS in 2018, where the intensity was 3×10^{10} protons per bunch.

The results of the intensity scan are summarised in Fig. 6.12, where the simulated emittance growth rate is plotted as a function of intensity. The intensity value during the SPS CC experiment of 2018 is given by the blue vertical line for reference. For small intensity values, $<\sim 0.7 \times 10^{10}$ protons per bunch, the emittance growth rates appear to be little affected by any change in intensity, and are close to the theoretically expected value of 25 nm/s. However, for intensity slightly larger than $\sim 0.7 \times 10^{10}$ protons per bunch there is a sudden drop in the obtained emittance growth rates. After that point, the emittance growth rates seem to decrease with increasing intensity. This dependence seems to saturate for larger intensity values, $>\sim 2.5 \times 10^{10}$ protons per bunch. It becomes apparent that the

intensity value of the SPS CC tests (blue line) is well inside the regime of strong suppression.

The important observation of this study is that the dependence of the suppression of the emittance growth on the intensity is consistent with a suppression mechanism based on the overlap between the coherent betatron tune and the incoherent tune spread distribution. To further validate this hypothesis, simulations were performed aiming to examine the frequency spectrum of the bunch, which should reveal more information on the overlap of the coherent mode frequency and the incoherent spectrum. These simulations will be discussed in the next subsection.

6.5.3 Spectral analysis of the bunch centroid motion

Here, the incoherent spectrum of the bunch is investigated for different intensities in an attempt to visualise and hence confirm that the mechanism for the suppression of the emittance growth is related to the separation of the coherent mode from the incoherent spectrum. The incoherent spectrum can be obtained from Fourier analysis of the turn-by-turn centroid motion. This method can be also found in the bibliography as Schottky noise method [109] and is often used for beam diagnostics as it can reveal information on important parameters such as tunes and chromaticity, and of course the incoherent tune spectrum.

For the spectral analysis studies presented here, the simulations presented previously (Section 6.5.2) were repeated but without applying any noise kick on the bunch to minimise the external perturbations and obtain a clear frequency signal. This approach is justified since the objective of the study is to see how the coherent tune is located compared to the incoherent betatron spectrum. The six-dimensional Gaussian distribution was now generated with an initial vertical offset of 0.2 times the rms vertical beam size. The reason behind this is that due to the offset the beam will undergo betatron oscillations with a sufficiently large amplitude to facilitate the Fourier analysis. Furthermore, this type of simulation requires longer tracking than the emittance growth studies, 10^6 turns instead of 10^5 , for better resolution in the frequency domain. Finally, 5×10^4 macroparticles

6. Simulation studies: Emittance growth suppression mechanism from the beam transverse impedance

were sufficient⁵ for this type of simulation which reduced significantly the computational time of the simulation.

The spectra that will be discussed below were obtained by applying the NAFF algorithm to the turn-by-turn data as described in Section 6.1.1. The amplitude of the spectral components is expressed as power spectral density in units of rad^2/Q_y as it is preferred over the amplitude of the spectral components of the Fourier transform which is in arbitrary units. The power spectral density of the motion of the centroid is obtained from the above-mentioned Fourier transform using Eq. (B.11).

The results are displayed in Fig. 6.13 which shows the vertical spectrum of the centroid (coherent) oscillation of the bunch for different intensity values, selected from the range studied in the previous Subsection 6.5.2, choosing cases for which the separation of the coherent tune from the incoherent spectrum is clearly visible. Each subplot shows the power spectral density of the motion of the centroid as a function of the frequency in tune units for a given intensity value, which increases from the top left to the bottom right. The frequency of the coherent mode is shown with the vertical magenta line and it corresponds to the frequency with the highest amplitude.

Comparing Fig. 6.13 with Fig. 6.12 it becomes evident that:

- The two upper spectra, where the coherent mode lies inside the incoherent spectrum, reside in the regime of no emittance growth suppression.
- The two middle spectra, where the coherent mode emerges from the incoherent spectrum, reside in the regime where the emittance growth suppression increases for higher intensity values.
- The two bottom spectra, where the coherent mode is well separated from the incoherent spectra, reside in the regime where the dependence on the intensity saturates.

⁵Following similar studies in [110] and exploratory studies confirmed that the number of macroparticles used does not affect the quality of the results.

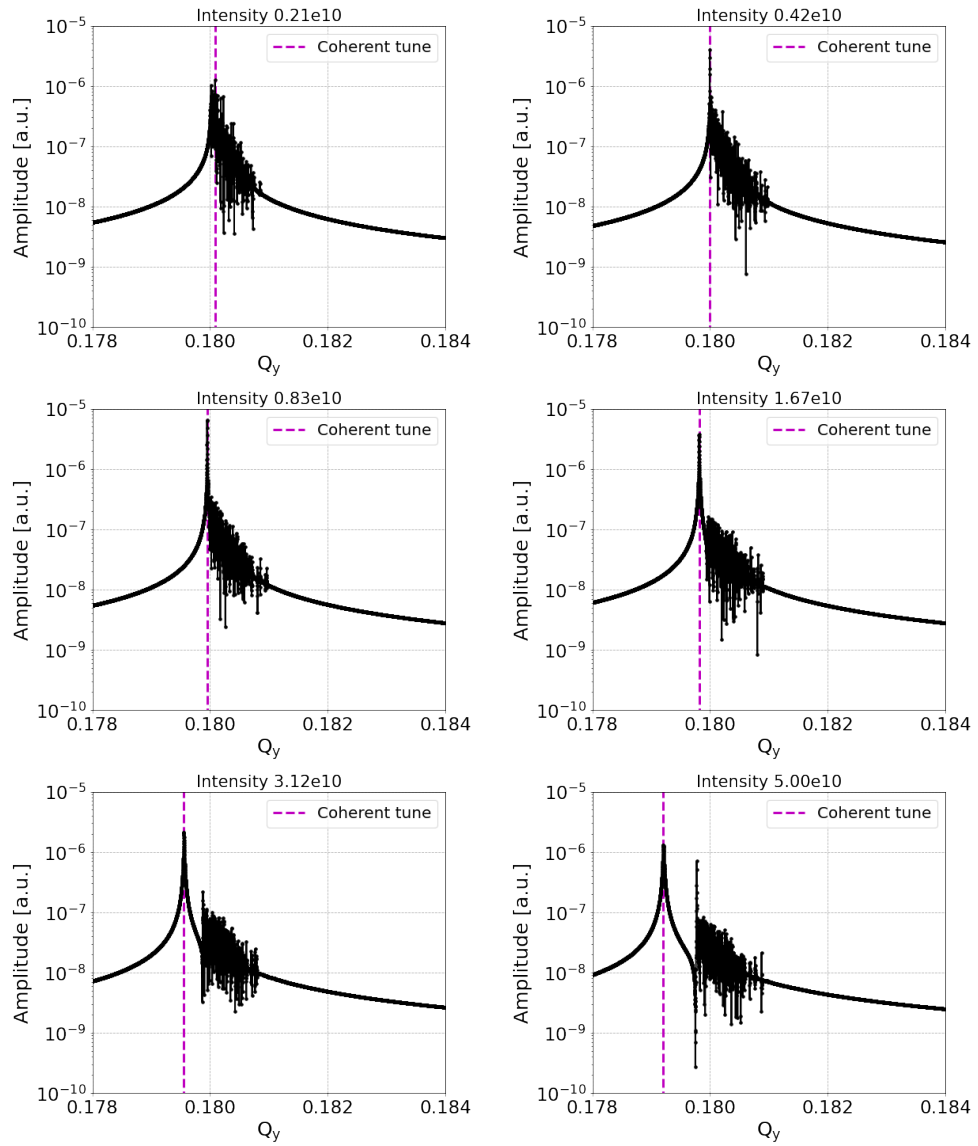


Figure 6.13: Power spectral density of the vertical bunch centroid motion on a logarithmic scale in the presence of the SPS transverse impedance model, calculated over 10^6 turns with 5×10^4 macroparticles for different values of intensity increasing from top left to bottom right.

6. Simulation studies: Emittance growth suppression mechanism from the beam transverse impedance

The above observation, confirms that the transverse impedance separates the coherent tune from the incoherent spectrum and this is related to the effective suppression of the Crab Cavity phase noise induced emittance growth.

According to the studies of Y. Alexahin [101] (which were performed in the context of the beam-beam modes) the separation of the coherent mode from the incoherent spectrum results in a suppression of the decoherence of the dipole oscillations and thus of the dipole and/or phase-noise-induced emittance growth. What happens is that only part of the energy from the noise kicks is absorbed by the incoherent spectrum and drives incoherent motion leading to irreversible emittance growth. The rest of the energy is absorbed by the coherent mode, which is damped⁶ by the impedance (for the experimental conditions of small positive chromaticity) without leading to emittance growth.

A similar effect seems to be happening in the case studied here, where the impedance induced tune shift pushing the coherent tune of the bunch outside of the incoherent spectrum results in the suppression of decoherence and thus of the CC noise induced emittance growth. A recent theoretical description of this phenomenon, triggered by the studies presented in this thesis was developed by X. Buffat [111, 112].

6.5.4 Dependence on bunch length

In this section, the emittance growth in the presence of CC RF phase noise and impedance is studied as a function of the bunch length. The goals of this study are: first, to complete the set of parametric studies presented already in this chapter; and second, to identify possible limitations on observing the effect of the emittance growth suppression introduced by the bunch length. The latter is very important for the second experimental campaign with CCs in the SPS that took place in early 2022 and that will be discussed in further detail in the following chapter.

This parametric study was conducted for the experimental beam and machine

⁶The damping rate of the coherent tune (mode 0) for the experimental parameters of 2018, was estimated to be 3.6 1/turns using Eq. (2.62)

conditions of 2018 as shown in Tables 6.1 and 6.2, and described in Section 6.3. The CC RF phase noise kick that was acting on the beam had a power spectral density of $1.68 \text{ rad}^2/\text{Hz}$, which results in an emittance growth rate of about 25 nm/s . The vertical amplitude detuning coefficient was set to $\alpha_{yy}=2000/\text{m}$ in order to reproduce the realistic rms tune spread ($\sim 2 - 3 \times 10^{-5}$) that was estimated for SPS during the 2018 experiments (from intrinsic non-linearities). The study was performed for a range of bunch lengths ($4\sigma_t$) from 0 to 4 ns. In practice no simulations were conducted for zero bunch length as it is not a realistic value.

Simulations are performed with and without wakefields. The PyHEADTAIL simulation results are summarised in Fig. 6.14, together with the predictions of the Mastoridis–Baudrenghien model (which does not include the effects of machine impedance).

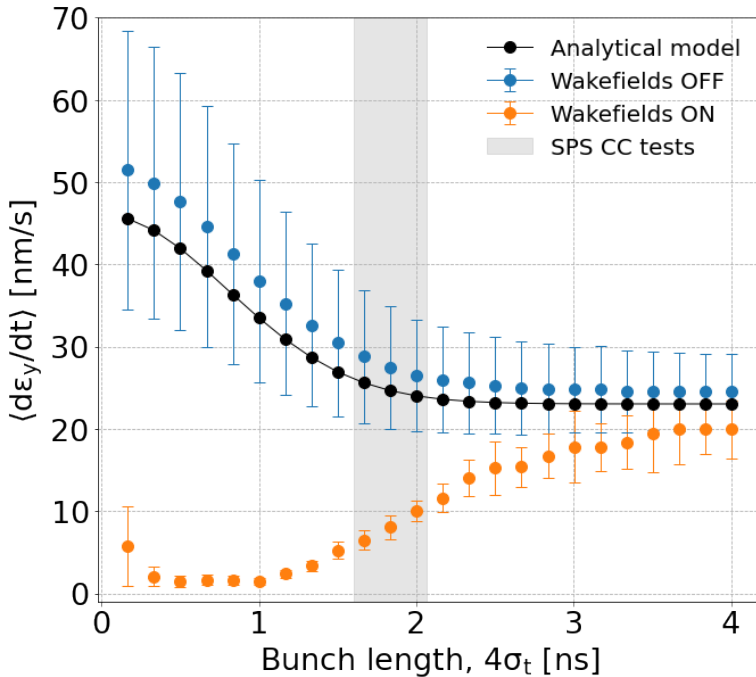


Figure 6.14: PyHEADTAIL simulations illustrating the impact of the bunch length on the transverse emittance growth driven by CC RF phase noise in the absence (blue) and in the presence (orange) of impedance effects. The analytically predicted emittance growth rates (not including impedance effects) are also shown (black). The regime of the realistic bunch length values during the SPS CC tests of 2018 is depicted with the grey stripe.

Figure 6.14 illustrates, as expected, that the simulation results without the wakefields (blue) are in very good agreement with the theoretical predictions

6. Simulation studies: Emittance growth suppression mechanism from the beam transverse impedance

(black model), within the error bars. However, there is some systematic difference, of a few microns per hour, between the mean emittance growth obtained from the simulations and the theory, which shrinks for longer bunches. The reason for this is not understood but it was not investigated further since for the regime of realistic bunch lengths values for the SPS experiments (grey stripe) the difference is insignificant and it does not affect the conclusions drawn from these studies.

In the presence of wakefields (orange) there is a clear dependence of the suppression of emittance growth on the bunch length. In particular for bunch length values smaller than 1 ns the suppression appears very strong, and is roughly independent of the precise value of the bunch length. For longer bunches, up to about 3.5 ns ($4\sigma_t$) the suppression factor appears to decrease with the bunch length. For bunches longer than 3.5 ns ($4\sigma_t$) the dependence of the emittance growth on the bunch length seems to saturate, and the emittance growth rates are also in agreement with the theoretical model which does not include the contribution from the wakefields. The suppression of the emittance growth is reduced for larger bunch lengths: this is consistent with the mechanism discussed in Sections 6.5.2 and 6.5.3, since the separation of the coherent tune from the incoherent tune spread is also reduced at larger bunch length. The behavior of the dependence, which is inversely proportional to the bunch length value is explained by the fact that the coherent tune shift from the impedance is also inversely proportional to the bunch length. In other words, for short bunches the coherent tune shift from the impedance is strong and thus the coherent mode emerges from the incoherent spectrum leading to the strong emittance growth suppression. For larger bunch lengths the shift of the coherent mode is weaker resulting in weaker suppression which eventually saturates once the coherent mode lies inside the incoherent spectrum.

Finally, it should be noted that for very small bunches the wake potential used for the simulations may not be a completely accurate representation of the actual wakefields in the machine. This may be the reason that the first point of the simulation results with the wakefields seems to not follow the otherwise smooth dependence on the bunch length. This appears to indicate the lower limit on the

bunch length, for which the simulation results may be reliable.

6.6 Conclusions

PyHEADTAIL simulations showed for the first time that the transverse beam impedance (not included in the theory nor in the numerical simulations so far) has a significant impact on the emittance growth driven by RF noise in the crab cavities. In particular, it was found that the transverse impedance can suppress the crab cavity noise-induced emittance growth once the coherent tune, which is shifted by the impedance, moves out of the incoherent tune spectrum. It turns out that, when the coherent tune is outside the incoherent tune spread, the rate of decoherence of betatron oscillations is reduced, leading to a suppression of the noise-induced emittance growth rate as shown by recently developed theoretical models [111, 112]. This mechanism, which has been observed in the past as a result of beam-beam interactions, is related to the transverse dipole oscillation of the beam. To this end, the suppression is not observed for amplitude but only for phase noise-induced emittance growth.

For the beam and machine conditions as in the 2018 SPS experiment, the simulations with the complete SPS transverse impedance model revealed a strong emittance growth suppression of about a factor 4-5, which agrees with the experimental observations and hence it appears to explain the observed discrepancy with the Mastoridis–Baudrenghien theoretical model of (see Chapter 4).

The PyHEADTAIL simulations also revealed a strong dependence of the emittance growth suppression factor on the amplitude-dependent tune shift, as it modifies the incoherent tune spectrum. This behaviour can be tested in the SPS with the use of the Landau octupoles. Based on this, an experiment was planned and took place in the SPS in 2022, aiming to reproduce the dependence of the emittance growth suppression on the amplitude detuning. Further details and the results of this additional experimental campaign with CCs in the SPS are presented in the next chapter.

7 | Experimental studies 2022: investigation of the effect of impedance on emittance growth

7.1 Motivation

As discussed in the previous chapter, PyHEADTAIL simulations including the SPS impedance model suggest that the beam coupling impedance leads to an effective suppression of the CC RF phase noise induced emittance growth through the separation of the coherent tune from the incoherent spectrum. This emittance growth suppression, which is related to the coherent (dipole) motion, can reach up to a factor of 4-5 for the experimental conditions of the first experimental campaign with CCs that took place in the SPS in 2018, and seems to be the explanation for the experimental observations (see Section 4.5.2).

This emittance growth suppression effect has not been observed before. To this end, another experimental campaign took place in the SPS in 2022 where the main objective was to validate experimentally the above-mentioned suggested emittance growth suppression mechanism. If successful, it would constitute the first experimental investigation and validation of this effect. Moreover, achieving a good understanding of the 2018 results is essential for developing confidence in the theoretical model and its predictions for the HL-LHC.

The experimental campaign of 2022 was organised in two proof-of-concept experiments. The first experiment was carried out in the presence of phase noise in the CC RF system. The second experiment took place with a pure dipolar noise

source: the beam transverse damper. This chapter reports on the preparation, the methodology, and the results of these experiments.

7.2 Experiment with CC as noise source

Due to the preceding PyHEADTAIL simulations which provided strong evidence that the observed discrepancy between the 2018 measurements and the theoretical predictions could be explained by the beam transverse impedance additional machine time was dedicated to emittance growth studies with CC in the SPS in 2022. The time allocated for the CC experiment was limited to about 10 hours. Taking into consideration the time needed for the setup and the CC calibration the time available for the emittance growth measurements is reduced even more. To this end, measurement repeatability is limited and the experimental procedure had to be carefully planned in advance.

7.2.1 Machine and beam configuration

The emittance growth measurements in 2022 were performed in "coast" mode at 270 GeV following the same setup as in 2018 (see Section 4.2) and very similar machine and beam conditions. The most relevant parameters are listed in Table 7.1.

This paragrphah needs to be revised. In the 2018 experiment, it was observed that the CC noise induced growth in the horizontal emittance which indicated that the betatron coupling in the machine was small but not zero. On this ground, for the 2022 experiment, there was an effort to reduce the betatron coupling in the SPS. The betatron coupling correction was performed before the start of the coast using the skew quadrupoles to minimse the tune signal from the horizontal (vertical) plane in the FFT measurements of the vertical (horizontal) plane.

The linear chromaticity was corrected to about zero units in both the horizontal and vertical planes. That was a result of miscommunication with the operator team of the SPS machine as the desired value was between 0.5 and 1.0. However, the analysis of the PyHEADTAIL simulations in Section 6.4.5 showed that the sensitivity of the

7. Experimental studies 2022: investigation of the effect of impedance on emittance growth

emittance growth suppression to the linear chromaticity values (for small positive values) is expected to be insignificant.

On the grounds that the last three (out of four) bunches used in 2018 experimental campaign were unstable, in 2022 the experiment was carried out with a single bunch. This choice allowed also to have better control on the beam conditions, avoiding possible effects from interactions between the bunches¹.

Table 7.1: Main machine and beam parameters for the emittance growth studies with CCs in SPS in 2022.

Parameter	Value
Beam energy, E_b	270 GeV
Main RF voltage / frequency, V_{RF} / f_{RF}	5 MV / 200.39 MHz
Horizontal / vertical betatron tune, Q_{x0} / Q_{y0}	26.13 / 26.18
Horizontal / vertical first order chromaticity, Q'_x / Q'_y	$\sim 0.0\text{-}0.5 / \sim 0.0\text{-}0.5$
Synchrotron tune, Q_s	0.0051
CC1 voltage / frequency, V_{CC} / f_{CC}	1 MV / 400.78 MHz
Number of protons per bunch, N_b	3×10^{10} p/b*
Number of bunches	1
Bunch length, $4\sigma_t$	1.83 ns*
Horizontal / vertical normalised emittance, $\epsilon_x^n / \epsilon_y^n$	2 μm / 2 μm *
Horizontal / vertical rms tune spread, $\Delta Q_x^{rms} / \Delta Q_y^{rms}$	$1.9 \times 10^{-5} / 2.1 \times 10^{-5}$ ‡

* These values corresponds to the requested intial value at the start of each coast.

† This value corresponds to the average rms measured bunch length over all the coasts of 2022.

‡ Here the rms betatron tune spread includes only the contribution from the detuning with amplitude present in the SPS machine. More details along with the calculations for the listed values can be found in Appendix C.2.

The average bunch length (over all settings) was measured to be about $4\sigma_t = 1.83$ ns. During the coasts, an increase in the bunch length of $\sim 5\% / h$ on average for each setting was observed. This small increase agrees with what is usually observed in the SPS in coast and will not be taken into consideration in the following analysis. The individual plots illustrating the evolution of the bunch length as measured with the Wall Current Monitor (introduced in Section 4.6.1) during the experiment are presented in Appendix C.6. Finally, looking at the dependence of the emittance growth suppression by the impedance on the bunch length in Fig. 6.14 it is evident that the bunch length of $4\sigma_t = 1.83$ ns belongs to the regime of the strong suppression.

¹Even though these effects should be insignificant due to the large bunch spacing, see Table 4.2.

The intensity was set to 3×10^{10} protons to be in agreement with the experiment of 2018. During the coasts of the 2022 experiment almost zero losses were observed. Therefore, the evolution of the intensity during the coasts will be not considered in the following.

CC RF noise

The noise injected in the CC RF system was again a mixture of phase and amplitude noise. The noise excitation extended from DC up to about 10 kHz and thus the noise was applied on the first vertical betatron sideband only, at ~ 8 kHz. The power spectral density values at ~ 8 kHz of the four different levels of artificial noise that were used in the experiment are listed in Table 7.2. By looking at the table, it becomes evident that the contribution of amplitude noise to the total emittance growth was found to be small (about 7%). To this end, in the post-processing of the 2022 data, the introduction of the effective phase noise (see Section 4.3) is not required. In the following, the measured growth rates will be displayed as a function of the measured RF phase noise only. This choice is also justified by the fact that the objective of the 2022 experimental campaign with CCs is to mainly reproduce the qualitative expected behavior from the impedance and not the exact values. This is discussed further in the next sections of this chapter.

Table 7.2: Phase and amplitude noise levels injected in the CC RF system for the emittance growth studies of 2022 along with the analytically expected growths. The listed noise values correspond to the power spectral density values at the first vertical betatron sideband, f_b , at ~ 8 kHz. The analytical emittance growth rates were computed using Eq. (3.11) and (3.12) for bunch length of $4\sigma_t = 1.83$ ns and the measured amplitude of CC voltage, $V_{CC,0} = 1.1$ MV.

10 log ₁₀ $\mathcal{L}(f)$ [dBc/Hz]		Analytical $d\epsilon_y/dt$ [$\mu\text{m}/\text{h}$]	
Phase noise	Amplitude noise	Phase noise	Amplitude noise
Level 1	-115.2	-124.6	1.64
Level 2	-109.5	-120.5	6.11
Level 3	-104.7	-116.0	18.44
Level 4	-100.1	-111.0	53.19

CC1 instead of CC2

In the 2022 campaign, CC1 was used instead of CC2 which was used in 2018. The reason behind this is that during the CC phase scan that was performed in 2022 to

7. Experimental studies 2022: investigation of the effect of impedance on emittance growth

calibrate the CC phase offset (see Section 7.2.3) CC2 tripped systematically. The issue is associated with the change of the RF phase but fixing this problem would have been time-consuming which was not an option due to the very limited machine time of the MD. Therefore, for the emittance growth measurements in 2022 CC1 was used.

SPS Wire Scanners

The emittance values were measured with the SPS Wire Scanners according to the procedure discussed in Section 4.5.1. In particular, wire scanners SPS.BWS.51637.H and SPS.BWS.41677.V were used for measurements in the horizontal and vertical planes, respectively. For both devices the data points from the second photomultiplier were used (PM2)². The beta functions of the respective plane at the locations of the wire scanners are 79.29 m, and 60.75 m.

As explained earlier (see Section 4.5.1) during each measurement with the wire scanners the beam profile is acquired two times as the wire crosses the beam in the forward direction (IN scan) and then in the reverse direction (OUT scan). For the experiment of 2022, the OUT scan was performed just 200 ms after the IN scan. However, it was observed that there are significant discrepancies between the measurements from IN and OUT scan, which in some cases reached up to 1 μm . By looking at the acquired profiles no reason was found to exclude or not one of the two scans (for reference see Fig. C.4a). A significant effort was done with the wire scanner experts during the emittance growth experiment trying to mitigate this effect without success due to limitations on the hardware of the current instrument. Therefore, it was decided that the post-process analysis would be performed taking into account only the IN scan measurements since they appeared to have systematically less fluctuation than in the OUT scan (see Appendix C.4.2). Finally, the acquisitions from the OUT scans were not completed correctly leading to unusable profiles.**corrupted profiles**.

It is worth commenting that this issue was not observed in the 2018 measurements.

²Each Wire Scanner device is equipped with four PMs. Each one of them provides a better resolution of the amplitude signal of the secondary particles for a different regime. The choice of PM2 for the emittance growth studies in 2022 was done "online", during the experiment, by examining the obtained beam profiles.

A possible explanation is that the wire scanner acquisitions of 2022 provide lower number of points to reconstruct the bunch profiles (compare Figs. 4.4 against C.4b) increasing the uncertainty of the obtained emittances. The reason behind this, is that between 2018 and 2022 the wire scanners had undergone an upgrade which increased their speed while crossing the bunch. A possible solution to this issue would be to reduce the speed of the wire for the emittance growth experiments in coast mode. This is currently in discussion with the team responsible for the wire scanners of the SPS.

Last, the low emittance growth rates showed a significant sensitivity to the fluctuation of the wire scanner measurements. For this reason, for the low CC noise levels, long measurement times of about 30-40 minutes were needed.

7.2.2 Experiment preparation and procedure

Objectives

The available machine time (~ 10 hours) for the CC experiment of 2022 was split into two parts. For the first part, the objective was to measure the emittance growth with the same noise levels and conditions as in 2018 in order a) to reproduce the observed scaling of emittance growth (see Fig. 4.6) and b) to benchmark the expected suppression factor from PyHEADTAIL simulations with the impedance model. This will be referred to as CC Experiment A in the following.

The objective of the second part was to investigate the effects of impedance and amplitude detuning on the emittance growth from CC phase noise. The preceding analysis of the PyHEADTAIL simulations revealed a significant sensitivity of the emittance growth suppression on amplitude-dependent tune shift (e.g. Fig. 6.5). This behavior can be tested experimentally in the SPS with the use of the Landau octupole families, which allow for the introduction of controlled detuning with amplitude. A successful reproduction of this behavior would provide the proof-of-concept for the emittance growth suppression mechanism from the beam transverse impedance. This will be referred to as CC Experiment B in the following. It should be mentioned, that for this experiment the octupoles of the LOD family are employed as they act mostly in the vertical plane which is the plane of interest

7. Experimental studies 2022: investigation of the effect of impedance on emittance growth

in this studies (vertical CC module which results in vertical emittance growth).

Preparatory studies with PyHEADTAIL simulations

In preparation for the CC experiments (A and B) the emittance growth in the presence of CC RF phase noise was simulated with PyHEADTAIL including the most up-to-date SPS impedance model [100] as a function of different octupole strengths, k_{LOD} . The beam and machine parameters are the ones reported in Table 7.1 which correspond to the experimental conditions of 2022. The emittance growth is induced by CC RF phase noise with a power spectral density of $1.68 \text{ rad}^2/\text{Hz}$ in the first betatron sideband which results in an emittance growth rate of about 25 nm/s . It should be highlighted that this noise level is much stronger than the levels of the injected artificial noise used in the experiment, in order for the growth to be easily observed in the simulation time of just 2.5 s . Therefore, the goal of the experiments was to reproduce the simulated suppression factor and behavior only and not the exact numbers. Finally, the simulation setup and the CC RF phase noise were simulated as discussed in Chapter 6.

The emittance growth was simulated over a range of twenty one k_{LOD} values equally spaced from $-28.2/\text{m}^4$ to $+28.3/\text{m}^4$. Nevertheless, in the simulations, no actual octupolar elements were used in order to avoid the excitation of resonances as discussed in Section 6.3. Instead, following the preceding PyHEADTAIL simulations, the effect of LODs is introduced as a change in the phase advance of the individual particles depending on their individual actions and defined by the corresponding detuning coefficients. The study was performed for zero horizontal detuning coefficient, $\alpha_{xx}=0$ since the horizontal coefficient does not affect the vertical emittance growth assuming zero coupling between the two transverse planes. The values of the vertical, α_{yy} , and the cross-term, α_{yx} , coefficients were estimated using MAD-X [50].

Figure 7.1 illustrates the dependence of the CC RF phase noise-induced emittance growth on the LOD strength, in the absence (blue) and the presence (orange) of the wakefields. The analytical prediction of the model Mastoridis–Baudrenghien is also given to facilitate the identification of the suppression factor from the impedance

(horizontal black dashed line). As usual, in the absence of wakefields, there is a very good agreement between the simulation results and the theoretical predictions. In the presence of wakefields, the expected dependence on the tune spread appears. The rms tune spread values (shown on the secondary horizontal axis) are computed taking into account both the α_{yy} and α_{yx} coefficients using Eq. (C.12).

The green and yellow areas indicate regimes where the octupoles require less than 200 A and 400 A respectively for their operation. The maximum operational current for the LODs in SPS is 400 A. However, due to their planned continuous operation in multiple coasts, the LOD current should stay below 200 A. The required current for the octupoles is computed from their strength, k_{LOD} , using Eq. (C.14)

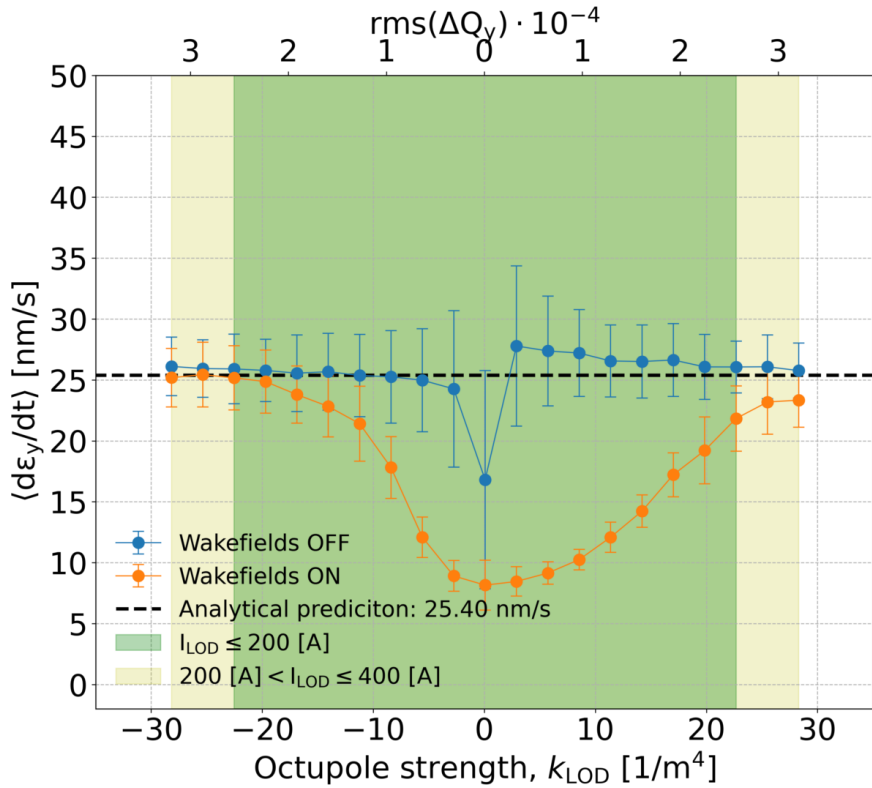


Figure 7.1: Transverse emittance growth driven by CC RF phase noise without (blue) and with (orange) the impedance effects. The green and yellow areas indicate regimes where the octupoles require less than 200 A and 400 A respectively for their operation.

From Fig. 7.1, we make the following observations:

1. The asymmetry in the suppression factor for positive and negative detuning with amplitude observed in the simulations for the 2018 experimental conditions (Chapter 6) seems to be mitigated here. Nevertheless, in order to

7. Experimental studies 2022: investigation of the effect of impedance on emittance growth

exit the suppression region the negative polarity of the octupoles (LOD) should be preferred.

2. Without powering the octupoles (2018 conditions), $k_{\text{LOD}}=0$, a suppression of a factor of about 3 is observed.
3. Even for the strongest octupole strengths, $|k_{\text{LOD}}| \approx 30 / \text{m}^4$, the required current remains below 400A. Consequently, no crucial limitations are introduced to the experiment from the octupoles operation.

Experimental procedure

The experiment was carried out on 16 May 2022, from 09:15 to 18:40. The steps taken during the experimental study were the following:

1. Calibration of the CC phase offset and voltage measurement.
2. Measurement of the background growth rate in "coast" mode: CC is switched on but with no additional noise injected in its RF system and the Landau octupoles switched off.
3. Measurement of the emittance growth with the Landau octupoles switched off and for four different CC noise levels as in 2018 (CC Experiment A). For each noise level a new bunch was injected.
4. Measurement of the emittance growth for a selected noise level and varying octupole strength (CC Experiment B). For each octupole setting a new bunch was injected in the SPS.

The details and the results of the above mentioned steps will be presented in the following subsections.

7.2.3 Calibration of CC phase offset and voltage measurement

The first step in the CC experiment in 2022 was to measure the CC voltage and calibrate the phase offset. It is reminded that in the experimental campaign of

2018, it was found that there was a phase offset between the CC inspector phase³ and the phase experience by the beam (see Section 4.4.1). Even though simulation studies showed that for the long bunches used in the CC experiments the CC phase has no significant impact on the phase noise induced emittance growth [77] an automated procedure was developed for identifying and correcting this phase offset for completeness. The same procedure can also provide the amplitude of the CC voltage.

To provide an overview, the calibration was performed by varying the inspector phase of CC1 from -180° to $+180^\circ$ in steps of 30° . For each step, the crabbing signal was acquired with the Head-Tail monitor and the CC voltage signal was reconstructed following the same procedure described in Section 4.4⁴. For each acquisition, the CC voltage at the center of the bunch, $t = 0$, was plotted as a function of the corresponding inspector phase. The results of the inspector phase scan for CC1 are summarised in Fig. 7.2 (blue dots). The three-parameter sinusoidal function of Eq. (4.7) which provides the amplitude, the phase and the vertical offset of the signal (A, θ, d) is used to fit the measured data.

The results of the sinusoidal fit (blue dashed line) are illustrated in the legend box in Fig. 7.2. Hence, it can be concluded that from the beam based measurements with the Head-Tail monitor the phase offset was found to be 12.21° . For the rest of the experiment, the inspector phase was set to the opposite of the phase offset so that the phase of the CC voltage experienced by the bunch is zero.

From the fit the amplitude voltage of CC1 was found to be (following the discussion in Section 4.4): $V_{0,CC} = A \pm d = 1.1 \pm 0.1$ MV, very close to the targeted one (1 MV). This approach of measuring the CC voltage experienced by the beam is preferred over the approach used in 2018, since now multiple Head-Tail acquisitions are taken into account in contrary with the single acquisition used in 2018.

³Inspector phase is the CC phase set by the CC operators.

⁴It is worth mentioning here that from the end of 2018 till the end of 2020, the CERN accelerator complex has undergone its second long shutdown in order to complete its scheduled upgrade program. Therefore, the calibration of the Head-Tail monitor which provides the normalisation factor that converts the measured intra bunch offset from arbitrary units to millimeters (more details in Appendix D.2) was repeated. The calibration factor for the Head-Tail monitor was measured to be 0.1037 in 2021(see Appendix C.5).

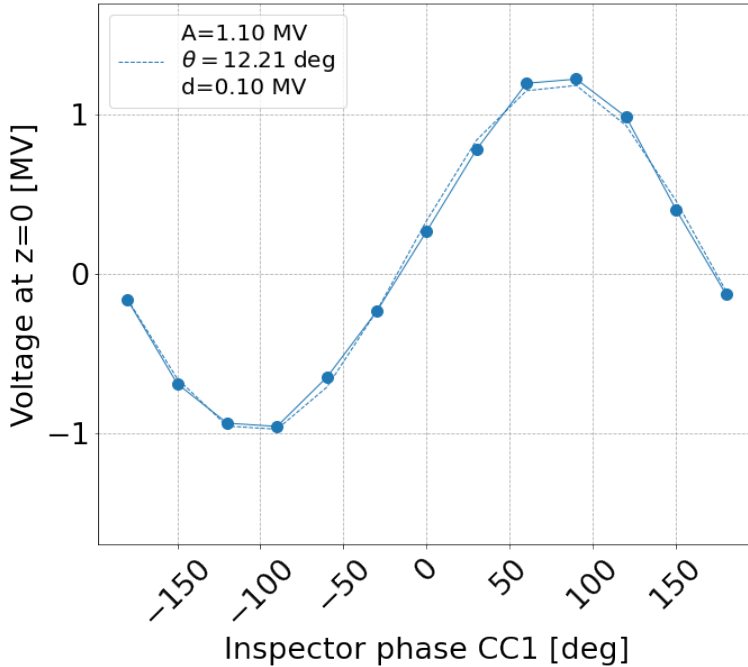


Figure 7.2: Calibration plot for the CC1 as obtained during the experiment on 16 May 2022, displaying the CC voltage at the center of the bunch $t = 0$ for different values of the inspector phase.

For reference, the calibration for CC1 took place at 270 GeV and it lasted for about 15 minutes (start: $\sim 09:40$, end: $\sim 09:52$).

Between $\sim 11:39$ and $\sim 11:45$ the same scan for CC2 was attempted. However, the cavity tripped systematically due to issues associated with the change of the RF phase. Fixing this issue would have been time-consuming, and was not possible due to the very limited machine time of the MD. Therefore, for the measurements in 2022 CC1 was used.

7.2.4 Measurement of background growth rate in "coast" mode

After the calibration of CC1, the coast at 270 GeV was set up for the emittance growth measurements. First, the background emittance growth, with no additional noise injected in the CC and the Landau octupoles switched off was measured. The background emittance growth was found to be similar in both transverse planes: $d\epsilon_x/dt = 0.81 \mu\text{m}$ and $d\epsilon_y/dt = 0.84 \mu\text{m}$ in the horizontal and vertical planes respectively. This measured background emittance growth is illustrated in Fig 7.3

for both the horizontal (blue) and vertical (red) planes.

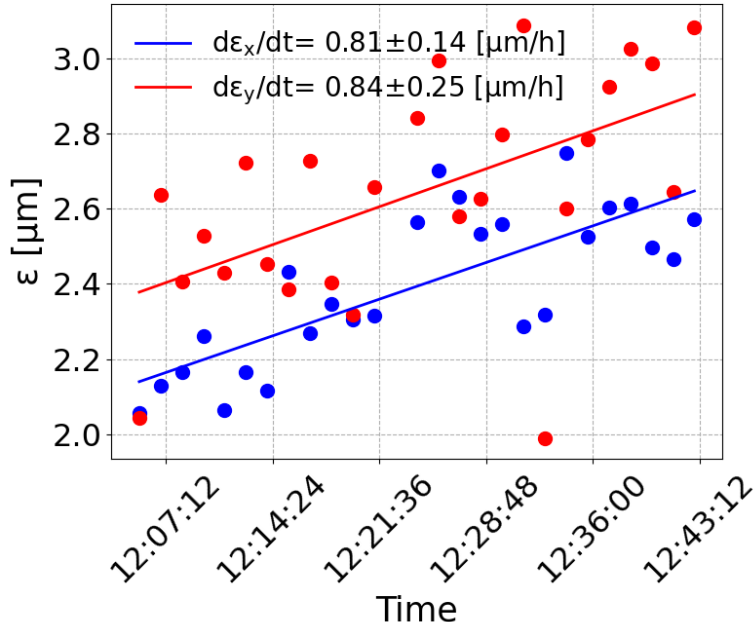


Figure 7.3: Horizontal (blue) and vertical (red) background emittance growth measured during the experiment with CC1 on May 16, 2022, with no artificial noise injected in the CC RF system and with the Landau octupoles switched off.

The applications used in the control room for the monitoring of the SPS machine have undergone an upgrade between the years 2018 and 2022. The latest applications which activate the wire scanners and automatically compute the emittance values from the profiles do not compute the respective errors. Nevertheless, the profile measurement data are available and thus the uncertainties of the emittance values can be calculated at a later post-processing stage. This post-processing showed that the uncertainties of the emittance values (computed as shown in Chapter 4) are 2-3 orders of magnitude smaller than the emittance values themselves (see Appendix C.4). Therefore, their impact is insignificant and the uncertainties of the emittance growth rates are dominated by the fluctuation of the Wire Scanner acquisitions. To this end, they are not shown in the emittance growth plot nor included in the fit to facilitate the analysis.

From the above figure, it is evident that there is a significant fluctuation in the emittance values in both transverse planes. By looking at the beam profiles, no evidence (e.g. corrupted profiles, abnormal tails, large errors on the gaussian fit results) was found to exclude some of the points. This fluctuation is introduced by

7. Experimental studies 2022: investigation of the effect of impedance on emittance growth

the Wire Scanners used for the measurements. As discussed with the experts it appears to be within the limitations of the instrument for these small emittance values. In order to reduce the sensitivity of the linear fit (from which the emittance growth rates are obtained) longer measurements are required (at least 40 minutes). For larger emittance growth rates, or in other words for larger emittance values, the effects of the fluctuations are mitigated.

Finally, for reference, the noise floor of the amplitude and phase noise of the CC at 8 kHz were measured to be -130.2 dBc/Hz and 125.7 dBc/Hz respectively. The theoretically [63] expected emittance growth from those noise levels was $0.08 \mu\text{m}/\text{h}$ and $0.2 \mu\text{m}/\text{h}$ in the horizontal and vertical planes respectively from both noise types combined. These analytically computed rates were obtained for bunch length, $4\sigma_t = 1.83 \text{ ns}$ and the measured amplitude of the CC voltage (see Section 7.2.3), $V_{0,\text{CC}} = 1.1 \text{ MV}$. The rest of the observed growth rates, is due to other sources which have not so far been identified (see discussion in Chapter 4).

7.2.5 Results of CC Experiment A: dependence of emittance growth rates on CC noise power

The objective of the first part of the experiment was to reproduce the dependence of the emittance growth rates on the CC noise power as observed in 2018. Four different levels of artificial noise were injected in the RF system of the CC as listed in Table 7.2 and the emittance evolution was recorded in coast mode every ~ 1.5 minute. For each noise level, a new bunch was injected so that all measurements took place with the same initial conditions. The duration of each coast varied from about 30 minutes for the low noise levels to about 20 minutes for the strong noise.

For the strong noise, less measurement time is sufficient since the growth rate obtained from the linear fit on the emittance values is less sensitive to the fluctuations in the wire scanner measurements. Additionally, for strong noise, the emittance reaches very quickly very large values, about $8\text{-}10 \mu\text{m}$, which eventually degrades the quality of the beam.

Figure 7.4 illustrates the transverse emittance growth measured in the SPS in 2022 for the four different noise levels injected in the CC RF system increasing from top left to bottom right. It can be seen, that there is a clear emittance growth in the vertical plane which is faster for stronger noise as expected. A growth in the horizontal emittance is also observed, but this appears to be independent of the growth in the vertical. This is also confirmed in Fig. 7.5 where the vertical and horizontal growth rates are plotted as a function of the four different phase noise levels. Consequently, even though in the 2018 analysis (see Chapter 4) the total emittance growth given by $d\epsilon_y/dt + d\epsilon_x/dt$ was considered (in order to account for effects of betatron coupling), in the following analysis of the 2022 experimental data the growth in the horizontal and vertical planes will be treated separately.

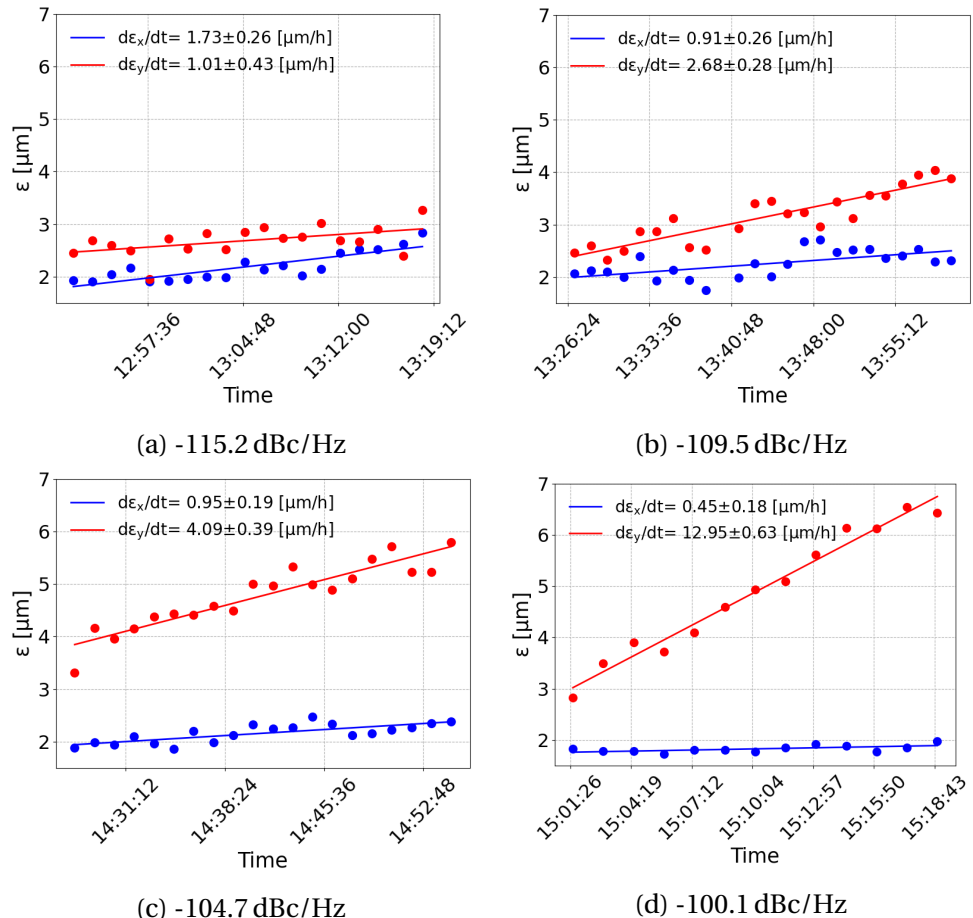


Figure 7.4: Horizontal (blue) and vertical (red) emittance evolution of a single bunch during the CC experiment on 16 May, 2022. The different phase noise levels injected in the RF system of CC1, are shown in the caption for each plot.

Figure 7.6 compares the measured (red) and the theoretically calculated (black)

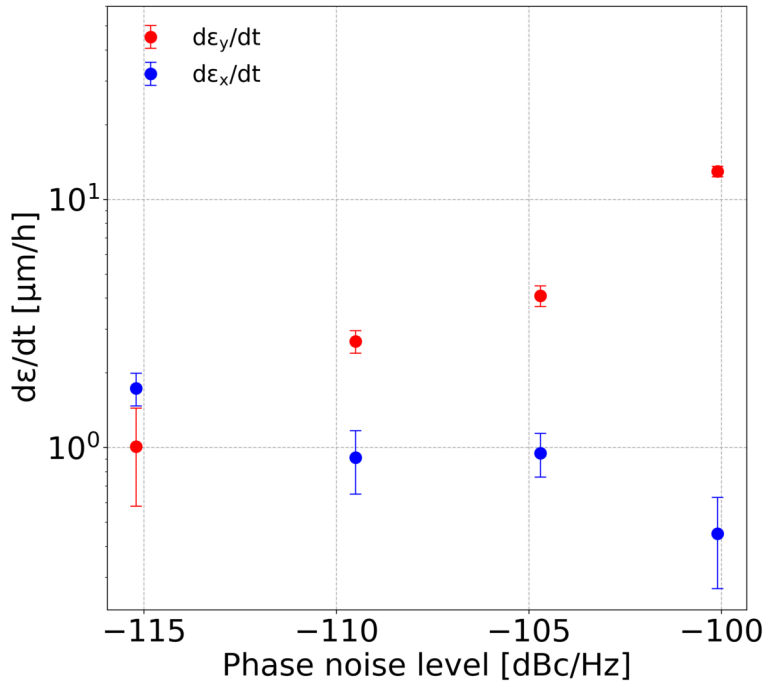


Figure 7.5: Overview plot of the emittance growth study with noise injected in the CC1 in 2022. The measured horizontal (blue) and vertical (red) emittance growth rates are shown as a function of the different power levels of applied phase noise. The error bars indicate the error of the linear fit to the emittance values (see Section 4.5).

vertical emittance growth rates for the different phase noise levels. For the comparison the background growth rate measured in the vertical plane (see Section 7.2.4) of $0.84 \mu\text{m}/\text{h}$ is subtracted from the measured values. The theoretically calculated values are obtained by inserting the phase noise levels of Table 7.2 in Eq. (3.12) for bunch length of $4\sigma_t = 1.83 \text{ ns}$, energy of 270 GeV , the measured CC voltage amplitude $V_{0,\text{CC}} = 1.1 \text{ MV}$, and the vertical beta function at the location of CC1, 76.07 m . The subtraction of the background has practically no impact on the high noise levels but it is significant for the small ones.

From Fig. 7.6 it becomes evident that the measured emittance growth rate increases for higher noise levels as expected. Furthermore, it is observed that the theory systematically overestimates the growth rates. The averaged discrepancy over all noise levels, but the first one, is a factor 4.5: numerical values are given in Table 7.3. In the computation of the average, the growth rates for the first noise level are not taken into account since the uncertainty of the corresponding measured growth is very big ($\sim 50\%$ of the emittance value itself).

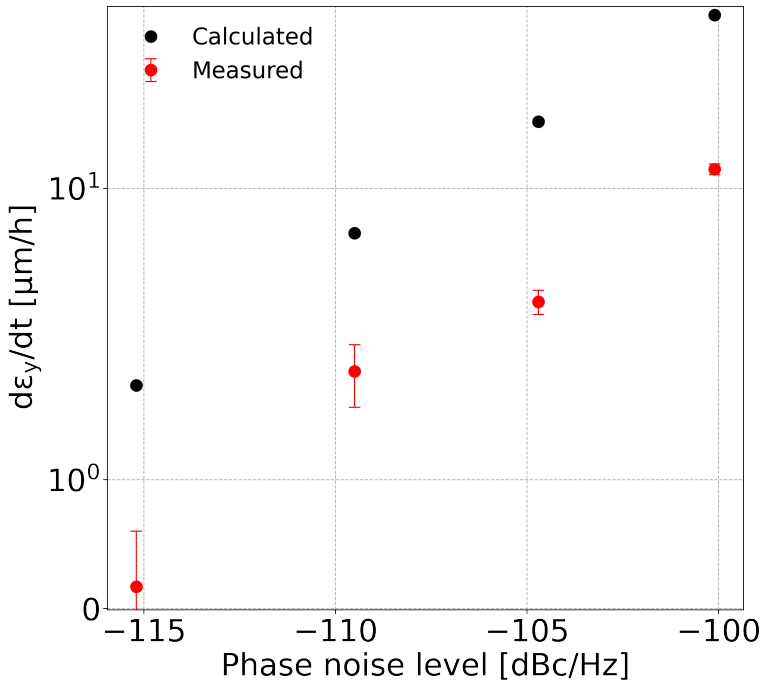


Figure 7.6: Summary plot of the emittance growth study with different noise levels injected in the RF system of CC1 in 2022. The vertical measured growth rate (red) and the expected growths from the Mastoridis–Baudrenghien model (black) are shown as a function of the different levels of applied phase noise. The error bars indicate the error of the linear fit on the emittance values (see Section 4.5)

Table 7.3: Comparison between the measured and the calculated transverse emittance growth rates for the different phase noise levels during the CC experiment of 2022. The analytical emittance growth rates were computed using Eq. (3.12) for bunch length of $4\sigma_t = 1.83$ ns and CC voltage, $V_{CC,0} = 1.1$ MV. The background growth rate measured in the vertical plane of $0.84 \mu\text{m}/\text{h}$ is subtracted from the measured values.

$10\log_{10}\mathcal{L}(f)$ [dBc/Hz]	Growth rate [μm/h]	
	Measured	Calculated
-115.2	0.17	1.73
-109.5	1.84	6.42
-104.7	3.25	19.38
-100.1	12.11	55.9

The results from CC Experiment A showed that:

- The measured emittance growth was found to scale with the noise power as expected from the theory.
- The measured growth rates were found to be systematically lower than the analytically expected values. This observation is in accordance with the

7. Experimental studies 2022: investigation of the effect of impedance on emittance growth

experimental observations of the 2018 campaign and validates the reproducibility of the experiment.

- The discrepancy between measured and theoretically expected values was found to be about a factor of 4, which is close to the suppression factor of 3 which is expected from the PyHEADTAIL simulations with impedance (see Fig. 7.1 for $k_{\text{LOD}} = 0$).

7.2.6 Results of CC Experiment B: sensitivity of emittance growth rates to amplitude-dependent tune shift

The second part of the experiment aimed to validate that the beam coupling impedance suppresses the CC phase noise-induced emittance growth through the mechanism described in Section 6.5. The strategy for this proof-of-concept experiment was to measure the emittance growth for one level of phase noise (-104.7 dBc/Hz or 3.4×10^{11} rad²/Hz) but for different octupole settings with the goal of reproducing the behavior shown in Fig. 7.1. In the limited time available for the experiment performing the full scan on the octupole settings was not feasible. Only five octupole strengths could be used, $k_{\text{LOD}} = \pm 5 \text{ m}^{-4}, 10 \text{ m}^{-4}$ and 15 m^{-4} . For each setting the bunch evolution was recorded for about 20 minutes by acquiring repeated Wire Scanner measurements and then performing a linear fit. For the measurements of each setting a fresh bunch was used so that the initial conditions each time are as close as possible.

The individual measurements of the transverse emittance evolution for each octupole setting are shown in Fig. 7.7. Two main observations can be made. First, there is a clear sensitivity of the measured evolution of the vertical emittance to the octupole strength as expected from the PyHEADTAIL simulations with the SPS transverse impedance model. The second observation is that a growth of $\sim 2 - 4 \mu\text{m}/\text{h}$ is also observed in the horizontal plane. However, it does not seem to depend on the octupole strength. Both observations are also seen in the summary plot of Fig. 7.9.

Following the measurements presented above, there was an attempt to measure

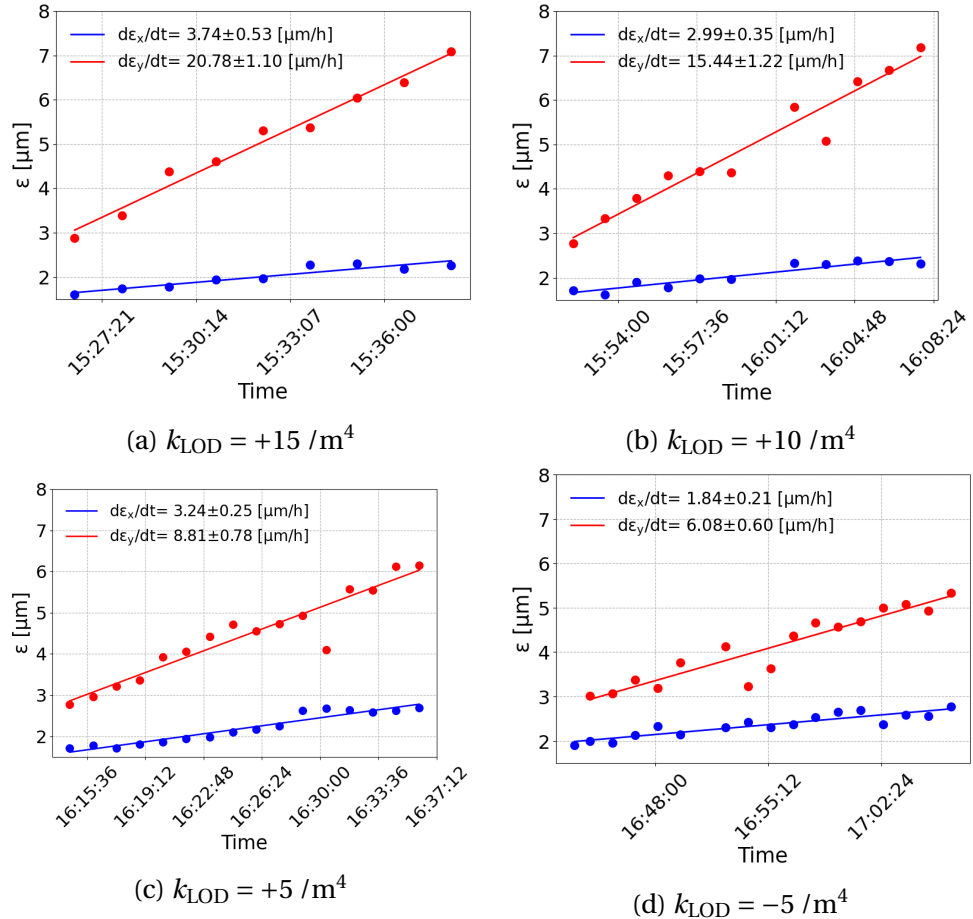


Figure 7.7: Horizontal (blue) and vertical (red) emittance evolution of a single bunch during the CC experiment on 16 May, 2022 driven by phase noise of -104.7 dBc/Hz. The different octupole settings are displayed in the captions of each plot.

7. Experimental studies 2022: investigation of the effect of impedance on emittance growth

the emittance growth for $k_{\text{LOD}} = -10 / \text{m}^4$. However, the bunch was found to be unstable in the horizontal plane which resulted to loss of the beam. The instability was observed in the turn-by turn-data acquired with the base-band tune (BBQ) measurement system of SPS [113], where the betatron oscillation amplitude appears to grow exponentially within a few seconds. This is illustrated in Fig. 7.8.

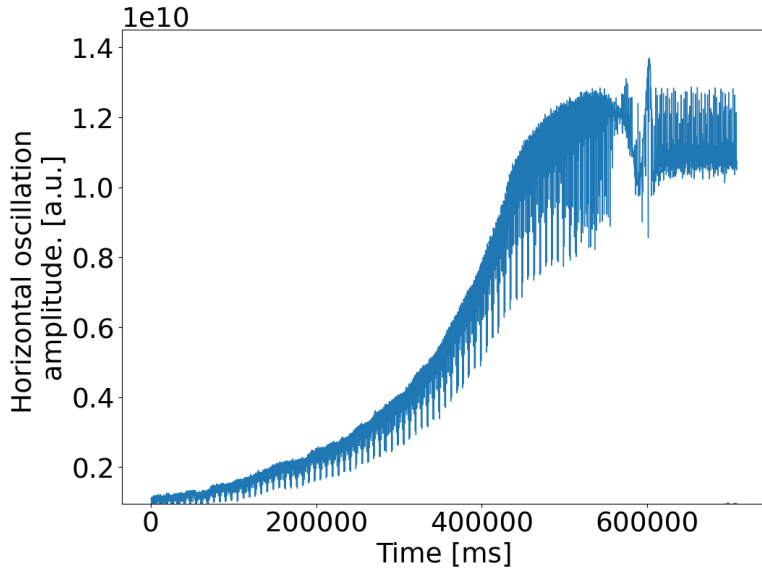


Figure 7.8: Example of the evolution of the horizontal oscillation of the bunch centroid during the CC measurements for $k_{\text{LOD}} = -10 / \text{m}^4$. This measurement is acquired with the BBQ instrument [113].

The setting of almost zero linear chromaticity is the most likely explanation for this instability. As mentioned in the introduction of this chapter, the linear chromaticity was set to slightly above zero instead of 0.5-1.0 as had been requested due to miscommunication with the SPS operating team. This increased the probability of the chromaticity sliding to small negative values, which for machines like the SPS which operate above transition can result in beam instabilities [114].

It is worth commenting, that the instability appeared in the horizontal plane. A possible explanation is that the k_{LOD} families used for the experiment act mainly in the vertical plane. Hence the resulted tune spread was sufficient to stabilise the beam through the mechanism of Landau damping⁵.

⁵Landau damping is a stabilising mechanism that is applied against beam instabilities. It is demonstrated in the transverse planes in the presence of incoherent betatron tune spread. Further

Summary plot

Figure 7.9 shows the measured emittance growth rates (in both planes) as functions of octupole strength. The error bars indicate the error of the linear fit on the emittance values during each coast. The background emittance growth observed in the SPS without any noise injected in the CC1 ($d\epsilon_x/dt = 0.81 \mu\text{m}/\text{h}$ and $d\epsilon_y/dt = 0.84 \mu\text{m}/\text{h}$) is subtracted from the measured values.

Similarly to the first part of the experiment (see Section 7.2.5), the growth in the horizontal plane seems independent of the growth in the vertical. Furthermore, Fig. 7.9 shows a clear dependence of the measured vertical emittance growth rate on the octupole strengths which appears similar to that expected from the simulations. The results from the experiment support the proposed explanation (in terms of the machine impedance) for the damping of the emittance growth from CC noise.

Additionally, for the measurements with the octupoles turned off, $k_{\text{LOD}} = 0$, the suppression factor is found to be $\sim 4\text{-}5$ which is similar to what is expected from impedance.

The measured vertical emittance growth for the large octupole strength, $k_{\text{LOD}}=+15 \text{ m}^4$, appears to agree with the analytical prediction of Mastoridis–Baudrenghien model. However, from PyHEADTAIL simulations with the impedance model this behavior is expected only for octupoles stronger than 20 m^4 in absolute value (see Fig. 7.1). This indicates that there is some uncertainty about the level of quantitative agreement: this will be discussed further in the following paragraph which provides a direct comparison of the measured data with the simulation results.

At this point, it should be highlighted that the degree of complexity of these studies is very high due to several reasons. First, the experiment aims to investigate the interplay of two effects: a) the CC noise-induced emittance growth and b) its suppression from impedance. For both effects, the existing knowledge and previous experience are very limited. Second, preparatory studies indicated that these effects are sensitive to many parameters, including the bunch length, bunch

details can be found in [36, 45], however a further discussion is out of the scope of this thesis.

7. Experimental studies 2022: investigation of the effect of impedance on emittance growth

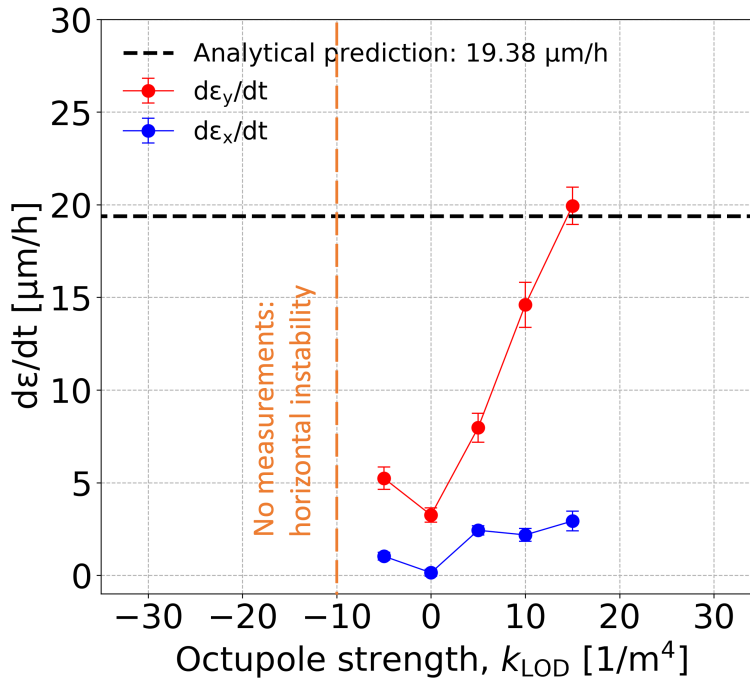


Figure 7.9: Measured horizontal (blue) and vertical (red) emittance growth driven by phase noise of -104.7 dBc/Hz injected in the RF system of CC1 for different octupole settings. The growth predicted from the analytical model without taking into account the impedance induced emittance growth suppression is $\sim 19 \mu\text{m}/\text{h}$.

intensity, beam energy, CC noise level, CC voltage, machine chromaticity, and tune spread. Third, a lot of uncertainties were introduced from the fact that the SPS did not operate in the usual mode. In particular, differences to the usual operational mode included the use of crab cavities, the noise injected in the CC RF system, the operation of SPS in storage ring mode, and the operation of the octupoles at unusually high strengths (requiring high currents in the coils for extended periods). Combining these factors, with the very limited machine time for the measurements, the fact that five data points were collected showing a clear dependence of emittance growth rate on octupole strength is significant.

Comparison of measurements against PyHEADTAIL simulations with the SPS impedance

Figure 7.10 provides a direct comparison of the vertical emittance growth measurements with the simulation results from PyHEADTAIL including the SPS transverse impedance model (discussed in Fig. 7.1). For the comparison, both

measured and simulated rates are normalised with the corresponding analytical prediction (using Eq. (3.12)).

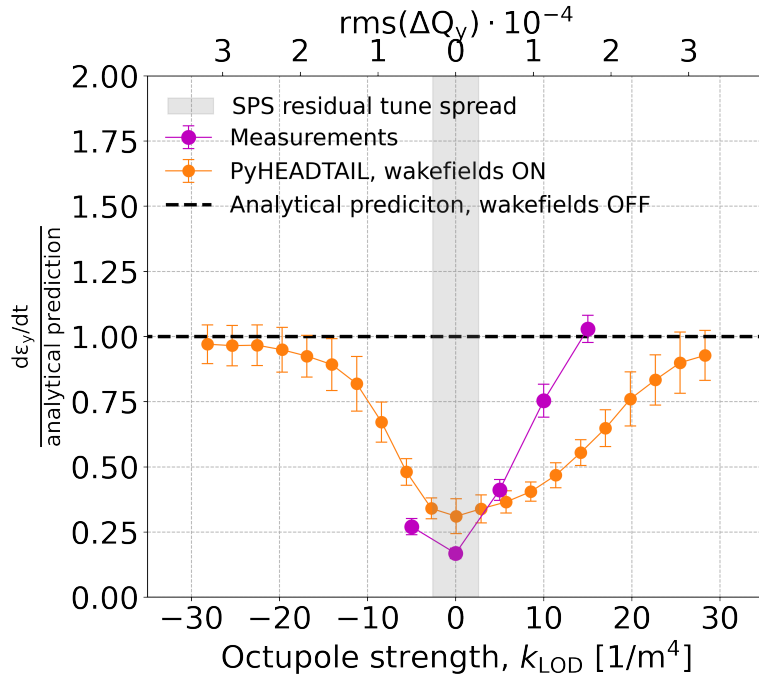


Figure 7.10: Measured (magenta) and simulated (orange) vertical emittance growth driven by phase noise injected in the RF system of CC1 for different octupole settings. Both measured and simulated rates are normalised with the corresponding prediction from the Mastoridis–Baudrenghien model.

It can be seen, that there is a very good qualitative agreement of the measurements with the simulations, supporting the hypothesis that the impedance leads to damping of the emittance growth rates. Regarding the degree of quantitative agreement, there is some uncertainty, as already discussed above. Nevertheless, this is not surprising due to the complex nature of the effects, involving many different parameters, as discussed in the previous paragraph. Further studies, simulations, and measurements will be needed to investigate the quantitative agreement. One of the possible factors that could explain that quantitative agreement is not yet obtained is the contribution from space-charge: this has not yet been studied, but could affect the tune spread. Space charge was not yet taken into account as its contribution is very small for the discussed experimental configurations. Nevertheless, the tune spread values in the regime of the studies are also very small, $10^{-6} – 10^{-4}$, which suggests that the space charge might play some role. This can be investigated in simulations even though it is

7. Experimental studies 2022: investigation of the effect of impedance on emittance growth

computationally challenging.

Investigations of space-charge effects may be carried out in the future, but are beyond the scope of the present work.

7.3 Experiment with dipole noise

The second proof-of-concept experiment to investigate the damping mechanism from the transverse impedance was conducted the night after the CC experiments described in the previous section. The emittance growth was induced by the beam damper acting as a pure dipolar noise source. This simplified the experimental procedure for two main reasons. First, there were no limitations and uncertainties introduced by the CC operation. Secondly, activating the beam damper does not require the teams which operate the CCs and inject artificial noise into their RF system and thus simplifies the organisation. This mitigates the restrictions on finding an available slot for this experiment which eventually was squeezed during the night shift after the measurements with CCs.

The strength of the damper kick was not calibrated and therefore the analytical expected emittance growth could not be computed. Nevertheless, the objective was to reproduce the strong dependence on the amplitude detuning which was presented in Fig. 6.9. To this end, the same procedure as for the second part of the CC experiment was followed: the emittance growth was measured in "coast" mode for constant strength of the noise excitation in the vertical plane but for different octupole settings. The beam and machine parameters are summarised in Table 7.1. The only update was that the linear chromaticity was corrected to $Q'_{x,y} = 1.3$ in both transverse planes to avoid instabilities due to possible shift of chromaticity to negative values (see Figs. 7.8).

The experiment lasted from about 23:50 on the May 16, 2022, until about 04:00 on the May 17, 2022. Even though the available machine time was ~ 4 hours, only seven octupole strengths could be tested: $+25, +15, +10, +5, 0, -15, -7.5 / \text{m}^4$. The reason is that one of the SPS quadrupole magnets tripped around 01:00 disabling the option for operation in "coast" mode, till around 03:00 when the quadrupole magnet could

once more be operated.

For each octupole setting, the bunch evolution was recorded for about 10 minutes by acquiring repeated measurements with the Wire Scanners (the same instruments were used for the CC experiment earlier that day). The short duration of the measurements was a result of the strong noise excitation which resulted in a clear linear growth of the vertical emittance which quickly reached large values. This can be seen in the individual measurements of the transverse emittance evolution for each octupole setting which are presented in the Appendix ???. For the measurements of each setting a fresh bunch was injected.

Summary plot

The experimental results are summarised in Fig. 7.11. The measured horizontal and vertical emittance growth are plotted as a function of the different octupole strengths with blue and red colors respectively. The error bars indicate the error of the linear fit on the emittance values during each coast. The background emittance growth without any noise excitation from the damper was not measured and thus is not subtracted from the displayed values. However, the impact of the background growth (usually measured to be between $0.5\text{-}1\mu\text{m}/\text{h}$ in both transverse planes) is insignificant for the emittance growth rates of this study ($> 10\mu\text{m}/\text{m}$).

The emittance growth observed in the horizontal plane appears to be independent of the octupole strengths, agreeing with the observations during the CC experiment (see Section 7.2).

In the vertical plane, there is a clear dependence of the measured emittance growth on the strength of the octupoles as expected (see Fig. 6.9). The results of the experiment thus further support the hypothesis that the suppression of emittance growth observed from CC noise is a consequence of the machine impedance. However, it is not clear if the used octupole strength was sufficient to be beyond the suppression region. More data points with higher octupole strength would be needed to confirm whether this was the case, and further experiments to investigate the limits in more detail are planned. This is planned to be tested in

7. Experimental studies 2022: investigation of the effect of impedance on emittance growth

dedicated future experiments.

Finally, it is worth commenting that, unlike the CC experiment that was conducted earlier that day, no horizontal coherent instability was observed in this experiment. It appears, that correcting to $Q'_{x,y} = 1.3$ was an effective way of avoiding it.

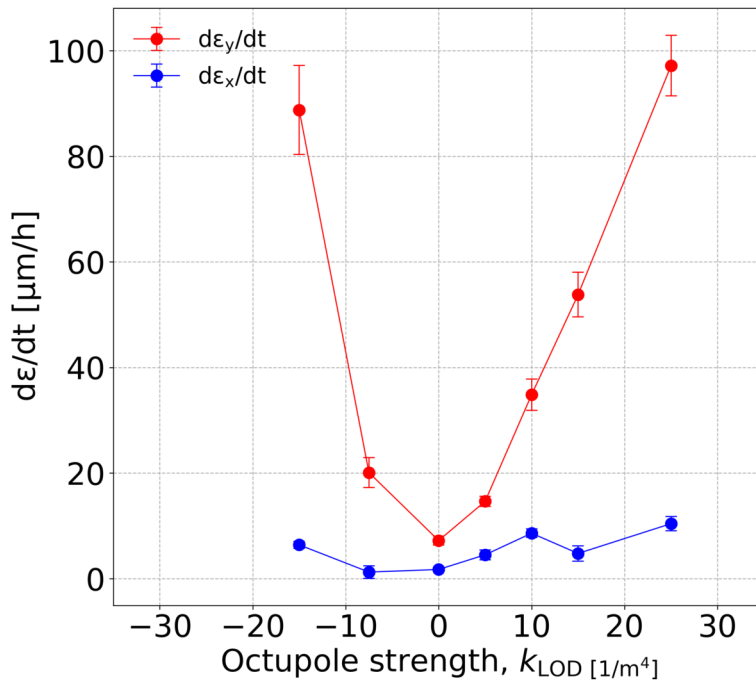


Figure 7.11: Measured horizontal (blue) and vertical (red) emittance growth driven by dipole noise introduced with the SPS beam kicker in the vertical plane for different octupole settings.

Underlying theory

It is worth mentioning that the simulation studies and experimental results (from 2018 and 2022) presented in this thesis, motivated the development of a theoretical description for the suppression of the noise-induced emittance growth from the beam transverse impedance. The theory was recently developed by the colleague X. Buffat [111, 112].

The theory developed is a simplification of the approach of Y. Alexahin (in the context of beam-beam interactions) [102]. In particular, X. Buffat, using the Van Kampen mode approach [115], adapted Y. Alexahin's approach for configurations featuring linear detuning and a complex tune shift from a collective force.

It was shown that the emittance growth driven by an external noise source can be significantly reduced by a collective force. To observe the suppression a damping

force is necessary. The suppression is enhanced in configurations where the real tune shift is larger than the spread of the betatron frequencies i.e. the coherent mode emerges from the incoherent spectrum [111].

This theory supports the studies presented in this thesis. It also explains the asymmetry in the dependence of the emittance growth suppression for positive and negative detuning coefficients observed in PyHEADTAIL simulations (see Chapter 6). Moreover, it was used to fit the experimental data measured during the experiment with dipole noise with very promising results.

7.4 Supplementary measurements with CC RF noise

Due to the very promising results of the experiments that took place in May 2022 some additional machine time (~ 12 hours) was allocated for emittance growth measurements with CC RF noise on 12 September, 2022. The objective of this new round of measurements was to investigate the vertical emittance growth in the presence of CC RF phase noise and strong octupoles $|k_{\text{LOD}}| \geq 20 / \text{m}^4$ for which the suppression mechanism is expected to be disabled (see Fig. 7.1).

7.4.1 Experimental setup

The emittance growth measurements described in this section, were performed in coast mode at 270 GeV following the same procedure with the May 2022 experiment and very similar machine and beam conditions. An overview of the parameters can be found in Table 7.1. The only updated parameters were the linear chromaticity and the bunch length. In particular, the linear chromaticity was corrected to $Q'_{x,y} = 0.65$ in both transverse planes to ensure the coherent stability of the bunch even for large negative octupole strengths⁶. The average bunch length (over all settings) was measured to be $4\sigma_t = 1.77 \text{ ns}$. The individual plots illustrating the evolution of the bunch length for each setting during the

⁶It is reminded, that the occurrence of horizontal coherent instabilities was a limiting factor in the emittance growth measurements that took place in May 2022, due to the almost zero values of linear chromaticity.

7. Experimental studies 2022: investigation of the effect of impedance on emittance growth

expereiment are presented in Appendix C.9.

7.4.2 Calibration of CC phase offset and voltage measurements

The CC calibration and the measurement of the CC voltage amplitude were performed following the procedure described in Section 7.2.3. The results from the inspector phase scan of CC1 are summarised in Fig. 7.12 (blue dots).

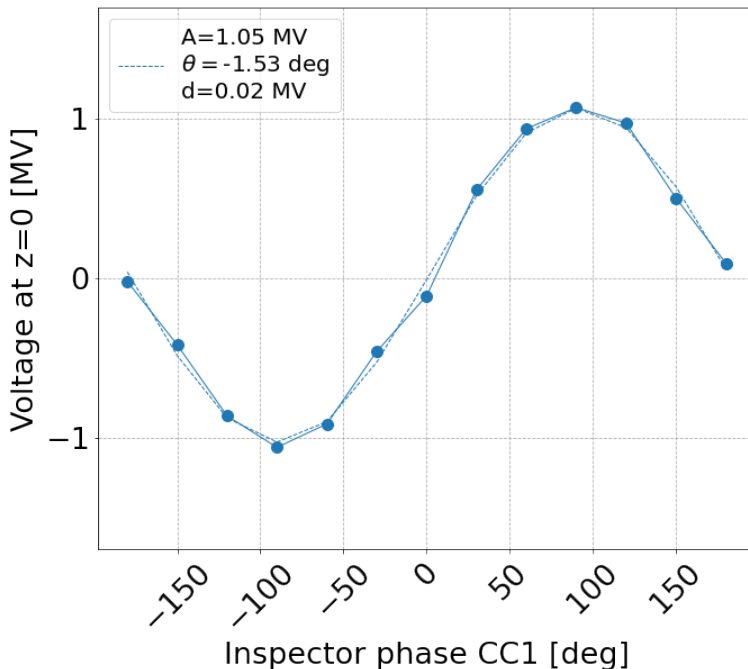


Figure 7.12: Calibration plot for the CC1 as obtained during the experiment on September 12, 2022, displaying the CC voltage at the center of the bunch $t = 0$ for different values of the inspector phase.

The results of the sinusoidal fit of Eq. (4.7) (blue dashed line) are given in the legend box of Fig. 7.12. From the beam-based measurements with the Head-Tail monitor the phase offset of CC1 was found to be -1.54° . For the rest of the experiment the inspector phase was set to $+1.54^\circ$ so that the phase of the CC voltage experienced by the bunch is zero.

The amplitude of the CC1 voltage was measured to be: $V_{0,\text{CC}} = A \pm d = 1.05 \pm 0.02 \text{ MV}$ very close to the targeted one of 1 MV.

7.4.3 Measurement of background growth rate in "coast" mode

After the calibration of CC1, the coast at 270 GeV was set up for the emittance growth measurements. First, the background transverse emittance growth, with no additional noise injected in the CC RF system, was measured. This time, the background was measured with the Landau octupoles switched ON, at $k_{\text{LOD}} = +30 / \text{m}^4$. The background emittance growth was found to be: $d\varepsilon_x/dt = 2.42 \mu\text{m}/\text{h}$ and $d\varepsilon_y/dt = 1.62 \mu\text{m}/\text{h}$ in the horizontal and vertical planes respectively. The measured background emittance growth is plotted in Fig. 7.14.

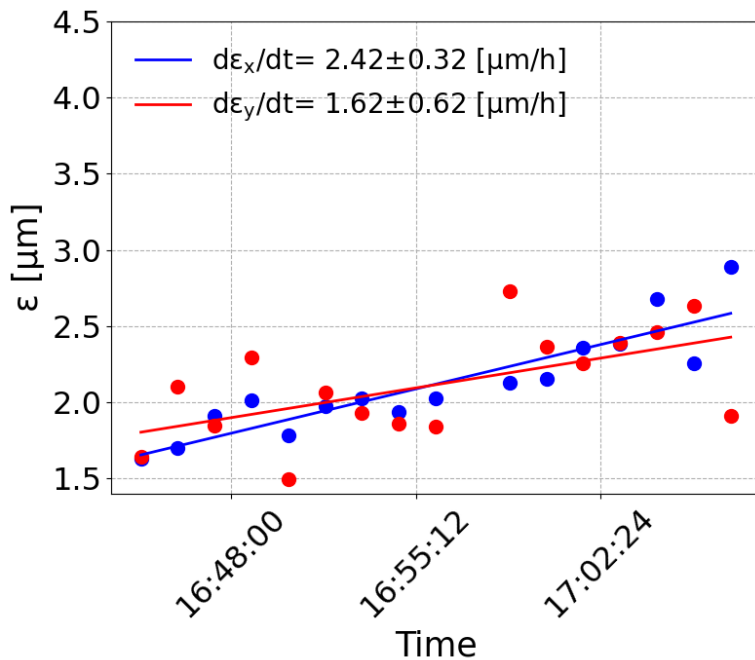


Figure 7.13: Horizontal (blue) and vertical (red) background emittance growth measured during the experiment with CC1 on September 12, 2022, with no artificial noise injected in the CC RF system and with $k_{\text{LOD}} = +30 / \text{m}^4$.

The background emittance growth was found to be faster than in May 16, 2022 (see Fig. 7.3). A possible explanation is that some growth in the transverse emittance could be driven by the operation of the Landau octupoles. Some detailed and careful investigation is required to identify the precise cause. However, due to the limited machine time, this issue should be addressed in future studies. Nevertheless, the background emittance growth is very small compared to the

7. Experimental studies 2022: investigation of the effect of impedance on emittance growth

noise-induced emittance growth. Therefore, the non-precise knowledge of the background emittance growth does not affect the conclusions drawn from these studies.

7.4.4 Emittance growth measurements with strong octupoles

For the experiment artificial noise was injected in the RF system of CC1. The noise was a mixture of both phase and amplitude noise with the phase noise being dominant. In particular, the amplitude and phase noise level at the betatron frequency were measured at -123.3 dBc/Hz and -103.3 dBc/Hz (slightly stronger than the phase noise used in the May experiment) respectively. From the Mastoridis–Baudrenghien model these noise levels are expected to result to a vertical emittance growth of $0.24 \mu\text{m}/\text{h}$ and $28.41 \mu\text{m}/\text{h}$ respectively. These rates are computed for $V_{0,\text{CC}} = 1.05 \text{ MV}$ and $4\sigma_t = 1.77 \text{ ns}$. It is evident that the contribution of the amplitude noise to the total emittance growth is negligible hence it will not be considered in the analysis presented in this section.

The emittance growth induced by the above mentioned RF noise was measured for five different octupole strengths, $k_{\text{LOD}} = \pm 30, \pm 10 / \text{m}^4$ and $-20 / \text{m}^4$. The octupole strengths $|k_{\text{LOD}}| \geq 20 / \text{m}^4$ are expected to restore the emittance growth rate to the values predicted by the Mastoridis–Baudrenghien model. For each octupole strength the bunch evolution was recorded for about 15-30 minutes by acquiring the emittance with repeated Wire Scanner measurements and then performing a linear fit on the emittance values. For the measurements of each setting a fresh bunch was used so that the initial conditions each time were as close as possible. The measurements of the emittance evolution for each octupole strength are presented in the Appendix C.8

Figure 7.14 shows the measured horizontal (blue) and vertical (red) emittance growth as a function of octupole strength. The error bars show the error of the linear fit on the evolution of the emittance values during each setting. The background emittance growth measured without artificial noise injected in the CC1 is subtracted from the measured values. The black dashed horizontal line shows the theoretically predicted emittance growth from the

Mastoridis–Baudrenghien model which does not include impedance induced effects.

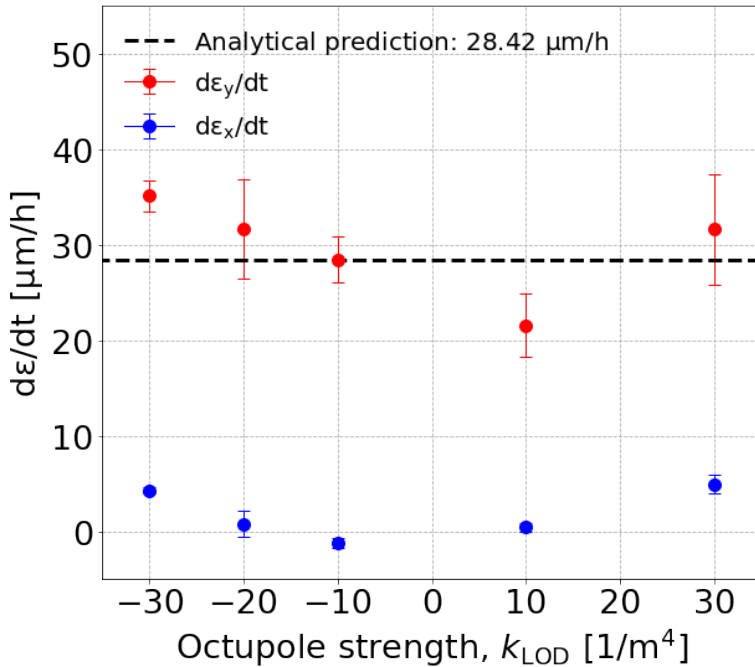


Figure 7.14: Measured horizontal (blue) and vertical (red) emittance growth driven by phase noise of -103.3 dBc/Hz injected in the RF system of CC1 for different octupole settings. The growth predicted from the analytical model without taking into account the impedance induced emittance growth suppression is $\sim 28 \mu\text{m/h}$.

It is evident that the measured vertical emittance growth rates for $-30, -20 / \text{m}^4$ and $+30 / \text{m}^4$ are in agreement (within the errorbars) and they are also very close to the theoretically predicted emittance growth from the Mastoridis–Baudrenghien model, $\sim 28 \mu\text{m/h}$. In particular, the measurements appear slightly larger than expected. However, the observed difference could be explained by e.g. 0.1 MV higher CC voltage⁷. An uncertainty of about 10% on the precise knowledge of the CC1 voltage amplitude is reasonable.

Furthermore, the vertical emittance growth for $k_{\text{LOD}} = -10 / \text{m}^4$ was measured to be larger than the rate for $k_{\text{LOD}} = +10 / \text{m}^4$. This asymmetry on the emittance growth rates for positive and negative octupole strength agrees with the observables of the PyHEADTAIL simulations which include the impedance effects (see Fig. 7.1).

Finally, it is evident that the emittance growth in the horizontal plane increases for

⁷For $V_{0,\text{CC}} = 1.15 \text{ MV}$ an emittance growth of $34 \mu\text{m/h}$ is expected from the Mastoridis–Baudrenghien model.

7. Experimental studies 2022: investigation of the effect of impedance on emittance growth

larger octupole strength (in absolute value). A possible explanation could be the operation of the Landau octupoles at very high currents. However, the precise source of the growth in the horizontal plane is not yet identified and further dedicated measurements are needed to provide conclusive outcome on the source of the horizontal emittance growth.

7.4.5 Comparison of measurements against PyHEADTAIL simulations with the SPS impedance model

Figure 7.15 compares the vertical measured emittance growth with the simulation results from PyHEADTAIL including the SPS impedance model. Both measured and simulated rates are normalised with the corresponding analytical prediction. The measured emittance vertical growth is plotted from the experiments of May (magenta) and September (green) 2022.

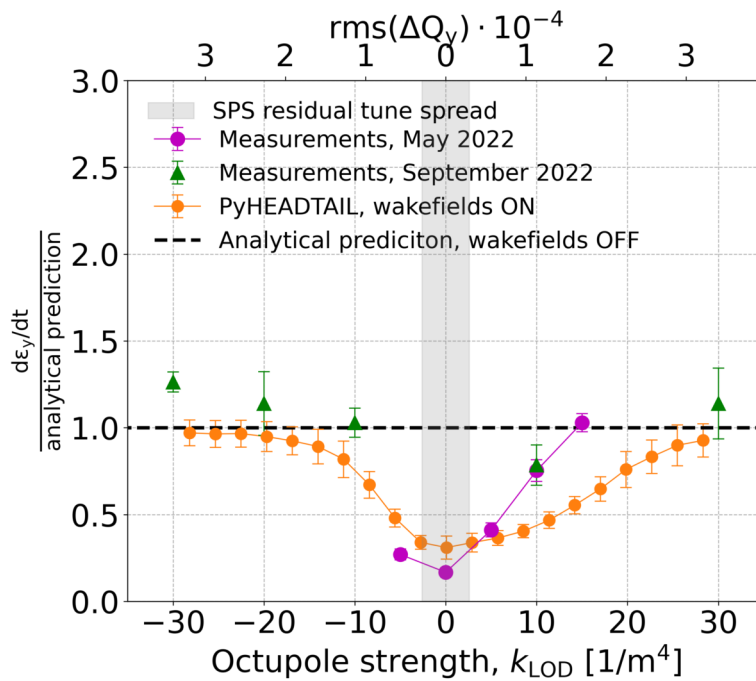


Figure 7.15: Measured (magenta-May 2022, green-September 2022) and simulated (orange) vertical emittance growth driven by phase noise injected in the RF system of CC1 for different octupole settings. Both measured and simulated rates are normalised with the corresponding prediction from the Mastoridis–Baudrenghien model.

Qualitatively, the experimental data (both from May and September) are in agreement with the simulations as they reproduce the dependence on the

amplitude dependent tune spread. There is some uncertainty on the level of quantitative agreement. This could be due to various reasons which has been addressed in Sections 7.2.6 and 7.4.4.

It is worth pointing out, that the vertical emittance growth rate measured for $k_{\text{LOD}}=10 \text{ /m}^4$ in May was found to be in excellent agreement with the emittance growth rate measured in September for the same octupole strength. This indicates the very good reproducibility of the measurements.

7.4.6 Emittance growth measurements with dominant amplitude noise

The last 15 minutes of the available machine time were dedicated to measure the emittance growth induced by CC RF amplitude noise.

The measurement was performed by injecting noise in the CC RF system which was a mixture of phase and amplitude noise but contrary to the experiments presented so far the amplitude noise was dominant. In particular, the amplitude and phase noise at 8 kHz were measured to be -102 dBc/Hz and -122 dBc/Hz, respectively. According to Mastoridis–Baudrenghien model this noise levels should result to about $32.4 \mu\text{m/h}$ and $0.38 \mu\text{m/h}$, respectively.

The emittance evolution, which was measured for $k_{\text{LOD}}=-30 \text{ /m}^4$, is illustrated in Fig. 7.16. It can be seen that the vertical emittance growth rate, as obtained from the linear fit on the vertical emittance values (red), agrees very well with the theoretically predicted rate. This is also in agreement with the simulation results with PyHEADTAIL including the SPS impedance model (see Section 6.4.2). It is reminded that in the emittance growth driven by CC RF amplitude noise is not suppressed by impedance induced effects and should be in agreement with the predictions of Mastoridis–Baudrenghien model for any value of amplitude-dependent tune spread.

7. Experimental studies 2022: investigation of the effect of impedance on emittance growth

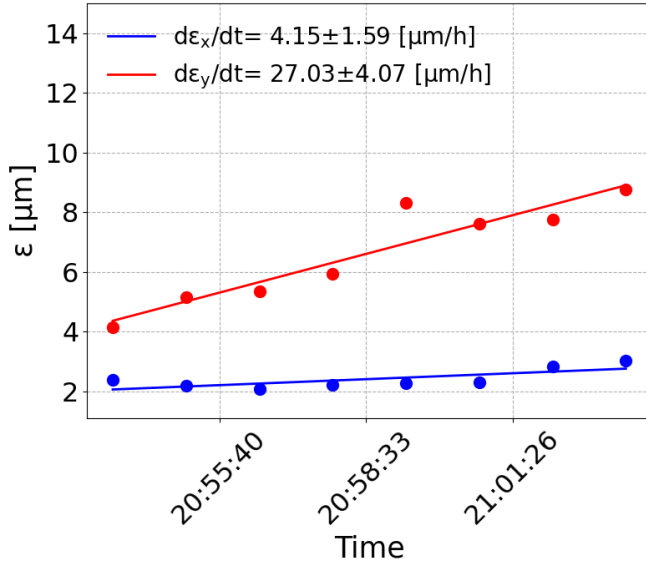


Figure 7.16: Horizontal (blue) and vertical (red) emittance growth measured during the experiment with CC1 on September 12, 2022

7.5 Conclusions and outlook

In this chapter, we have summarised the results of the experiments of May and September 2022 to investigate emittance growth in SPS driven by CC phase and amplitude noise. The main aim was to determine whether suppression of the growth rates might result from the machine impedance. The two specific objectives were a) to reproduce the scaling of the emittance growth with noise power that was observed in 2018, and b) to confirm that the beam coupling impedance can effectively suppress the CC phase noise-induced emittance growth. For the latter, the strategy was to reproduce the strong dependence of the suppression factor on the amplitude-dependent tune shift as obtained from PyHEADTAIL simulations with the SPS impedance model.

Despite the limited available machine time and the numerous uncertainties resulting from operation of the SPS outside of the usual mode, the experiment yielded useful data.. In particular, the experiment demonstrated that the vertical emittance increased for stronger noise in agreement with the observables of 2018 and the expectations from the available Mastoridis–Baudrenghien theory. Moreover, the measurements showed good qualitative agreement with the expected impact of impedance and amplitude detuning: they represent a proof of

concept for the mechanism of emittance growth suppression from the transverse impedance. Further studies, simulations (e.g. contribution of space charge), and measurements (e.g. accuracy of beam-based measurement of CC voltage, impact of linear chromaticity, and the sensitivity to transverse instabilities), will be needed to refine the experimental observations and to investigate the quantitative agreement.

Finally, additional measurements with emittance growth driven by a pure dipolar noise source (the beam transverse damper) clearly demonstrated the dependence of the emittance growth suppression on the amplitude-dependent tune shift. This further supports the conclusions from the experiments using the CC, regarding the hypothesis that suppression of the emittance growth can result from the machine impedance.

8 | Conclusions

To extend the physics reach of the main experiments of the Large Hadron Collider (LHC) at CERN, the machine will undergo a major upgrade during the coming years. This upgrade, namely the High-Luminosity LHC (HL-LHC) project, aims at about a five-fold increase of the yearly luminosity production with proton beams comparing to the present LHC operation. Reaching these ambitious luminosity goals the precise control and minimization of beam degradation (such as losses and emittance growth) is critical. A particular challenge is associated with the fact that HL-LHC will employ Crab Cavities to compensate the crossing angle of the colliding bunches, and hence to restore the head-on collisions, in the two main experiments (ATLAS and CMS). However, these Crab Cavities are expected to result in undesired transverse emittance growth due to noise in their RF control system, and therefore loss of luminosity. Given the very tight HL-LHC target values for luminosity loss and emittance growth from the Crab Cavities (the values are given in the Introduction chapter) a solid understanding of the emittance growth due to Crab Cavity RF noise is essential.

To study the transverse emittance growth induced in the presence of the Crab Cavities, two prototype Crab Cavities were installed in the SPS in 2018, for experimental tests. From the first round of experimental studies, the measured emittance growth was found to be a factor 2-3 lower than predicted from the available theoretical model of T. Mastoridis and P. Baudrenghien [63]. This PhD thesis set out to understand the results of experimental tests of Crab Cavities in the SPS. Understanding the results is crucial for gaining confidence in the predictions of the theoretical models and the specifications set for the noise limits on Crab Cavities in HL-LHC (which depend on the theoretical model).

The first step was to revisit thoroughly the experimental data from the SPS tests of 2018 in order to identify any misinterpretations that could explain the observed discrepancy. These studies are presented in Chapters ?? and 4. The outcome of this analysis was that the machine configuration and the measurement method could not explain the observed discrepancy. However, these studies provided a clear understanding of the operational aspects of the Crab Cavities in the SPS and of beam-based measurements of the Crab Cavity voltage which were not documented before. Furthermore, an automated procedure for the calibration of the Crab Cavities during operation was established and will be used in future experiments (and was already used in experiments in 2022). Moreover, the quality of the Gaussian fit on the transverse beam profiles used to obtain the emittance values was verified and the impact of the measurement errors was included in the computation of the emittance growth rates. Open questions, like a possible relation of the transverse emittance growth to the longitudinal beam evolution or the beam intensity, were addressed. Finally, an interesting finding was that the four bunches used in the experiment had different emittance growth rates and only one of them was longitudinally stable. To this end, it was decided that future experimental studies would be performed with a single bunch. Focusing the analysis on the stable bunch the difference between its measured emittance growth rates and the ones predicted from the analytical model was then found to be even larger than had been estimated from the initial analysis at the time of the experiments. Up to a factor of five lower growth rates were observed in the measurements as compared to the theoretical prediction.

In the following years, 2019-2020, a significant effort with theoretical and simulation studies was made to investigate possible explanations for the discrepancy. These studies are summarised in Chapter 5. The sensitivity of the emittance growth rates to possible uncertainties on the measured Crab Cavity voltage and the rms bunch length was tested. Furthermore, the Mastoridis-Baudrenghien theoretical model was benchmarked against different simulation codes, PyHEADTAIL and Sixtracklib, for conditions close to the experimental configuration of 2018. In PyHEADTAIL the emittance growth driven by Crab Cavity RF noise was simulated using a simple representation of the SPS

8. Conclusions

consisting of one transfer map and an interaction point where the noise from the Crab Cavities was modeled as kicks on the angle co-ordinates of the particles. The same studies were repeated with Sixtracklib but the tracking was performed using the detailed optics of the SPS, a more detailed model of the Crab Cavity, the measured noise spectra, and also including the non-linearities of the SPS lattice. It was found that none of the above-mentioned points could explain the discrepancy. An important conclusion that was drawn from these studies was that the emittance growth driven by Crab Cavity noise simulated with PyHEADTAIL was in excellent agreement with the Sixtracklib results and with the predictions of the Mastoridis-Baudrenghien theoretical model. This means that there is no sensitivity of the noise-induced emittance growth to the detailed optics of the machine, to the orbit shift from a real Crab Cavity element, or to the non-linearities of the SPS lattice. The use of PyHEADTAIL, for the rest of the studies presented in the thesis, was considered appropriate, since it appears that it includes the necessary beam dynamics for studying this phenomenon.

Finally, a second round of PyHEADTAIL simulations showed that the transverse beam impedance (not included in the theory nor the simulations so far) has a significant impact on the transverse emittance growth for the SPS experimental conditions. These studies are discussed in Chapter 6. In particular, the simulations using the most up to date impedance model of the SPS demonstrated that the decoherence and thus the emittance growth is suppressed once the detuning induced by the impedance moves the coherent tune outside of the incoherent tune spectrum. A conceptually similar effect of decoherence suppression was studied in the past in the context of beam-beam modes. Detailed investigations have shown that the decoherence suppression is related purely to the rigid or dipole bunch motion (head-tail mode 0) of the beam. In the case of Crab Cavity induced noise kicks, this dipolar excitation is provided by the phase noise kicks. For the experimental configuration of the SPS Crab Cavity tests in 2018 it was found that this mechanism results in an emittance growth suppression by a factor up to about 4 which is very close to the observed discrepancy. It is concluded, that this result suggests that the impedance effects might explain the discrepancy between the measured and theoretically estimated emittance growth rates. The PyHEADTAIL

simulations with the SPS transverse impedance model also suggested that the suppression of the emittance growth as a result of the transverse impedance depends on the amplitude-dependent tune shift. This dependence was tested experimentally in the SPS in 2022.

Another experimental campaign took place in SPS in 2022 to investigate the effects of impedance and amplitude detuning on emittance growth from Crab Cavity phase noise. The objective was to validate experimentally the suggested suppression mechanism of the emittance growth by the beam transverse impedance, by reproducing its dependence on amplitude-dependent tune spread (introduced by the Landau octupoles). The results of the experimental measurements with Crab Cavity noise that took place in 2022 are presented in Chapter 7. Despite the very limited available machine time, the results demonstrated a clear dependence of the measured emittance growth on the octupole strength, which supports the hypothesis that the impedance provides a damping mechanism, and may offer an explanation for the observations made in 2018. However, quantitative agreement between theory (taking the impedance into account) and experimental results has not yet been demonstrated. Possible additional factors, such as space charge, have been identified and further studies, including simulations and measurements, are foreseen to investigate the quantitative agreement. An additional experiment in the SPS with emittance growth driven by a pure dipolar source (beam transverse damper), supported the results from the Crab Cavity experiment since it also successfully reproduced the dependence of the suppression on the amplitude-dependent tune shift. This improves the confidence in the current understanding of the experimental results with Crab Cavities.

To summarise, this thesis addresses issues of significant importance for HL-LHC as it demonstrates the first experimental beam dynamic studies with Crab Cavities and proton beams. Additionally, it constitutes the first investigation and experimental validation of the suppression mechanism of the Crab Cavity RF phase noise or dipolar noise-induced emittance growth by the beam transverse impedance. The identification of the suppression from the impedance is a

8. Conclusions

significant step forward in the understanding of the mechanism of the transverse emittance growth driven by noise in the Crab Cavity RF systems which directly impacts the HL-LHC performance.

The project also provides a strong starting point for future additional studies. Specifically, additional measurements are planned in the SPS to refine the experimental observations, by obtaining more data points showing emittance growth rate as a function of amplitude-dependent tune shift. Furthermore, the interplay of the dipolar noise or Crab Cavity RF phase noise with the beam transverse impedance and the space charge needs to be checked to make another step towards the full understanding of the emittance growth suppression mechanism. Finally, dedicated experiments are foreseen to study the emittance growth in the presence of amplitude noise which is related to head-tail modes ± 1 which are not damped by the impedance (for the slightly positive chromaticity of the experimental configuration). Another interesting study would be to investigate the impact of linear chromaticity on the suppression factor and the possible transverse instabilities.

8.1 Implications for HL-LHC

The studies reported in this thesis investigated the emittance growth due to noise in the Crab Cavity RF system experimentally and in simulations for one SPS machine configuration. However, the main motivation of these studies was the planned use of the Crab Cavities in the HL-LHC and the importance of the effect of the emittance growth suppression for the HL-LHC. To this end, it is considered appropriate to discuss here the implications of the results of this thesis to the HL-LHC project. Additionally, it will be explained why simulation studies for the HL-LHC case were not strongly motivated.

The studies in the SPS machine are very different from the HL-LHC case. Some of the main machine and beam design parameters are summarised in Table 8.1 for the SPS and HL-LHC. Some of the most important differences (in the context of emittance growth and impedance interaction) between the two machines are the

beam energy, the intensity, the bunch length, the type of the crabbing scheme, the frequency of the main RF system, and of course the presence or not of beam-beam interactions and collisions. Therefore, as stated in the Introduction, the pure objective of the SPS studies was to validate the predictions of the available theoretical models, in terms of Crab Cavity RF noise-induced emittance growth. Then, one should be able to extrapolate the predictions to the HL-LHC case. It appears that the results obtained in the SPS cannot be directly applied, in a straightforward way, to HL-LHC.

Table 8.1: Overview of the design parameters for the SPS and HL-LHC [4]. The listed values for the SPS correspond to its operation as a storage ring for studying the long-term emittance evolution. The listed values for HL-LHC case are for beams at collision energy.

Parameter	SPS	HL-LHC
Circumference, C_0	6.9 km	26.7 km
Beam energy, E_b	270 GeV	7 TeV (per beam)
Rms bunch length, σ_z	12-16 cm	7.55 cm
Frequency of main RF system, f_{RF}	400 MHz	200 MHz
Number of bunches	1	2808 (per ring)
Intensity, N_b	3×10^{10} protons/bunch	2.2×10^{11} protons/bunch
Crab Cavity scheme	Global	Local
Beam-beam interaction	No	Yes
Interaction points	No	Yes
Crossing angle	No	Yes

Regarding the suppression mechanism from the beam coupling impedance

Past studies for the LHC and HL-LHC operational conditions which feature complex bunch train structures, multiple interaction points with asymmetric phase advance, and chromaticity have shown that the coherent modes (dominated by the beam-beam interactions) are expected to lie inside the incoherent spectrum [116, 117].

Furthermore, in the HL-LHC operational scenarios, the main source for suppressing emittance growth is the transverse feedback (which is also known as ADT [118]). For the foreseen gain values for this device, the damping time is much faster than the damping time from impedance in the potential (though unlikely) case where the coherent modes would emerge from the incoherent spectrum. This is supported by simulation results, which include noise, beam-beam interactions, wakefields, and

8. Conclusions

the transverse feedback [117].

To this end, two conclusions are made:

- First, that the mechanism of the emittance growth suppression from impedance (or beam-beam effects) due to the separation of the coherent modes from the incoherent spectrum does not appear for the HL-LHC operational configuration. The experimental observation of the effect of the suppression from the impedance in the SPS was possible due to its operation with very small incoherent betatron tune spread. The possibility of applying this mechanism in other machines with similar conditions could be investigated.
- Second, that the results of the studies presented in this thesis do not challenge the available models [112] which predict the emittance growth for the HL-LHC from the external noise sources that have been identified for LHC [117] (Crab Cavities are not considered).

Theoretical predictions for emittance growth driven by Crab Cavity RF noise

However, the results presented in this thesis, and in particular the experimental results of 2022, with Crab Cavity RF phase noise (see Figs. 7.7 and 7.10) challenge the predictions of the analytical models for emittance growth driven by Crab Cavity RF noise. As shown in Figs. 7.9 and 7.10 the measured Crab Cavity RF noise emittance growth might be larger than predicted. The data points acquired during the 2022 measurements are not sufficient to conclude on this issue since it is not clear yet if the saturation of the suppression mechanism (which is expected for strong octupole settings) was reached. This is planned to be addressed in the foreseen experiments with Crab Cavities in SPS. This is highlighting the need for an effective transverse feedback system which is discussed in the next paragraph.

Necessity for alternative mitigation methods

The HL-LHC estimates [119], show that the expected emittance growth from noise present in the Crab Cavity RF system is about $15.4\%/h$. In the presence of the transverse damper, which is also known as ADT [118], (assuming damping time of

10 turns) this emittance growth is reduced to about $5.3\%/h$. These rates correspond to the emittance growth from both amplitude and phase noise. It becomes clear that an additional reduction of $3\%/h$ is required to meet the target value of the HL-LHC ($2\%/h$).

Reducing the noise floor of the Crab Cavity is technologically very challenging as it is already improved and lies well below the noise floor of the main RF cavities [119].

For the above-mentioned reasons, it is clear that unfortunately the suppression mechanism from the beam transverse impedance cannot be used to mitigate the expected emittance growth from the Crab Cavity RF. This highlights the necessity for an effective feedback system that will suppress the noise effects from the Crab Cavities.

Therefore, the further reduction from $\sim 5\%/h$ to $2\%/h$ should come from a proposed feedback system that uses transverse beam measurements. This system has already been proposed in 2019 but its necessity is highlighted in the results presented in this thesis. To provide some information, this Crab Cavity feedback system would use an already existing pickup (the same with the transverse damper, ADT) and it could act on both amplitude and phase noise. Furthermore, the transverse damper and the feedback could be used together, to provide a more effective reduction of the emittance growth, but one should keep in mind that the result is not additive. This system is described in detail in Ref. [120] and it is still under construction.

Another alternative solution would be to operate HL-LHC with slightly flat optics (with different horizontal and vertical β^* values¹) [121]. This configuration would allow smaller beta functions in the crabbing plane at the locations of the Crab Cavities and thus the impact from the noise present in their RF system is smaller. **To be confirmed.**

Conclusions

To conclude, the emittance growth suppression mechanism from the beam

¹ β^* is often used to refer to the beta function at an interaction point.

. Conclusions

transverse impedance which was identified and validated through the work presented in this thesis will not appear in the HL-LHC configuration, for which it is expected that the coherent modes lie within the incoherent beatron spectrum. Furthermore, the presence of the transverse feedback, in the HL-LHC operational scenario outweighs any potential damping mechanism from impedance due the faster damping time of the former.

The following paragraph needs to be revised. However, the experimental results of 2022, challenge the predictions for the emittance growth in the presence of Crab Cavity noise. This, accompanied with the fact that the current predictions for the emittance growth from Crab Cavity RF noise are almost double than required stress out the need for an effective feedback system on the Crab Cavities. As discussed, there is lot of challenging and critical work currently in progress to reach the required $2\%/\sqrt{h}$ emittance growth rate from Crab Cavity RF noise.

.

A | Definitions and methods of statistical analysis

A.1 Basic terminology

This appendix, introduces the basic terminology of statistical analysis and gives the definitions that are used in this thesis. The definitions follow the book by R. J. Barlow [122] where one can find a more detailed insight.

A.1.1 Averages

Arithmetic mean

For a data set of N data $\{x_1, x_2, x_3, \dots, x_N\}$ the arithmetic mean or just mean of the value of x is:

$$\langle x \rangle = \frac{1}{N} \sum_{i=1}^N x_i. \quad (\text{A.1})$$

Below, two properties of the arithmetic mean are discussed as they are used in this thesis.

- The mean of the sum of two variables x and y is equal to the sum of their means, ie:

$$\langle x + y \rangle = \langle x \rangle + \langle y \rangle \quad (\text{A.2})$$

- If x and y are independent the mean of their product equals:

$$\langle x \cdot y \rangle = \langle x \rangle \cdot \langle y \rangle \quad (\text{A.3})$$

A. Definitions and methods of statistical analysis

Another notation for the arithmetic mean that is often found in bibliography is, \bar{x} .

Root mean square

In the classical definition in mathematics, the root mean square (rms) is an alternative to the arithmetic mean and is defined as:

$$x^{rms} = \sqrt{\frac{x_1^2 + x_2^2 + x_3^2 + \dots + x_N^2}{N}} = \sqrt{\langle x^2 \rangle}. \quad (\text{A.4})$$

- **Disclaimer:** It is common in physics and in sciences in general for the term rms to correspond to what is actually defined as standard deviation (see definition in Appendix A.1.2). This convention, is also followed in this thesis.

A.1.2 Measuring the spread

Variance

For a data set of N data $\{x_1, x_2, x_3, \dots, x_N\}$ the variance of x expresses how much it can vary from the mean value, $\langle x \rangle$. The variance, $\text{Var}(x)$, is defined as:

$$\text{Var}(x) = \frac{1}{N} \sum_{i=1}^N (x_i - \langle x \rangle)^2. \quad (\text{A.5})$$

Alternatively, the variance can be expressed in a simpler way as follows (see Ref. [122] p.24-25):

$$\text{Var}(x) = \langle x^2 \rangle - \langle x \rangle^2. \quad (\text{A.6})$$

Standard deviation

The square root of the variance is the standard deviation (std):

$$\sigma_x = \sqrt{\text{Var}(x)} = \sqrt{\frac{1}{N} \sum_{i=1}^N (x_i - \langle x \rangle)^2}, \quad (\text{A.7})$$

or as follows from Eq. (A.6):

$$\sigma_x = \sqrt{\langle x^2 \rangle - \langle x \rangle^2}. \quad (\text{A.8})$$

The spread in a data set is usually expressed with the standard deviation instead of

the variance, as the standard deviation has the same units with the variable x .

Full width half maximum

An alternative measure of the spread is the full width half maximum (FWHM).

A.1.3 Data sets with more than one variables - Covariance

In the case that each element of the data set consists of a pair of variables, $\{(x_1, y_1), (x_2, y_2), (x_3, y_3), \dots, (x_N, y_N)\}$ the covariance expresses the extent to which x and y tend to vary together. The covariance between x and y is defined as:

$$\text{Cov}(x, y) = \frac{1}{N} \sum_{i=1}^N (x_i - \langle x \rangle)(y_i - \langle y \rangle). \quad (\text{A.9})$$

It can be seen that the covariance of variable x with itself equals the variance. In particular, it is written:

$$\text{Cov}(x, x) = \sqrt{\frac{1}{N} \sum_{i=1}^N (x_i - \langle x \rangle)^2} = \text{Var}(x) = \sigma_x^2. \quad (\text{A.10})$$

Covariance matrix

The covariance as defined above is only calculated between two variables. To express the covariance values of each pair of variables, the covariance matrix or Sigma matrix is introduced as follows and is:

$$\Sigma = \begin{pmatrix} \text{Cov}(x, x) & \text{Cov}(x, y) \\ \text{Cov}(y, x) & \text{Cov}(y, y) \end{pmatrix} = \begin{pmatrix} \sigma_x^2 & \text{Cov}(x, y) \\ \text{Cov}(y, x) & \sigma_y^2 \end{pmatrix} \quad (\text{A.11})$$

as the covariance between the same variables equals to the variance (Eq. (A.10)).

If the data set is a distribution the covariance matrix is a parameter of the distribution.

A.2 Least squares fitting

In sciences, many quantities can not be measured directly but can be inferred from measured data by fitting a model function to them. Common model functions are the Gaussian, polynomial, or sinusoidal. The fitting procedure followed in this thesis is called "least squares" and is described below based on Ref. [123].

Suppose that we have N data points (x_i, y_i) and that $y = f(x, \alpha, \beta)$ is the model function that describes the relationship between the points. The objective of the fit is to determine the optimal parameters α, β such as the model function describes best the data points. This is done by minimising the χ^2 statistics with respect to α and β :

$$\chi^2 = \sum_{i=1}^N [y_i - f(x_i, \alpha, \beta)]^2, \quad (\text{A.12})$$

where y_i is the observed value and $f(x_i, \alpha, \beta)$ the expected value from the model. In other words, χ^2 is a measure of deviation between the measurement and the expected result, and thus its minimisation results in the best fit i.e. to the optimal parameters α, β .

Weighted least squares fitting

Suppose that we have N data points $(x_i, y_i \pm \Delta y_i)$, where Δy_i is the uncertainty of y_i and that $y = f(x, \alpha, \beta)$ is the model function that describes the relationship between the points. To define the optimal parameters α, β taking into account the impact of the uncertainty Δy_i , Eq. (A.12) is written as:

$$\chi^2 = \sum_{i=1}^N \frac{[y_i - f(x_i, \alpha, \beta)]^2}{\Delta y_i^2} \quad (\text{A.13})$$

Error of the fit

The standard deviation of the fit results, $\sigma_\alpha, \sigma_\beta$, is estimated by the square root of the diagonal of their covariant matrix:

$$\begin{pmatrix} \sigma_\alpha^2 & \text{Cov}(\alpha, \beta) \\ \text{Cov}(\beta, \alpha) & \sigma_\beta^2 \end{pmatrix} \quad (\text{A.14})$$

In this thesis, the uncertainties of the fit results, $\Delta\alpha, \Delta\beta$, are defined as the standard deviation, σ_α and σ_β , of the corresponding optimal parameters.

The values of the optimal parameters and their covariance matrix are computed in this thesis using the `scipy.curve_fit` [124] function of the Python programming language.

A.3 Propagation of uncertainty

Suppose that y is related to N independent variables $\{x_1, x_2, \dots, x_N\}$ with the following function:

$$y = f(x_1, x_2, \dots, x_N). \quad (\text{A.15})$$

If $\{\Delta x_1, \Delta x_2, \dots, \Delta x_N\}$ the uncertainties of $\{x_1, x_2, \dots, x_N\}$ respectively, the uncertainty of y , is given by [122]:

$$\Delta y = \sqrt{\left(\frac{\partial f}{\partial x_1} \Delta x_1\right)^2 + \left(\frac{\partial f}{\partial x_2} \Delta x_2\right)^2 + \dots + \left(\frac{\partial f}{\partial x_N} \Delta x_N\right)^2} \quad (\text{A.16})$$

B | Fundamentals of signal analysis and measurement

This appendix discusses the basic terminology of signal processing and gives the definitions which are used in this thesis. The focus is on Fourier transform and the power spectral density. First the most general mathematical definitions which concern signals continuous in time and with infinite time duration are discussed. Secondly, the definitions are given for signals sampled at a finite number of points, which are considered for the measurements and for the computational analysis. Furthermore, the quantities that are used most often for noise power spectrum measurements and their relationship to the mathematical definitions of the power spectral density are discussed. Finally, the way of applying a measured noise spectrum in numerical simulations is described.

B.1 Continuous-time analysis

Fourier transform

A physical process (or signal or time series) can be described in the time domain by a continuous function of time, e.g. $y(t)$, or else in the frequency domain, where the process is specified by giving its amplitude \hat{y} as a function of frequency, e.g. $\hat{y}(f)$ with $f \in (-\infty, +\infty)$. In other words, $y(t)$ and $\hat{y}(f)$ are essentially different representations of the same function. In general, $\hat{y}(f)$ can be a complex quantity, with the complex argument giving the phase of the component at the frequency f .

One can switch between these two representations using the Fourier transform

method. In this thesis the Fourier transform of a time series $y(t)$, which will be denoted in this document by \hat{y} , is defined as [125]:

$$\hat{y}(f) = \int_{-\infty}^{\infty} y(t) e^{-2\pi i t f} dt, \quad (\text{B.1})$$

where f stands for any real number. If the time is measured in seconds the frequency, f , is measured in hertz.

The inverse Fourier transform, which is used to re-create the signal from its spectrum, is defined as:

$$y(t) = \int_{-\infty}^{\infty} \hat{y}(f) e^{2\pi i t f} df. \quad (\text{B.2})$$

Power spectral density and total power

The power spectral density, $S_{yy}(f)$, of a signal (or a time series), $y(t)$, will be used extensively in this thesis: it describes the distribution of the power in a signal between its frequency components, and is defined as the Fourier transform of the autocorrelation function, $R_{yy}(t)$ [126]:

$$S_{yy}(f) = \hat{R}_{yy}(f) = \int_{-\infty}^{\infty} R_{yy}(\tau) e^{-2\pi i \tau f} d\tau. \quad (\text{B.3})$$

The continuous autocorrelation $R_{yy}(\tau)$ is defined as the continuous cross-correlation integral of $y(t)$ with itself, at lag τ [127]:

$$R_{yy}(\tau) = (y * y)(\tau) = \int_{-\infty}^{\infty} \bar{y}(t) y(t + \tau) dt, \quad (\text{B.4})$$

where $*$ denotes the convolution operation and $\bar{y}(t)$ represents the complex conjugate of $y(t)$.

According to the cross-correlation theorem [127]:

$$\hat{R}_{yy}(f) = \bar{\hat{y}}(f) \hat{y}(f) = |\hat{y}(f)|^2, \quad (\text{B.5})$$

where $\hat{y}(f)$ is the Fourier transform of the signal as defined in Eq. (B.1).

B. Fundamentals of signal analysis and measurement

From Eq. (B.3) and Eq. (B.5) the power spectral density of a signal $y(t)$ can be simply written as the square of its Fourier transform:

$$S_{yy}(f) = |\hat{y}(f)|^2, \quad (\text{B.6})$$

with $f \in (-\infty, +\infty)$.

B.2 Discrete-time analysis

Discrete-time signals

Figure B.1 shows a part of a continuous signal $y(t)$. As already mentioned, for the measurements and the computational analysis, signals (or time series) sampled at a finite number of points are considered. Such signals are called discrete-time signals and in most cases they are sampled at equal points in time. For example, in Figure B.1, it is assumed that the continuous signal, $y(t)$, is sampled at intervals Δt creating a set of N points. The length in time between the first and final sample is $T_{\text{sample}} = \frac{N-1}{N} T$, where $T = N\Delta t$.

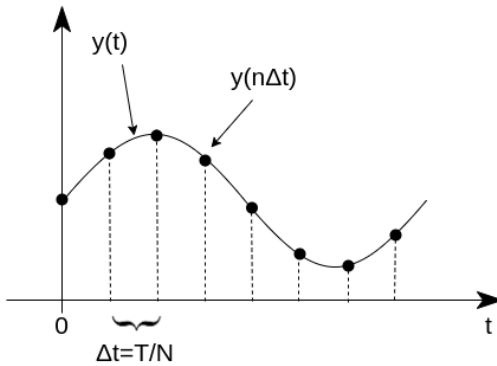


Figure B.1: Sampling of the continuous signal $y(t)$ at a finite number of points N . The sampled signal is the discrete-time signal $y(n\Delta t)$ with Δt the sampling interval and n an integer such that $n \in [0, N - 1]$.

Discrete Fourier transform

Let us consider a discrete-time signal, y_n which is sampled at N consecutive samples, $y_n = y(n\Delta t)$, with $n \in [0, N - 1]$ such that Δt is the sampling interval. For later convenience, we assume that N is an odd integer. As a first step, we note that

the integral of Eq. (B.1) can be represented by a discrete sum in the limit that $\Delta t \rightarrow 0$:

$$\hat{y}(f) = \int_{-\infty}^{\infty} y(t) e^{-2\pi i f t} dt = \lim_{\Delta t \rightarrow 0} \sum_{n=-\infty}^{\infty} y(n\Delta t) e^{-2\pi i f n\Delta t} \Delta t. \quad (\text{B.7})$$

Based on the expression for the summation in Eq. (B.7), we define the discrete Fourier transform as follows:

$$\hat{y}_k = \sum_{n=0}^{N-1} y(n\Delta t) e^{-2\pi i \frac{kn}{N}}. \quad (\text{B.8})$$

Here, the index k is an integer in the range $-\frac{N-1}{2}$ to $\frac{N-1}{2}$. Each component \hat{y}_k of the discrete Fourier transform is related to the component $\hat{y}(f)$ of the continuous Fourier transform of $y(t)$, for $f = k/T$, in the limit $\Delta t \rightarrow 0$ and $N \rightarrow \infty$ (and where it is assumed that $y(t) = 0$ for $t < 0$ and for $t > T$).

It should be noted that the discrete Fourier transform is calculated only at integer values of k , and therefore for N samples the discrete Fourier transform will consist of N numbers. The components of the discrete Fourier transform are calculated at frequencies f_k that are integer multiples of $\Delta f = 1/T = f_s/N$, with $f_s = 1/\Delta t$ the sampling frequency. In that case, $f_k \in [-\frac{N-1}{2T}, \frac{N-1}{2T}]$. An example of a discrete Fourier transform is shown in Fig. B.2.



Figure B.2: Example of a signal sampled at discrete time intervals, and the corresponding discrete Fourier transform.

B. Fundamentals of signal analysis and measurement

The inverse discrete Fourier transform is defined as:

$$y_n = y(n\Delta t) = \frac{1}{N} \sum_{k=-\frac{N-1}{2}}^{\frac{N-1}{2}} \hat{y}_k e^{2\pi i \frac{kn}{N}}, \quad (\text{B.9})$$

where $n \in [0, N - 1]$ and where n and k are both integers.

The definitions given in Eq. (B.8) and Eq. (B.9) are consistent with those used in numpy, in the numpy.fft function [128] package of the Python programming language.

Power spectral density

Following Eq. (B.6) the power spectral density of a discrete-time signal should be estimated as follows:

$$S_{yy}(f_k) = A |\hat{y}_k(f_k)|^2, \quad (\text{B.10})$$

where $f_k \in [-\frac{N-1}{2T}, \frac{N-1}{2T}]$. A is a normalisation constant which is introduced in order to obtain the correct amplitudes at each frequency and thus the correct noise power. There are several different conventions for the choice of this normalization. In this thesis, the following normalization is considered (see more details in the dedicated paragraph at the end of this section):

$$S_{yy}(f_k) = \frac{1}{N^2 \Delta f} |\hat{y}_k(f_k)|^2, \quad (\text{B.11})$$

where $\Delta f = 1/T$ the frequency resolution and N the number of samples.

Figure B.3 shows an example power spectrum of the time-domain signal shown in Fig. B.2a. It can be seen that the spectrum that results from the analysis above is two-sided, which means that it has both positive and negative frequencies. It is also symmetric around the DC component ($f = 0$ Hz), which is actually a property of a real signal.

The power spectral density is expressed in terms of the square of the amplitude of the signal per unit frequency. For example, for a signal defined in units of voltage, V,

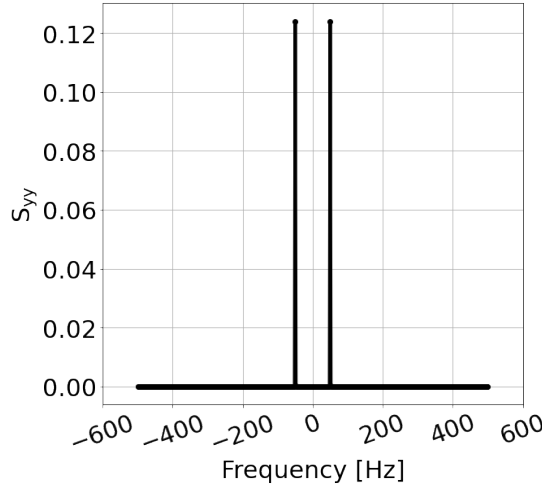


Figure B.3: Power spectrum of $y = \sin(2\pi f t)$, $f = 50$ Hz.

(e.g. from an oscillator) the units are V^2/Hz .

Conversion of a two-sided power spectrum to a single-sided power spectrum

As already mentioned, the frequency spectrum of a real signal is symmetric around the DC component and therefore the information contained in the negative frequency is redundant. For this reason, most of the instruments used in experiments to display a frequency analysis show just the positive part of the spectrum (single-sided spectrum).

In order to convert from a two-sided spectrum to a single-sided spectrum, the negative part of the spectrum is discarded, and the amplitudes of the positive frequency components (excluding the DC component, so for $f > 0$) are multiplied by a factor 2:

$$G_{yy}(f_k) = \begin{cases} 0, & f_k < 0 \\ S_{yy}(f_k), & f_k = 0 \\ 2S_{yy}(f_k), & f_k > 0 \end{cases} \quad (\text{B.12})$$

where $S_{yy}(f_k)$ is the two-sided spectrum and $G_{yy}(f_k)$ the single-sided spectrum. Figure B.4 illustrates the single-sided spectrum of the signal shown in Fig. B.2a.



Figure B.4: Single-sided power spectrum of the signal shown in Fig. B.2(a).

Normalisation factor for the power spectral density of a discrete-time signal

This paragraph, discusses the choice of the normalisation factor $A = 1/(N^2\Delta f)$ for the power spectral density of a discrete-time signal defined in Eq. (B.10):

$$S_{yy}(f_k) = A |\hat{y}_k(f_k)|^2. \quad (\text{B.13})$$

Consider the example of a discrete-time series $y_n = y(n\Delta t)$ where n is an integer such that $n \in [0, N-1]$. y_n represents a sequence of successive points equally spaced in time, drawn from a normal distribution with known standard deviation σ and zero mean, $\mu = 0$. The variance of this collection of N equally spaced values is given by:

$$\sigma^2 = \frac{1}{N} \sum_{n=0}^{N-1} |y_n|^2. \quad (\text{B.14})$$

According to Parseval's theorem [127], the variance can be written as:

$$\sigma^2 = \frac{1}{N^2} \sum_{k=-\frac{N-1}{2}}^{\frac{N-1}{2}} |\hat{y}_k|^2, \quad (\text{B.15})$$

where \hat{y}_k is the discrete Fourier transform of y_n .

Using Eq. (B.3), the autocorrelation function $R_{yy}(\tau)$ for a continuous-time signal can

be found from the inverse Fourier transform of $S_{yy}(f)$:

$$R_{yy}(\tau) = \int_{-\infty}^{\infty} \bar{y}(t) y(t + \tau) dt = \int_{-\infty}^{\infty} S_{yy}(f) e^{2\pi i t f} df. \quad (\text{B.16})$$

For zero lag, this becomes:

$$R_{yy}(0) = \int_{-\infty}^{\infty} S_{yy}(f) df = \sigma^2. \quad (\text{B.17})$$

This expresses the fact that the autocorrelation of a zero-mean stochastic process (such as y_n) is equal to the variance. It should be noted here that this integration over the spectral components yields the total power of the process.

For a discrete-time signal, we require that the power spectral density $S_{yy}(f_k)$ corresponds to the power spectral density for the continuous-time signal. In that case, Eq. (B.17) becomes:

$$\sigma^2 = \sum_{k=-\frac{N-1}{2}}^{\frac{N-1}{2}} S_{yy}(f_k) \Delta f. \quad (\text{B.18})$$

From Eq. (B.15) and Eq. (B.18) this leads to:

$$\frac{1}{N^2} \sum_{k=-\frac{N-1}{2}}^{\frac{N-1}{2}} |\hat{y}_k|^2 = \sum_{k=-\frac{N-1}{2}}^{\frac{N-1}{2}} S_{yy}(f_k) \Delta f, \quad (\text{B.19})$$

and hence:

$$\sum_{k=-\frac{N-1}{2}}^{\frac{N-1}{2}} \frac{|\hat{y}_k|^2}{N^2 \Delta f} = \sum_{k=-\frac{N-1}{2}}^{\frac{N-1}{2}} S_{yy}(f_k). \quad (\text{B.20})$$

Therefore, to satisfy the requirement that the power spectral density for the discrete-time signal corresponds to that for the continuous-time signal, we define the power spectral density for a discrete-time signal:

$$S_{yy}(f_k) = \frac{|\hat{y}_k|^2}{N^2 \Delta f}. \quad (\text{B.21})$$

Hence, the normalisation factor in Eq. (B.10) is chosen to be:

$$A = \frac{1}{N^2 \Delta f}. \quad (\text{B.22})$$

Discussion

At this point it is worth elaborating on the computation of the power spectral density, in the context of the noise effects in a synchrotron that are studied in this thesis.

In Chapter 3 it was discussed that the noise effects are modeled as kicks which update the angle co-ordinates of the particles and which are applied to them once per turn and thus they consist of a discrete-time signal. The power spectral density of that noise signal is given by Eq. (B.18). Now, given the fact that in an accelerator the particles receive the noise kicks once per turn, the sampling frequency, f_s equals the revolution frequency of the machine, f_{rev} . This means that the frequency resolution, Δf , can be written as $\Delta f = f_s/N = f_{\text{rev}}/N$, where N is the number of samples (or size) in the noise signal.

Furthermore, the studies consider white noise, which is a random signal with the same amplitude (intensity) at all the frequencies which results in a uniform power spectral density. The white noise can be treated in the discrete-time domain as a sequence of uncorrelated random variables taken from a Gaussian distribution with mean zero and finite standard deviation, σ_{white} . Since by definition the power spectral density is the same in every frequency, Eq. (B.18) is re-written as:

$$\sigma_{\text{white}}^2 = NS_{yy}(f_k)f_{\text{rev}}/N = S_{yy}(f_k)f_{\text{rev}}, \quad (\text{B.23})$$

which becomes:

$$S_{yy}(f_k) = \frac{\sigma_{\text{white}}^2}{f_{\text{rev}}}. \quad (\text{B.24})$$

In other words, the power spectral density at a given frequency, f_k , for a white noise spectrum modeled as described above, equals the variance of the noise signal over the revolution frequency of the machine

B.3 Measuring amplitude and phase noise

Amplitude and phase modulation are two of the main types of noise in the output signal of an oscillator. The instantaneous output voltage of an ideal oscillator can

be expressed as:

$$V(t) = V_0 \sin(2\pi f_0 t), \quad (\text{B.25})$$

where V_0 is the nominal peak voltage amplitude and f_0 the nominal frequency.

However, in practice, small inaccuracies will introduce amplitude and phase modulations. These modulations are included in the above signal by adding stochastic processes, represented by $\phi(t)$ and $\epsilon(t)$, as follows:

$$\begin{aligned} V(t) &= (V_0 + \epsilon(t)) \sin(2\pi f_0 t + \phi(t)), \\ &= \left(1 + \frac{\epsilon(t)}{V_0}\right) V_0 \sin(2\pi f_0 t + \phi(t)), \\ &= (1 + \alpha(t)) V_0 \sin(2\pi f_0 t + \phi(t)), \end{aligned} \quad (\text{B.26})$$

where $\phi(t)$ is the deviation from the nominal phase $2\pi f_0 t$, $\epsilon(t)$ is the deviation from the nominal amplitude and $\alpha(t) = \epsilon(t)/V_0$ is the normalised amplitude deviation. An example of a signal with phase and amplitude noise is shown in Fig. B.5.

Following the IEEE [74] conventions, the amplitude and phase modulation are measured by one-sided spectral densities, $G_{yy}(f)$. From Eq. (B.11) and Eq. (B.12), the amount of amplitude noise can be expressed as:

$$G_\alpha(f_k) = 2S_\alpha(f_k) = \frac{2}{N^2 \Delta f} \left(\frac{|\hat{\epsilon}(f_k)|}{V_0} \right)^2 = \frac{2}{N^2 \Delta f} |\hat{\alpha}(f_k)|^2, \quad (\text{B.27})$$

and the amount of phase noise can be expressed:

$$G_\phi(f_k) = 2S_\phi(f_k) = \frac{2}{N^2 \Delta f} |\hat{\phi}(f_k)|^2, \quad (\text{B.28})$$

where f_k lies in a range of positive frequencies and $\hat{\alpha}(f_k)$ and $\hat{\phi}(f_k)$ are the discrete Fourier transforms of the modulation signals $\alpha(t)$ and $\phi(t)$ respectively. The units of the $G_\alpha(f_k)$ are $1/\text{Hz}$ and the units of $G_\phi(f_k)$ are rad^2/Hz .

However, instruments used in experiments do not usually display directly the single-sided spectral density G_{yy} . Instead, the quantity $10 \log_{10} \mathcal{L}(f_k)$ [dBc/Hz] is



Figure B.5: Instantaneous voltage of an oscillator in the presence of (a) amplitude noise, (b) phase noise, and (c) both amplitude and phase noise.

shown, with [74]:

$$\mathcal{L}(f_k) = G_{yy}(f_k)/2, \quad (\text{B.29})$$

where f_k ranges from 0 over the positive part of the spectrum. It should be emphasised that here \mathcal{L} is two-sided, as defined in [74], though it is considered that the instrument displays only the positive frequencies.

B.4 Applying a measured noise spectrum in numerical simulations

The goal of this section is to describe how one can convert the measured noise spectrum from a spectrum analyzer to a discrete time series that can be used for numerical simulations.

B.4.1 Crab cavity noise in numerical simulations

As follows from the discussion in section ??, phase and amplitude noise can be represented by discrete time series $\phi_n = \phi(n\Delta t)$ and $\alpha_n = \alpha(n\Delta t)$ respectively, so that the crab cavity (CC) instantaneous voltage is given by:

$$V_{\text{CC}}(n\Delta t) = V_0(1 + \alpha(n\Delta t)) \sin(2\pi f_0 n\Delta t + \phi(n\Delta t)), \quad (\text{B.30})$$

where V_0 and f_0 are the nominal crab cavity voltage and frequency respectively, $n \in [1, N - 1]$ and N is the number of samples.

In numerical simulations, N is taken to be equal to the number of turns in the simulation. The total time simulated is $T = N\Delta t$, where Δt is the sampling interval. Since the phase and amplitude noise are sequences of noise kicks which are applied to the CC voltage every turn, Δt is equal to the time needed for one turn around the machine. For the SPS, with a revolution frequency $f_{\text{rev}} = 43.38$ kHz, $\Delta t = 1/f_s = 1/f_{\text{rev}} \approx 23$ μ s.

B.4.2 Measured noise spectrum

In the experiment performed in 2018, the amplitude and phase noise levels were measured with a spectrum analyser E5052B [73] and are expressed in terms of the quantity $10\log_{10} \mathcal{L}(f_k)$ [dBc/Hz] (see section ??). Figure B.6a shows an example of a phase noise spectrum acquired during the experiment, and which extends from 1 kHz to 10 MHz. The spectral lines observed at high frequencies correspond to harmonics of the revolution frequency.

B.4.3 Generating time series

In the following, the steps required to generate the discrete time series α_n and ϕ_n from the measured noise spectrum are discussed. The procedure involves converting the measured noise power to the two-sided power spectral density $S_\phi(f_k)$ and then using the inverse Fourier transform to produce the discrete-time series of noise kicks. In detail, the steps are as follows:

B. Fundamentals of signal analysis and measurement

1. Convert the measured noise power $10\log_{10}\mathcal{L}(f_k)$ [dBc/Hz] to $G_\phi(f_k)$ [rad^2/Hz] using Eq. (B.29) (Fig. B.6b).
2. Re-sample the noise spectrum. The measured noise power values are equally spaced in frequency on a logarithmic scale. A linear interpolation is needed such that they are equally spaced on a linear scale, every $\Delta f = f_s/N$. As already mentioned, since the beam encounters the crab cavities once each turn, $f_s = f_{rev}$ ($= 43.38$ kHz for the SPS). To this end, the linear interpolation extends up to $f_s/2$ as illustrated in Fig. B.6c. In our simulations, $N = 10^5$ turns are used.
3. Create the positive spectral components of the two-sided power spectrum, S_ϕ , using Eq. (B.12) for $f_k > 0$. The result is shown in Fig. B.6d.
4. Compute the amplitude of the spectral components of the Fourier transform, $|\hat{\phi}_n(f_k)|$ according to Eq. (B.11). It should be noted, however, that this computation is done only for the positive part of the spectrum. Fig. B.6e depicts the result of this computation.
5. Generate the phase information for each positive spectral component. By definition the power spectral density does not contain any information about the phase of the frequency components. Therefore, one should generate this information by giving a random phase $\theta(f_k)$ obtained from uniform distribution between 0 and 2π .
6. Construct a one-sided frequency domain signal, $\hat{\phi}_n^{\text{os}}(f_k) = |\hat{\phi}_n(f_k)| e^{i\theta(f_k)}$. Once again this computation is done only for the positive spectral components, with $f_k \in [\Delta f, +\frac{f_s}{2}]$.
7. Construct the two-sided Fourier transform spectrum. First, create the negative components of the Fourier transform by taking the complex conjugate of the positive components. Furthermore, the information for the zero frequency component (DC) is missing from the measured spectrum, since this extends from 1 kHz to 10 MHz. In order to do the conversion correctly, the zero frequency term is set to 0, so that $\hat{y}_n(0) = 0$. The two-sided

Fourier transform is then given by:

$$\hat{\phi}_n(f_k) = \begin{cases} |\hat{\phi}_n^{\text{os}}(f_k)| e^{i\theta(|f_k|)}, & f_k \in \left[-\frac{f_s}{2}, -\Delta f_s\right] \\ |\hat{\phi}_n^{\text{os}}(f_k)| = 0, & f_k = 0 \\ |\hat{\phi}_n^{\text{os}}(f_k)| e^{i\theta(|f_k|)}, & f_k \in \left[+\Delta f_s, +\frac{f_s}{2}\right] \end{cases} \quad (\text{B.31})$$

It is clear that $\hat{\phi}_n(f_k)$ has both positive and negative frequencies and the magnitude is symmetric in f_k .

8. Finally, apply the inverse Fourier transform, Eq. (B.9), to $\hat{\phi}_n(f_k)$. The output is a random discrete time series of N values sampled every $\Delta t = 1/f_s = 1/f_{rev}$. In other words, ϕ_n forms the sequence of noise kicks that will act on the particles in the beam on each turn in the simulations.

B.4.4 Validation of the time series reconstruction

This section describes the benchmarks that were carried out to ensure that the method described in section B.4.3 produces a valid time series for a set of noise kicks, for a given power spectrum.

Comparison of measured and reconstructed power spectrum

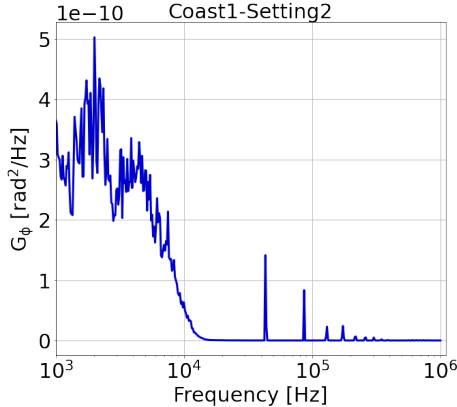
Figure B.7 shows the results of the first benchmark, comparing the measured power spectral density with the power spectral density computed from the generated time series ϕ_n . The two power spectra appear to be consistent with each other, which supports the validity of the method described above for generating the sequence of noise kicks from a given power spectrum.

PyHEADTAIL simulations

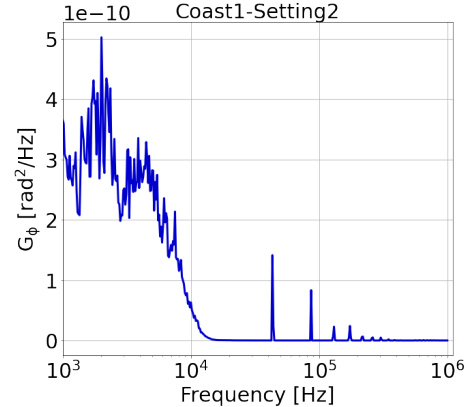
Another way to validate the method for producing a sequence of noise kicks from a measured power spectrum is to perform numerical simulations using the generated noise kicks, and compare the resulting emittance growth with the predictions from an analytical model [63].

In the simulations, which were performed with PyHEADTAIL, the beam was

B. Fundamentals of signal analysis and measurement



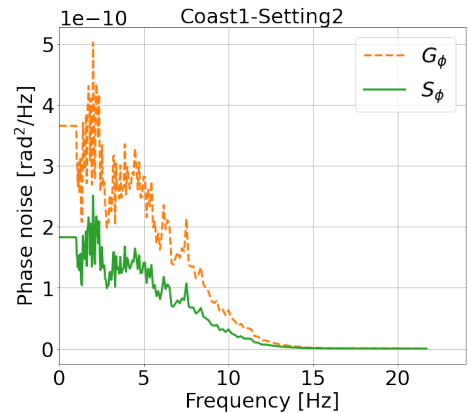
(a) Phase noise spectrum measured with a spectrum analyzer E5052B, in units dBr/Hz .



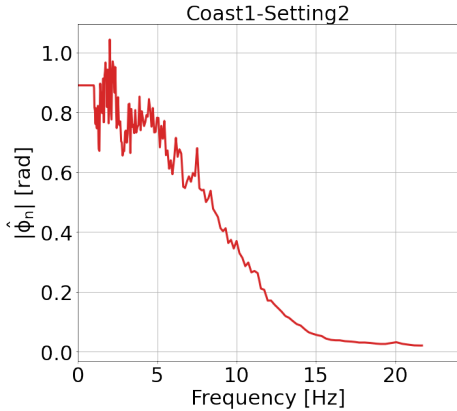
(b) Measured phase noise spectrum in units rad^2/Hz .



(c) Linear interpolation of the measured noise spectrum.



(d) Positive spectral components of the two-sided power spectrum S_ϕ .



(e) Amplitudes of the spectral components of the Fourier transform.

Figure B.6: Steps required to generate the sequence of noise kicks to be applied in the simulations from the measured noise spectrum.

tracked for 10^5 turns which corresponds to about 2.5 s in the SPS. A kick representing the effect of the crab cavities was applied on each turn. The noise kicks that the beam encounters every turn at the CC location were generated from

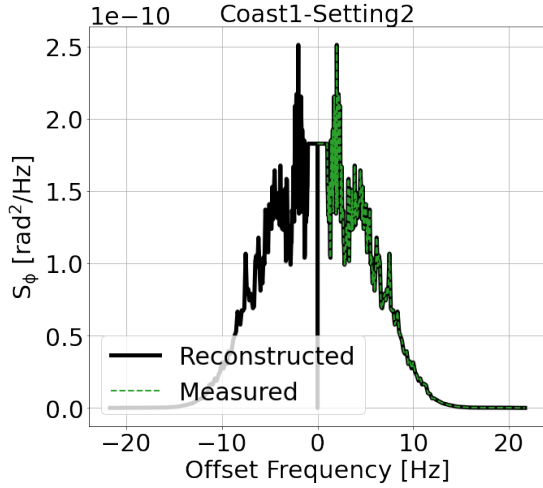


Figure B.7: Power spectral density computed from the time series ϕ_n produced from a measured power spectrum (black), compared with the original measured power spectrum (green).

the phase and amplitude noise spectra of from Coast1-Setting2 of 2018 (Fig. 4.1).

It should be noted, however, that the sequence of noise kicks includes a random factor through the set of random phases $\theta(f_k)$. To reduce the uncertainty in the results, multiple simulation runs were conducted. The set of random phases was regenerated randomly for each of 10 runs with a different seed each time. For each run, the initial bunch distribution was also regenerated randomly 3 times. The mean and the standard deviation of the emittance values obtained from the tracking were computed over all trials. The emittance growth rate was computed by performing a linear fit to the mean of the emittance values.

Figures B.8a and B.8b show the emittance growth for the case of amplitude noise and phase noise respectively. The emittance evolution in the presence of both types of noise is also illustrated in Fig. B.8c. The simulated emittance growth rates show very good agreement with the predictions from the analytical model. The results again support the validity of the method for generating a sequence of noise kicks from a measured noise power spectrum, described in section B.4.3.

B. Fundamentals of signal analysis and measurement

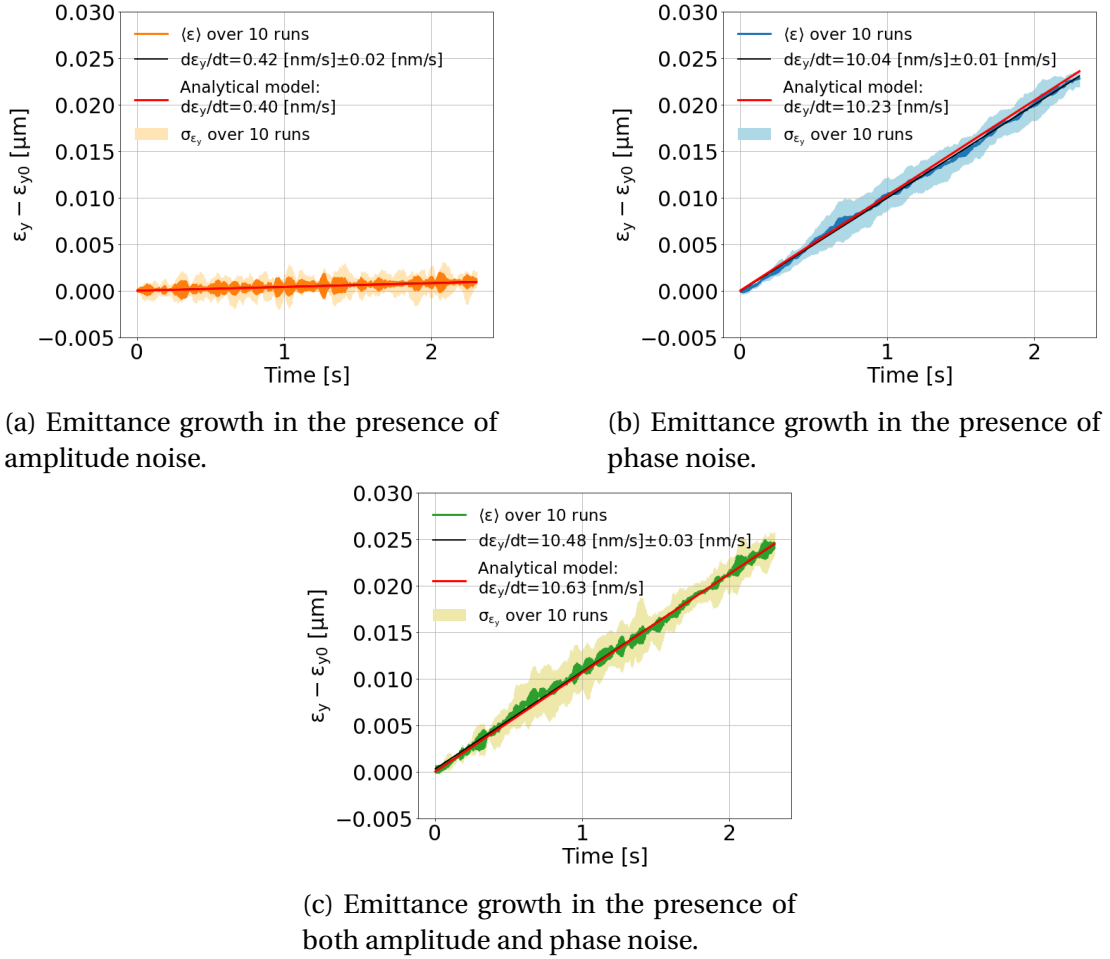


Figure B.8: Comparison between emittance growth found from simulations in PyHEADTAIL and emittance growth expected from an analytical model [63]. The emittance growth is driven by amplitude and phase noise, with kicks in the simulations generated from a measured power spectrum.

C | Appendix C

C.1 Solutions of betatron equations

The calculations here are performed according to the discussion in Ref. [80] and Ref. [129].

By inserting Eq. (2.13) in Eq. (2.11) it results to:

$$u' = Aw'(s) \cos(\psi_u(s) + \psi_{u,0}) + Aw(s)[- \sin(\psi_u(s) + \psi_{u,0})]\psi'_u(s) \quad (\text{C.1})$$

which becomes:

$$\begin{aligned} u''(s) = & Aw'' \cos(\psi_u(s) + \psi_{u,0}) + Aw'(s)[- \sin(\psi_u(s) + \psi_{u,0})]\psi'_u(s) + \\ & + Aw'(s)[- \sin(\psi_u(s) + \psi_{u,0})]\psi'_u(s) + \\ & + Aw(s)[- \cos(\psi_u(s) + \psi_{u,0})]\psi'^2_u(s) + \\ & + Aw(s)[- \sin(\psi_u(s) + \psi_{u,0})]\psi''_u(s) + \\ & + A\{\cos(\psi_u(s) + \psi_{u,0})[w'' - w(s)\psi''_u(s)] + \\ & - \sin(\psi_u(s) + \psi_{u,0})[2w'(s)\psi'(s) + w(s)\psi''_u(s)]\} \end{aligned} \quad (\text{C.2})$$

Now, inserting $u(s)$ and $u''(s)$ in Eq. (2.13) gives:

$$\begin{aligned} u''(s) + K_u(s)u(s) = & [w''(s)w(s)\psi'^2_u(s) + K(s)w(s)]\cos(\psi_u(s) + \psi_{u,0}) + \\ & - [2w'(s)\psi'_u + w(s)\psi''_u(s)]\sin(\psi_u(s) + \psi_{u,0}) = 0. \end{aligned} \quad (\text{C.3})$$

In the above equation, for the functions $w(s)$ and $\psi_u(s)$ to not depend in a particular motion they must not vary with $\psi_{u,0}$ [80]. To fulfill this requirement the coefficients

of sine and cosine must vanish individually.

Multiplying with $w(s)$ the coefficient of sine gives:

$$2w(s)w'(s)\psi'_u(s) + w^2(s)\psi''_u(s) = [w^2(s)\psi'_u(s)]' = 0, \quad (\text{C.4})$$

which by integration is written as:

$$\psi_u(s) = \oint_C \frac{ds}{w^2(s)} \quad (\text{C.5})$$

Replacing $\psi'_u(s)$ in the coefficient of cosine gives:

$$w^3(s)(w''(s) + K_u(s)w(s)) = 1. \quad (\text{C.6})$$

C.2 Detuning with amplitude

The linear detuning is given by the following formula, for octupole components

The detuning with amplitude is computed by:

$$\Delta Q_x = 2(\alpha_{xx}J_x + \alpha_{xy}J_y) \quad (\text{C.7})$$

$$\Delta Q_y = 2(\alpha_{yy}J_y + \alpha_{yx}J_x) \quad (\text{C.8})$$

where α_{yy} , α_{xx} and α_{yx} are the detuning coefficients with units [1/m] and J_x , J_y the action variables.

Rms detuning with amplitude

From the definition of variance, the variance of the vertical amplitude detuning is

given by:

$$\begin{aligned}
 \text{Var}(\Delta Q_y) &= \langle \Delta Q_y^2 \rangle - \langle \Delta Q_y \rangle^2 \\
 &= \langle 2^2(\alpha_{yy}J_y + \alpha_{yx}J_x)^2 \rangle - \langle 2(\alpha_{yy}J_y + \alpha_{yx}J_x) \rangle^2 \\
 &= 2^2 [\langle (\alpha_{yy}J_y + \alpha_{yx}J_x)^2 \rangle - \langle \alpha_{yy}J_y + \alpha_{yx}J_x \rangle^2] \\
 &= 2^2 [\langle (\alpha_{yy}J_y)^2 + 2\alpha_{yy}\alpha_{yx}J_yJ_x + (\alpha_{yx}J_x)^2 \rangle - (\langle \alpha_{yy}J_y \rangle + \langle \alpha_{yx}J_x \rangle)^2] \\
 &= 2^2 [\alpha_{yy}^2 \langle J_y^2 \rangle + 2\alpha_{yy}\alpha_{yx} \langle J_yJ_x \rangle + \alpha_{yx}^2 \langle J_x^2 \rangle - \alpha_{yy}^2 \langle J_y \rangle^2 - 2\alpha_{yy}\alpha_{yx} \langle J_y \rangle \langle J_x \rangle - \alpha_{yx}^2 \langle J_x \rangle^2] \\
 &= 2^2 [\alpha_{yy}^2 \langle J_y^2 \rangle + \cancel{2\alpha_{yy}\alpha_{yx} \langle J_yJ_x \rangle} + \alpha_{yx}^2 \langle J_x^2 \rangle - \alpha_{yy}^2 \langle J_y \rangle^2 - \cancel{2\alpha_{yy}\alpha_{yx} \langle J_yJ_x \rangle} - \alpha_{yx}^2 \langle J_x \rangle^2] \\
 &= 2^2 [\alpha_{yy}^2 (\langle J_y^2 \rangle - \langle J_y \rangle^2) + \alpha_{yx}^2 (\langle J_x^2 \rangle - \langle J_x \rangle^2)] \\
 &= 2^2 [\alpha_{yy}^2 \text{Var}(J_y) + \alpha_{yx}^2 \text{Var}(J_x)]
 \end{aligned} \tag{C.9}$$

In the development of Eq. C.9 the properties of the mean discussed in Eq. (A.2) and (A.3) are used.

Now, according to the definitions introduced in Appendix A.1, the root mean square (rms) for the vertical amplitude detuning is written:

$$\begin{aligned}
 \Delta Q_y^{rms} &= \sigma_{\Delta Q_y} = \sqrt{\text{Var}(\Delta Q_y)} \\
 &= \sqrt{2^2 [\alpha_{yy}^2 \text{Var}(J_y) + \alpha_{yx}^2 \text{Var}(J_x)]} \\
 &= 2 \sqrt{\alpha_{yy}^2 (\sigma_{J_y})^2 + \alpha_{yx}^2 (\sigma_{J_x})^2} \\
 &= 2 \sqrt{[\alpha_{yy} (\sigma_{J_y})]^2 + [\alpha_{yx} (\sigma_{J_x})]^2}
 \end{aligned} \tag{C.10}$$

where σ_{J_y} and σ_{J_x} stand for the standard deviation of the action variables J_y and J_x respectively

For a Gaussian distribution the actions, J_x and J_x follow an exponential distribution¹. It is known that for an exponential distribution the mean equals the standard

¹The charge density function for a Gaussian beam in u, u' , where $u = (x, y)$ is expressed in terms of the Twiss parameters as: $\rho(u, u') = e^{-(\gamma_u u^2(s) + 2\alpha_u(s)u(s)u'(s) + \beta_u(s)u'^2(s))/(2\epsilon_u^{\text{geom}})} = e^{-J_u/\epsilon_u^{\text{geom}}}$.

C. Appendix C

deviation. Therefore, Eq. C.10 can be written as follows:

$$\Delta Q_y^{rms} = 2\sqrt{[\alpha_{yy}\langle J_y \rangle]^2 + [\alpha_{yx}\langle J_x \rangle]^2}. \quad (\text{C.11})$$

Following Eq. (??), the rms tune spread from amplitude detuning can be also written as:

$$\Delta Q_y^{rms} = 2\sqrt{(\alpha_{yy}\epsilon_y^{geom})^2 + (\alpha_{yx}\epsilon_x^{geom})^2}. \quad (\text{C.12})$$

Equivalently, the horizontal rms tune spread from amplitude detuning is given by:

$$\Delta Q_x^{rms} = 2\sqrt{(\alpha_{xx}\epsilon_x^{geom})^2 + (\alpha_{yx}\epsilon_y^{geom})^2}. \quad (\text{C.13})$$

Disclaimer: In the analysis presented above, the actions J_x and J_y refer to the initial distribution, for which they are actually independent. The actions later in time, are coupled due to the non-linear of the lattice.

C.2.1 Residual rms tune spread in the SPS

Here the rms tune spread in the SPS that is present in the SPS with the Landau octupoles being switched off is estimated. For the estimation only the detuning with transverse amplitude is considered.

this needs to be checked.

As discussed in Section 5.3.6 a non-linear model of the SPS was developed through beam-based measurements including the contributions from the chromatic sextupoles and the SPS multipole components in the main dipoles [71, 72]. However, further experimental studies[130, 81] indicated stronger amplitude detuning than predicted from these multiple components. The measured amplitude detuning can be reproduced in simulations by switching on the Landau octupole families with strengths $k_{LOF} = k_{LOD} = 1 / m^4$.

Using the values of the multipoles listed in Table 5.3 and setting the strength of both octupole familes at $11/m^4$ the corresponding detuning coefficients are obtained with MAD-X [50]. In particular, $\alpha_{xx} = 923.45 / m$, $\alpha_{yx} = -1122.451 / m$, α_{yy}

$= 705.15 \text{ /m}$. It should be noted that these values are obtained for zero linear chromaticity in both transverse planes.

The tune spread is computed for the requested initial emittances for the emittance growth measurements of 2018 and 2021, $\epsilon_x = \epsilon_y = 2 \mu\text{m}$. Using Eq. (2.36) it can be seen that these values corresponds to geometric emittances of $\epsilon_x^{\text{geom}} = \epsilon_y^{\text{geom}} = 7.2 \text{ nm}$. By inserting these values of detuning coefficients and geometric emittances in Eq. (C.13) and Eq. (C.12) the rms tune spread is found to be, $\Delta Q_x^{rms} = 1.9 \times 10^{-5}$ and $\Delta Q_y^{rms} = 2.1 \times 10^{-5}$, in the horizontal and vertical planes respectively.

C.3 SPS octupoles calibration

In this section, the relation between the current and the strength of the focusing (LOF) and defocusing (LOD) SPS octupoles is described. First, the calibration curves are extracted for both octupole families from the LHC Software Architecture (LSA) [131]. They are shown in Figs. C.1 and C.2 for the LOF and LOD family respectively.

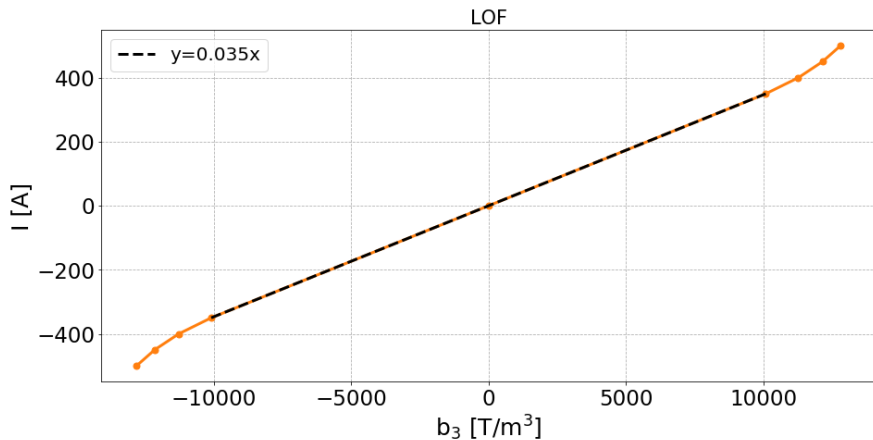


Figure C.1: Calibration curve for the LOF SPS family as obtained from LSA. b_3 is defined in Eq. (2.4).

For the studies in the area of low to moderate current (up to 300 A) the relation between the current and the strength b_3 appears to be linear. In the SPS experimental campaign of 2022, the octupole current stayed below 250 A. Therefore, focusing on the area of linear dependence is a valid approximation for

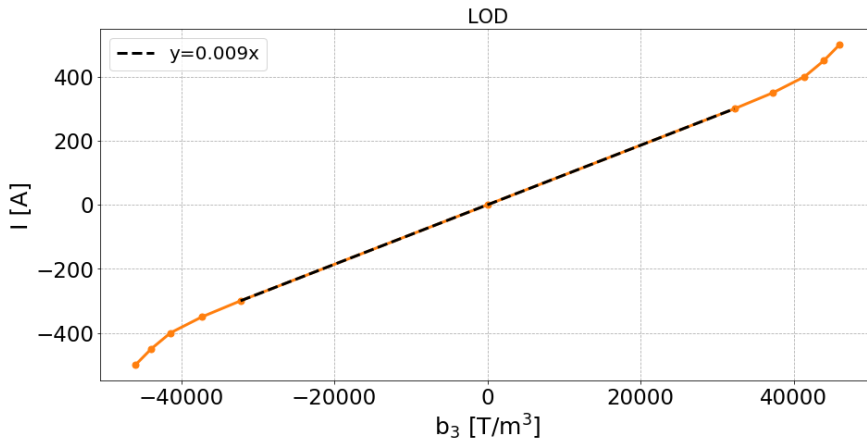


Figure C.2: Calibration curve for the LOD SPS family as obtained from LSA. b_3 is defined in Eq. (2.4).

the studies presented in this thesis.

Subsequently, the relation between the octupole current and strength is obtained by a linear fit on the above-discussed calibration curves which it is also shown in black color. From the fit, it occurs that:

$$I_{\text{LOF}} = 0.035 \times b_3 = 0.035 \times k_{\text{LOF}} \times B\rho[A] \quad (\text{C.14})$$

$$I_{\text{LOD}} = 0.009 \times b_3 = 0.009 \times k_{\text{LOD}} \times B\rho[A] \quad (\text{C.15})$$

, where b_3 is defined in Eqs. (2.4) while $k_{\text{LOF}}, k_{\text{LOD}}$ correspond to the k_3 defintion of Eq. (2.5). It is worth mentioning that the definitions for b_3 and k_3 are the same for LSA and MAD-X which also use the same units in general.

C.4 Wire Scanner measurements in 2022

C.4.1 Example beam profiles

Figures C.4a and C.4b show an example horizontal and vertical beam profile as obtained from the SPS.BWS.51637.H and SPS.BWS.41677.V instruments respectively during the experiment with CC1 in SPS in 2022. The data points from the IN (OUT) scan are shown with a blue (orange) color.

The measured data points (light blue) are fitted with a four-parameter gaussian

(orange) following the procedure discussed in Section 4.5.1 to obtain the beam size. Thereafter, the emittance values and their uncertainties are computed from Eqs. (4.9) and (4.10) respectively. The results of the fit are also shown in the plots. It is evident that the calculated uncertainties are two orders of magnitude smaller than the corresponding emittance values themselves. This is the case for all acquisitions. However, not all the profiles are displayed in this thesis for practical reasons.

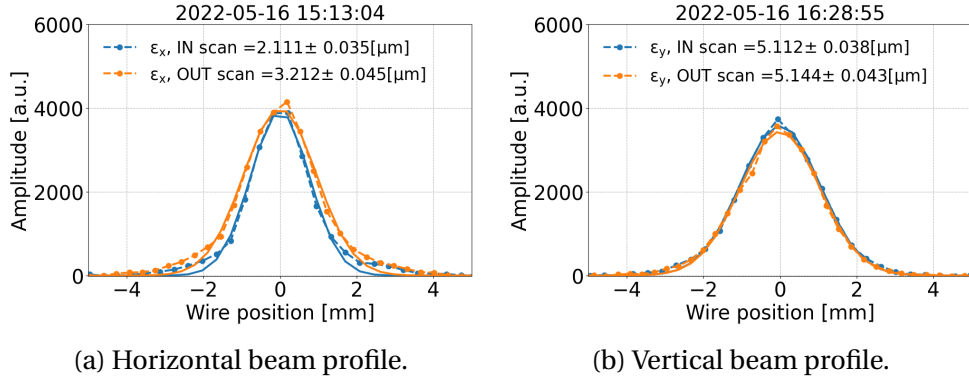
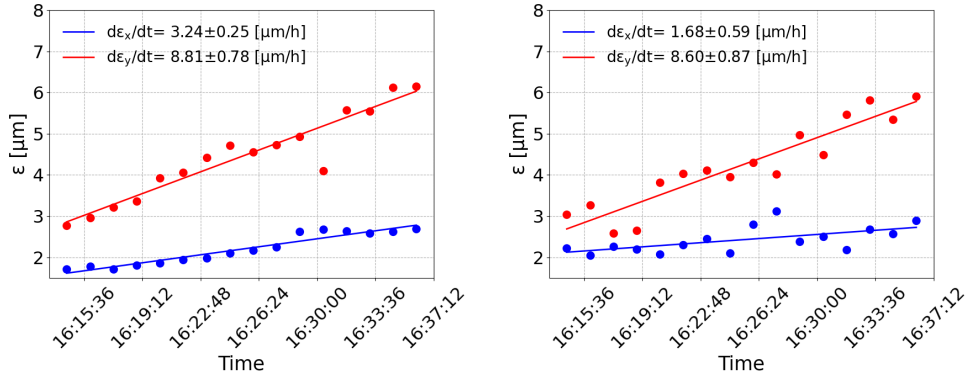


Figure C.3: Transverse beam profiles as obtained from SPS.BWS.51637.H during the CC experiment in the SPS in 2022. The data points from the IN (OUT) scan are shown with blue (orange) color.

C.4.2 Example emittance growth measurements

Figure C.4 shows the transverse emittance evolution acquired with SPS.BWS.51637.H and SPS.BWS.41677.V for horizontal and vertical planes respectively during the experiment with CC noise on May 16, 2022. The emittance values acquired during the IN scan are shown on the left while the ones acquired during the OUT scan are shown on the right.

It can be seen that the emittance values obtained from the OUT scan appear to be more fluctuated than the values from the IN scan. In this particular example, this is enhanced in the horizontal plane (blue). It is also clearly visible for the acquisitions during the first half of the coast.



(a) Emittance evolution from IN scan. (b) Emittance evolution from OUT scan.

Figure C.4: Transverse beam profiles as obtained from SPS.BWS.51637.H during the CC experiment in the SPS in 2022. The data points from the IN (OUT) scan are shown with blue (orange) color.

C.5 Head-Tail monitor calibration for the 2022 analysis

From the end of 2018 till the end of 2020, the CERN accelerator complex has undergone its second long shutdown in order to complete its scheduled upgrade program. Therefore, the calibration of the Head-Tail monitor was repeated to provide the normalisation factor required for the scaling of its reading (see Section D.2). The calibration factor was found to be 0.1037 in November 2021, as shown in Fig. C.5 (slope value).

C.6 Bunch length measurements in May 2022

In this section, the bunch length measurements acquired during the emittance growth experiments with CC noise in 2022 are presented. The measurements took place with the Wall Current Monitor instrument (introduced in Section 4.6.1) and the responsible person for the acquisitions was N. Bruchon ².

²Email contact: niky.bruchon@cern.ch

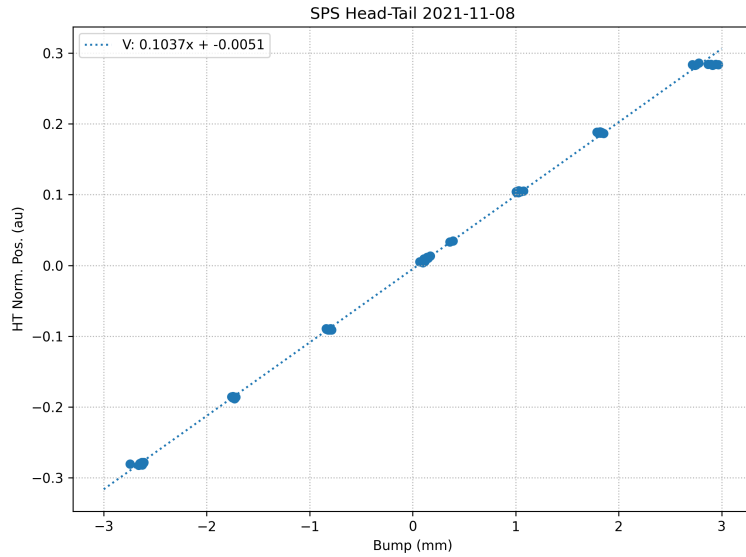


Figure C.5: The calibration was performed by T. Levens by performing orbit bumps (around the reference orbit) and measuring the normalised position of the bunch in the vertical plane (plane of interest). The normalised position is obtained as the difference of the signal divided by the sum. More details on the calibration procedure are given in [132]. This plot is courtesy of T. Levens .

C.6.1 Measurements during the experiment where the scan on the noise levels was performed

Figure C.6 illustrates the evolution of the rms bunch length measured in the SPS on May 16, 2022, for the four different levels of phase noise injected in the CC RF system increasing from the top left to bottom right. The Wall Current monitor acquires the longitudinal bunch profiles, from which the bunch length is computed, once per turn. In the figures below, each point corresponds to the average bunch lengths from the profiles over 100 turns while the error bars indicate the standard deviation between them. **Is it correct that is acquires profiles once per turn?**

C.6.2 Measurements during the experiment where the scan on the octupole strength was performed

Figure C.6 illustrates the evolution of the rms bunch length measured in the SPS on May 16, 2022, for the four different octupole strengths used during the CC MD increasing from the top left to bottom right. The Wall Current monitor acquires the longitudinal bunch profiles, from which the bunch length is computed, once per

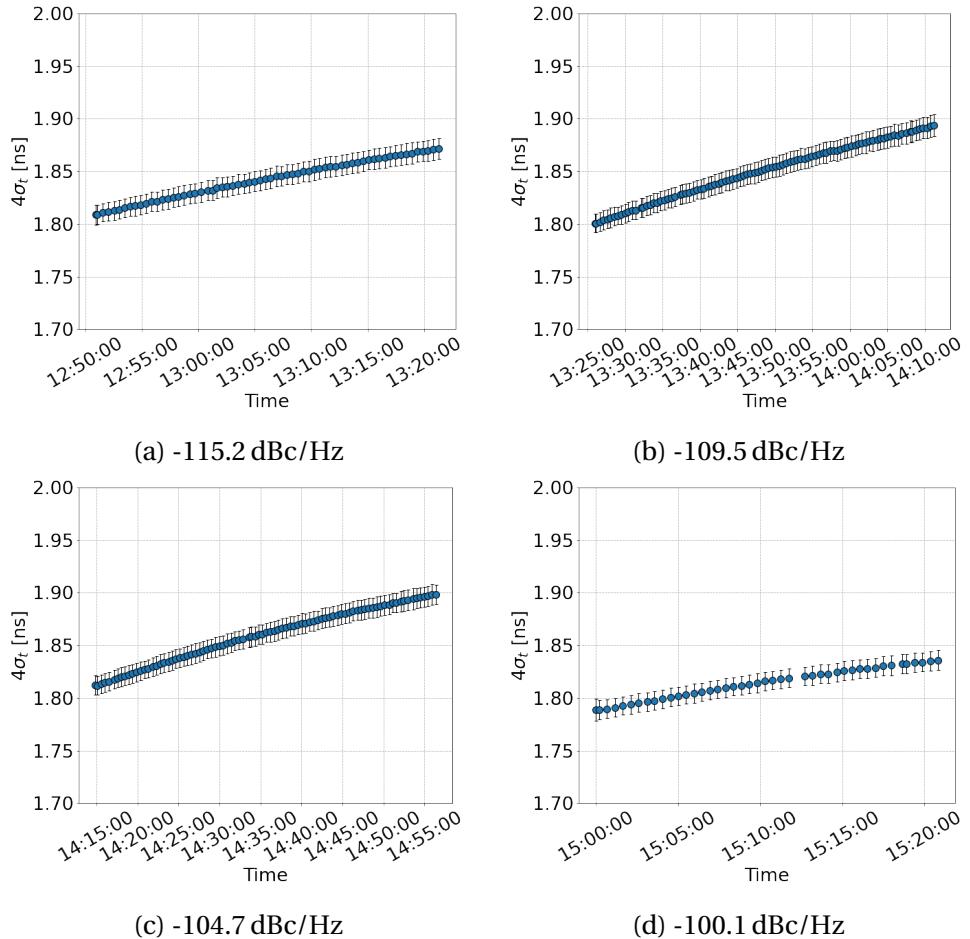


Figure C.6: Evolution of the bunch length during the CC experiment on May 16, 2022. The different phase noise levels injected in the RF system of CC1, are displayed at the captions of each plot.

turn. In the figures below, each point corresponds to the average bunch lengths from the profiles over 100 turns while the error bars indicate the standard deviation between them. **Is it correct that is acquires profiles once per turn?** This figure can be considered complementary of the plots in Fig. 7.7.

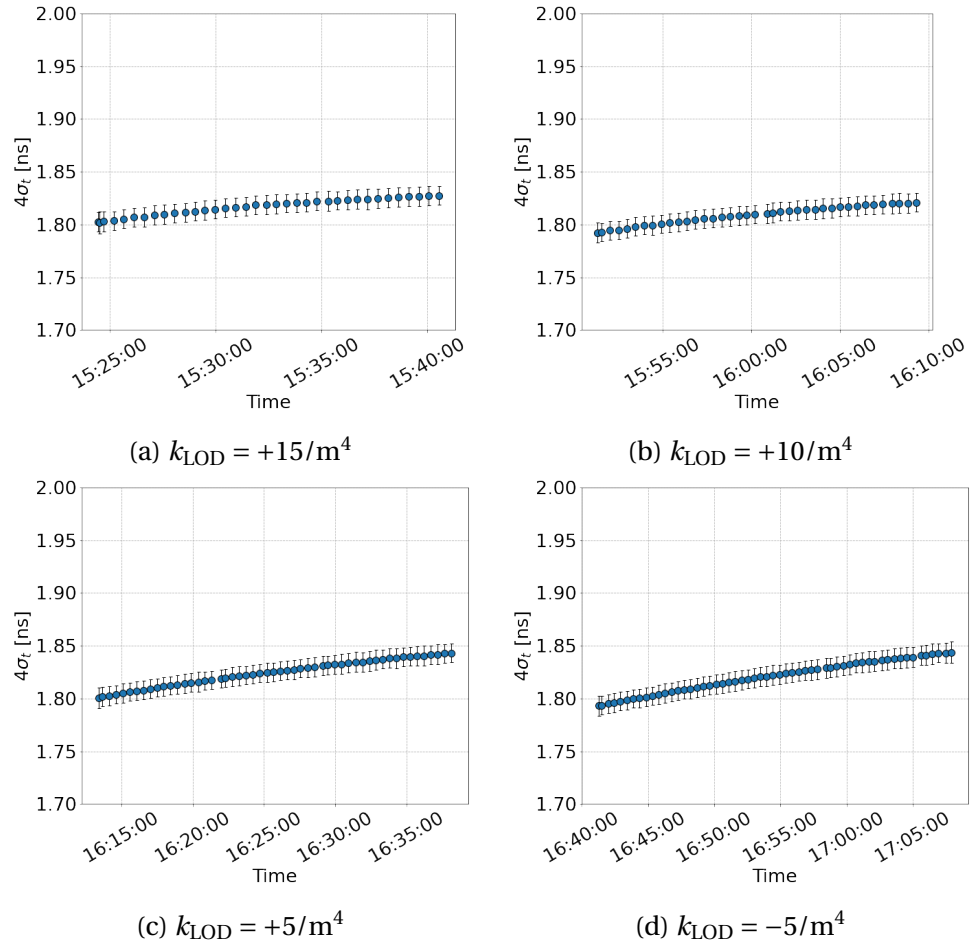


Figure C.7: Evolution of the bunch length during the CC experiment on May 16, 2022. The different octupole settings are displayed at the captions of each plot.

The average measured bunch length over all above coasts in 2022, was found to be, $4\sigma_t=1.83$ ns.

C.7 Transverse emittance growth measurements with dipole noise in 2022

The individual measurements of the transverse emittance evolution for each octupole setting during the experiment with dipole noise (see Section 7.3) are illustrated in Fig. C.8. The subplots are plotted in chronological order.

C. Appendix C

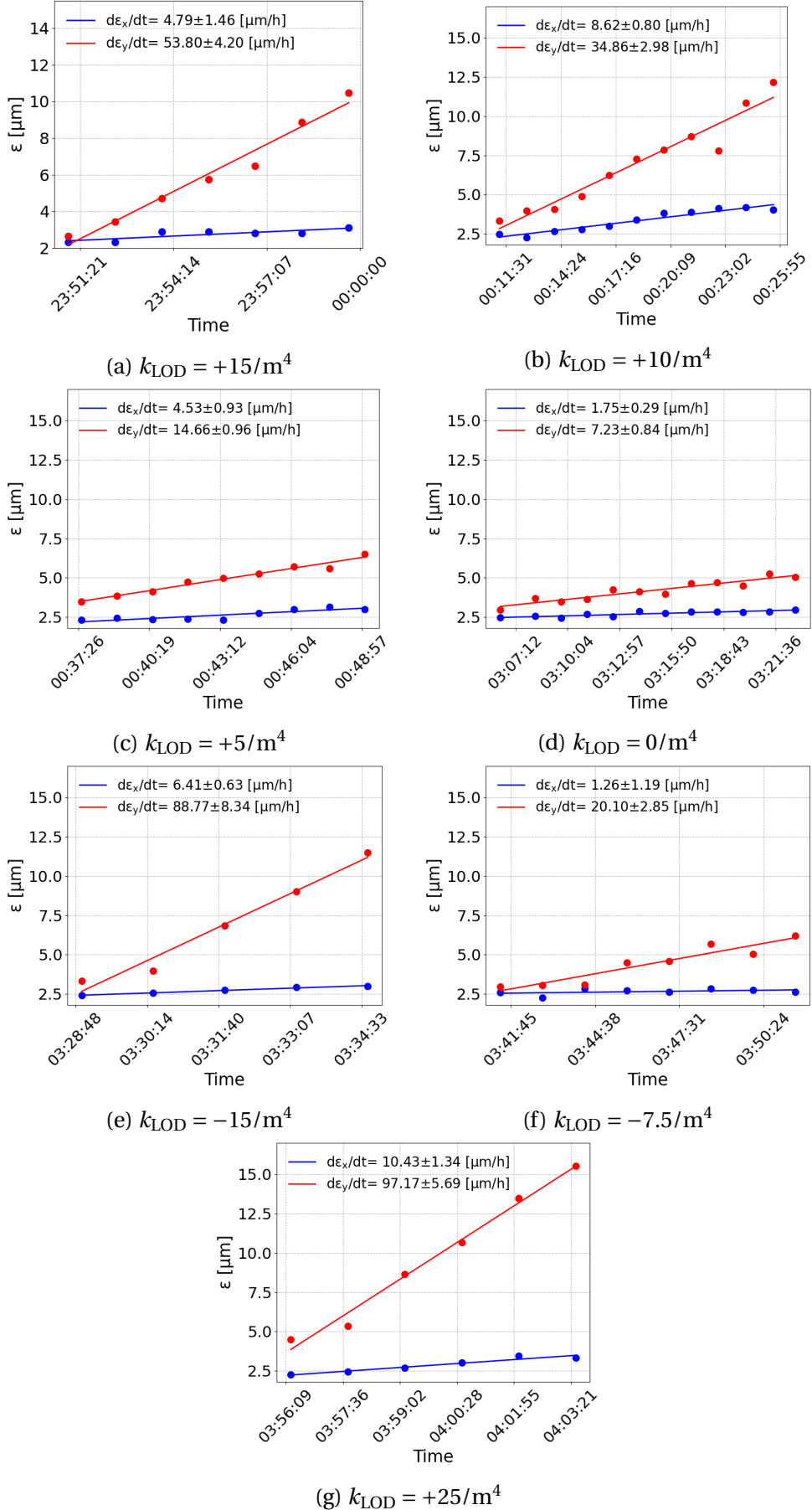


Figure C.8: Horizontal (blue) and vertical (red) emittance evolution of a single bunch during the experiment with dipole noise on May 16-17, 2022. The different quadrupole settings are displayed at the captions of each plot.

C.8 Transverse emittance growth measurements with CC RF noise - September 12, 2022

The individual measurements of the transverse emittance evolution for each octupole setting during the experiment with CC RF noise that took place on September 12, 2022 (see Section 7.4) are illustrated in Fig. C.9. The subplots are plotted in chronological order.

The measurements were conducted with artifical noise injected in the CC RF system which was a mixture of amplitude and phase noise. The phase noise was always dominant. The amplitude and phase noise level at the betatron frequency were measured to be -123.3 dBc/Hz and -103.3 dBc/Hz respectively.

C.9 Bunch length measurements in September 2022

Figure C.10 illustrates the evolution of the bunch length measured in the SPS on the September 12, 2022, for the five different octupole strengths used during the CC MD as acquired with the Wall Current Monitor. The subplots are plotted in chronological order. The Wall Current monitor acquires the longitudinal bunch profiles, from which the bunch length is computed, once per turn. In the figures below, each point corresponds to the average bunch lengths from the profiles over 100 turns while the error bars indicate the standard deviation between them. **Is it correct that is acquires profiles once per turn?**

The average measured bunch length over all above coasts in 2022, was found to be, $4\sigma_t=1.77$ ns.

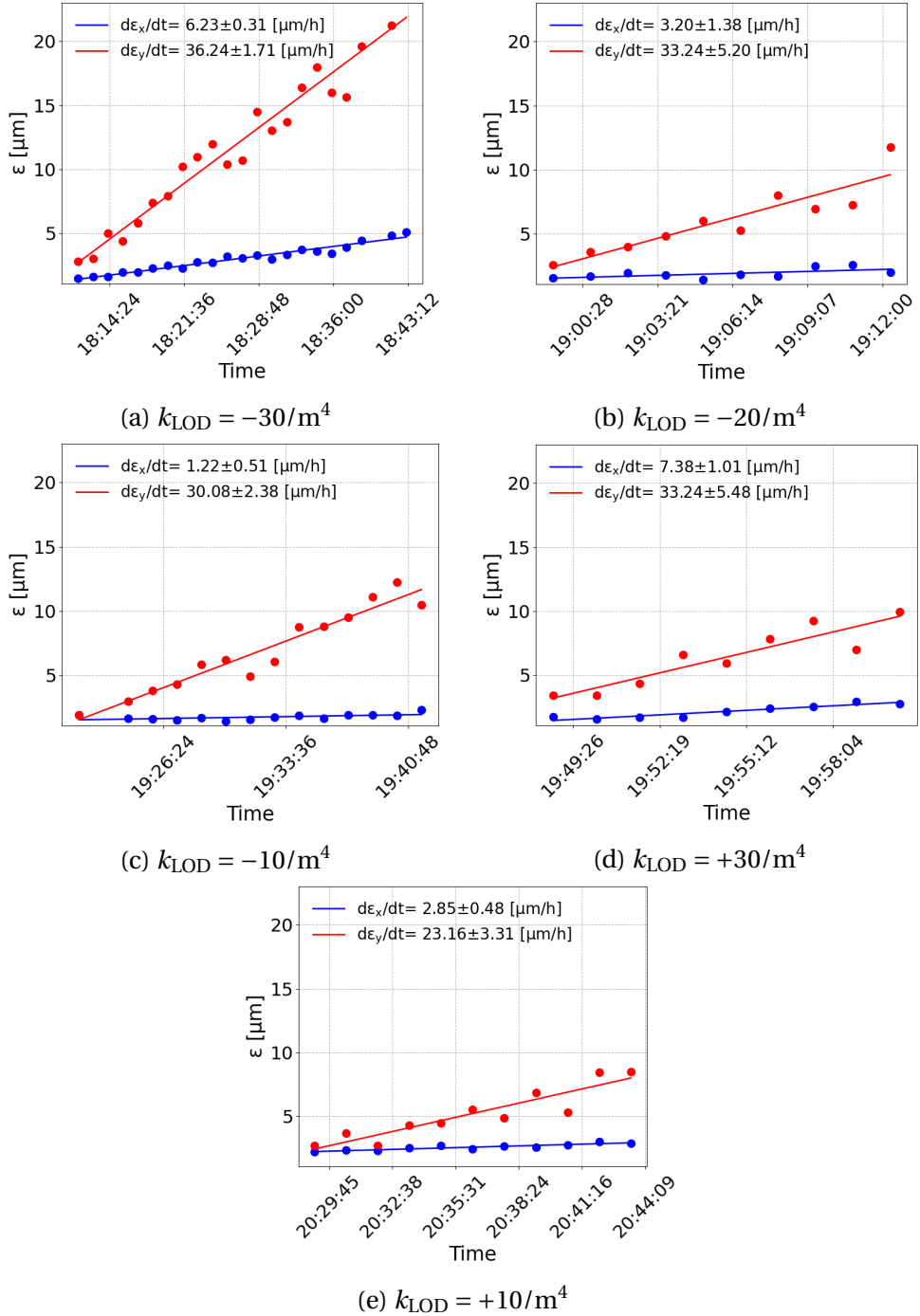


Figure C.9: Horizontal (blue) and vertical (red) emittance evolution of a single bunch during the experiment with dipole noise on September 12, 2022. The different octupole settings are displayed at the captions of each plot.

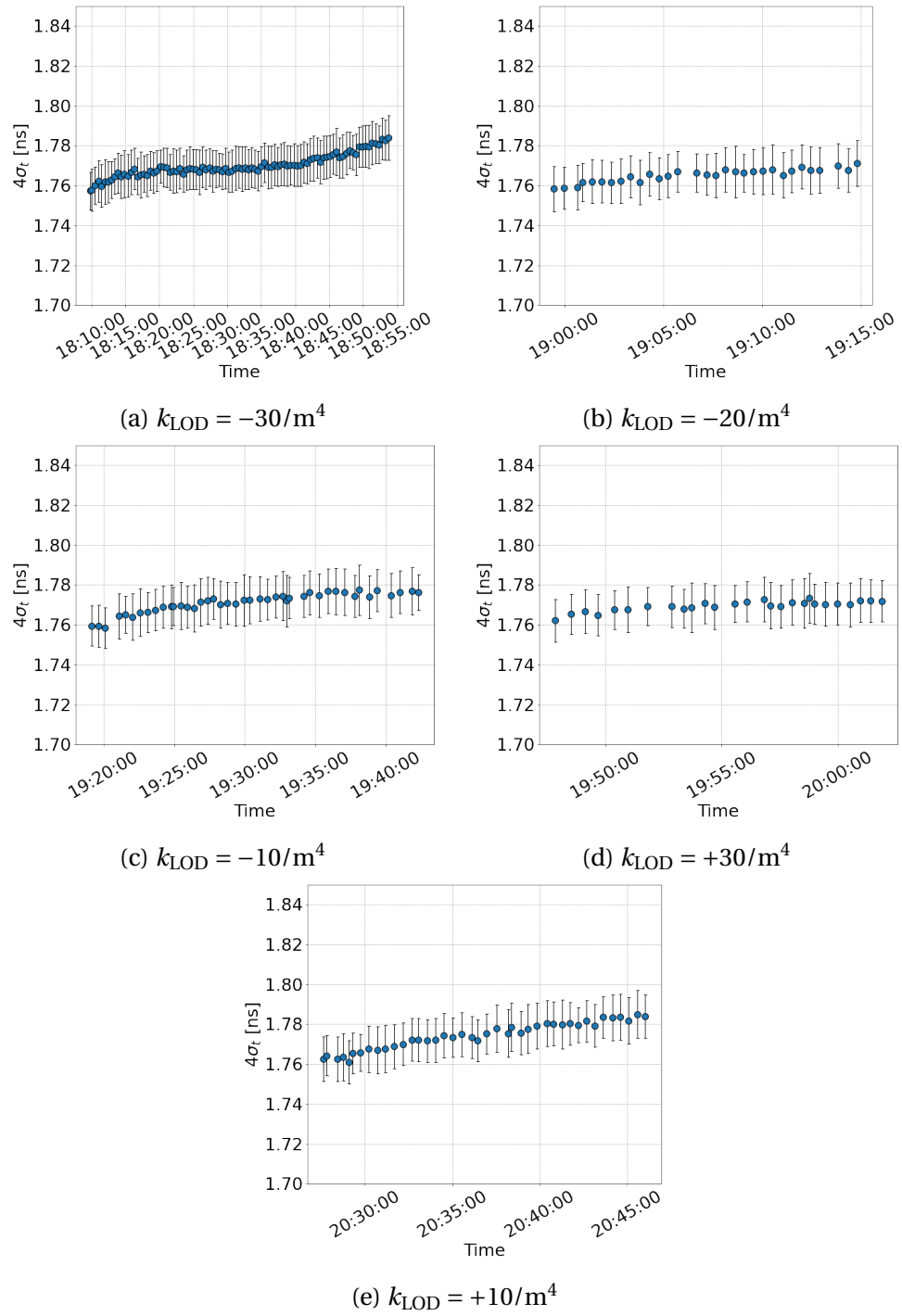


Figure C.10: Evolution of the bunch length during the CC experiment on September 12, 2022. The different octupole settings are displayed at the captions of each plot.

D | SPS Head-Tail monitor as the main diagnostic for the Crab Cavity studies

The SPS is equipped with a high bandwidth pick-up of approximately 2 GHz allowing to resolve the intra-bunch motion. This instrument is called Head-Tail (HT) monitor and was originally designed for measuring chromaticity and transverse instabilities. However, in the SPS CC tests, the Head-Tail monitor was the main diagnostic device deployed for the demonstration of the crabbing and the measurement of the CC voltage (explained in details in Section ??). Therefore its use as a crabbing diagnostic should be explained here. The methods and procedures described in this section were developed at CERN and they are described here for the completeness of the thesis.

In the first part of this section some general information on the instrument along with example signals will be presented. Subsequently, the post processing of the Head-Tail signal in the presence of the CC will be discussed. Last, the calibration of the CC voltage from the Head-Tail data is described and the visualisation of the crabbing is displayed. The experimental data presented in this section were acquired, on May 30, 2018 (time-stamp: 13:51:05), at the SPS injection energy of 26 GeV with only one CC, CC1, at phase $\phi_{\text{CC}} = 0$ (this means that the particle at the center of the bunch doesn't receive any transverse deflection) for simplicity. That energy of 26 GeV was chosen to provide a better understanding of the methods used as the orbit shift from the CC kick is stronger and thus more visible than at higher energies.

D.1 General information

As already mentioned, the Head-Tail monitor [75] is a high bandwidth version of a standard beam position monitor, which means that it can measure the transverse displacement within the bunch. For reference it has a resolution of 100 ps while the length of the bunches is $4\sigma_t \sim 2$ ns [133]. This makes it ideal for the measurement of the intra-bunch offset caused from the CC kick. Its reading consists of the sum (Σ) and the difference (Δ) of the electrode signals of a straight stripline coupler (Fig. D.1) [134, 135] over a defined acquisition period. The sum signal is the longitudinal line density while the difference signal corresponds to the intra-bunch offset. The system operates on timescales such that the signals are given as a function of the position within the bunch.

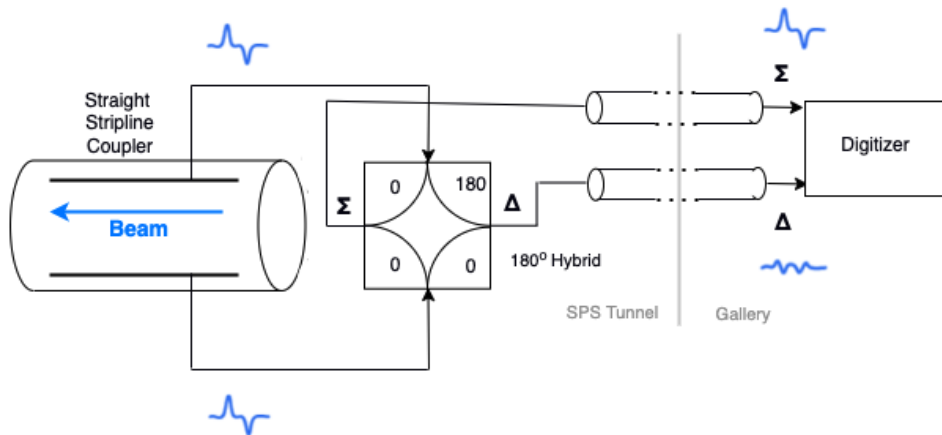


Figure D.1: Diagram of the SPS Head-Tail monitor [135]. The beam is passing through a straight stripline coupler which is followed by a 180° hybrid. This configuration provides the sum (Σ) and the difference (Δ) signal of the two electrodes.

The raw signals from the Head-Tail monitor require a specific post-processing procedure [135], in order to provide useful information. Figure D.2 shows some example signals obtained from the Head-Tail monitor after the basic post-processing is applied. Moreover, Fig. D.3 shows a 2D representation of the Head-Tail monitor reading. It is worth noting here that in the specific example a clear modulating pattern in time of the vertical intra-bunch offset (vertical Δ) signal is observed. This is a result of the phase slip between the CC and the main RF system because they are not yet synchronised.

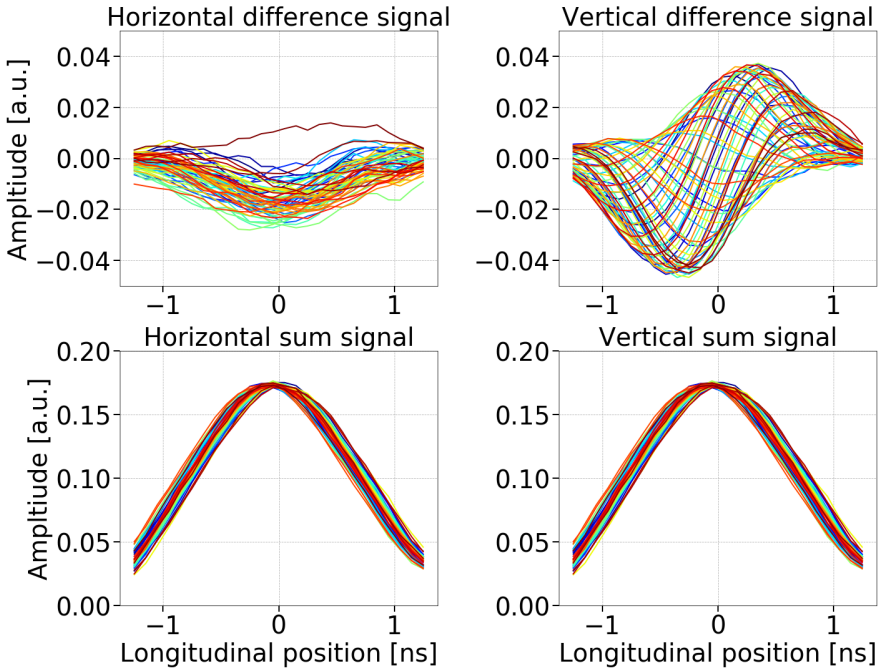


Figure D.2: Example difference and sum signals (top and bottom plots, respectively) from the Head-Tail monitor, in time scale, with respect to the longitudinal position within the bunch over several SPS revolutions, after the basic post processing [135] but before the baseline correction. The different colors indicate the signals from different turns (every 100 turns).

D.2 Post processing in the presence of Crab Cavities

To obtain useful information from the Head-Tail monitor signal in the presence of the CCs there are a few steps that differ from the standard post processing procedure and they are described below.

D.2.1 Head-Tail monitor baseline correction

The Head-Tail monitor measurement has a baseline on the difference signal which needs to be removed. The baseline is a result of orbit offsets and non-linearities of the instrument and is constant from turn to turn [135]. Therefore, during the normal post processing procedure (without CCs), the baseline is computed as the mean of the difference signals over all turns and then the correction is achieved by subtracting this static offset from the signal of each turn. However, in the SPS tests, where the CCs are well synchronised with the main RF system (Section 4.1.1), the

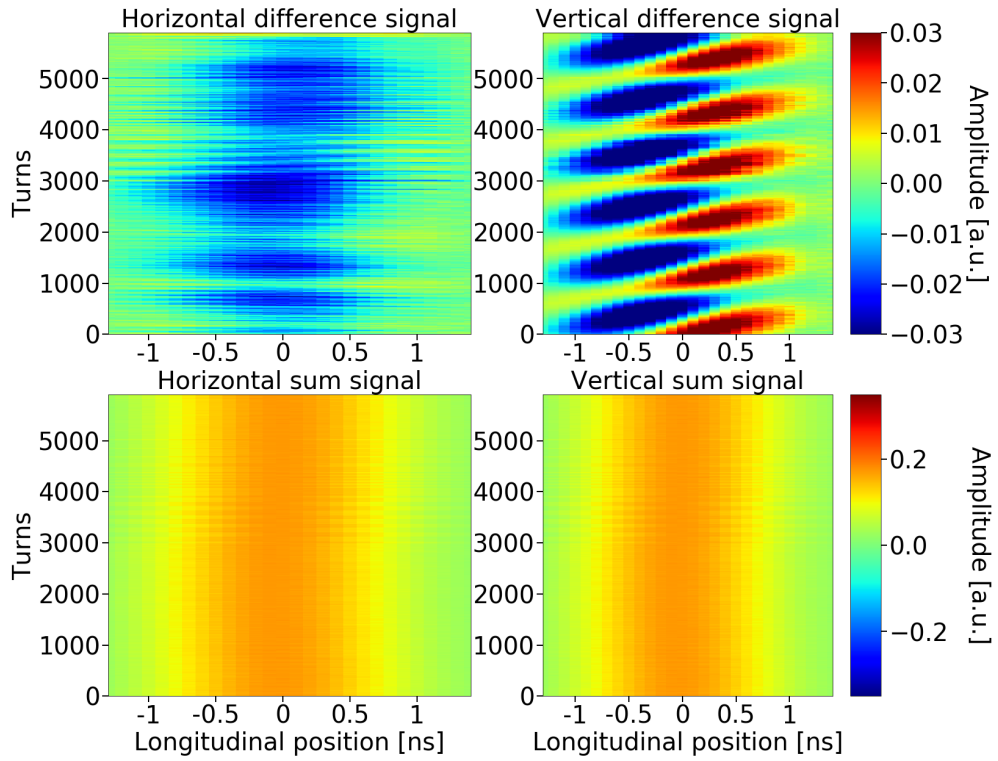


Figure D.3: 2D representation of example difference and sum signals with respect to the longitudinal position within the bunch obtained from the Head-Tail monitor over several SPS revolutions.

crabbing signal is also a static intra-bunch position offset and thus would also be removed with the usual method. Because of technical limitations it was not feasible to switch off the CC for those kind of measurements. Thus, the following technique was used.

For the CC experiments a reference measurement had first to be made with the CC not being synchronous with the main RF system. The baseline was computed as the mean of the difference signals over this reference period and subsequently it was subtracted from the average of the difference signals acquired after the synchronisation (Fig D.4). The datasets before and after synchronisation are easily distinguishable in the 2D HT monitor reading as displayed in Fig. D.5.

Head-Tail monitor scaling

The last step to make the Head-Tail acquisitions meaningful is to convert the measured intra bunch offset (the mean of the difference signals following phase synchronisation and baseline correction) from arbitrary units to millimeters. The scaling is achieved by dividing by the mean of the sum signals (which is a function

D. SPS Head-Tail monitor as the main diagnostic for the Crab Cavity studies

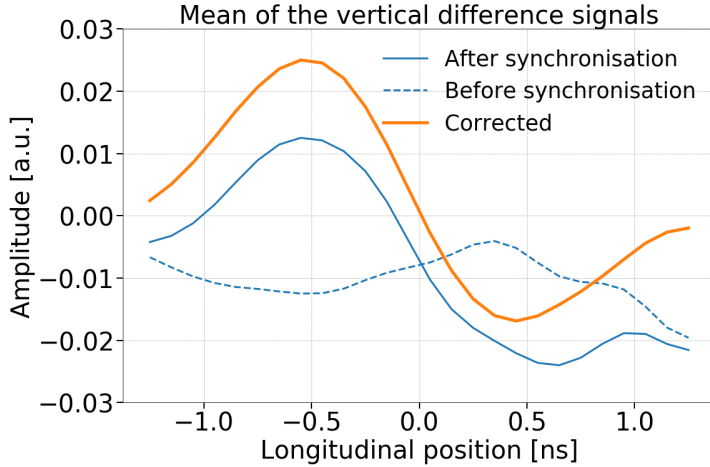


Figure D.4: Head-Tail monitor baseline correction for the SPS CC tests. The baseline signal (blue dashed line) refers to the mean of the difference signals acquired before the CC - main RF synchronisation. The measured signal (blue solid line) corresponds to the mean of the difference signal acquired after the synchronisation. Last, the corrected signal (orange solid line) is obtained after subtracting the baseline from the measured signal.

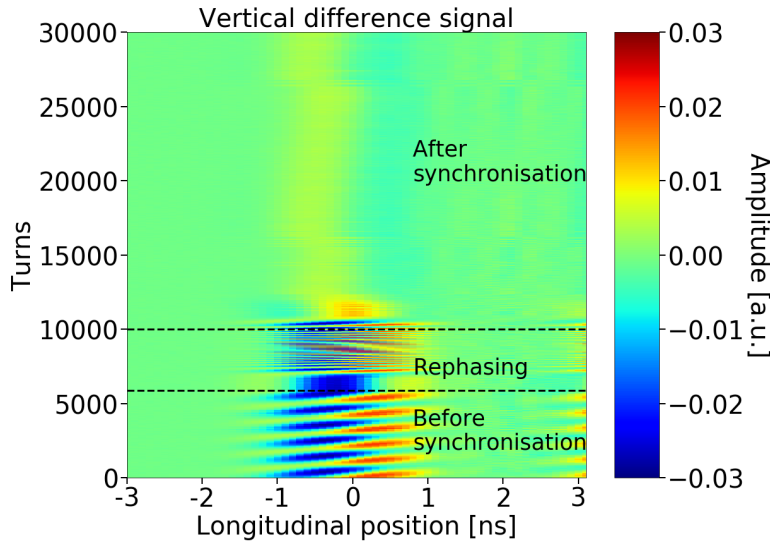


Figure D.5: Head-Tail acquisitions before and after the synchronisation of the SPS main RF with the CC.

of the position along the bunch and is calculated for each point individually over many turns) after the synchronisation and with a normalisation factor which is provided by the calibration of the Head-Tail monitor [132]. The normalisation factor for the SPS was measured at 0.1052 in 2018 [136]. Figure D.6 shows the intra-bunch offset from the CC kick in millimeters and after the baseline correction.

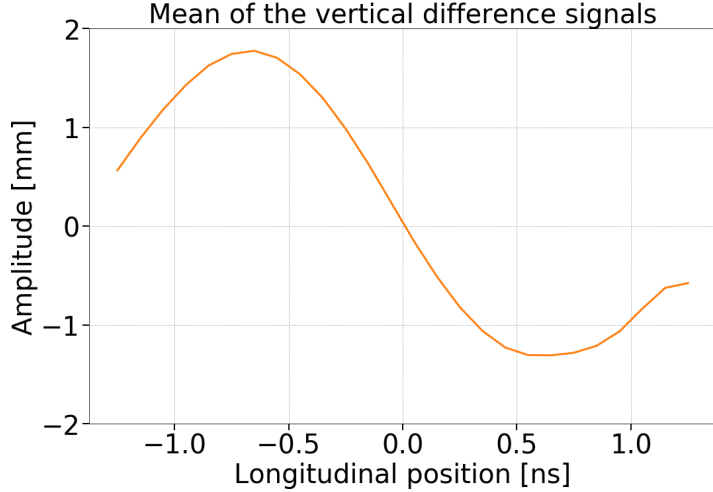


Figure D.6: Intra-bunch offset from the CC kick expressed in millimeters after the removal of the baseline.

D.2.2 Crab Cavity voltage reconstruction

This section discusses the reconstruction of the CC voltage from the HT monitor signal. First, Eq. (D.1) was used to calculate the CC kick, θ , required to reconstruct the measured intra-bunch offset. Equation (D.1), which is obtained from Eq. (1) from chapter 4.7.1 in Ref. [89], gives the vertical orbit shift (in meters) from the CC kick, θ , at the Head-Tail monitor location as follows:

$$\Delta y_{HT} = \frac{\sqrt{\beta_{y,HT}}}{2 \sin(\pi Q_{y0})} \theta \sqrt{\beta_{y,CC}} \cos(\pi Q_{y0} - |\psi_{y,HT} - \psi_{y,CC}|), \quad (D.1)$$

where β_y is the beta function, Q_{y0} is the tune, and $|\psi_{y,HT} - \psi_{y,CC}|$ is the vertical phase advance (in radians) between the CC and the Head-Tail monitor. The same applies for the horizontal plane. The subscripts Head-Tail and CC indicate quantities at the location of the Head-Tail monitor and CC respectively.

The CC voltage is then reconstructed from the CC kick which is written as $\theta = -\frac{qV_{CC}(t)}{E_b}$, where q is the charge of the particle, E_b the beam energy and $V_{CC}(t) = V_{CC} \sin(2\pi f_{CC} t + \phi_{CC})$ is the voltage that a particle experiences while passing through the CC. In the context where the HT monitor measures the signal as a function of time, t , the voltage in the above formula is expressed accordingly as $V_{CC}(t)$, where $t = 0$ the center of the bunch as it passes through the Head-Tail

monitor.

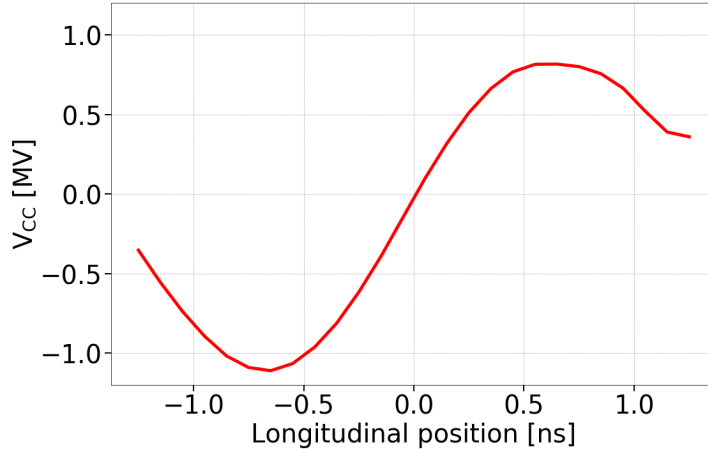


Figure D.7: CC voltage reconstruction from the HT monitor.

It should be noted here, that the measured intra-bunch offset, Δy_{HT} , is inserted in Eq. (D.1) after removing the baseline and converting it to millimeters as discussed in Section D.2. Figure D.7 illustrates the cavity voltage computed from the Head-Tail signals shown already in this section. The corresponding beam and optic parameters are listed in Table D.1.

Table D.1: Parameters for computing the CC voltage from the example Head-Tail monitor measurements discussed in this chapter.

Parameter	Value
Beta function at the Head-Tail monitor, $\beta_{y,HT}$	49.19 m
Phase advance to the Head-Tail monitor*, $\psi_{y,HT}$	$15.68 \times 2\pi$
Beta function at the CC1, $\beta_{y,CC1}$	76.07 m
Phase advance to the CC1*, $\psi_{y,CC1}$	$23.9 \times 2\pi$
Vertical betatron tune, Q_{y0}	26.18
Beam energy, E_b	26 GeV

* The phase advances are measured from the start of the lattice which is considered the element QE10010 that is a focusing quadrupole.

D.2.3 Demonstration of crabbing with proton beams

Additionally, the measurements from the Head-Tail monitor were used for reconstructing the crabbing and representing schematically the beam projection in the transverse plane. The technique for reconstructing the crabbing was developed at CERN in 2018 and was extensively used throughout the experimental campaign with CCs since (together with the calibrated voltage) it gives a straightforward estimate of the applied CC kick, as illustrated in Fig. D.8.

To obtain this schematic representation, which in practice is a density plot showing the effect of the CC kick on the beam, one needs to multiply the measured longitudinal profile (the mean of the sum signals acquired after phase synchronisation) with the measured intra-bunch offset, mean of the difference signals acquired after the synchronisation. An example of this is shown in Fig. D.6. For the transverse plane a gaussian distribution is considered with σ obtained from the wire scanner (addressed in more detail in the Section 4.5.1). The color code of Fig. D.8 is normalised to the maximum intensity within the bunch.

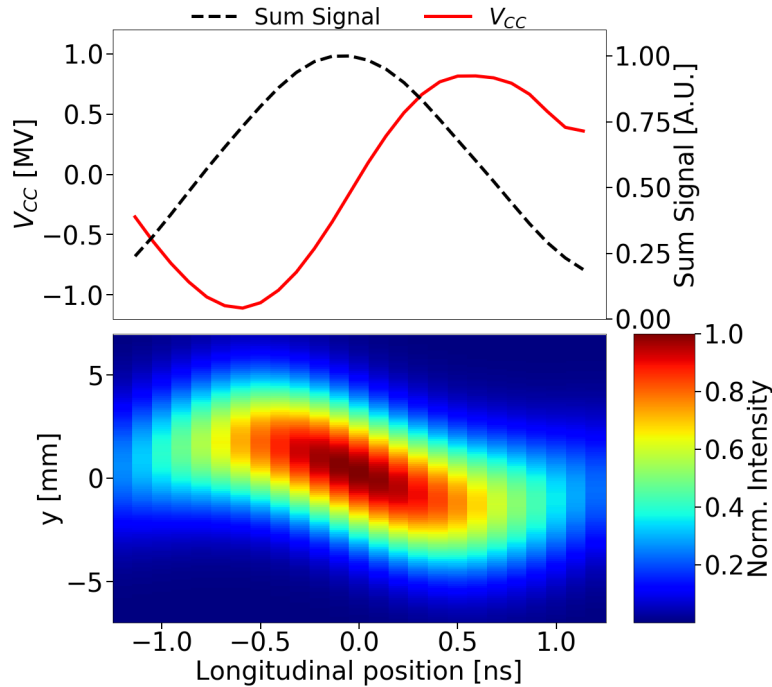


Figure D.8: Demonstration of the crabbing from the Head-Tail monitor signal. CC voltage and sum signal (longitudinal line density) measured from the Head-Tail monitor (top) together with the density plot (bottom) which visualises the effect of the CC kick on the beam.

E | Glossary and definitions

Peak to peak: Peak-to-peak (pk-pk) is the difference between the maximum positive and the maximum negative amplitudes of the wave.

<https://electronics.stackexchange.com/questions/313269/peak-to-peak-vs-amplitude>

Landau octupoles

Check the HL-LHC report to take ideas.

Bibliography

- [1] Oliver Sim Brüning et al. *LHC Design Report*. CERN Yellow Reports: Monographs. Geneva: CERN, 2004. doi: 10.5170/CERN-2004-003-V-1. URL: <https://cds.cern.ch/record/782076>.
- [2] ATLAS collaboration. “Observation of a new particle in the search for the Standard Model Higgs boson with the ATLAS detector at the LHC”. In: *Physics Letters B* 716 (1) (2012), pp. 1–29. URL: <https://www.sciencedirect.com/science/article/pii/S037026931200857X>.
- [3] CMS collaboration. “Observation of a new boson at a mass of 125 GeV with the CMS experiment at the LHC”. In: *Physics Letters B* 716 (1) (2012), pp. 30–61. URL: <https://www.sciencedirect.com/science/article/pii/S0370269312008581>.
- [4] CERN Yellow Reports: Monographs. *CERN Yellow Reports: Monographs, Vol. 10 (2020): High-Luminosity Large Hadron Collider (HL-LHC): Technical design report*. en. 2020. doi: 10 . 23731 / CYRM - 2020 - 0010. URL: <https://e-publishing.cern.ch/index.php/CYRM/issue/view/127>.
- [5] Oliver Brüning and Lucio Rossi. *The High Luminosity Large Hadron Collider*. WORLD SCIENTIFIC, Feb. 2015. doi: 10.1142/9581. URL: <https://doi.org/10.1142/9581>.
- [6] W. Herr. “*Particle Colliders and Concept of Luminosity*”. at CERN Accelerator School. 2012. URL: <https://cas.web.cern.ch/sites/default/files/lectures/constanta-2018/l1.pdf>.

E. Bibliography

- [7] O. Brüning and L. Rossi. *The High Luminosity Large Hadron Collider: the New Machine for Illuminating the Mysteries of Universe*. Vol. 24. World Scientific Publishing Company, 2015.
- [8] Rama Calaga. “Crab Cavities for the High-luminosity LHC”. In: (2018), THXA03. 5 p. DOI: 10 . 18429 / JACoW - SRF2017 - THXA03. URL: <https://cds.cern.ch/record/2673544>.
- [9] Hans Peter Beck. *First Results from the Large Hadron Collider*. Accessed: 24-06-2022. URL: <https://www.sps.ch/artikel/progresses/first-results-from-the-large-hadron-collider-24>.
- [10] Silvia Verdú-Andrés. *Design and Prototyping of HL-LHC Double Quarter Wave Crab Cavities*. Talk presented at th International Particle Accelerator Conference in 2015, Richmond VA (USA). Accessed: 24-06-2022. URL: https://accelconf.web.cern.ch/IPAC2015/talks/mobd2_talk.pdf.
- [11] Silvia Verdú-Andrés et al. “Crab cavities for colliders: past, present and future”. In: *Nucl. Part. Phys. Proc.* 273-275 (2016), 193–197. 5 p. DOI: 10 . 1016 / j . nuclphysbps . 2015 . 09 . 025. URL: <https://cds.cern.ch/record/2263119>.
- [12] C. et al Zanoni. “Design of Dressed Crab Cavities for the HL-LHC Upgrade”. In: (2015), THPB070. 5 p. DOI: 10.18429 / JACoW- SRF2015 - THPB070. URL: <https://cds.cern.ch/record/2288282>.
- [13] Subashini De Silva et al. “Electromagnetic Design of 400 MHz RF-Dipole Crabbing Cavity for LHC High Luminosity Upgrade”. In: (2015), THPB053. 5 p. DOI: 10 . 18429 / JACoW - SRF2015 - THPB053. URL: <https://cds.cern.ch/record/2288607>.
- [14] Binping Xiao et al. “Design, prototyping and testing of a compact superconducting double quarter wave crab cavity”. In: *Phys. Rev. Spec. Top. Accel. Beams* 18 (Feb. 2015), 041004. 10 p. DOI: 10 . 1103 / PhysRevSTAB . 18 . 041004. arXiv: 1502 . 04088. URL: <https://cds.cern.ch/record/1992565>.

- [15] S Verdú-Andrés et al. “Design and Prototyping of HL-LHC Double Quarter Wave Crab Cavities for SPS Test”. In: (May 2015), 3 p. URL: <https://cds.cern.ch/record/2113440>.
- [16] N Toge. *KEK B-factory Design Report*. Tech. rep. Tsukuba: KEK, 1995. URL: <https://cds.cern.ch/record/475260>.
- [17] T. et al. Abe. “Beam operation with crab cavities at KEKB”. In: *2007 IEEE Particle Accelerator Conference (PAC), Albuquerque, New Mexico, USA*. Vol. TUPAN045. 2007, pp. 1487–1489. DOI: 10.1109/PAC.2007.4440798.
- [18] Y. Funakoshi. “Operational experience with crab cavities at KEKB”. In: (Oct. 2014). Comments: 10 pages, contribution to the ICFA Mini-Workshop on Beam-Beam Effects in Hadron Colliders, CERN, Geneva, Switzerland, 18-22 Mar 2013, 27–36. 10 p. DOI: 10.5170/CERN-2014-004.27. arXiv: 1410.4036. URL: <https://cds.cern.ch/record/1955812>.
- [19] K. Oide et al. “Compensation of the Crossing Angle with Crab Cavities at KEKB”. In: *Proc. PAC'07* (Albuquerque, NM, USA, Jun. 2007). JACoW Publishing, Geneva, Switzerland, pp. 27–31. URL: <https://jacow.org/p07/papers/MOZAKI01.pdf>.
- [20] R. et al. Calaga. “First demonstration of the use of crab cavities on hadron beams”. In: *Phys. Rev. Accel. Beams* 24 (2021), 062001. 6 p. DOI: 10.1103 / PhysRevAccelBeams.24.062001. URL: <https://cds.cern.ch/record/2773279>.
- [21] Androula Alekou et al. “Beam dynamics simulations with Crab Cavities in the SPS machine”. In: (2019), MOPGW095. 4 p. DOI: 10 . 18429 / JACoW - IPAC2019 - MOPGW095. URL: <https://cds.cern.ch/record/2696109>.
- [22] C. Zanoni et al. “The crab cavities cryomodule for SPS test”. In: 874 (July 2017), p. 012092. DOI: 10 . 1088 / 1742 - 6596 / 874 / 1 / 012092. URL: <https://doi.org/10.1088/1742-6596/874/1/012092>.
- [23] Luis Eduardo Medina Medrano et al. *Effective pile-up density as a measure of the experimental data quality for High-Luminosity LHC operational scenarios*. Tech. rep. Geneva: CERN, Jan. 2018. URL: <https://cds.cern.ch/record/2301928>.

E. Bibliography

- [24] T. Mastoridis P. Baudrenghien. *Crab Cavity RF noise: Update 2*. Accessed: 27-06-2022. URL: https://indico.cern.ch/event/1044711/contributions/4389271/attachments/2264292/3861025/CC_Noise_Feedback_PB.pdf.
- [25] I. Ilias Efthymiopoulos. *Luminosity estimates including noise from crab cavities (without feedback)*. Accessed: 27-06-2022. URL: https://indico.cern.ch/event/1044711/contributions/4389268/attachments/2264203/3844208/ie_WP2CCemitBU_14.06.2021.pdf.
- [26] Andrzej Wolski. *Beam Dynamics in High Energy Particle Accelerators*. Imperial College Press, 2014.
- [27] Helmut Wiedemann. *Particle accelerator physics; 4th ed.* Berlin: Springer, 2015. DOI: 10 . 1007 / 978 - 3 - 319 - 18317 - 6. URL: <https://link.springer.com/content/pdf/10.1007/978-3-319-18317-6.pdf>.
- [28] S Y Lee. *Accelerator physics; 3rd ed.* Singapore: World Scientific, 2012. URL: <https://cds.cern.ch/record/1425444>.
- [29] R A Beth. “Complex Methods for Three-Dimensional Magnetic Fields”. In: (1971). URL: <https://cds.cern.ch/record/889480>.
- [30] Tarsi Prebibaj. *Transverse Emittance and Brightness Studies at Extraction of the CERN PS Booster*. Accessed: 12-07-2021. URL: https://indico.cern.ch/event/849052/contributions/3567761/attachments/1910604/3166225/semfe_thesis_presentation_tprebibaj_final.pdf.
- [31] Jean Buon. “Beam phase space and emittance”. In: (Dec. 1990), 23 p. DOI: 10.5170/CERN-1991-004.30. URL: <https://cds.cern.ch/record/216507>.
- [32] Bernhard Holzer. *Introduction to Accelerator Physics Beam Dynamics for Summer Students*. Accessed: 13-07-2021. URL: https://indico.cern.ch/event/91711/attachments/1096595/1564350/Summer_Stud_Holzer_2010.pdf.
- [33] David Newton and Andy Wolski. *Design of Electron Storage and Damping Rings, Part 5: Coupling and Alignment*. Accessed: 13-07-2021. URL: <https://uspas.fnal.gov/materials/13CSU/Lecture5.pdf>.

- [34] G Rumolo. “Beam Instabilities”. In: (2014). Comments: 21 pages, contribution to the CAS - CERN Accelerator School: Advanced Accelerator Physics Course, Trondheim, Norway, 18-29 Aug 2013, 21 p. DOI: 10.5170/CERN-2014-009.199. URL: <https://cds.cern.ch/record/1982422>.
- [35] Jacques Gareyte, Jean-Pierre Koutchouk, and F Ruggiero. *Landau damping dynamic aperture and octupole in LHC*. Tech. rep. revised version number 1 submitted on 2003-08-21 14:12:02. Geneva: CERN, Feb. 1997. URL: <https://cds.cern.ch/record/321824>.
- [36] W Herr. “Introduction to Landau Damping”. In: (2014). Comments: 27 pages, contribution to the CAS - CERN Accelerator School: Advanced Accelerator Physics Course, Trondheim, Norway, 18-29 Aug 2013, 27 p. DOI: 10.5170 / CERN-2014-009.377. URL: <https://cds.cern.ch/record/1982428>.
- [37] Elias Metral. *Longitudinal beam dynamics*. Accessed: 19-07-2021. URL: http://emetal.web.cern.ch/JUAS/2016/LongitudinalBeamDynamics_JUAS2016_EM.pdf.
- [38] Edwin M. McMillan. “The Synchrotron-A Proposed High Energy Particle Accelerator”. In: *Phys. Rev.* 68 (1945), pp. 143–144. DOI: 10.1103/PhysRev.68.143.
- [39] Veksler V. I. “A new method of accelerating relativistic particles”. In: *Dokl. Akad. Nauk SSSR* 44 (1944). (in Russian), pp. 346–348.
- [40] Veksler V. I. “About the bew method of accelerating relativistic particles”. In: *Dokl. Akad. Nauk SSSR* 44 (1944). (in Russian), pp. 393–366.
- [41] Frank Zimmermann. “Introduction to Collective Effects in Particle Accelerators”. In: *ICFA Beam Dyn. Newslett.* 69 (2016), 8–17. 10 p. URL: <https://cds.cern.ch/record/2264408>.
- [42] Giovanni Rumolo and Kevin Li. *Instabilities Part II: Longitudinal wake fields - impact on machine elements and beam dynamics*. Accessed: 20-07-2022. URL: https://indico.cern.ch/event/509762/contributions/2450946/attachments/1515079/2373718/London2_Longitudinal_v04a.pdf.

E. Bibliography

- [43] Benoit Salvant. *Building the impedance model of a real machine*. Accessed: 20-07-2022. URL: https://accelconf.web.cern.ch/ipac2019/talks/weyp1s1_talk.pdf.
- [44] Alexander Wu Chao. *Physics of collective beam instabilities in high energy accelerators*. New York, NY: Wiley, 1993. URL: <http://cds.cern.ch/record/246480>.
- [45] Michael Schenk. “A novel approach to Landau damping of transverse collective instabilities in future hadron colliders”. Presented 05 Feb 2019. 2019. URL: <https://cds.cern.ch/record/2665819>.
- [46] A Vlasov. “On the kinetic theory of an assembly of particles with collective interaction”. In: *Russ. Phys. J.* 9 (1945), pp. 25–40. URL: <http://cds.cern.ch/record/426186>.
- [47] Frank James Sacherer. *Methods for computing bunched-beam instabilities*. Tech. rep. Geneva: CERN, Sept. 1972. URL: <https://cds.cern.ch/record/322545>.
- [48] F J Sacherer. “Transverse bunched beam instabilities - Theory”. In: (Apr. 1974), 5 p. URL: <https://cds.cern.ch/record/322645>.
- [49] N. Biancacci, E. Métral, and M. Migliorati. “Fast-slow mode coupling instability for coasting beams in the presence of detuning impedance”. In: *Phys. Rev. Accel. Beams* 23 (12 Dec. 2020), p. 124402. DOI: 10 . 1103 / PhysRevAccelBeams . 23 . 124402. URL: <https://link.aps.org/doi/10.1103/PhysRevAccelBeams.23.124402>.
- [50] Laurent Deniau (editor). *MAD-X: Methodical Accelerator Design*. Accessed: 20-07-2022. URL: <https://mad.web.cern.ch/madx/>.
- [51] *Official optics repository of the CERN accelerators*. Accessed: 20-07-2022. URL: <https://gitlab.cern.ch/acc-models>.
- [52] *Official optics repository of the CERN Super Proton Synchrotron (official name SPS)*. Accessed: 16-2-2022. URL: <https://gitlab.cern.ch/acc-models/acc-models-sps/-/tree/2021/>.

- [53] *PyHEADTAIL code repository*. Accessed: 19-6-2022. URL: <https://github.com/PyCOMPLETE/>.
- [54] Adrian Oeftiger. *An overview of PyHEADTAIL*. Accessed: 05-06-2022. URL: <https://cds.cern.ch/record/2672381/files/CERN-ACC-NOTE-2019-0013.pdf>.
- [55] Michael Schenk. *Beam dynamics simulations with the PyHEADTAIL and PyECLOUD macroparticle codes*. Accessed: 05-06-2022. URL: https://www2.kek.jp/accl/legacy/seminar/file/PyHEADTAIL_PyECLOUD_2.pdf.
- [56] Benoit Salvant. “Impedance model of the CERN SPS and aspects of LHC single-bunch stability”. Presented on 04 Mar 2010. 2010. DOI: 10.5075/epfl-thesis-4585. URL: <https://cds.cern.ch/record/1274254>.
- [57] Volodymyr Rodin, A. Oeftiger, and Carsten Welsch. “Simulation of intra-beam scattering in PyHEADTAIL”. In: Nov. 2021. DOI: 10.18429/JACoW-IPAC2021-WEPAB215.
- [58] *Sixtracklib code repository*. Accessed: 20-07-2022. URL: <https://github.com/SixTrack/sixtracklib>.
- [59] Martin Schwinzerl et al. *Introducing Sixtracklib*. Accessed: 20-07-2022. URL: https://indico.cern.ch/event/833895/contributions/3577803/attachments/1927226/3190636/intro_sixtracklib.pdf.
- [60] Martin Schwinzerl et al. “Optimising and Extending A Single-Particle Tracking Library For High Parallel Performance. OPTIMISING AND EXTENDING A SINGLE-PARTICLE TRACKING LIBRARY FOR HIGH PARALLEL PERFORMANCE”. In: (Sept. 2021). DOI: 10 . 18429 / JACoW - IPAC2021 - THPAB190. URL: <https://cds.cern.ch/record/2781835>.
- [61] V Lebedev et al. “Emittance growth due to noise and its suppression with the feedback system in large hadron colliders”. In: *Part. Accel.* 44 (Mar. 1993), 147–164. 28 p. URL: <https://cds.cern.ch/record/248620>.
- [62] V Lebedev. “Computer simulation of the emittance growth due to noise in large hadron colliders”. In: *Part. Accel.* 44 (Mar. 1993), 165–199. 57 p. URL: <https://cds.cern.ch/record/248622>.

E. Bibliography

- [63] P. Baudrenghien and T. Mastoridis. “Transverse emittance growth due to rf noise in the high-luminosity LHC crab cavities”. In: *Phys. Rev. ST Accel. Beams* 18 (10 Oct. 2015), p. 101001. DOI: 10.1103/PhysRevSTAB.18.101001. URL: <https://link.aps.org/doi/10.1103/PhysRevSTAB.18.101001>.
- [64] K. Ohmi et al. “Response of colliding beam-beam system to harmonic excitation due to crab-cavity rf phase modulation”. In: *Phys. Rev. ST Accel. Beams* 14 (11 Nov. 2011), p. 111003. DOI: 10.1103/PhysRevSTAB.14.111003. URL: <https://link.aps.org/doi/10.1103/PhysRevSTAB.14.111003>.
- [65] Rama Calaga, Ofelia Capatina, and Giovanna Vandoni. “The SPS Tests of the HL-LHC Crab Cavities”. In: (2018), TUPAF057. 4 p. DOI: 10.18429/JACoW-IPAC2018-TUPAF057. URL: <https://cds.cern.ch/record/2649807>.
- [66] Carver Lee. *First proton beam dynamics results with crab cavities*. Accessed: 10-11-2021. URL: https://indico.cern.ch/event/800428/attachments/1804664/2945632/CrabCavity_BE_Seminar.pdf.
- [67] Philippe Baudrenghien. *SPS Crab Cavity test RF Test Program*. Accessed: 11-11-2021. URL: <https://indico.cern.ch/event/718127/contributions/2951305/attachments/1645650/2629988/SPSCCTestv3.pdf>.
- [68] R Calaga et al. “Proton-beam emittance growth in SPS coasts”. In: *Conf. Proc. C1205201* (May 2012), THPPP007. 3 p. URL: <https://cds.cern.ch/record/1451286>.
- [69] A Alekou et al. *Emittance growth in coast in the SPS*. Accessed: 26-11-2021. URL: https://indico.cern.ch/event/609486/contributions/2457542/attachments/1433340/2318716/EmittanceEvolutionCoastSPS_2017_April.pdf.
- [70] Fanouria Antoniou et al. “Emittance Growth in Coast in the SPS at CERN”. In: *J. Phys.: Conf. Ser.* 1067 (2018), MOPMF061. 7 p. DOI: 10.18429/JACoW-IPAC2018-MOPMF061. URL: <https://cds.cern.ch/record/2649815>.
- [71] Michele Carlà et al. “Studies of a New Optics With Intermediate Transition Energy as Alternative for High Intensity LHC Beams in the CERN SPS”. In: (2018), TUPAF022. 4 p. DOI: 10.18429/JACoW-IPAC2018-TUPAF022. URL: <https://cds.cern.ch/record/2664976>.

- [72] Androula Alekou et al. “SPS Long Term Stability Studies in the Presence of Crab Cavities and High Order Multipoles”. In: (2018), WEP2PO008. 3 p. DOI: 10.18429/JACoW-HB2018-WEP2PO008. URL: <https://cds.cern.ch/record/2640326>.
- [73] K. Gheen. *Phase Noise Measurement Methods and Techniques*. Accessed November 5, 2020. Agilent Technologies. URL: <https://studylib.net/doc/18034081/phase-noise-measurements>.
- [74] “IEEE Standard Definitions of Physical Quantities for Fundamental Frequency and Time Metrology—Random Instabilities”. In: *IEEE Std Std 1139-2008* (2009), pp. c1–35. DOI: 10.1109/IEEESTD.2008.4797525.
- [75] Kevin Shing Bruce Li. *SPS Head-Tail Monitor*. Accessed: 27-09-2022. URL: https://indico.cern.ch/event/931117/contributions/3913554/attachments/2096199/3523367/014_HeadtailMonitor.pdf.
- [76] Tom Levens. *Head-Tail Monitor for CC Diagnostics*. Accessed: 11-04-2022. URL: https://indico.cern.ch/event/826475/contributions/3457525/attachments/1872464/3081710/2019-07-02_HL_WP2_tlevens.pdf.
- [77] N. Triantafyllou et al. *Investigating the discrepancy between measured and expected emittance growth in SPS Crab Cavity tests*. Accessed: 27-09-2022. URL: https://indico.cern.ch/event/965718/contributions/4064170/attachments/2135267/3596606/WP4_3November_CCnoiseStudies.pdf.
- [78] J. Bosser et al. “Transverse emittance measurement with a rapid wire scanner at the CERN SPS”. In: *Nuclear Instruments and Methods in Physics Research Section A: Accelerators, Spectrometers, Detectors and Associated Equipment* 235.3 (1985), pp. 475–480. ISSN: 0168-9002. DOI: [https://doi.org/10.1016/0168-9002\(85\)90096-8](https://doi.org/10.1016/0168-9002(85)90096-8). URL: <https://www.sciencedirect.com/science/article/pii/0168900285900968>.
- [79] OE Berrig et al. *CERN-SPS Wire Scanner Impedance and Wire Heating Studies*. Tech. rep. Geneva: CERN, Sept. 2014. URL: <https://cds.cern.ch/record/1972478>.

E. Bibliography

- [80] Federico Roncarolo. “Accuracy of the Transverse Emittance Measurements of the CERN Large Hadron Collider”. Presented 2005. 2005. URL: <https://cds.cern.ch/record/1481835>.
- [81] *H. Bartosik personal communication, March, 2022.*
- [82] Rogelio Tomas et al. “Improved algorithms to determine the non-linear optics model of the SPS from non-linear chromaticity”. In: July 2007, pp. 4231–4233. ISBN: 978-1-4244-0916-7. DOI: 10.1109/PAC.2007.4439986.
- [83] Department of Physics University of Pennsylvania and Lab manual astronomy. *Managin errors and uncertainties*. Accessed: 18-03-2022. URL: <https://www.physics.upenn.edu/sites/default/files/Managing%20Errors%20and%20Uncertainty.pdf>.
- [84] Philippe Baudrenghien. *LLRF experience for SPS & HL-LHC Outlook*. Accessed: 11-11-2021. URL: <https://indico.cern.ch/event/787363/contributions/3367294/attachments/1865644/3067685/HL-LHC19v6.pdf>.
- [85] F. Follin G. Papotti. *Online bunch length measurement for SPS OP*. Accessed: 26-11-2021. URL: https://indico.cern.ch/event/774525/contributions/3218683/attachments/1756129/2847423/20181120_LIUSPSBD.pdf.
- [86] G. Papotti. “A Beam Quality Monitor for LHC Beams in the SPS”. In: (Sept. 2008), 4 p. URL: <https://cds.cern.ch/record/1124099>.
- [87] T. Argyropoulos. *Private communication, Nov 2020.*
- [88] *T. Mastoridis and P. Baudrenghien, personal communication, November 25, 2020.*
- [89] Alexander Wu Chao et al. *Handbook of accelerator physics and engineering; 2nd ed.* Singapore: World Scientific, 2013. DOI: 10.1142/8543. URL: <https://cds.cern.ch/record/1490001>.
- [90] *Repository of SPS impedance model*. Accessed: 3-6-2022. URL: https://gitlab.cern.ch/IRIS/SPS_IW_model.
- [91] Carlo Zannini. “Electromagnetic Simulation of CERN accelerator Components and Experimental Applications”. Presented 15 Apr 2013. Mar. 2013. URL: <https://cds.cern.ch/record/1561199>.

- [92] B Salvant et al. “Update of the SPS Impedance Model”. In: (June 2010), 3 p.
URL: <https://cds.cern.ch/record/1271349>.
- [93] Carlo Zannini et al. “Benchmarking the CERN-SPS Transverse Impedance Model with Measured Headtail Growth Rates”. In: (2015), MOPJE049. 4 p.
URL: <https://cds.cern.ch/record/2141779>.
- [94] J. Laskar. “The chaotic motion of the solar system: A numerical estimate of the size of the chaotic zones”. In: *Icarus* 88.2 (1990), pp. 266–291. ISSN: 0019-1035. DOI: [https://doi.org/10.1016/0019-1035\(90\)90084-M](https://doi.org/10.1016/0019-1035(90)90084-M). URL: <https://www.sciencedirect.com/science/article/pii/001910359090084M>.
- [95] Sofia Kostoglou et al. “Development of Computational Tools for Noise Studies in the LHC”. In: (2017), THPAB044. 4 p. DOI: 10 . 18429 / JACoW - IPAC2017 - THPAB044. URL: <https://cds.cern.ch/record/2289645>.
- [96] *NAFFlib code repository*. Accessed: 05-08-2022. URL: <https://github.com/PyCOMPLETE/NAFFlib>.
- [97] Mario Beck. “Numerical and experimental studies to model and reduce the impedance in the CERN Super Proton Synchrotron (SPS). Numerische und experimentelle Studien zur Modellierung und Reduzierung der Strahlimpedanz im Super Proton Synchrotron (SPS) Teilchenbeschleuniger”. Presented 08 Feb 2019. Dec. 2018. URL: <http://cds.cern.ch/record/2683038>.
- [98] H Bartosik et al. “TMCI thresholds for LHC single bunches in the CERN SPS and comparison with simulations”. In: (June 2016), 4 p. URL: <https://cds.cern.ch/record/1742183>.
- [99] Carlo Zannini et al. *SPS impedance-induced observables pre and post LS2*. Accessed: 06-08-2022. URL: https://indico.cern.ch/event/919160/contributions/3863191/attachments/2040319/3417759/SPS_pre_and_postLS2_HSC.pdf.
- [100] *Updated SPS wakefields model repository*. Accessed: 12-08-2022. URL: https://github.com/natriant/exploring_SPS/tree/master/updated_wakefields_model.

E. Bibliography

- [101] Yu I Alexahin. “On the Landau Damping and Decoherence of Transverse Dipole Oscillations in Colliding Beams”. In: *Part. Accel.* 59 (Aug. 1996), 43–74. 19 p. URL: <https://cds.cern.ch/record/314169>.
- [102] Yu I Alexahin. “A study of the Coherent Beam-Beam Effect in the Framework of the Vlasov Perturbation Theory”. In: *Nucl. Instrum. Methods Phys. Res., A* 480 (2002), 253–88. 33 p. DOI: 10.1016/S0168-9002(01)01219-0. URL: <https://cds.cern.ch/record/485304>.
- [103] J. Qiang et al. “Simulation of beam-beam interaction with crab cavities for LHC upgrade”. In: *Nuclear Instruments and Methods in Physics Research Section A: Accelerators, Spectrometers, Detectors and Associated Equipment* 900 (2018), pp. 53–59. ISSN: 0168-9002. DOI: <https://doi.org/10.1016/j.nima.2018.05.055>. URL: <https://www.sciencedirect.com/science/article/pii/S0168900218306740>.
- [104] X. Buffat et al. “Modeling of the emittance growth due to decoherence in collision at the Large Hadron Collider”. In: *Phys. Rev. Accel. Beams* 23 (2 Feb. 2020), p. 021002. DOI: 10.1103/PhysRevAccelBeams.23.021002. URL: <https://link.aps.org/doi/10.1103/PhysRevAccelBeams.23.021002>.
- [105] Sondre Vik Furuseth et al. “Emittance growth suppression with a multibunch feedback in high-energy hadron colliders: Numerical optimization of the gain and bandwidth”. In: *Phys. Rev. Accel. Beams* 24 (1 Jan. 2021), p. 011003. DOI: 10.1103/PhysRevAccelBeams.24.011003. URL: <https://link.aps.org/doi/10.1103/PhysRevAccelBeams.24.011003>.
- [106] Yu I Alexahin et al. “Coherent Beam-Beam Effects in the LHC”. In: (Apr. 2001), 10 p. URL: <https://cds.cern.ch/record/497415>.
- [107] Werner Herr and M P Zorzano-Mier. *Coherent Dipole Modes for Multiple Interaction Regions*. Tech. rep. Geneva: CERN, Feb. 2001. URL: <https://cds.cern.ch/record/486007>.
- [108] W. Herr and T. Pieloni. “Beam-Beam Effects”. In: (Jan. 2016). 29 pages, contribution to the CAS - CERN Accelerator School: Advanced Accelerator Physics Course, Trondheim, Norway, 18-29 Aug 2013, 431–459. 29 p. DOI:

- 10 . 5170 / CERN - 2014 - 009 . 431. arXiv: 1601 . 05235. URL:
<https://cds.cern.ch/record/1982430>.
- [109] Friedhelm Caspers. “Schottky signals for longitudinal and transverse bunched-beam diagnostics”. In: (2009). DOI: 10.5170/CERN-2009-005.407. URL: <https://cds.cern.ch/record/1213284>.
- [110] M P Zorzano-Mier and Frank Zimmermann. “Simulations of coherent beam-beam modes at the Large Hadron Collider”. In: *Phys. Rev. Spec. Top. Accel. Beams* 3 (2000), p. 044401. DOI: 10.1103/PhysRevSTAB.3.044401. URL: <https://cds.cern.ch/record/446334>.
- [111] Xavier Buffat. “Suppression of Emittance Growth by a Collective Force: Van Kampen Approach”. In: *JACoW IPAC2022* (2022), WEPOTK059. DOI: 10.18429/JACoW-IPAC2022-WEPOTK059.
- [112] X. Buffat. *Crab Cavity experiments and underlying theory*. Accessed: 07-09-2022. URL:
https://indico.cern.ch/event/1170242/contributions/4915101/attachments/2476586/4250387/2022-07-07_crabMD-expanded.pdf.
- [113] A Boccardi et al. *The FPGA-based Continious FFT Tune Measurement System for the LHC and its test at the CERN SPS*. Tech. rep. Geneva: CERN, 2007. URL: <https://cds.cern.ch/record/1055568>.
- [114] K. Li. *Collective effects, Part IV: Coherent beam instabilities*. Accessed: 05-09-2022. URL: https://cas.web.cern.ch/sites/default/files/lectures/-27%20March%202022/Chavannes4_Instabilities.pdf.
- [115] N.G. Van Kampen. “On the theory of stationary waves in plasmas”. In: *Physica* 21.6 (1955), pp. 949–963. ISSN: 0031-8914. DOI: [https://doi.org/10.1016/S0031-8914\(55\)93068-8](https://doi.org/10.1016/S0031-8914(55)93068-8). URL: <https://www.sciencedirect.com/science/article/pii/S0031891455930688>.
- [116] Tatiana Pieloni. “A study of beam-beam effects in hadron colliders with a large number of bunches”. Presented on 4 Dec 2008. 2008. URL: <https://cds.cern.ch/record/1259906>.

E. Bibliography

- [117] X Buffat et al. “Modeling of the emittance growth due to decoherence in collision at the Large Hadron Collider”. In: *Phys. Rev. Accel. Beams* 23 (2020), 021002. 9 p. DOI: 10 . 1103 / PhysRevAccelBeams . 23 . 021002. URL: <https://cds.cern.ch/record/2712068>.
- [118] D. Valuch. *The LHC transverse damper: a multi-purpose system*. Accessed: 13-09-2022. URL: https://indico.cern.ch/event/775147/contributions/3366413/attachments/1913791/3164486/MCBI2019_-_LHC_transverse_feedback_a_multi_purpose_system.pdf.
- [119] P. Baudrenghien. *Crab Cavity RF Noise: Update 2*. Accessed: 13-09-2022. URL: https://indico.cern.ch/event/1044711/contributions/4389271/attachments/2264292/3861025/CC_Noise_Feedback_PB.pdf.
- [120] Philippe Baudrenghien, Themistoklis Mastoridis, and Benjamin Nicholas Miller. “Crab Cavity RF Noise Feedback and Transverse Damper Interaction”. In: (2019). URL: <https://cds.cern.ch/record/2665950>.
- [121] E. Metral. *Run 4 operational scenario and status of optics v1.6*. Accessed: 13-09-2022. URL: https://indico.cern.ch/event/1197424/contributions/5035904/attachments/2507124/4308131/HLLHCCollaborationMeeting_Uppsala_19-09-2022_EM.pdf.
- [122] R. J. Barlow. *Statistics. A Guide to the Use of Statistical Methods in the Physical Sciences*. Manchester Physics Series. Wiley, 2013. ISBN: 9781118723234. URL: <https://liverpool.idm.oclc.org/login?url=https://search.ebscohost.com/login.aspx?direct=true&db=cat00003a&AN=lvp.b3130057&site=eds-live&scope=site>.
- [123] K. K. Gan. *Chi Square Distribution (χ^2) and Least Squares fitting*. Accessed: 03-03-2022. URL: <https://www.asc.ohio-state.edu/gan.1/teaching/spring04/Chapter6.pdf>.
- [124] *SciPy API Documentation*. Accessed: 16-2-2022. URL: https://docs.scipy.org/doc/scipy/reference/generated/scipy.optimize.curve_fit.html.

- [125] William H. Press et al. *Numerical Recipes: The Art of Scientific Computing*. 3rd ed. USA: Cambridge University Press, 2007. ISBN: 0521880688. URL: http://www.e-maxx-ru.lgb.ru/bookz/files/numerical_recipes.pdf.
- [126] A. Papoulis. *Probability, Random Variables, and Stochastic Processes*. Communications and Signal Processing. McGraw-Hill, 1991. ISBN: 9780070484771. URL: <https://books.google.ch/books?id=4IwQAQAAIAAJ>.
- [127] R. Bracewell. *The Fourier Transform and its Applications*. 2nd ed. McGraw-Hill, 1986.
- [128] NumPy Project and Community. *NumPy API Documentation*. Accessed November 5, 2020. URL: <https://numpy.org/doc/stable/reference/routines.fft.html>.
- [129] Yannis Papaphilippou. *Transverse motion*. United States Particle Accelerator School, University of California - Santa Cruz, Santa Rosa, CA. Accessed: 14-07-2022. 2008. URL: <https://yannis.web.cern.ch/teaching/transverse.pdf>.
- [130] Hannes Bartosik et al. “Improved Methods for the Measurement and Simulation of the CERN SPS Non-linear Optics”. In: (2016), THPMR036. 4 p. DOI: 10 . 18429 / JACoW - IPAC2016 - THPMR036. URL: <https://cds.cern.ch/record/2207443>.
- [131] G. Kruk et al. *LHC SOFTWARE ARCHITECTURE [LSA] – EVOLUTION TOWARD LHC BEAM COMMISSIONING*.
- [132] T. E. Levens et al. “Automatic detection of transverse beam instabilities in the Large Hadron Collider”. In: *Phys. Rev. Accel. Beams* 22 (11 Nov. 2019), p. 112803. DOI: 10.1103/PhysRevAccelBeams.22.112803. URL: <https://link.aps.org/doi/10.1103/PhysRevAccelBeams.22.112803>.
- [133] Lee Carver et al. “First machine development results with HL-LHC crab cavities in the SPS. First machine developments result with HL-LHC crab cavities in the SPS”. In: (2019), MOPGW094. 4 p. DOI: 10 . 18429 / JACoW - IPAC2019 - MOPGW094. URL: <https://cds.cern.ch/record/2696108>.

E. Bibliography

- [134] R. Jones and H. Schmickler. “The measurement of Q' and Q" in the CERN-SPS by head-tail phase shift analysis”. In: *PACS2001. Proceedings of the 2001 Particle Accelerator Conference (Cat. No.01CH37268)*. Vol. 1. 2001, 531–533 vol.1. DOI: 10.1109/PAC.2001.987561.
- [135] Thomas Levens, Kacper Łasocha, and Thibaut Lefèvre. “Recent Developments for Instability Monitoring at the LHC”. In: (2017), THAL02. 4 p. DOI: 10 . 18429 / JACoW - IBIC2016 - THAL02. URL: <https://cds.cern.ch/record/2313358>.
- [136] Tom Levens. *Beam instrumentation with SPS Crabs*. Accessed: 11-11-2021. URL: https://indico.cern.ch/event/718127/contributions/2951309/attachments/1646050/2630808/BI_SPS_Crabs.pdf.